Terrestrial Planet Formation: Water & Chaos

Dissertation

zur

Erlangung der naturwissenschaftlichen Doktorwürde
(Dr. sc. nat.)

vorgelegt der

Mathematisch-naturwissenschaftlichen Fakultät

der

Universität Zürich

von

Volker Hoffmann

aus

Deutschland

Promotionskomitee

Prof. Dr. Ben Moore (Vorsitz)
Prof. Dr. Romain Teyssier
Prof. Dr. Lucio Mayer

Zürich, 2016

Volker Hoffmann
Center for Theoretical Astrophysics and Cosmology
Institute for Computational Science
University of Zurich
Winterthurerstrasse 190
CH-8057 Zürich
Switzerland
volker@physik.uzh.ch

Contents

List of Figures

List of Tables

Abstract

In this thesis, we cover the assembly of terrestrial planets by means of N-Body simulations. We cover the growth of embryos from planetesimals within the first 10 million years as well as their late-stage stochastic assembly of terrestrial planets from embryos over the next 150 million years. During the first few million years, we also model the hydrodynamic and gravitational feedback of the gaseous protoplanetary disks on the planetesimals, embryos, and planets. By exploring a variety of initial planetesimal distributions, gas disk lifetimes, and orbits for giant planets, we establish their influence on the final orbital architecture of the planets, their feeding zones, and their expected water contents. In doing so, we pay particular attention to the statistical spread of simulations run as well as differences with to previous simulations which initialised from an initial embryos distribution instead of modelling their growth. We find four key results.

First, in simulations with giant planets, sweeping secular resonances are the main drivers that sculpt the architecture of the final system. In regions beyond the reach of giant planets or simulations without them, dynamics are driven by two-body dynamics between planetesimals, hydrodynamic drag and interactions with the gravitational potential of the disk.

Second, the orbits of the giant planets determine the evolution of the secular resonances. As such, systems with giant planets on eccentric orbits generate the most massive terrestrial planets (10 percent exceed $M_{90} \sim 1.27$ $M_\oplus$) on tight orbits (median semi-major axis $a_{50} \sim 0.86$ AU). If the giant planets are on circular orbit, terrestrial planets tend be less massive ($M_{90} \sim 1.02$ $M_\oplus$) and are on wider orbits ($a_{50} \sim 1.2$ AU). In systems without giant planets, terrestrial planets are the least massive ($M_{90} \sim 0.61$ $M_\oplus$) and on the widest orbits ($a_{50} \sim 2.4$ AU).

Third, terrestrial planets that form in the absence of giant planets appear, irrespective of disk profile and disk mass, extremely wet, and most host a few hundreds of terrestrial oceans worth of water. These values are above those previously reported from simulations, which is caused by the larger feeding zones we obtain when considering the planetesimals being embedded in a gas disk. Therefore, self-consistent growth of planetesimals embedded in a gas disk is essential when attempting to reconstruct the final chemical composition of planets. We do caution that the initial water contents as well as avenues for water loss during the planetary evolution are currently ill-constrained.

Fourth, the chaotic nature of the gravitational dynamics problems causes an even tiny ($<$ mm) initial displacement of a single planetesimal to propagate and completely diverge all planetesimals orbits in given simulation. Owing to perturbations induced by round-off errors, this means that every single simulation produces a different architecture of terrestrial planets. Therefore, individual simulations have no predictive power and only statistical properties taken over suites of simulations are meaningful.

Zusammenfassung

In der vorliegenden Dissertation widmen wir uns der Entstehung und dem Wachstum erdähnlicher Planeten mithilfe von N-Körper Simulationen. Wir betrachten sowohl das Wachstum sogennanter Embryoen innerhalb der ersten 10 Millionen Jahre des Sonnensystems sowie deren Entwicklung zu erdähnlichen Planeten innerhalb der nachfolgenden 150 Millionen Jahre. In den ersten paar Millionen Jahren modellieren wir neben der Hydrodynamik auch die Schwerkraft der protoplanetaren Scheibe und deren Einfluss auf das Wachstum von Planetesimalen und Embryoen. Indem wir eine eine Reihe anfänglicher Planetesimalverteilungen, Lebensdauern der protoplanetaren Scheibe sowie Umlaufbahnen der Gasriesen betrachten, ermitteln wir deren Einfluss auf die Umlaufbahnen der entstandenen inneren Planeten, deren Einzugszonen sowie deren Wassergehalt. In Rahmen dieser Betrachtungen widmen wir uns insbesondere der statistischen Dispersion einzelner Simulationen sowie den Unterschieden zu vorhergehenden Simulationen welche direkt mit anfänglichen Verteilungen von Embryoen initialisiert wurden (anstelle diese auf natürliche Art wachsen zu lassen). Wir kommen zu vier wichtigen Ergebnissen.

Erstens stellen wir fest, dass in Simulationen mit Gasriesen sogennante sekuläre Resonanzen, welche durch das Sonnensystem fegen, zum hauptsächlichen Teil für die schlussendlichen Umlaufbahnen der Planeten verantwortlich sind. In Regionen, wo diese nicht wirken, wird die Dynamik des Systems durch Zweikörper-Wechselwirkungen zwischen Planetesimalen, hydrodynamischen Strömungswiderständen, sowie durch Interaktion mit dem Schwerkraftpotential der protoplanetaren Gassscheibe angetrieben.

Zweitens haben wir bestimmt, dass es die Umlaufbahnen der Gasriesen sind, welche die Entwicklung der sekulären Resonanzen bestimmten. Simulationen mit Gasriesen auf exzentrischen Bahnen führen zu den massivsten terrestrischen Planeten (10% haben Massen oberhalb von $M_{90} \sim 1.27$ $M_\oplus$) auf engen Umlaufbahnen (der Median der grossen Halbachsen ist $a_{50} \sim 0.86$ AE). Haben die Gasriesen eher kreisefömige Umlaufbahnen, tendieren die erdähnlichen Planeten zu kleineren Massen ($M_{90} \sim 1.02$ $M_\oplus$) und leicht weiteren Umlaufbahnen ($a_{50} \sim 1.2$ AE). In Konfigurationen ohne Gasriesen sind die inneren Planeten am wenigsten massereich ($M_{90} \sim 0.61$ $M_\oplus$) mit den weitesten Umlaufbahnen ($a_{50} \sim 2.4$ AE).

Drittens stellen wir fest, dass terrestrische Planeten, welche in System ohne Gasriesen entstehen, zu sehr hohen Wassergehalten von mehreren hundert Ozeanmassen tendieren. Dies ist unabhängig ob der anfänglichen Verteilung der Planeteismale und Lebensdauer der Gasscheibe. Solche Wassergehalte liegen oberhalb derer früherer Simulationen, was durch die grösseren Einzugszonen unserer Embryonen begründet ist. Wir schlussfolgern deshalb, dass die Modellierung des Wachstums von Planeteismalen zu Embryonen und Planeten in der Anwesenheit der protoplanetaren Scheibe essentiell ist, wenn man an der chemischen Komposition der finalen Planeten interessiert ist. Wir müssen jedoch auch darauf hinweisen, dass sowohl die anfängliche

Verteilung von Wasser im Sonnensytem als auch die Prozesse, welche zu Verlust von Wasser auf Planeten führen, derzeit leider nur schwach charakterisierbar sind.

Viertens haben wir ermittelt, dass die chaotische Natur der Gravitationsdynamik dazu führt, dass sich kleinste Verschiebungen ($<$ mm) in der anfänglichen Position eines einzelnen Planeteismales schnell durch das gesamte System verbreitet, welche dazu führt, dass die Durch Rundungsfehler hervorgerufenen Störungen führen deshalb dazu, dass anfänglich identische Simulationen schlussendlich zu grundverschiedenen Planetensystem führen. Folglich haben einzelne Simulationen keinerlei Vorhersagekraft, und lediglich statistische Beschreibungen einer Gruppe von Simulationen sind bedeutsam.

"Would you tell me, please, which way I ought to go from here?"

"That depends a great deal on where you want to get to," said the Cat.

"I don't much care where–" said Alice.

"Then it doesn't matter which way you go," said the Cat

– Lewis Carroll, *Alice's Adventures in Wonderland (1865)*

Preface

Embarking on a PhD is – at least in my experience – much akin to Alice's first steps into Wonderland and her encounter of the enigmatic Cheshire Cat. Not really knowing anything, the way forward is decidedly unclear and – as the Cat remarks – as long as one is making some progress towards somewhere, it does not really matter where that somewhere is. In practice, somewhere tends to be literature reviews, winter schools with more skiing than schooling, and the command line on a login node of some compute cluster.

Over time, the veil of confusion slowly begins to lift and our initial toy models and test simulations gradually give way to somewhat defined research projects. Over the course of the next few years, these projects mature, are written up as papers, found to be inconsistent, tested again, are rewritten, and finally submitted to a journal to face the academic gauntlet.

This thesis is the result of years of learning as well as two research articles; one in review, and one about to be submitted. I hope it has turned out be an entertaining read, which hopefully produces one or two new insights in the reader and – most importantly – raises new and exciting questions.

Hereafter, I drop the pronoun 'I' in favour of 'We' in an effort to emphasize the collaborative nature of research.

Acknowledgments

First of all, I'd like to thank Ben Moore for sponsoring my time in Zurich and consistently coming up with fun research ideas to follow up on. I'd also like to thank Romain Teyssier, Doug Potter, Joachim Stadel, and Lucio Mayer for inspirations and insights into physics and computing.

Second, I'd like to extend special gratitude to Simon Grimm, who was always available to fix bugs as well as implement any and all bizarre feature requests in Genga I may have had – even those that never really ended up in research and (at least up to now) firmly belong in the realm of 'fun to see' (such as the dancing worms in the Poincaré map). It's safe to say that much of this work wouldn't have been possible without his efforts.

Third, I'd like to thank everyone that was – in some capacity or another – involved in planet formation discussions with me during my time in Zurich and Switzerland. In addition to the above, this includes Amaury Thiabaud, Joanna Drążkowska, Miles Timpe, Clement Surville, Christian Reinhardt, Luc Senecal, as well as the entire PlanetZ and PlanetS groups with rosters too long to list here. I particularly happy that Maria Schönbächler and Robert Steele introduced us to the wonderful world of cosmochemistry and the meticulous lab work involved.

Fourth, it's only appropriate to thank our tireless administrative staff Regina Schmid and Suzanne Wilde for their efforts in always managing to have every single thing they have to organise for us complete in a timely and efficient manner.

Penultimately, I'd like thank my family and my wonderful girlfriend Christin for supporting and encouraging me throughout my quest towards this thesis.

Last but not least, my gratitude goes to the external reviewer Sean Raymond for his time in reading through and suggesting improvements to this work.

1

Introduction

Up to the early 1990s, all was well for theorists and observers employed in the field of planet formation and evolution. The Solar System was the only known planetary system and more and more observational as well as chemical data of decent quality had steadily become available from both telescopes and space probes. Given the deluge of data and persistence of modellers, it was only a matter of time until the secrets of how the Solar Systems formed would be laid bare.

In the past 20 years, we have had become more cautious with optimism. Backed by detections of large numbers of exoplanetary systems, researchers (and hopefully the public) are now aware that the peculiar dynamical configuration of our own Solar System is hardly the single natural outcome of the process of star- and planet formation. The Galaxy is teeming with stars hosting planets with such illustriously named categories as 'Hot Jupiters', 'Super-Earths' and 'Sub-Neptunes'. Although observational constraints currently preclude us from accessing the full range of planetary masses and orbital configurations, there is little to suggest we won't find other interesting arrangements or even systems mimicking our own.

Constructing a working end-to-end model of planet formation is difficult, especially one capable of accounting for the cacophony of observed architectures. To make headway, the problem is generally broken down into more manageable individual chunks which are researched in isolation. In rough chronological order, these address the collapse of a molecular core into a protostar surrounded by a protoplanetary disk, the growth of dust into rocky planetesimals, the growth of planetesimals into either terrestrial planets or the cores of more massive giant planets, and the subsequent the evolution of the young planetary systems. Fuelled by ever-increasing computational power and algorithmic advances, sophisticated numerical simulations are now commonly used in the modelling of all stages of planet formation.

In this work, we focus on the intersection of numerical methods and model assumptions and how they affect the results of simulations that model growth of planetesimals into terrestrial planets. To this end, we begin with a general outline

of physical processes and steps involved in planet formation in Chapter 2. Owing to a rich history of prior research, the Solar System is still the most suitable testbed for planet formation models. We review such formation models and the constraints they have to match in Chapter 3. We follow this up by setting the stage for extrasolar systems in Chapter 4 where we review observational techniques, architectural properties, and model attempts.

Chapters 5 and 6 make up the original research in this work. The chapters are reproductions of research articles that have either been submitted for publication (Chapter 5) or are close to submission (Chapter 6). In Chapter 5 (*"Chaos in Terrestrial Planet Formation"*), we discuss the far-reaching consequences of seemingly innocuous round-off errors in simulations. We discover that identical initial conditions lead to distinctly different system architectures. As such, individual simulations have no predictive power and we must rely on statistical approaches instead, which we apply to a number of models. In Chapter 6 (*"Wet Terrestrial Planets: Fact or Artifact?"*), we explore the water content of planets in hypothetical extrasolar systems that consist of terrestrial planets only. Along the way, we find that self-consistent end-to-end modelling of planetesimals growing into terrestrial planets is extremely important and gives drastically different results than when one uses any of the commonly employed short-cuts to conserve computational resources. Applying this lesson to a suite of simulations, it appears that many extrasolar terrestrial planets may well be 'water-worlds', but we must caution that this result warrants further scrutiny as many of the assumptions and model ingredients remain poorly understood.

Finally, we synthesize our work and attempt to identify the most relevant and promising future endeavours in Chapter 7.

2

Planet Formation: Methods & Models

"*The treasures hidden in the heavens are so rich, precisely in order that the human mind shall never be lacking in fresh nourishment.*"

– Johannes Kepler, *Mysterium Cosmographicum (1596)*

Although the history of astronomy ostensibly traces back some 10′000 years (Gaffney et al., 2013), astrophysics originates in the renaissance with Johannes Kepler's development of celestial mechanics based on Tycho Brahe earlier observations (Brahe, 1610; Kepler, 1609). First formalized by Newton (1687), progress based on an understanding of gravitational forces eventually lead to the Laplace-Lagrange solutions for the secular motions of Jupiter and Saturn (Laplace et al., 1829).

Born out of this impressive lineage, modern day astrophysics marries celestial dynamics and fluid mechanics (which comes with its own fascinating history) and equips us with the tools required to model the formation of planets, which we now outline. In Section 2.1, we describe some of the mathematical tools and underlying physical processes for our models and simulations. In Section 2.2. we follow this up by walking through the sequence of events that leads from collapsing interstellar clouds to planets.

2.1. Mathematical Models & Numerical Methods

2.1.1. Astrophysical Fluid Dynamics

At is core, astrophysical fluid (or gas) dynamics is based on sets of hyperbolic conservation laws for fluids, which are derived from the Boltzmann equation using pertur-

bative methods (Shu, 1992, Chapters 2 and 3). In order, these are the Navier-Stokes equations for mass, momentum, and internal energy conservation, viz.

$$\frac{\partial \rho}{\partial t} + \frac{\partial}{\partial x_k}(\rho u_k) = 0, \tag{2.1}$$

$$\frac{\partial}{\partial t}(\rho u_i) + \frac{\partial}{\partial x_k}(\rho u_i u_k + P\delta_{ik} - \pi_{ik}) = -\rho \frac{\partial \mathcal{V}}{\partial x_i}, \tag{2.2}$$

$$\frac{\partial}{\partial t}(\rho \mathcal{E}) + \frac{\partial}{\partial x_k}(\rho \mathcal{E} u_k) = -P\frac{\partial u_k}{\partial x_k} - \frac{\partial F_k}{\partial x_k} + \pi_{ik}\frac{\partial u_i}{\partial x_k}, \tag{2.3}$$

where u is the velocity, ρ the density, P the pressure, $\mathcal{E}$ the internal energy, δ_{ik} the Kronecker delta, and $\partial\mathcal{V}/\partial x_i$ an external force term that that arises from coupling to gravity, magnetic fields, or radiation fields.[1] The viscous shear tensor π_{ik} arises from the fluid's resistance to deformation, i.e.

$$\pi_{ik} = \mu D_{ik}, \qquad D_{ik} = \frac{\partial u_i}{\partial x_k} + \frac{\partial u_k}{\partial x_i} - \frac{2}{3}\frac{\partial u_j}{\partial x_j}\delta_{ik}, \tag{2.4}$$

where $\mu = \nu\rho$ is the dynamic viscosity, ν the kinematic viscosity, and D_{ik} the deformation rate tensor. Finally, $\partial F_k/\partial x_k$ describes the conductive heat flux in the gas at temperature T and thermal conductivity $\mathcal{K}$, i.e.

$$F_k = -\mathcal{K}\frac{\partial T}{\partial x_k}. \tag{2.5}$$

In typical astrophysical systems, the mean free path of the gas molecular is comparatively large and viscous timescales tend to be much larger than the dynamical time of the system. Heat flux, on the other hand, tends to be extremely efficient and the systems are in thermal equilibrium. Therefore, viscous effects and conductive heat transport terms are frequently dropped ($F_k = \pi_{ik} = 0$) and Eqns. (2.1), (2.2), and (2.3) reduce to the Euler equations.

Combined with a closure relation $P = f(\rho, T)$ describing the thermodynamical properties of the gas, the Euler equations can be solved on either a grid or can be recast as particle dynamics conservation laws. On a grid, the conservation laws are typically solved by finite volume schemes (Teyssier, 2002; Toro, 1997). When recast in particle form, we arrive at Smoothened Particle Hydrodynamics where the fluid is evolved by advection of representative particles instead (Springel, 2010; Wadsley et al., 2004). Hybrid methods exist.

2.1.2. Reynolds Stress, Effective Viscosity, Turbulence, Alpha Disks

Now consider decomposing the fluid velocity into a time-averaged and a fluctuating part, i.e. $u(\vec{x}, t) \to \bar{u}(\vec{x}) + u'(\vec{x}, t)$, where we have used the position vector $\vec{x}$ and time coordinate t to clarify the split. This is called Reynolds decomposition. Substituting this into Eqn. (2.2) in the absence of external forces ($\partial\mathcal{V}/\partial x_k = 0$) yields, after some

[1] Each of these fields then brings along their own conservation laws and equations of motion. For example, gravity brings the Poisson equation or magnetic hydrodynamics the induction equation.

manipulation, the momentum equation for the Reynolds Averaged Navier Stokes (RANS) equations, viz.

$$\rho \frac{\partial \bar{u}_i}{\partial t} + \rho \bar{u}_k \frac{\partial \bar{u}_i}{\partial x_k} = \frac{\partial}{\partial x_k} \left(-\bar{P}\delta_{ik} + \bar{\pi}_{ik} + \rho \overline{u_i' u_k'} \right), \tag{2.6}$$

where $\bar{\pi}_{ik}$ and $\bar{P}$ are the mean viscous tensor and mean pressure. Interestingly enough, the rightmost term $\rho \overline{u_i' u_j'}$ appears in the same mathematical construct as the pressure and stress, so we can identify it as a fluid stress that arises from averaging over fluctuations along different directions of the velocity field. This is called Reynolds stress and is solely dependent on velocity fluctuations. It is not related to kinematic stresses that arise from velocity shear, i.e. it appears even if $\pi_{ik} = 0$.

Analogous to the decomposition of π_{ik} in Eqn. (2.4), we can write the Reynolds stress as the product of some constant with the deformation tensor of the velocity field. However, instead of the deformation of the total velocity field D_{ik}, we use the deformation of the mean velocity field $\bar{D}_{ik}$ to describe fluctuations. In other words,

$$-\rho \overline{u_i' u_k'} = \rho \, \nu_{\text{Eff}} \bar{D}_{ik}, \qquad \bar{D}_{ik} = \frac{\partial \bar{u}_i}{\partial x_k} + \frac{\partial \bar{u}_k}{\partial x_i} - \frac{2}{3} \frac{\partial \bar{u}_j}{\partial x_j} \delta_{ik}, \tag{2.7}$$

where ν_{Eff} is an effective viscosity induced by velocity fluctuations arising from turbulent motions within the fluid. These motions are conceptualised by the picture of 'eddies within eddies' (Frisch, 1996) that transport energy injected at large scales to small scales where it ultimately dissipates. This type of effective viscosity is called 'eddy viscosity' and dates back to Jacques Boussinesq (Schmitt, 2007).

In principle, astrophysical simulation codes based on the Euler equations support turbulence (and therefore the effective viscosity provided by Reynolds stresses) naturally, provided that a mechanism capable of driving turbulence is present (for example, fluid, gravitational, or magnetic instabilities). In the practical business of simulations, however, things are bit more complicated for three reasons. Firstly, the injection scale of turbulence must be well-defined and captured by the simulation. In accretion disks, the largest possible eddies are on the order of the disk scale-height. In galaxies, eddies are constrained by the scale height of the galaxy. In both cases, this means that simulations that do not model the entire system (for example, when focussing on molecular cloud or a local shearing box approximation of the accretion disk), turbulence must be driven artificially through boundary conditions. Secondly, to accurately model the turbulent energy transport from large to small scales, the range of scales that is resolved needs to be sufficiently large. In practice, this requires very good numerical resolution which is computationally expensive.[2] Thirdly, at small enough scales, energy is in fact dissipated through molecular viscosity, which is not modelled in the Euler equations by the argument that molecular viscosity is not effective at astrophysical scales (in a non-turbulent medium). As such, energy at small scales is dissipated through the numerical dissipation inherent to the scheme, which may not be a faithful representation of the process. We should thus avoid trusting smallest scale phenomena too much.

[2] Simulations of turbulence in the interstellar medium suggest that even at spatial resolutions of 1024^3 grid cells some statistical descriptors remain unconverged (Federrath et al., 2010).

To sidestep the pains associated with numerical simulations of sufficiently high resolution and dynamic range as well as to facilitate theoretical model building, Shakura & Sunyaev (1973) proposed encapsulating the effective viscosity provided by the turbulence (more specifically, by Reynolds stresses) in a parameter α. Noting that the largest eddy scale for accretion disks is the scale height h and that perturbations propagate with the sound speed c_s, we have

$$\nu_{\text{Eff}} = \alpha c_s h. \tag{2.8}$$

For a given disk model, c_s and h are set, and the choice of α is up to how well the modeller understands the processes that induce turbulent motion. Given that, we obtain value of ν_{Eff} which we can use in simplified disk models. We briefly describe these in Section 2.2.1.

2.1.3. N-Body Methods

At its core, evolving the orbits of planetesimals and planets is a gravitational dynamics problem. For two point particles of mass m_i and m_j separated by $\vec{r}_{ij}$, the gravitational force is

$$\vec{F}_{ij} = -\mathcal{G}\,\frac{m_i m_j}{|\vec{r}_{ij}|^2}\,\hat{\vec{r}}_{ij}, \tag{2.9}$$

where $\hat{\vec{r}}_{ij}$ is the unit vector of the separation. For a system of a $N = 2$ particles of mass $m_i = M$ and $m_j = m$, where $M \gg m$, we recover the Kepler problem. Here, the orbit of the less massive particle around the (much) more massive one is a conic section, viz.

$$\frac{1}{r} = -\frac{\mathcal{G}Mm}{L^2}\left[1 + e\cos\theta\right], \tag{2.10}$$

where r is the radial separation, $L = mr^2\dot{\theta}$ is the angular momentum, e the eccentricity of the orbit, θ the orbital phase, and $\mathcal{G}$ the gravitational constant. For $N > 2$, such analytical solutions cannot be constructed,[3] and we have to resort to numerical techniques. Typically, these first compute interparticle forces and then update particle velocities and positions to varying precision. For example, the most obvious scheme would calculate forces via Eqn. (2.9) and then use Euler's method to integrate the configuration of the system over some timestep.

The accuracy of numerical methods is judged by how accurate forces are computed and how well the integrator conserves energy. Integrators based on Taylor expansions (for example, explicit Euler and Runge-Kutta schemes) tend to have a secular energy error that piles up over time. In orbital mechanics, this results in the orbit spiralling out or inward which is obviously undesired. More suitable methods are symplectic, i.e. they preserve the structure of Hamiltonian from one step to the next. For example, if we can split the Hamiltonian $\mathcal{H}$ into its potential and

[3] This is not entirely true. There exists a proverbial zoo of fascinating periodic solutions for orbits in the restricted three-body problem. See, for example, Bruno (1994) or Henon (1997).

kinetic energy terms, we can construct a leap-frog integrator which has an oscillating energy error, but very small secular trends. For a system of N particles, such a decomposition yields

$$\mathcal{H} = \mathcal{T} + \mathcal{V} = \sum_{j=0}^{N-1} \frac{p_j^2}{2m_j} - \sum_{j=0}^{N-2} \sum_{k=j+1}^{N-1} \frac{\mathcal{G} m_j m_k}{r_{jk}} \tag{2.11}$$

where $\mathcal{T}$ and $\mathcal{V}$ are the kinetic and potential energy, p_i and m_i the linear momentum and mass of particle i, and r_{jk} the distance between particles j and k (Murray & Dermott, 1999, Chapter 2). A leap-frog integrator constructed from such an Hamiltonian would tend to oscillate particles about their true orbit, but they would not spiral away. There is, however, a secular phase error.

Similarly, the force accuracy depends on the method. If energy accuracy is not terribly important[4] and the number of steps is on the order of 10^4 to 10^5, tree methods can significantly speed up code execution because they bring down computational cost from $\mathcal{O}(N^2)$ to $\mathcal{O}(N \log N)$ (Barnes & Hut, 1986). Some cosmological simulations fall in this regime because high-accuracy results are statistically identical to lower accuracy results and dynamical times can be on the order the simulation time (Doug Potter, Private Communication, 13 January 2016). The latter is obviously not true for simulations that aim to track the growth of terrestrial planets from planetesimals accretion through the late-stage accretion.[5]

If one of the masses (such as a star) absolutely dominates the gravitational potential of the system, we can construct an even better scheme by splitting the Hamiltonian into a Keplerian (the motion about the central mass) and an interaction (interactions between all other masses) part. For a system of N point masses, a suitable splitting results in

$$\mathcal{H} = \underbrace{\sum_{j=1}^{N-1} \left(\frac{\tilde{p}_j^2}{2\tilde{m}_j} - \frac{\mathcal{G} m_0 m_j}{\tilde{r}_j} \right)}_{\mathcal{H}_{\text{Kepler}}} + \underbrace{\sum_{j=1}^{N-1} \frac{\mathcal{G} m_0 m_j}{\tilde{r}_j} - \sum_{j=0}^{N-2} \sum_{k=j+1}^{N-1} \frac{\mathcal{G} m_j m_k}{r_{jk}}}_{\mathcal{H}_{\text{Interaction}}}, \tag{2.12}$$

where m_0 is the central mass, m_j and r_{jk} as before, and $\tilde{p}_j$ and $\tilde{r}_j$ the momentum and position of particle j in Jacobi coordinates, i.e. in a frame relative to the barycentre of all preceding particles in the sum. From such a Hamiltonian we can construct the symplectic map (a.k.a. *mixed-variable symplectic integrator*) first described in Wisdom & Holman (1991) and subsequently extended to higher order by Kinoshita et al. (1991). Here, the Keplerian orbits of the particles around the star are evolved analytically and separately from the mutual gravitational perturbations of the particles. For a comprehensive description, see also Chapter 9.5.4 in Murray & Dermott (1999).

However, this scheme requires the interaction term of the Hamiltonian to be much smaller than the Keplerian part, which breaks down if particles enter close

[4] By 'not terribly important', we mean whether numerical tests show (statistical) convergence at different accuracy levels.

[5] We discuss the timescales of terrestrial planet formation below. For now, note that a typical formation simulation is evolved for ~ 150 Myr and does $\sim 9 \times 10^9$ steps.

encounters, i.e. they cross within a few Hill radii of one another. To deal with this, Eqn. (2.12) can be rewritten so that $\mathcal{H}_{\text{Kepler}}$ absorbs a close encounter term that is activated by means of a suitable changeover function as particles enter close encounters (Chambers, 1999). As a useful side-effect, such rewriting transforms the description into democratic coordinates where the evaluation order is not dependent on the ordering of particles as is the case for Jacobi coordinates.

This is the essence of the N-Body code GENGA (Grimm & Stadel, 2014) which we use in the simulations discussed in Chapters 5 and 6. Due do its symplectic nature, GENGA has excellent energy conservation properties, and resolves close encounters to machine precision. To maintain good energy conservation over millions of orbits, GENGA uses direct force evaluations for the interaction part of the Hamiltonian, which in principle slows the code down. To offset this slowdown, GENGA runs entirely on Graphics Processing Units.

2.1.4. Disturbing Function, Secular Resonances

While N-Body simulations derived from the considerations outlined above are a powerful tool, they bear the danger of obscuring physical insights into the processes at work. As most of this work is concerned with the application of celestial dynamics, we now summarise a powerful model for understanding some of the processes in a planet forming system.

As discussed, the gravitational two-body problem is integrable and readily solved analytically. For three and more bodies, the problem has no analytical solution and needs to be integrated numerically. However, for any given object,we can approximate the influence of all other bodies by encapsulating their collective effects into a disturbing function $\mathcal{R}$. Consider a system of two point masses (m, m') orbiting a central mass (M). We can write the gravitational acceleration the inner[6] of the two bodies experiences as

$$\frac{\mathrm{d}^2\vec{r}}{\mathrm{d}t^2} = \nabla\left(\mathcal{U} + \mathcal{R}\right), \tag{2.13}$$

where

$$\mathcal{U} = -\mathcal{G}\left(\frac{M+m}{r}\right) \tag{2.14}$$

is the contribution of the central potential and

$$\mathcal{R} = \frac{\mathcal{G}m'}{|\vec{r}-\vec{r}'|} - \mathcal{G}m\frac{\vec{r}\cdot\vec{r}'}{r'^3}, \tag{2.15}$$

[6]For the outer mass, we can write down an equivalent formulation. In fact, the procedure applies equally to any number of bodies.

the contribution of the outer mass. Finally, letting ψ be the angle between the position vectors $\vec{r}$ and $\vec{r}'$ for the outer and inner body, we can write $\mathcal{R}$ as a sum over Legendre polynomials, i.e.

$$\mathcal{R} = \frac{Gm'}{r'} \sum_{\ell=2}^{\infty} \left(\frac{r}{r'}\right)^{\ell} P_{\ell}(\cos\psi). \tag{2.16}$$

By expanding ψ as a linear combination of orbital elements of the bodies, we will eventually arrive at a parametrisation of the disturbing function of the form

$$\mathcal{R} = \mathcal{G}m' \sum S(a, a', e, e', I, I') \cos\varphi, \tag{2.17}$$

where a, a', e, e', I and I' are the semi-major axes, eccentricities, and inclinations of the two bodies and

$$\phi = j_1\lambda' + j_2\lambda + j_3\bar{\omega}' + j_4\bar{\omega} + j_5\Omega' + j_6\Omega, \tag{2.18}$$

where $\sum_{k=1}^{6} j_k = 0$ and $\bar{\omega}'$, $\bar{\omega}$ are the longitudes of perihelion of the two bodies, Ω', Ω the longitudes of the ascending nodes, and λ', λ are related to the orbital phases. Actually expanding $\mathcal{R}$ as well as properly classifying the result in terms of secular and mean-motion resonances is a lengthy and arduous affair best left to textbooks (Murray & Dermott, 1999, Chapter 6). At this point, we opt to proceed with only a small example of how $\mathcal{R}$ can be used which will turn out to be relevant to the dynamics of planetesimals in the presence of Jupiter and Saturn.

By following a separate line of involved mathematical manipulations (Brouwer & Clemence, 1961), we may obtain Lagrange's planetary equations, which relate secular variations in the orbital elements of a given planet to the disturbing function $\mathcal{R}$ generated by the perturbers in the system. To first order, (some of) these are

$$\frac{\mathrm{d}e}{\mathrm{d}t} = -\frac{1}{na^2e}\frac{\partial\mathcal{R}}{\partial\bar{\omega}}, \qquad \frac{\mathrm{d}\bar{\omega}}{\mathrm{d}t} = \frac{1}{na^2e}\frac{\partial\mathcal{R}}{\partial e}, \tag{2.19}$$

and

$$\frac{\mathrm{d}I}{\mathrm{d}t} = -\frac{1}{na^2I}\frac{\partial\mathcal{R}}{\partial\Omega}, \qquad \frac{\mathrm{d}\Omega}{\mathrm{d}t} = \frac{1}{na^2I}\frac{\partial\mathcal{R}}{\partial I}, \tag{2.20}$$

where n is the mean motion (Murray & Dermott, 1999, Chapter 6.8). In other words, given some description of $\mathcal{R}$, it seems that e, I, $\bar{\omega}$, and Ω will exhibit secular variations given by the appropriate derivates of the disturbing function. Preparing to shed some light onto this, let us make one more change of coordinates,

$$h = e\sin\bar{\omega}, \qquad k = \cos\bar{\omega}, \tag{2.21}$$

and

$$p = I\sin\Omega, \qquad q = I\cos\Omega. \tag{2.22}$$

Now, let us return to our system of two bodies orbiting a central mass. Denoting the bodies by $j = 1, 2$ and writing down a suitably averaged form of $\mathcal{R}$,[7] we can expand Eqns. (2.19) through (2.22) to obtain a set of coupled differential equations for h_j, k_j, p_j, and q_j (Murray & Dermott, 1999, Chapter 7.2). These equations have solutions of the form

$$h_j(t) = \sum_{i=1}^{2} e_{ji} \sin\left(g_i t + \beta_i\right), \qquad k_j(t) = \sum_{i=1}^{2} e_{ji} \cos\left(g_i t + \beta_i\right), \tag{2.23}$$

and

$$p_j(t) = \sum_{i=1}^{2} I_{ji} \sin\left(f_i t + \gamma_i\right), \qquad k_j(t) = \sum_{i=1}^{2} I_{ji} \cos\left(f_i t + \gamma_i\right). \tag{2.24}$$

Ignoring the phase constants $\beta_{1,2}$ and $\gamma_{1,2}$, it would appear as if our system has four fundamental frequencies $g_{1,2}$ and $f_{1,2}$ which dictate oscillations in their orbital elements. For example, substituting orbital and physical parameters for the Jupiter-Saturn system, we find oscillation frequencies (Murray & Dermott, 1999, Chapter 7.3) of

$$g_1 \sim 9.6 \times 10^{-4}\ ^\circ/\text{yr}, \qquad g_2 \sim 6.1 \times 10^{-3}\ ^\circ/\text{yr}, \tag{2.25}$$

and

$$f_1 = 0, \qquad f_2 \sim -7.1 \times 10^{-3}\ ^\circ/\text{yr}. \tag{2.26}$$

Now consider an extension of this treatment to include the motion of a massless test particle which is subjected to the gravitational perturbation of Jupiter and Saturn. Neither of the two will be affected by the massless test particle, but we find oscillation frequencies A and B for the test particle depending on its semi-major axis. Analogous to the above, the oscillations in h, k, p, and q are

$$h(t) = -\sum_{i=1}^{2} \frac{\nu_i}{A - g_i} \sin\left(g_i t + \beta_i\right), \qquad k(t) = -\sum_{i=1}^{2} \frac{\nu_i}{A - g_i} \cos\left(g_i t + \beta_i\right), \tag{2.27}$$

$$p(t) = -\sum_{i=1}^{2} \frac{\mu_i}{B - f_i} \sin\left(f_i t + \gamma_i\right), \qquad q(t) = -\sum_{i=1}^{2} \frac{\mu_i}{B - f_i} \cos\left(f_i t + \gamma_i\right), \tag{2.28}$$

[7] This is a loaded statement which we use to handwave away a complicated expansion and classification of terms in the disturbing function. In short, $\mathcal{R}$ can be decomposed into fast angles and slow angles. By averaging over the fast angles (i.e., linear combinations involving the orbital phase), we retain a form of $\mathcal{R}$ that describes only the slow angles $\bar{\omega}$, Ω as well as a, e, and I. For more details, please see Chapter 6 in Murray & Dermott (1999).

where $\beta_{1,2}$ and $\gamma_{1,2}$ are phase constants,

$$\nu_i = \sum_{k=1}^{2} A_k e_{ki}, \qquad \mu_i = \sum_{k=1}^{2} B_k e_{ki}, \tag{2.29}$$

and A and B depend on the masses of Jupiter and Saturn (and the primary) as well as the semi-major axis at which we place the test particle (Murray & Dermott, 1999, Chapter 7.4). This means that there will be choices where the semi-major axis takes values such that $A \sim g_{1,2}$ or $B \sim f_{1,2}$. Here, h, k, p, and q diverge! This is the nature of secular resonances between the Jupiter-Saturn system and other bodies in the system that are much lighter. Customarily, these resonances are labelled as follows: $A = g_1$ is ν_5, $A = g_2$ is ν_6, $B = f_1$ is ν_{15}, and $B = f_2$ is ν_{16}.

Finally, we may consider the contribution of a protoplanetary disk. If the disk is massive enough, it will bring along its own gravitational potential. This modifies the disturbing function, which moves secular resonances to a different location. As the disk dissipates, the location of the secular resonances sweep through the disk, depending on how exactly the dissipation proceeds (Nagasawa et al., 2000). This sweep can excite and shepherd bodies along.

2.2. Formation and Evolution of Planetary Systems

Before we describe the peculiarities of the Solar System in Chapter 3, we first review the general sequence of events that is thought to lead to the formation of planetary systems. These events are estimated to unfold on timescales of a few hundred million years. However, the lifetime of planetary systems is much longer, on the order of billions of years, and important dynamics can alter the system architecture on such timescales. While we do not specifically address such long term dynamics here, we refer to Davies et al. (2014) for an overview.

2.2.1. From Molecular Clouds to Protoplanetary Disks

Giant molecular clouds are the nurseries for the formation of stars and their associated planetary systems (McKee & Ostriker, 2007). They are very cold structures (< 30 K) predominately hosting molecular hydrogen. They measure sizes of 2 to 20 pc for mean densities and total masses of 10^2 to 10^3 H_2/cm^3 and 10^2 to 10^6 $M_\odot$ with free-fall times on the order of 0.3 to 3 Myr. Observed velocity dispersions are on the order of 1 to 10 km/s and observations with CO tracers reveal turbulent motions and substantial fractal substructures. These are driven by the local gravitational collapse of overdensities, the densest of which (molecular cores) have masses on the order of a few solar masses. They spread out over fractions of a pc, implying mean densities that may exceed 10^5 H_2/cm^3 (Bergin & Tafalla, 2007; Klessen, 2011). They are also extremely cold (7 to 12 K), so that further gravitational collapse can proceed until the densities become high enough for radiative cooling to become ineffective. At this point, further collapse increases both densities and temperatures until nuclear fusion is ignited. A star is born.

To conserve angular momentum, the gas surrounding the young star collapses into a rotating disk structure. At this point, the protostellar disk can extend for hundreds of AU and host masses of up to 90 per cent of this host star, depending on the initial angular momentum of the core (Perryman, 2011). Keplerian shear, self-gravity, and magnetic instabilities induce turbulent motions which help to dissipate energy through Reynolds stresses, thereby moving mass toward the star and angular momentum outwards. Close to the star (fractions of an AU), its magnetic field connects to the gas disk and funnels material onto the surface which releases energy in accretion shocks (Bouvier et al., 2007). Accretion rates onto the star are highly variable ranging from 10^{-8} to 10^{4} $M_{\odot}$/yr with bursts likely triggered by fragmentation induced by gravitational instabilities (Dunham et al., 2014; Vorobyov & Basu, 2010). Within a few 10^{5} years, the bulk of the gas clears and the inward transport of mass and accretion onto the star decreases to rates of 10^{-9} to 10^{-7} $M_{\odot}$/yr as the systems enter the T-Tauri phase (Gullbring et al., 1998), although some stars retain bursts of accretion (Hartmann & Kenyon, 1996). Both the star and the disk are now exposed and can be readily detected by their characteristic spectral infrared emission profile (Williams & Cieza, 2011). At this point, we may describe the disks as protoplanetary instead of protostellar.

Although dominated by molecular hydrogen and helium, the molecular clouds from which the stars form also host trace amounts of other elements and molecules, which are now also bound up in the protoplanetary disk. Depending on the parlance, these are usually referred to as dust or presolar grains.[8] In total, these grains account for about a hundredth of the total disk mass, setting the canonical dust-to-gas ratio at 0.01. Unfortunately, this number is not very well constrained because of the inherent difficulty of astronomically probing the gas and dust separately in the same disk regions.[9] It is from this dust that the terrestrial planets as well as the cores of the larger planets form. As the mass and density of the gas disk drops, cooling becomes more efficient, the disk temperature drops, and the dust embedded the gas begins to condense out. The order and location of condensing aggregates is set by the temperature profile and initial chemical composition. For a given composition, the order at which different condensates form as the temperature falls is called the *condensation sequence*. Conversely, given a temperature profile, there will be a distinct heliocentric distance beyond which a condensate forms called the *snow line*.

At this point, let us take stock of the chemical composition as well as physical processes of protoplanetary disks and attempt to link them to observations. Figure 2.1 shows a cross-sectional (a side-on cut) sketch of a typical protoplanetary disk around a young star. This is a simplified illustration and real disks are neither fully

[8] Dust refers to aggregates with sizes up to a few μm that absorb photons of various wavelengths and reemit in the infrared. We may also hear the term 'metals', which refers to any elements that are not hydrogen or helium.

[9] There are two problems here. Firstly, dust in protoplanetary disks is observed at infrared wavelengths, but the mass which is reconstructed from observations is sensitive to the assumed grain-size distribution. Secondly, molecular hydrogen (H_2) is extremely difficult to observe directly because it has very weak transition lines. Instead, it is usually traced by observing CO, but this is complicated by the fact that the disk is optically thick towards CO (Pascucci et al., 2006). Recent work suggests using lines from hitherto unused CO isotopes that are more readily observed, but the key issue of linking CO mass to H_2 mass remains (Miotello et al., 2014).

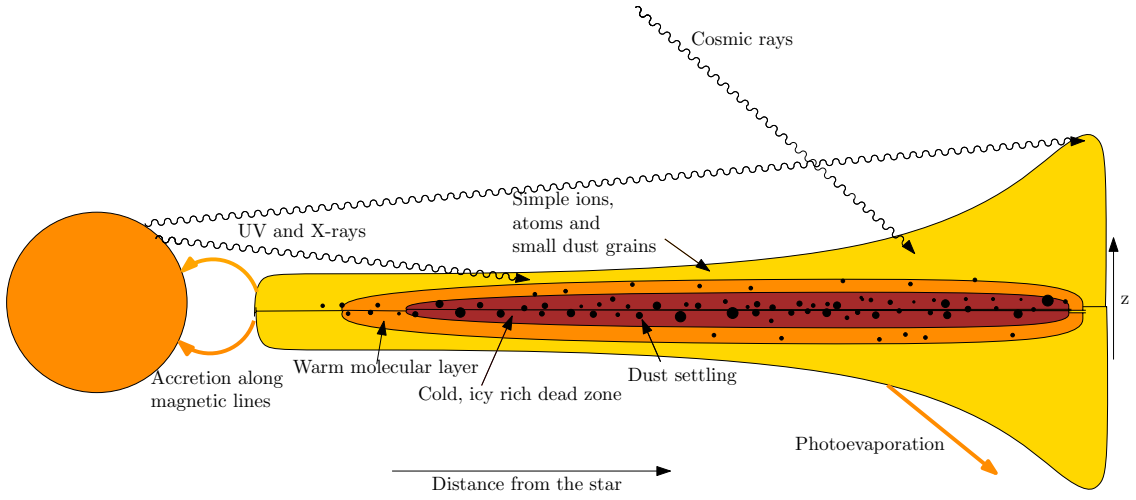

Figure 2.1. Cross-sectional sketch of a protoplanetary disk (right) around a young star (left) and the various physical and chemical processes governing the evolution of dust and gas. The figure has been adapted from Grimm (2015) with permission.

rotationally symmetric, symmetric around the midplane, nor do they follow only the one particular flaring profile we suggest. Nevertheless, it is illustrative of the most important aspects.

Dust & Gas Dynamics Dust grains have a much larger mean free path than the gas constituents. Therefore, the dust continuum is essentially pressureless. Gas, on the other hand, has internal pressure-forces (gradients) that can balance external gravitational forces. This has two important consequences. Firstly, dust grains are pulled towards the disk midplane due to the vertical component of the gravity of the star. The gaseous disk, on the other hand, puffs up as it establishes a vertical pressure gradient. Secondly, while dust orbits the host star on Keplerian trajectories, the gas can orbit at either sub- or super-Keplerian velocity, depending on the direction of pressure gradients.

We can easily verify this by writing down the vertical and radial force balances in the limit of negligible gas disk mass, viz.

$$\frac{1}{\rho}\frac{\partial P}{\partial z} = \frac{\partial \Phi_\star}{\partial z} = \frac{\mathcal{G} M_\star z}{(z^2 + r^2)^{3/2}}, \tag{2.30}$$

and

$$\frac{v_{\mathrm{Orbit,T}}^2}{r} = \frac{\partial \Phi_\star}{\partial r} + \frac{1}{\rho}\frac{\partial P}{\partial r} = \frac{\mathcal{G} M_\star r}{(z^2 + r^2)^{3/2}} + \frac{1}{\rho}\frac{\partial P}{\partial r}, \tag{2.31}$$

where $v_{\mathrm{Orbit,T}}$ is the tangential orbital velocity, $\mathcal{G}$ the gravitational constant, $M_\star$ the mass of the star, P and ρ the gas pressure and density, r the radial distance from the star, z the vertical distance from the midplane, $\Phi_\star$ the gravitational potential of the star, and we have assumed locally isothermal gas. For gas,

the vertical pressure gradient $\partial P/\partial z$ balances the gravity in a hydrostatic equilibrium. The radial pressure gradient $\partial P/\partial r$ modifies the orbital velocity $v_{\rm Orbit}$, depending on its sign. For dust, $\partial P/\partial z = \partial P/\partial r = 0$, so that (i) grains must settle in the midplane ($z = 0$) to fulfill $0 = \partial\Phi_\star/\partial z$, and (ii) grains orbit at Keplerian speeds $v^2_{\rm Orbit,T} = \mathcal{G}M_\star/r$ (for $z = 0$).[10]

Density Structure To first approximation, we can assume the disk to be in vertical hydrostatic equilibrium as outlined above. Assuming the disk is locally isothermal (the sound speed c_s is constant along the vertical z), has an equation of state $P = \rho c_s^2$, and is thin ($z \ll r$), Eqn. (2.30) integrates to

$$\rho(r, z) = \rho_0(r)\, \mathrm{e}^{\left(-\frac{1}{2}\frac{z^2}{h^2}\right)}, \tag{2.32}$$

where ρ_0 is the midplane volume density, h the scale height, and

$$\frac{h}{r} = \frac{v_{\rm K}}{c_s} \tag{2.33}$$

is the disk aspect ratio. Here, $v_{\rm K} = v_{\rm Orbit,T}$ is the Keplerian orbital velocity, and we find the aspect ratio to be proportional to the Mach number of the flow. Detailed modelling indicates aspect ratios to vary between 0.05 at a few AU and 0.5 at hundreds of AU (Chiang & Goldreich, 1997; D'Alessio et al., 1998; Dullemond et al., 2002), suggesting that protoplanetary disks are supersonic and flared. Integrating Eqn. (2.32) along the vertical relates the surface density Σ to the midplane volume density and scale height, viz.

$$\rho_0(r) = \frac{\Sigma(r)}{\sqrt{2\pi}h(r)}. \tag{2.34}$$

Observationally, disk surface density profiles can be reconstructed through interferometric observations in the sub-mm regime. There are two major challenges. First, owing to insufficient resolution, the inner ($\lesssim 20$ AU) are difficult to resolve. Second, the outer regions ($\gtrsim 200$ AU) of the disks are very cool and have low densities, so they tend not to emit very strongly. Nevertheless, to within observational constraints, disk surface densities appear to be best described by a power law which is exponentially truncated at a cutoff radius. This appears in line with viscous modelling (see below) of protoplanetary disks which suggests profiles of the form

$$\Sigma(r) = (2-\gamma)\,\frac{M_{\rm Disk}}{2\pi r_{\rm c}}\left(\frac{r}{r_{\rm c}}\right)^{-\gamma} \mathrm{e}^{-\left[\left(\frac{r}{r_{\rm c}}\right)^{2-\gamma}\right]}, \tag{2.35}$$

[10] If the disk mass is not neglible, we must replace the stellar gravitational potential with the total potential, i.e. $\Phi_\star \to \Phi_\star + \Phi_{\rm Disk}$. Although this modifies the solution, the dynamical differences between dust and gas remain.

where M_{Disk} is the total disk mass, $\gamma \propto r^{\nu_{\text{Eff}}}$ encapsulates the radial dependence on the effective viscosity, and r_c is a characteristic radius at which the surface density begins to steepen significantly (Williams & Cieza, 2011).

Total disk masses M_{Disk} are inferred from integrated dust infrared emissions, subject to the uncertainties mentioned previously, and tend to be in the range 10^{-3} to 10^{-1} $M_\odot$ (Williams & Cieza, 2011, Fig. 1). Structural parameters of the disk require interferometric mapping and have yielded characteristics radii of r_c ranging from 20 to 200 AU (Andrews et al., 2009, 2010; Hughes et al., 2008; Isella et al., 2009). Getting a firm handle on γ is more difficult and some surveys claim robust mean values of $\gamma \sim 0.9$ (Andrews et al., 2009, 2010; Hughes et al., 2008) while others report significant spreads with γ ranging from -0.8 to 0.8 (Isella et al., 2009). Negative values correspond to Σ increasing with radius (up to r_c) which may be a signature of an actively evolving disk. Finally, we note that observational fits that determine γ are partial to fitting into the exponentially decreasing part of the density at large radii. Comparing γ to the more traditional disk steepness p – which assumes a pure power-law of the form $\Sigma \sim r^{-p}$ – therefore requires caution. In general, p is larger than γ because it explicitly fits into the exponential instead of considering it a correspondingly steeper power law and tends to be in the range of 0 to 1 (Andrews & Williams, 2007; Kitamura et al., 2002; Mundy et al., 1996), although the Minimum Mass Solar Nebular (see Section 3.5) pegs $p \sim 1.5$ (Hayashi, 1981; Weidenschilling, 1977).

Mass Transport, Dead Zones If the flow in the disk is turbulent instead of laminar (i.e., strictly Keplerian), Reynolds stresses can dissipate energy from the flow. More specifically, the turbulent cascade moves kinetic energy from large to small scales where it dissipates into heat. For a given parcel of gas, loss of kinetic energy transfers it to a smaller orbit, while global conservation of angular momentum requires angular momentum to be transported outwards at the same time.

Rewriting Eqns. (2.1) and (2.2) in cylindrical coordinates, setting $\pi_{ik} = 0$, integrating along the vertical and azimuthal direction, and considering the flow in a Keplerian potential, we recover the evolution for the surface density (Lynden-Bell & Pringle, 1974; Pringle, 1981),

$$\frac{\partial \Sigma}{\partial t} = \frac{3}{r} \frac{\partial}{\partial r} \left[r^{1/2} \frac{\partial}{\partial r} \left(\nu_{\text{Eff}} \Sigma r^{1/2} \right) \right], \tag{2.36}$$

where Σ is the surface density and ν_{Eff} the effective viscosity. A change of coordinates reveals Eqn. (2.36) to have the form of a diffusion equation (Armitage, 2007, Section C.1) with diffusion timescale $\tau \sim r^2/\nu_{\text{Eff}}$, which we can use to constrain ν_{Eff} (Hartmann et al., 1998). Conversely, assuming some viscosity, we can estimate the diffusion timescales for the disk. In fact, substituting a typical molecular viscosity, we find $\tau \sim 10^{13}$ years – many orders of magnitude larger than typical disk lifetimes (Armitage, 2007, Section II.C.4), which em-

phasizes that molecular viscosity is unable to remove sufficient energy from a laminar flow to explain observed disk lifetimes on the order of 10^6 years.

Turbulence is driven by instabilities which induce deviations from a laminar velocity profile. In protoplanetary disks, there are two sources for such instabilities – gravitational instabilities and magnetic instabilities. Hydrodynamic instabilities, on the other hand, do not appear to contribute to turbulent motions because the Keplerian flow is formally stable against a linear shearing (Kelvin-Helmholtz) instability.

Gravitational instabilities require the disk to be sufficiently massive and cold for self-gravity to overcome the stabilising influence of pressure forces and differential rotation. As such, gravitational instabilities are constrained to large (dozens to hundreds of AU) distances from the star where Keplerian rotation is slow and the disk is cold. More quantitatively, the disk is susceptible to gravitational instabilities if

$$Q = \frac{\kappa c_s}{\pi \mathcal{G} \Sigma} < 1, \tag{2.37}$$

where κ is the epicyclic frequency, c_s is the sound-speed, and Σ the disk surface density (Safronov, 1960; Toomre, 1964).[11] For Keplerian disks, $\kappa \sim \Omega$, where Ω is the angular orbital frequency.

For disks that are marginally stable ($Q \sim 1$), density perturbations can induce spiral modes in the disk. These lead to local over- and underdensities, which in turn stir the velocity field through torques, thereby driving turbulence. Unstable disks ($Q < 1$) produce more pronounced spiral modes and can locally fragment, although survival of fragments depends sensitively on the cooling efficiency (Gammie, 2001; Johnson & Gammie, 2003). Massive fragments and more pronounced spiral modes will again stir the disk, inducing turbulent velocity fields.

In the inner regions, disk temperatures and orbital velocities are too high for gravitational instabilities to operate. Instead, turbulence is likely induced by the magneto-rotation instability (Balbus & Hawley, 1998). Here, the magnetic fields couple to the gaseous disk provided the disk is sufficiently ionised. Under the assumption that the field lines are perfectly frozen into the gas (ideal magneto-hydrodynamics), the vertical component of the magnetic field between two neighbouring gas parcels are pulled apart due to Keplerian shear, resulting in a restoring force, which stirs the disk and induces turbulent velocity fluctuations. However, coupling the magnetic field to the fluid requires a sufficiently ionisation fraction.

[11] Strictly speaking, the original derivation of the stability criterion for Q is valid only for a thin disk of stars, which are dynamically non-collisional. However, the theory can be extended to a collisional gaseous disk (Binney & Tremaine, 2008, Section 6.2). In either case, it is important for the wavelengths of the perturbations to be larger than the disk scale-height. Otherwise, the disk is no longer thin and the analysis becomes more involved (Romeo, 1992). The same requirement also sets a resolution limit for numerical simulations wishing to resolve gravitational instabilities.

The disk can be ionised either thermally, by stellar x-rays, cosmic rays, or far-UV radiation (Armitage, 2007, Section II.D.3). For thermal ionisation to be effective, the disk temperature needs to exceed 1000 AU, which only happens close to the star. Ionisation from incident photons, on the other hand, is limited by their finite penetration depth. Taken together, this suggests that the magneto-rotational instability only operates close to the star or – at larger distance – only in the surface layers of the disk. We thus expect a dead zone in the disk midplane where no turbulence is induced (Gammie, 1996). The relative quiet of this dead zone may aid growth of dust aggregates into planetesimals.

Temperature Structure The gas pressure is determined by the density and temperature structure of the disk, the latter depending on the balance of heating and cooling. Heating is provided primarily by stellar irradiation of the surface layers as well as dissipation of kinetic energy through Reynolds stresses. Cooling is provided by radiation into space, although radiative transport must be modelled properly for all but the most shallow surface layers.

The simplest possible disk model is that of a thin disk where only the surface layers intercept the stellar flux and the inner disk remains cool. Balancing the stellar irradiation with the blackbody radiative cooling of the disk yields a disk temperature profile $T_{\mathrm{Disk}} \propto r^{-3/4}$ which in turn implies the aspect ratio to scale as

$$\frac{h}{r} \propto r^{1/8}. \tag{2.38}$$

In other words, the disk flares at larger radii. However, this also means that the disk intercepts a larger stellar stellar flux further out, increasing the local heating rate, which leads to a shallower temperature profile $T \propto r^{1/2}$ (Kenyon & Hartmann, 1987).

Given a distribution of dust grain sizes, we can use a disk temperature model to predict the spectral energy distribution (i.e., the exact shape of the infrared excess used to detect disks in the first place). As it turns out, the simple temperature model just outlined does not fit the observations very well, although splitting the disk into a hot outer layer and cooler inner layer produces satisfactory results (Chiang & Goldreich, 1997).

If the disk is actively accreting, kinetic energy is dissipated and the disk heats up where it is sufficiently turbulent. This modifies the temperature structure which we can estimate as follows. Assuming that the effective viscosity is some function of the heliocentric distance, $\nu_{\mathrm{Eff}} \sim r^{\gamma}$, we can extract a self-similar steady-state solution from Eqn. (2.36) relating a given accretion rate $\dot{M}$, surface density profile $\Sigma(r)$, and effective viscosity, viz.

$$\nu\Sigma = \frac{\dot{M}}{3\pi}\left(1 - \frac{r_\star}{r}\right), \tag{2.39}$$

where $r_\star$ is the stellar radius (Armitage, 2007, Section II.C.2), which leads to the temperature profile (Frank et al., 2002) of the form

$$T_{\rm Disk} \propto (\Sigma\nu)^{1/4}\, r^{-3/4}. \tag{2.40}$$

There is a final catch here. Dissipation of kinetic energy heats the disk locally and this heat needs to be transported to the outer layers where it is ultimately radiated away to space. Although the efficiency of radiative transport (and thus cooling) through the disk depends on the opacity, we generally find turbulent layers to be much hotter than the coronal surface layers. Again, if we wish for condensation and subsequent aggregation of dust to proceed, the existence of cool dead zones with laminar flows is attractive.

Disk Dispersal Protoplanetary disks disappear on timescales of a few Myr (Hernández et al., 2008; Ribas et al., 2014; Williams & Cieza, 2011). The modelling details are subject to debate, but it is generally agreed to be some combination of accretion of disk material onto the host star and photoevaporation. Photoevaporation is caused by the stellar irradiation that excites surface layers particles sufficiently to become gravitationally unbound (Alexander et al., 2006; Bally & Scoville, 1982; Shu et al., 1993). This is especially effective at later times when the disk is less massive and the inner disk is sufficiently depleted to afford very little shielding from stellar radiation to the outer regions. See also Alexander et al. (2014) for a review.

In summary, protoplanetary disks appear to evolve as follows. After the formation of the young star, significant mass (depending on the angular momentum of the ancestral molecular core) may fall onto the extended disk. At large heliocentric distances, gravitational instabilities induce turbulent velocity fields which transport mass inwards. At some radius, the disk rotates sufficiently fast and is warm enough to be stable against gravitational perturbations. However, if the disk is sufficiently hot and ionised in at least parts of vertical profile, the magneto-rotational instability continues to drive mass inwards until it is close enough to the star to connect with its magnetic field. At the same time, photoevaporation erodes particles from the surface layers of the disk. Dust grains settle in the disk midplane where they are shielded from radial drift by dead zones, allowing them to grow (Armitage, 2011).

2.2.2. From Dust to Planetesimals

Above, we have used the description of dust as a pressureless fluid to argue that dust grains settle towards the midplane and orbit at a different velocity than the gaseous disk. This is a simplified and somewhat disingenuous view because the dust and gas are dynamically coupled through aerodynamic drag forces, which act to minimize the relative velocity between the dust and the gas.

In general, the aerodynamic drag force is of the form

$$f_{\rm D} = -\frac{1}{2} C_{\rm D}\, \pi s^2\, \rho v_{\rm Rel}^2, \tag{2.41}$$

where πs^2 is the interaction cross section of the particle, ρ the volume density of the gas surrounding the particle and v_{Rel} the relative velocity between the gas and the dust. The drag coefficient C_{D} depends on the relation between the mean free path of the gas λ and the size of the particle s. At small sizes ($s < (9/4)\,\lambda$, where λ is typically on the order of cm), we are in the Epstein regime. Here, momentum is exchanged between the gas and dust by individual collision between dust and gas particles. The drag is therefore linear in the velocity difference, i.e.

$$C_{\mathrm{D}} = \frac{8}{3}\frac{\bar{v}}{v_{\mathrm{Rel}}} \qquad \Rightarrow \qquad f_{\mathrm{D,Epstein}} = -\frac{4}{3}\,\pi s^2\,\bar{v}\,\rho v_{\mathrm{Rel}}, \tag{2.42}$$

where $\bar{v} = c_s\sqrt{8/\pi}$ is the mean thermal velocity of gas molecules at sound speed c_s. For larger particles ($s > (9/4)\,\lambda$), we enter the Stokes regime, where momentum is exchanged by viscous effects between the gas and the particles. The drag becomes a function of the Reynolds number $\mathrm{Re} = 2sv_{\mathrm{Rel}}/\nu$ (ν is the dynamic viscosity of the gas), and becomes successively more nonlinear with v_{Rel} at higher Reynolds numbers, i.e.

$$C_{\mathrm{D,Stokes}} = \begin{cases} 24\,\mathrm{Re}^{-1} & \mathrm{Re} < 1, \\ 24\,\mathrm{Re}^{-0.6} & 1 < \mathrm{Re} < 800, \\ 0.44 & \mathrm{Re} > 800, \end{cases} \qquad \Rightarrow \qquad f_{\mathrm{D,Stokes}} \propto \begin{cases} v_{\mathrm{Rel}}, \\ v_{\mathrm{Rel}}^{1.4}, \\ v_{\mathrm{Rel}}^{2}. \end{cases} \tag{2.43}$$

Having defined the drag forces on the dust grains finally allows us to write down force balance equations to finally derive timescale for settling and growth as well as radial drift of dust aggregates as a function of their size. Deferring to Section III.A in Armitage (2007) for the gory details, we now summarise the results.

Vertical Settling, Coagulation From the vertical force balance, we find – absent turbulence and other complications – settling timescales on the order of 10^5 years for a representative μm-sized dust grain placed one scale height above the disk at a heliocentric distance of 1 AU. For smaller particles, the timescale increases substantially. An exemplary 0.1 μm sized grain placed at the same location has a settling time on the order of a few Myr. Over the lifetime of the disk, the smallest grains thus remain suspended above (and below) the disk, whereas progressively larger particles indeed sink towards the midplane. As particles sink, they also coagulate by electrostatic forces, which again accelerates settling. Models that take coagulation into account give settling timescales on the order of a few thousand years. In this time, initially sub-mm sized particles grow to mm sizes (Dullemond & Dominik, 2005).

Radial Drift, The Meter-Size Barrier As discussed, dust grains and particles are pressureless and do not feel the radial pressure gradient of the gas. They therefore orbit at velocities different from the gas which leads to a net drift, the rate of which depends on the grain size. For standard negative disk pressure gradients, the drift is towards the star, but inverted pressure gradients will in fact drift particles outward.

It turns out that for meter scale particles at 1 AU, the drift timescale is on the order of 100 years, which is much shorter than the disk lifetime. In other words, a meter-size object at 1 AU will fall into the star in 100 years. This is the famous *meter-sized barrier*, and we have two principal options to overcome it. Either we find some mechanism that grows objects fast enough ('through the barrier', as it were) or we find a way to stop, slow, or reverse the inward drift of particles.

As it turns out, fast growth beyond mm-scales by coagulation is difficult because collisions between particles tend to result in bouncing rather than sticking (Zsom et al., 2010). An alternative approach is the formation of sufficiently large objects past the meter sized barrier by gravitational instabilities (Goldreich & Ward, 1973). In this scenario, regions of the disk collapse gravitationally to generate objects on timescales of a few thousand years producing objects large enough that are unaffected by radial drift. However, at typical densities and temperatures, the instability criterion requires extremely thin disks, which cannot form without being dispersed by hydrodynamic instabilities (Cuzzi et al., 1993).

Trapping particles to hinder their radial drift can be achieved by imposing local pressure maxima.[12] Pressure maxima can either result from vortex structures (Barge & Sommeria, 1995), zonal flows in disks with magnetic fields (Johansen et al., 2009), spiral arms (or rings) which are global modes of marginally gravitationally unstable disks (Durisen et al., 2005; Rice et al., 2004), or gaps carved out by previously formed giant planets.

Pebble Accretion If at least a few objects make it past the meter-size barrier, further accretion of cm-sized objects ('pebbles') onto these seeds can proceed extremely efficiently because hydrodynamic drag enhances the seeds' collisional cross-section significantly (Lambrechts & Johansen, 2012). This is called *pebble accretion*. Although originally developed to explain growth timescale of giant planet cores (Levison et al., 2015a), more recent iterations claim to address the growth of terrestrial mass planets in the inner Solar System as well (Levison et al., 2015b).

2.2.3. From Planetesimals to Embryos

Once particles have penetrated the meter-size barrier, there is in principle little in the way of further aggregation into km-sized bodies – planetesimals. At this point, the dominating force on planetesimals are the gravitational interactions with all other planetesimals, the host star, the gaseous disk, and whatever giant planets may have formed in the system.

[12] Let us explain. Normally, the radial pressure gradient in protoplanetary disks is negative such that particles drift inwards. If we somehow generate a maximum, the pressure gradient vanishes at its location and the gas orbits at the same Keplerian velocity as the dust grains. Even better, to reach a maximum from the interior disk, the pressure gradient must be positive, resulting in an outward drift of particles towards the maximum, hence the trapping.

Let us begin by considering how a planetesimal of mass M, radius R, and surface escape velocity $v_{\rm Esc}$ grows if we embed it in a sea of field planetesimals. Using simple geometry, we can estimate the growth rate as

$$\frac{{\rm d}M}{{\rm d}t} = \underbrace{\pi R^2 \left(1 + \frac{v_{\rm Esc}^2}{\sigma^2}\right)}_{\text{Interaction Cross-Section}} \overbrace{(n_{\rm P} m_{\rm P} v_{\rm Rel})}^{\text{Encountered Mass}}, \tag{2.44}$$

where σ is the velocity dispersion of the field planetesimals, $n_{\rm P}$ their volume number density, $m_{\rm P}$ their mass, and $v_{\rm Rel}$ the relative velocity between the field planetesimals and the planetesimal we consider. Note that gravitational focussing increases the interaction cross-section of our planetesimal beyond its geometric cross-section (Safronov, 1964). Setting $\sigma = v_{\rm Rel}$ and noting that we can relate the volume number density to the surface density $\Sigma_{\rm P}$ as $n_{\rm P} = \Sigma_{\rm P}/(2h_{\rm P})$ with scale-height $h_{\rm P} \sim \sigma/\Omega$, we arrive at

$$\frac{{\rm d}M}{{\rm d}t} = \pi R^2 \left(1 + \frac{v_{\rm Esc}^2}{\sigma^2}\right) \frac{1}{2} \Sigma_{\rm P}\, \Omega. \tag{2.45}$$

This simple form reveals three features about growth of planetesimals: (i) the velocity of field planetesimals enters only through the gravitational focussing factor, (ii) larger surface densities (more massive planetesimals disks) grow planetesimals faster, and (iii) growth proceeds faster at smaller heliocentric radii, where surface densities Σ (assuming standard profiles) and orbital speeds Ω are larger. We have also assumed that Σ and σ are not affected by M, which is only true in the early stages of planetesimal growth, i.e. while $M \approx m_{\rm P}$. Since $R \sim M^{1/3}$ and $v_{\rm Esc} \sim M^{1/3}$, we also find that

$$\frac{1}{M}\frac{{\rm d}M}{{\rm d}t} \propto M^{1/3}. \tag{2.46}$$

In other words, the growth rate of planetesimals increases with their mass so that larger planetesimals grow faster. This is called *runaway growth* – the first planetesimals to grow a bit larger than the others start to 'run away' from the other field planetesimals in their mass and size.

As our runaway planetesimals become larger and more massive, they will eventually begin to influence the local surface density $\Sigma_{\rm P}$ and velocity dispersion σ of field planetesimals through accretion and dynamical friction. Through dynamical friction, they excite random motions in the field planetesimals as $\sigma \propto M^{1/3}$ (Ida & Makino, 1993), so that (2.45) becomes

$$\frac{1}{M}\frac{{\rm d}M}{{\rm d}t} \propto \Sigma_{\rm P}\, M^{-1/3}. \tag{2.47}$$

suggesting that growth slows down for larger objects. At this point, we have a few large (about 100 times as massive as the mean planetesimal) *oligarchs* that grow at approximately the same rate. They are equally spaced at about ten mutual Hill radii, where they are kept by mutual orbital repulsion.[13]

[13] Orbits are repulsed by gravitational coupling between the embryos and the surviving field planetesimals. As oligarchs approach one another, their orbits become more excited. Dynamical

Orbital repulsion is not always successful at keeping oligarchs from colliding with one another. Through mutual collisions and further accretion of planetesimals, they eventually grow into *planetary embryos*. These objects absorb most of the planetesimals within their gravitational sphere of influence as they grow to their *isolation mass* – the mass corresponding to the total planetesimal mass available in an annulus traced out by the embryo's orbit, viz.

$$M_{\rm Isolation} \sim 2\pi a b\, \Sigma_{\rm P}, \tag{2.48}$$

where b is the width of an annulus at the orbital distance (semi-major axis) a and surface density $\Sigma_{\rm P}$. For a typical embryo $a \sim 10$ AU from the star, we find $M_{\rm Isolation} \sim 0.1\ {\rm M}_\oplus$. At this point, we meet an apparent dichotomy. To form planets like the Earth and Venus, we require another stage of evolution where ~ 10 embryos collide to build up more massive planets. On the other hand, objects like Mars or Mercury are in fact of masses comparable to their isolation mass, so they are essentially planetary embryos. We revisit this observation in Section 3.6.

The dynamical evolution of planetesimals and embryos is driven by two-body encounters between planetesimals and is quantitatively very similar to stellar dynamics. Here, the velocity dispersion σ is the deviation of planetesimals from uninclined ($i = 0$) and circular ($e = 0$) orbits, i.e.

$$\sigma \simeq v_{\rm K} \left(\sqrt{\langle e^2 \rangle + \langle i^2 \rangle} \right), \tag{2.49}$$

where $v_{\rm K}$ is the Keplerian velocity, $\langle e \rangle$ and $\langle i \rangle$ the mean eccentricity and inclination of planetesimals taken over a suitable annulus in the disk. Assuming a population of planetesimals of equal mass m, a given planetesimals has a gravitational cross section $\mathcal{G}m/\sigma^2$, such that it encounters $(n\pi\sigma)\,(\mathcal{G}m/\sigma^2)$ planetesimals that induce a 90° deflection per unit time (Binney & Tremaine, 2008). In other words, the two-body relaxation timescale is

$$t_{\rm Relax} = \frac{\sigma^2}{\frac{{\rm d}\sigma^2}{{\rm d}t}} \simeq \frac{\sigma^3}{n\pi\mathcal{G}m^2 \ln\Lambda}, \tag{2.50}$$

where $\ln\Lambda$ is the Coulomb logarithm. Viscous stirring refers to dynamical excitation of equal mass planetesimals through gravitational two-body encounters, effectively transferring Keplerian shear into random motions (Ida, 1990). Assuming that relative velocities are mostly due to the planetesimal velocity dispersion instead of Keplerian shear (i.e., $\sigma \gg ({\rm d}v_{\rm K}/{\rm d}r)\,{\rm d}r$), viscous stirring increases eccentricities at a rate

$$\frac{{\rm d}\langle e^2 \rangle}{{\rm d}t} \sim \frac{\langle e^2 \rangle}{t_{\rm Relax}}. \tag{2.51}$$

For typical planetesimal distributions, $n \sim 1/\sigma$ so that $\sigma \propto t^{1/4}$. For example, numerical experiments show that on timescales of 10^4 years, $\langle e \rangle$ increases by factors of ~ 4 (Kokubo & Ida, 2012). Note, however, that dynamical excitements will be

friction dumps this excitation into planetesimals and recircularises the oligarchs orbits at slightly larger radial separations (Kokubo & Ida, 1995).

dampened significantly if the planetesimals are embedded in a gaseous disk which provides hydrodynamic drag.

As discussed above, runaway growth leads some planetesimals to grow faster than others, leading to a population of embryos that are embedded among field planetesimals. Dynamical friction acts to equipartition energy between the embryos and planetesimals. Effectively, this dampens the eccentricities of the embryos and excites those of the planetesimals (Ida & Makino, 1992a,b) at a rate of

$$\frac{\mathrm{d}e_M^2}{\mathrm{d}t} \sim -\frac{m}{M}\frac{e_M^2}{t_{\mathrm{Relax}}}, \tag{2.52}$$

where M and e_M are the mass and eccentricity of an embryo surrounded by field planetesimals. Note that the rate of e_M only depends on the volume mass density of planetesimals and not on their mass as Eqn. (2.52) would suggest, since $t_{\mathrm{Relax}} \sim 1/(nM^2)$ leads to $\mathrm{d}e_M^2/\mathrm{d}t \propto nm \sim \rho$ (Kokubo & Ida, 2012).

2.2.4. From Embryos to Terrestrial Planets

Let us review. We started out with a population of km-sized field planetesimals, some of which accreted more mass than others and 'ran away'. These became oligarchs that occasionally collided, but generally retained sufficiently large orbital spacing to sweep up substantial amounts of field planetesimals in their sphere of influence to reach isolation mass. We are left with dozens of embryos and a residual population of planetesimals that managed to avoid being accreted.

The next stage of evolution (*late-stage accretion*) is comparatively simple. We just need to wait long enough for the mutual gravitational perturbations of the embryos to perturb each other enough to either be ejected from the system, fall into the star, or collide with other embryos. At the same time, the surviving planetesimals are dragged along in this dynamic dance, at the end of which they will find themselves either in the star, in deep space, smashed up against a much larger embryo, or in some regions of the planetary system where they are shielded from the dynamical effects of the other embryos.

This stage is best probed with dynamical simulations because most of the outlined events are stochastic in nature and do not occur sufficiently often to warrant a statistical treatment. Much effort has been devoted to suitable modelling and exploration of this stage in the literature (Chambers, 2001; Chambers & Wetherill, 1998; Raymond et al., 2004, 2006). For more recent reviews, see also Morbidelli et al. (2012) and Raymond et al. (2014).

2.2.5. Formation of Giant Planets

Gas giants are structurally very different from terrestrial planets. While the latter are almost exclusively made up of rocky materials such as silicates and iron and host a comparatively thin gaseous atmosphere, giant planets may have comparatively small solid core, but host huge envelopes of gas; possibly in multiple distinct shells with ices in between. As such, their formation timescales are constrained to within the first few Myr before the gas disk dissipates.

There are two leading theories for the formation of giant planets – core accretion and gravitational instability. In the core accretion model, the initial stages are similar the formation of terrestrial planets. First, a massive rocky core forms. Once the core becomes massive enough for the surface escape velocity to exceed to sound speed, the core starts to accrete the surrounding gas, which can initially maintain hydrostatic equilibrium. As gas keeps piling up, gravitational forces eventually overpower the pressure gradients that maintain hydrostatic equilibrium, and the gas collapses onto the core. This happens at the critical mass, which sensitively depends on the opacity of the gas. At this stage, accretion accelerates significantly which rapidly drains the surrounding gas disk and terminates gas accretion. If this process happens before the gas disk is dissipated, however, the giant planet might migrate towards regions with more gas, where accretion restarts (Pollack et al., 1996).

In the gravitational instability model, a disk below the threshold for gravitational instability can locally collapse. As we've shown earlier, the disk can fragment for values of the Toomre parameter

$$Q = \frac{\kappa c_s}{\pi \mathcal{G} \Sigma} < 1, \tag{2.53}$$

where, as before, c_s is the disk sound speed, Σ the surface density, and κ the epicyclic frequency ($\kappa \sim \Omega_K$ for a Keplerian disk). In practice, for fragments to continue collapsing, we require the cooling timescale of the gas to be short enough – on the order of less than three Keplerian times (Gammie, 2001). Otherwise, fragments self-stabilise and stop collapsing. Unfortunately, modelling cooling processes is a challenging affair, especially when the gas transitions from an optically thin to an optically thick state.

Irrespective of the model we might favour, formation of giant planets is easier at larger distances > 10 AU from the host star for a number of reasons. In core formation, low density gas tends to be more opaque, which makes for more efficient radiative cooling, thereby hastening core collapse along. High temperatures and pressures would also act to counter the core-collapse when gravity overcome stabilising pressure gradients. In the gravitational instability scenario, low temperatures ($\sim c_s$) and small Keplerian velocities and shear rates ($\sim \kappa$) act to destabilise the disk against gravitational fragmentation.

2.2.6. Disk-Driven Migration

Both giant planets as well as the embryos of terrestrial planets form rapidly enough for the gas disk to still be present when they arrive on the scene. Depending on the (square of the) mass of the planet and the surface density of the disk, planets will interact more or less strongly with the disk. Primarily, this leads to radial migration of planets, but also affects the structure of the disk, which may feed back onto the ongoing formation of other planetesimals, embryos, or giants in the system. We distinguish between type I and type II migration.

In either case, the interaction can be understood as the exchange of angular momentum between the planet and the disk at corotation as well as Lindblad resonances (Binney & Tremaine, 2008; Goldreich & Tremaine, 1979) and is largest at those resonances which are about a disk scale height away from the planetary orbit

(Ward, 1997). Gas exterior to the planet orbits slower and therefore gains angular momentum from an interaction with the planet while the planet looses angular momentum. Conversely, gas interior to the planet looses angular momentum from the interaction while the planet gains angular momentum. In short, interactions with the interior gas push the planet outward and interactions with the exterior gas push the planet inwards. At the same time, the exchange of angular momentum repels gas from the planet. Whether the planet ends up migrating inward or outward depends on the pressure profile of the disk, but for negative pressure gradients, migration is generally inwards. Elementary calculations suggest migration timescales on the order of a few 10^5 to 10^6 years for Jupiter and Earth mass planets, respectively (Armitage, 2007, Section IV.A.1). We therefore expect all planets to migrate, which makes an good understanding of migration imperative.

Planets with masses on the order of an Earth mass experience type I migration (Ward, 1997) which tends to cause inward drift, although the details are difficult to evaluate and an exact prediction of migration rates depends sensitively on the thermal properties (Casoli & Masset, 2009; Kley et al., 2009; Kley & Crida, 2008; Paardekooper et al., 2010; Paardekooper & Papaloizou, 2009) of the disk model and whether the computation is carried out in two or three dimensions (Tanaka et al., 2002). More massive planets can excite spiral arms in the disk that may modify ongoing planet formation.

Larger planets with masses on the order of a few Jupiter masses experience type II migration. Owing to their large mass, these planets clear a gap in the gas disk by pushing gas out of an annulus of width equivalent to few disk scale heights (Goldreich & Tremaine, 1980; Lin & Papaloizou, 1980). In particular, there are two conditions that need to be met for the planet to open a gap. Firstly, it must have a Hill sphere with radius on the order of the local disk scale height. Secondly, the angular momentum exchange through the Lindblad resonances must be strong enough to repel the gas even as it attempts to fill the gap due to the mass flux driven by the effective viscosity of the disk. Once the gap is opened, the radial drift is determined by the balance of Reynolds stress in the disk and the strength of Lindblad resonances. Again, the details of the resulting migration depend on the structure of the protoplanetary disk, especially the level of turbulence which drives inward mass flux (Armitage & Rice, 2005)

In a turbulent disk, the velocity and density fields can fluctuate wildly in both space and time. This, in turn, induces an essentially random distribution of torques on any planets that embedded within. The integral effect of these torques can also lead to radial drift of planets and is called stochastic migration. By its very nature, stochastic migration does not lend itself very well to analytical treatment and requires suitable hydrodynamic simulations to investigate. For example, Nelson & Papaloizou (2004) suggest that migration timescales from stochastic migration are comparable to steady type I migration as discussed above.

3

Reverse Engineering the Solar System

"*Once upon a time, we soared into the Solar System. For a few years. Then we hurried back. Why? What happened? What was 'Apollo' really about?*"

– Carl Sagan, *The Pale Blue Dot: A Vision of the Human Future in Space (1997)*

On 14 July 2015, the Pluto flyby of the New Horizons spacecraft finally concluded the exploration of the original nine planets. First named 'wanderers' by the ancient Greeks, our modern understanding of planetary orbits dates back to the Copernican Revolution (Copernicus, 1543) and the observations of the Galilean moons (Galilei, 1610). We have come a long way since the Renaissance and now (believe to) have a decent handle on the dynamics and properties of the Solar System objects, which we review in this Chapter. In Sections 3.1 and 3.2 we review our present understanding of the Solar System and its evolution. We follow this up by describing the chemical and dynamical constraints models must match in Sections 3.3 and 3.4, before we describe such models in Sections 3.5 and 3.6.

3.1. Taking Stock: Present-Day Solar System

3.1.1. The Sun

The Sun is the most illustrious object in the Solar System. About 330′000 times more massive than the Earth, it accounts for 99.87 per cent of the total mass. Of this, 73.46 and 24.85 per cent are hydrogen and helium, which drive the release of staggering amounts of energy through nuclear fusion. Every second, the Sun radiates

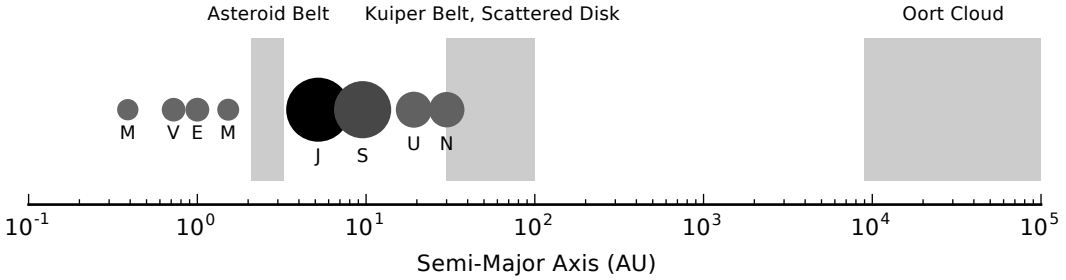

Figure 3.1. Sketch of the Solar System. Filled circles indicate the planets with area and shading proportional to the mass. Shaded regions mark the primary reservoirs of minor objects in the Solar System.

energy equivalent to about 650′000 times the estimated yearly consumption of our entire civilization.[1]

3.1.2. Planets & Moons

Beyond the Sun, our Solar System hosts a dizzying array of planets, their moons, and minor bodies totalling roughly 446 Earth masses, which we have sketched out in Figure 3.1. We also summarise the eight major planets in Table 3.1.2. The largest planets – Jupiter and Saturn – account for 92 cent of the remaining mass budget. Bulk density and gravity field measurements suggest that these giant planets have rocky cores which are enveloped by layers of hydrogen and helium (Helled et al., 2014). Most of the remaining mass is locked up in Uranus and Neptune. They are significantly less massive than Jupiter or Saturn, and their higher bulk densities suggest larger fraction of ices (or a larger rocky core) than for Jupiter and Saturn. Together, the four giants also host the majority of (detected) natural satellites in the Solar System that were either captured or formed from a circumplanetary disk as the giant planets formed.

The inner Solar System is dominated by the terrestrial planets – Mercury, Venus, Earth, and Mars. Their orbital separations are much tighter than those of the giants, and they are much less massive. Of the four, Earth is the most massive, and the only object in the Solar System known to host life. Mean bulk densities for the inner planets are also higher, evidently a consequence of their predominantly rocky composition. Seismic measurements of Earth suggest a complex interior structure consisting of a core, mantle, and crust (Hart, 1969). Although we lack seismic data from other planets, there is no reason to assume the absence of a similar structural layout from Venus (Schubert et al., 1997) or Mars (Mocquet et al., 2011; Zuber, 2001). As suggested by its small size, Mercury may be the surviving core of a larger terrestrial planet, which might explain why it appears to have a disproportionately large core compared to its mantle and crust (Benz et al., 1988; van Hoolst et al., 2007). Evidently, plate tectonics are active on Earth, although it appears to be the only terrestrial planet to feature these at present. This may have been different in the past.

[1] http://www.iea.org/publications/freepublications/publication/KeyWorld2014.pdf

Planet	a (AU)	e	i (Deg)	m ($M_\oplus$)	R (km)	ρ (g/cm^3)	N_{Moons}
Mercury	0.4	0.21	7.0	0.05	2′440	5.4	
Venus	0.7	0.01	3.4	0.81	6′052	5.2	
Earth	1.0	0.02	0.0	1.00	6′371	5.5	1
Mars	1.5	0.09	1.8	0.11	3′390	3.9	2
Jupiter	5.2	0.05	1.3	317.70	69′911	1.3	67
Saturn	9.5	0.05	2.5	95.13	58′232	0.7	61
Uranus	19.2	0.05	0.8	14.53	25′362	1.3	27
Neptune	30.0	0.01	1.8	17.14	24′622	1.6	14

Table 3.1. Summary of the Solar System planets. Here, a is the semi-major axis, e the eccentricity, i the inclination, m the planetary mass (in Earth Masses; $M_\oplus$), R the planetary radius, ρ the mean bulk density, and N_{Moons} the detected number of natural satellites. Orbital elements are for 01 January 2014, are heliocentric, and inclinations are relative to the ecliptic in J2000.

Venus and Earth are the only terrestrial planets to host notable amounts of gases as atmospheres. On Earth, atmospheric pressure at surface level is 0.1 MPa and the atmosphere dominated by nitrogen and oxygen (78 and 21 per cent). On Venus, surface pressures exceed 9 MPa and the atmosphere is dominated by carbon dioxide (96.5 per cent), suggesting a runaway greenhouse effect in the past (Chaisson & McMillan, 2005). By contrast, the Martian atmosphere exerts surface pressures of 0.001 MPa. Lacking a protective magnetic field, it was likely blown away by the Solar wind in the past (Fraknoi et al., 2000). Atmospheric composition is similar to Venus, which may also have had significant atmospheric blow-off (Donahue & Hodges, 1992).

Compared to the giant planets, terrestrial planets host very few natural satellites. In particular, Earth hosts a single moon with compositional similarities to its host, suggested it may have formed from debris of giant impact (Canup, 2004). Two moons orbit Mars, but lack of evidence does not allow us to discriminate whether they were captured or resulted from a collision (Citron et al., 2015).

3.1.3. Asteroids, Comets, Dwarf-Planets

Where surveyed, all terrestrial planets as well as the moons feature impact craters, hinting at another population of objects in the Solar System. Naturally, the size and frequency of observed impact craters greatly depends on the geological activity, weathering, and atmospheric of the target body. As such, only Mars, our own Moon, and – to a certain extent – Mercury provide adequate laboratories from which we can reconstruct the size and frequency of minor objects in the inner Solar System by counting impact craters. For our Moon, radioactive dating of return samples from the Apollo missions as well as meteorites allow us to reconstruct the impact history of the moon (Neukum et al., 2001).

Beyond counting and sampling of impact craters, astronomical surveys helped us to catalogue the minor objects in the Solar System. The three primary reservoirs for these objects are the asteroid belt ($1.8 \lesssim a \lesssim 4.5\,\mathrm{AU}$, where a is the semi-major axis), the Kuiper belt including the scattered disk ($30 \lesssim a \lesssim 100\,\mathrm{AU}$), and the Oort cloud ($a \sim 10'000$ to $100'000\,\mathrm{AU}$). As of yet, no direct observations of Oort cloud objects are available, but the region is hypothesized on dynamical grounds (Shannon et al., 2015).[2]

Neither of the other two reservoirs are exclusive to hosting minor objects, but they do host the bulk of detected objects (Figure 3.2). In particular, as of 19 March 2015, observations (orbital solutions and brightness) are available for 678′814 objects, totalling 0.19 Earth masses, which correspond to 0.04 per cent of the total mass in major and minor Solar System bodies. Out of these, 662′894 objects populate the asteroid belt, accounting for 97.65 per cent of all observed objects, but only for 4.6 per cent of the mass. Objects detected in the Kuiper belt beyond Neptune (Trans-Neptunian Objects, TNOs), on the other hand, number only 1′655, but contribute 95.4 per cent of the total mass, although there is most certainly a serious detection-bias at work. In both regions, most mass is distributed over a few objects, the five most massive of which we list in Table 3.1.3.

Of the remaining 14′255 minor bodies, one half populates the inner Solar System ($a \leq 1.8\,\mathrm{AU}$), while the other half is spread out between the giant planets at semi-major axes $4.5 \leq a \leq 30\,\mathrm{AU}$. Over half of these objects have orbital eccentricities exceeding $e > 0.15$ which puts them on planet crossing trajectories, some of them close to Earth which necessitates monitoring. Populations are classified according to orbital regions they occupy. This need not only be in terms of semi-major axis, but also in terms of eccentricity and inclination, which are shaped by resonant interactions with other Solar System planets (Murray & Dermott, 1999).

The total number of objects in the Solar Systems remains unknown, but is likely to be much larger than the number of observed objects in publicly available databases. By counting impact rates in simulations and calibrating these against the cratering records of the Moon, our own test runs indicate the Solar System to host on the order of trillions of objects with diameters $D > 1\,\mathrm{km}$. Unfortunately, this work remains unpublished for the time being.

3.1.4. Notes on Observations

Above, we have used three public resources to describe the Solar System, which we now refer to. First, orbital elements and physical parameters for the eight major planets are obtained by querying the NASA/JPL HORIZONS system.[3] Second, physical parameters and counts for their natural satellites were also obtained from parameter

[2] We have also performed our own test simulations with regards to the Oort cloud. In these runs, objects on long-period orbits pick up angular momentum from gravitational encounters with the Solar System planets, thereby increasing their semi-major axis and eccentricity. As the semi-major axis approaches 10′000 AU, orbits tend to become hyperbolic, such that $a \sim 10'000\,\mathrm{AU}$ appears to be natural dynamic cut-off to the extent of orbits bound to the Sun.

[3] http://ssd.jpl.nasa.gov/?horizons

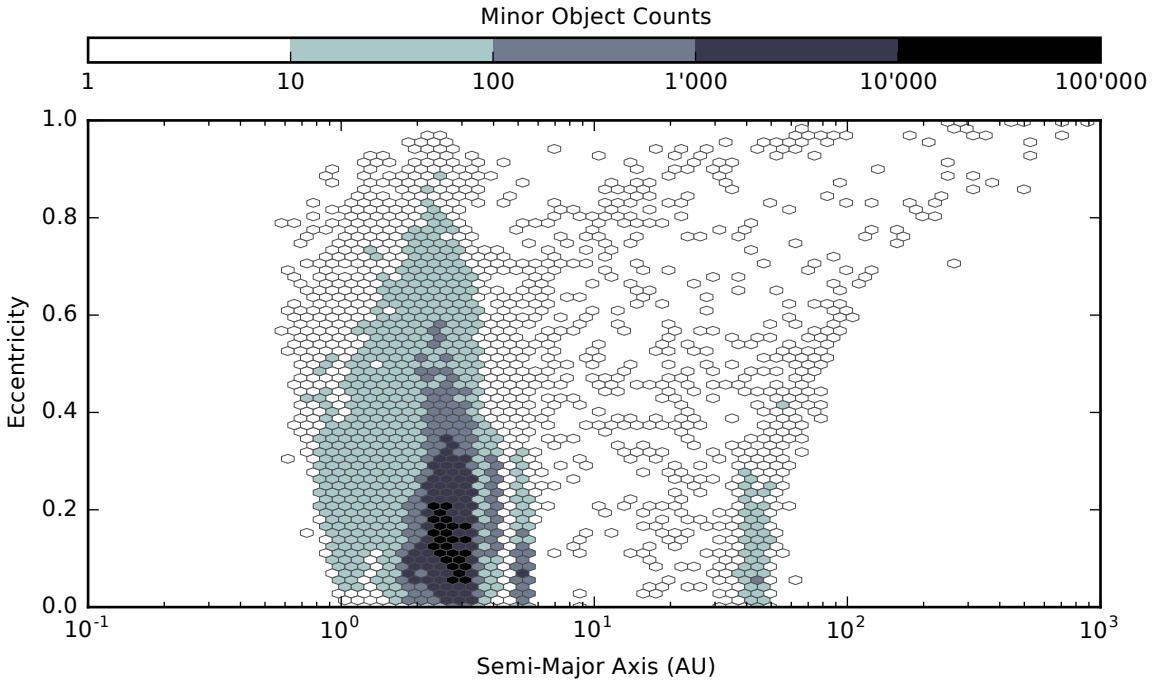

Figure 3.2. Distribution of minor bodies in the Solar System. We show hexagonally binned object density on a logarithmic scale, i.e. $\mathrm{d}N/\mathrm{d}(\log(a)\,e)$, where N is the number of objects, a the semi-major axis, and e the eccentricity. Only regions hosting objects are marked with hexagons and density is rescaled to a minimum non-zero value of 1.

Body	a (AU)	e	i (Deg)	m ($M_\oplus$)	D (km)	ρ (g/cm^3)
Ceres	2.8	0.08	10.6	8.0×10^{-5}	848	1.5
Pallas	2.8	0.23	34.8	3.8×10^{-5}	498	3.5
Vesta	2.4	0.09	7.1	3.2×10^{-5}	468	3.5
Hygiea	3.1	0.11	3.8	8.9×10^{-6}	407	1.5
Sylvia	3.5	0.09	10.9	5.4×10^{-6}	261	3.5
Eris	67.8	0.44	44.1	2.9×10^{-3}	2349	2.5
Pluto	39.4	0.25	17.2	2.8×10^{-3}	2581	1.9
Makemake	45.7	0.16	29.0	9.9×10^{-4}	1700	2.3
Haumea	43.2	0.19	28.2	8.1×10^{-4}	1460	3.0
Sedna	520.7	0.85	11.9	1.7×10^{-4}	1173	(1.2)

Table 3.2. The five most massive minor bodies (excluding moons) in the Solar System interior (top) and exterior (bottom) of 4.5 AU. Here, a is the semi-major axis, e the eccentricity, i the inclination, m the mass (in Earth Masses; $M_\oplus$), D the diameter, and ρ the mean bulk density. Orbital elements are for 19 March 2015 and are heliocentric. Inclinations are relative to the ecliptic in J2000. The density for Sedna is unknown and we use an estimated value.

tables available from the same group.[4] Third, orbits and brightness measurements of the minor bodies were taken from the ASTORB database.[5]

For the minor bodies, only some diameters are known and density and mass measurements are not included in the database. However, using a range of assumptions on how albedo and brightness depend on the material of the object, these can be reconstructed. For asteroid belt objects ($a < 4.5\,\mathrm{AU}$), we follow the mapping from asteroid type to albedo and density as outlined in the caption of Figure 1 in Petit et al. (2001). For objects $a > 4.5\,\mathrm{AU}$, we take albedo and density measurements published in the literature (Stansberry et al., 2008) for Eris, Pluto, Charon, Varuna, Makemake, and Haumea. For Sedna, only the albedo is available. For all remaining objects, we assume an albedo of 0.6 and a density of $1.2\,\mathrm{g/cm^3}$. Finally, we map albedo and measured brightness to diameter via

$$D = 10^{6.244 - 0.4H - \log_{10} P_\nu}, \tag{3.1}$$

where H is the absolute brightness and P_ν the albedo (Petit et al., 2001).

3.2. Isotopic Chronology of the Solar System

3.2.1. Isochrone Dating

Establishing the chronology of the Solar System relies on our understanding of isotopic decay systems and measurements of chemical abundances in meteorites, Earth's crust, as well as lunar return samples. Lacking knowledge of initial abundances, simple radiogenic dating (which relates the abundances of a single parent and daughter isotope) is not an option. Instead, we must resort to isochrone dating, which relates the abundance between a parent isotope to its daughter isotope relative to a non-radiogenic daughter isotope.

As an example, consider the rubidium-strontium (Rb-Sr) system. Here, ^{87}Rb (the parent P) decays to ^{87}Sr (the daughter D). The non-radiogenic isotope ^{86}Sr (D_{NR}) serves as a reference we can normalise to. Let us now consider a homogeneous molten rock with initial ratios of P/D_{NR} and D/D_{NR}. Over time, P decays into D such that P/D_{NR} decreases and D/D_{NR} increases in like fashion. As luck would have it, our rock has cooled so that it starts to crystallise, which forms different minerals, each incorporating varying fractions of P/D_{NR}, but identical ratios for D/D_{NR}. As time marches on, decay of P to D continues within each mineral, giving us multiple points in (D/D_{NR},P/D_{NR}) that evolve colinear. By fitting a line through these points, we construct an isochrone which tells us how long ago (more precisely, how many half-lifes of P ago) the rock crystallised.

Using suitable decay systems, we can therefore use isochrone dating to establish ages for various Solar System objects and events. However, even after mitigating problems such as source contaminations, non-homogeneous material distributions, or non-uniform cooling, a key issue remains. We require long-lived radionuclides (e.g. ^{238}U, ^{87}Rb, or ^{40}K) with multi-Gyr half-lifes to determine ages over long timescales,

[4] http://ssd.jpl.nasa.gov/?sat_phys_par
[5] ftp://cdsarc.u-strasbg.fr/pub/cats/B/astorb/astorb.html

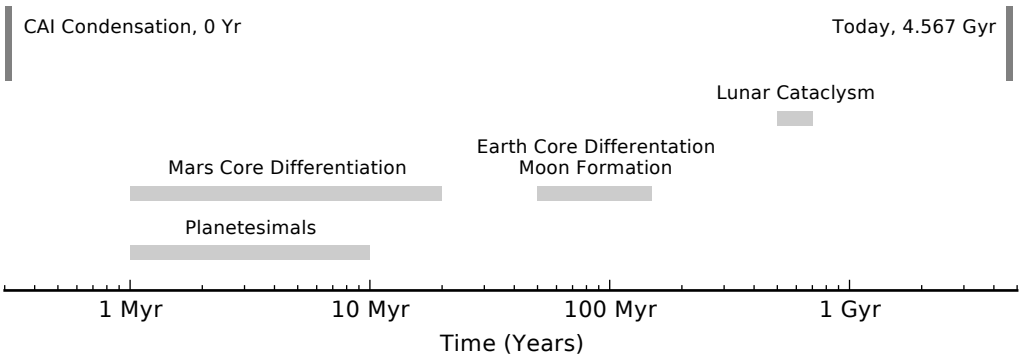

Figure 3.3. Sketch of the Solar System chronology. Data is derived from isochrone-dating of different meteorites as well as in-situ samples from the Moon and Earth.

but these come at the expense bad time-resolution. To achieve good resolution and date sequences of events on (sub-)Myr timescales, we require short lived radionuclides (SLRs) such as ^{41}Ca, ^{26}Al, or ^{182}Hf. Unfortunately, these have become extinct by now, and their abundance must be inferred from stable daughter isotopes. This is a complicated affair and we refer to the review of McKeegan & Davis (2003).

3.2.2. The First Few Hundred Million Years

Using isotopic decay systems from a variety of meteoritic and in-situ measurements on the Moon and Earth, we can come up with a rough chronology of the first few hundred million years of the Solar System. Having sketched this out in Figure 3.3, the sequence of events is constrained as follows.

Firstly, we define some reference time as the time the first solids condense out of the protosolar nebular. Today, these survive as *calcium-aluminum-rich inclusions* (CAIs) in chondrite meteorites, which we can use to date CAI condensates to 4567.2 Myr ago. This defines the age of the Solar System. Within the first few Myr, planetesimals accrete, and the first planetary cores form. Then, within 20 Myr, Mars is the first terrestrial planet to be completely formed and differentiated.[6] Our next constraint is the core-mantle differentiation and crystallisation of Earth's crust, presumably following a collision with a hypothetical object Theia which resulted in the formation of the Moon. This happened between 50 and 150 Myr after CAIs and frequently referred to as the *moon-forming impact*. Finally, the last piece of chronological evidence comes from timing the crystallisation of the lunar crust from meteorite and return samples provided by the Apollo expeditions. These suggest that, about 600 Myr after CAIs, there was significant decreases in the flux of objects hitting the Moon. To date, it remains debated whether this represents the tail end of steadily decreasing flux of impactors or is the result of brief spike in collision rates.

We now address each of these cosmochemical constraints in a little more detail and provide literature references.

[6]The early differentiation and lower mass of Mars compared to Earth and Venus gives rise to the concept of Mars being a 'failed planet'. See also Section 3.6.

Age of the Solar System Calcium-aluminum-rich inclusions (CAIs) and chondrules are mineral inclusions embedded in the matrix of chondritic meteorites. Their compositions correspond to condensation temperatures in excess of 1300 K (CAIs) or just below 1000 K (chondrules). In particular, CAIs are suggested to be among the first chemical structures to have condensed out of the cooling protosolar nebular. Using isochrone dating based on ^{206}Pb, ^{207}Pb, and ^{204}Pb, they have been used to constrain the age of the first solids in the Solar System to 4′567.2 Myr (Amelin et al., 2002). Based on their visual textures, CAIs appear to be direct condensates from the protosolar nebula while chondrules are aggregates, although both have likely been subjected to significant reprocessing (cycles of condensation, melting, and evaporation). Until recently, isotopic dating indicated CAIs to predate chondrules by 1 to 3 Myr, which is in line with them being aggregate structures. More recently, this picture has been challenged and ages of some CAIs and chondrules now overlap (Connelly et al., 2012).

Planetesimals, Planets, and the Moon Accretion of the first planetesimals is constrained primarily by Mn-Cr dating of meteorites thought to originate from the 4 Vesta (a 525 km minor planet in the asteroid belt) parent body. Isochrone-dating of various meteorites (H4 chondrites, eucrites, and achondrites) point towards crystallisation within 2 to 10 Myr after CAI formation. This sets the accretion timescale for planetesimals (McKeegan & Davis, 2003).

The hafnium-tungsten (^{182}Hf-^{182}W) decay system is well suited to date melting and differentiation of planetesimals as well as core-mantle differentiation of the terrestrial planets, although the latter is somewhat challenging due to their size. Tungsten is siderophile ('iron-loving') and dissolved readily into an iron core, while hafnium is lithophile ('rock-loving') and prefers to remain in the rocky layers. During core-formation, very little hafnium makes it into the core where it would decay to tungsten. Therefore, a deficit of tungsten when compared to a primitive (undifferentiated) bodies can be used to time core-formation.[7] Data from magmatic iron meteorites suggests melting and differentiation of their planetesimal parent bodies within the first Myr after CAI, which pegs the first planetesimals into this time range (Kleine et al., 2009).

The Hf-W system can also be used to constrain the timing of core-formation of Mars and the Earth to 0 to 20 Myr and 30 to 100 Myr after CAI. Although the ranges are large, it is clear that Mars was fully formed and differentiated much earlier than the Earth. If we subscribe to a scenario where the Moon formed from a collision between a Mars-sized object (dubbed Theia) with the Earth, the timing of this impact is evidently the last major disruption before the final settling of the core. Such a scenario is supported by the compositional similarities between lunar samples and the Earth (Asphaug, 2014), suggest Theia's origin near the Earth (Halliday, 2000), and peg differentiation of the Earth between 50 and 150 Myr after CAI. Thusly derived ages for Earth

[7] http://www.psrd.hawaii.edu/Nov03/Hf-W.html

are also consistent with the timing of crustal solidification from uranium-lead isochrone-dating (Halliday, 2003; Harrison, 2009).

The Lunar Cataclysm The last pieces of the chronological puzzle we wish to address at this point are impact craters, especially those that are accessible for dating. They provide constraints about the dynamical state of the Solar System in the past, and serve as important probes on its evolution on timescales beyond the first 200 Myr. Impact craters on the Earth sample the more recent history (< 2 Gyr ago, or > 2.5 Gyr after CAI) because older craters have been removed in geological processes. We do not discuss these here as our primary aim is to establish constraints for the formation of the Solar System, and not its long-term evolution. Fortunately for us, the Moon lacks geological activity, and dating of Apollo samples and lunar meteorites provides a snapshot into the late stages (200 Myr to ~ 1 Gyr after CAI) of planet formation.

Isochrone dating using ^{40}Ar-^{39}Ar and ^{87}Rb-^{87}Sr systems strongly suggests the upper lunar crust to have been rapidly molten and solidified ~ 3.9 Gyr ago (Warren & Taylor, 2014), corresponding to a timing of ~ 600 Myr after CAI. Although the crystallisation of the surface resulting from a decrease of an intense bombardment is undisputed, the bombardment history up to this point remains controversial. One camp argues that the relative lack of melt > 3.9 Gyr ago suggests an impact spike (Ryder, 1990, 2001; Ryder et al., 2000),[8] while the other camp maintains that the crystallisation at ~ 3.9 Gyr ago is a result of the decay of an initially much higher impact flux that kept resetting isotopic abundances by continuous delivery of fresh material (Chapman et al., 2007; Hartmann, 1975; Hartmann et al., 2007).

3.3. Compositional Constraints

Beyond reconstructing the chronology of the Solar System, cosmochemical evidence and modelling can also give us hints about the present-day composition of the Earth and its origin. As usual, the literature is comprehensive and opaque to the uninitiated, so we focus only on two of the most important aspects here. For an introductory review, we direct the reader to Drake & Righter (2002).

The Deuterium/Hydrogen Ratio Deuterium and hydrogen have the largest ratio of elemental masses in the periodic table and their ratio is therefore an attractive tracer of chemical processes in the early Solar System. After inheriting some fiducial ratio from the interstellar medium (Cleeves et al., 2014), chemical reactions of the form

$$\mathrm{HD} + \mathrm{H_2O} \quad \leftrightarrows \quad \mathrm{HDO} + \mathrm{H_2} \tag{3.2}$$

proceed. For a wide range of H bearing molecules (H_2O, in this example), these reactions almost invariably lead to isotopic enhancement of D relative

[8] In the context of some dynamical models, the impact spike is caused by an orbital reconfiguration of the giant planets, cf. Section 3.6.

to H (Robert, 2006). At high temperatures, the enrichment of D relative to H proceeds faster than at low temperatures, such that the reactions slow down as the protoplanetary disk cools and dissipates, eventually leading to a characteristic imprinted D/H ratio for all Solar System objects.[9] By comparing D/H ratios across the planets, chondritic meteorites, and comets, we can get a first clue as to from where the water reservoirs of the terrestrial planets water may have been delivered (Altwegg et al., 2015; Hartogh et al., 2011).

In particular, chondritic meteorites tracing back to the population of the asteroid belt best match the terrestrial D/H ratio, whereas most Oort cloud and Jupiter family comets have ratios a few factors in excess of the terrestrial value. Overall, this suggests that at most 10 per cent of the present day water content on the Earth can be accounted for by cometary delivery (Eberhardt et al., 1995; Robert, 2001), indicating that the remaining 90 per cent (i) have either been delivered from asteroid belt objects (Morbidelli et al., 2000), (ii) that the primary building blocks of the Earth and the asteroid belt objects share a common ancestry, or (iii) that original building blocks of the Earth are now extinct, but shared their initial D/H ratio with the asteroid belt objects (Drake & Righter, 2002). We partially cover this issue in our paper on *Wet Terrestrial Planets: Fact or Artifact?* presented Chapter 6, where we show that a large fraction of the material making up the terrestrial planets originates over a wide range of the disk.

Highly Siderophile Elements in the Crust A similar chemical puzzle relates to the abundance of highly siderophile elements (HSEs) in the upper layers of the Earth. By combining the timing the last giant impact and subsequent crystallisation of the magma ocean with the expected abundance of elements derived from the condensation sequence, chemically motivated mixing models would suggest the bulk of siderophile elements to have been dragged down into the core. Strongly siderophile elements include (but are not limited to) gold, rubidium, or iridium. However, there appears to be an excess of siderophile elements in the crust and upper mantle.[10] This argues for either an insufficient understanding of core-formation or the late delivery (a 'late veneer') of additional material to our planet (Jones & Drake, 1986).

While geochemical researchers concentrate on improving mixing models by considering incomplete core segregation models (Jones & Drake, 1986) or temperature (Brett, 1984) and compositional variations (Murthy, 1991), dynamical modellers attempt to pin down possible sources and timing for a late

[9] That is not to say that the D/H ratio completely stops evolving for a reservoir. For example, an atmosphere hosting deuterium and hydrogen preferentially outgases lighter hydrogen. This increases the D/H ratio over time and can be used to constrain the initial atmospheric water content on, for example, Venus (Donahue, 1999; Donahue & Hodges, 1992). Similarly, measurements of the D/H ratio of sea water on the Earth may reflect reprocessing from recycling of water between rocks and the ocean (Hallis et al., 2015).

[10] More specifically, experimental studies of HSE behaviour suggest depletion factors of HSEs with respect to silicates on the order of $\sim 10^{-4}$ (Jones & Drake, 1983), but both Mars and Earth upper layers are only depleted by factors of ~ 200 with respect to chondritic meteorites (Morgan et al., 1981; Ringwood, 1966).

delivery of material. In such a scenario, the most recent estimates argue for the delivery of about 4.8×10^{-3} $M_\oplus$ of material (Walker, 2009), either as a result of an increased impactor flux following orbital instabilities of the giant planets (Marchi et al., 2014), or stochastically delivered by a leftover population of surviving planetesimals (Bottke et al., 2010; Raymond et al., 2013). For a more comprehensive overview, we refer to Morbidelli & Wood (2015).

3.4. Dynamical Constraints

From a dynamical point of view, the constraints that any model for the formation and evolution of the Solar System must fulfil are fairly self-evident. At a qualitative level, models need to reconstruct the masses and orbits of the major planets as well as equivalent populations of minor planets with their associated mass functions and orbital locations. At a more quantitative level, the orbital distribution of the inner planets can be described by the angular momentum deficit (AMD) and the radial mass concentration (RMC). The AMD is

$$\mathrm{AMD} = \max\left(\frac{\sum_j m_j}{\sum_j m_j \left[\log_{10}\left(a/a_j\right)^2\right]}\right), \tag{3.3}$$

where the sum is over the mass m_j and semi-major axis a_j of the terrestrial planets, and we search the maximum in the range of semi-major axes populated by the terrestrial planets (Laskar, 1997). The RMC is

$$\mathrm{RMC} = \frac{\sum_j m_j \sqrt{a_j}\left(1 - \cos(i_j)\sqrt{1-e_j^2}\right)}{\sum_j m_j \sqrt{a_j}}, \tag{3.4}$$

where m_j, a_j, e_j, and i_j are the mass, semi-major axis, eccentricity, and inclinations of the terrestrial planets (Chambers, 2001).

3.5. Example Terrestrial Planet Formation Simulation

The focus of this work is to address some aspects of the late stages of terrestrial planet formation which are accessible to use through numerical simulations. These simulations begin with an initial distribution of planetesimals which we assume have somehow pushed through the growth and bouncing barriers. This is a leap of faith, which exemplifies a major hallmark of research in planet formation: split up the timeline into manageable chunks and hopefully manage to match their boundaries before reaching retirement age.

Initial conditions for our planetesimal distribution are broadly based on the concept of the Minimum Mass Solar Nebula (Hayashi, 1981; Weidenschilling, 1977), which is reconstructed by grinding up the planets, distributing the mass, and asking how this mass is distributed and how much there is in total. For the inner Solar System, distributing about five Earth masses of solids between 0.5 and 4.0 AU with a projected surface density profile $\Sigma \propto r^{-p}$ (with p typically between 0.5 and 1.5) satisfied this condition. Assuming that the initial planetesimals would have radii on

the order of a km at volume density of 2 g/cm^3, distributing this mass would require $\sim 3 \times 10^{12}$ planetesimals. This is far beyond the capabilities of planetary dynamics codes which require $\mathcal{O}(N^2)$ force evaluations per step to accurately resolve close encounters. Realistically, GENGA can evolve up to 8192 planetesimals (corresponding to initial radii of about 750 km), but even this requires two to three months of runtime on even the fastest Graphics Processing Units.[11]

This raises the question of what we are actually modelling. Arguably, the least objectionable answer is that we are performing dynamical modelling of the 8192 most massive objects among the planetesimals, which means that we are conveniently skipping over some essential questions. How and on what timescale do these most massive objects assemble? Should their location coincide with the fiducial initial distributed based on grinding up the inner planets? Are there important small scale dynamics that may be relevant to the interior evolution of planetesimals? Are low speed collisions between smaller planetesimals relevant for their chemical evolution? To some degree, other simulation codes address these issue by considering each particle to be a statistical ensemble of smaller particles that evolves along with its host (Levison et al., 2012; Morishima, 2015), although this still leaves small bodies which are not contained within the large simulation particles unresolved.

Deferring final judgement on whether this is a reasonable business to be in to the future, we can at least attempt to determine whether we are doing a somewhat decent job through numerical convergence studies, i.e. by repeating a given (suite of) simulations at different numerical resolutions. For example, we could evolve twelve runs with identical disk masses, but distributed over 2000, 4000, and 8000 particles, respectively. Doing so, we would find some weak trends in the number of final planets assembled, their median mass, semi-major axis, and chemical composition. On the other hand, the distributions of collision geometry and impact energies will be very different. We partially address these issues in our paper on *Wet Terrestrial Planets: Fact or Artifact?* in Chapter 6. Finally, we note that on timescales of a few 10^4 years, the mass functions (the number of particles at a given mass) evolves away from a delta-function (equal mass) distribution into a power law distribution. As such, we should be weary of trusting the first few 10^4 years of our simulations before the objects relax into their apparently more natural mass function.

Complications and trust issues aside, let us now have a look at a representative simulation run. Figure 3.4 shows time slices of a simulation that started out with 2000 equal mass planetesimals distributed between 0.5 and 4.0 AU with a total mass of 5 $M_\oplus$. The planetesimals were distributed to follow a $\Sigma \propto r^{-3/2}$ surface density profile and Jupiter and Saturn are included in the simulations on their present-day eccentric orbits. The simulations also include a gaseous disk (a source of hydrodynamic drag and type I migration) that decays exponentially in time with an e-folding timescale of 1 Myr such that the majority (99 per cent) of the gas is gone after 5 Myr. Dynamically, both columns show the same distribution of objects with semi-major axis and eccentricity. On the left, the colour indicates the precursors of each of the final five planets. On the right, the shading shows the water mass fraction determined by the collisional history encoded on the left and some initial water mass

[11] At the time of writing, NVIDIA TESLA K80 cards are the fastest available units. See also http://www.nvidia.com/object/tesla-k80.html.

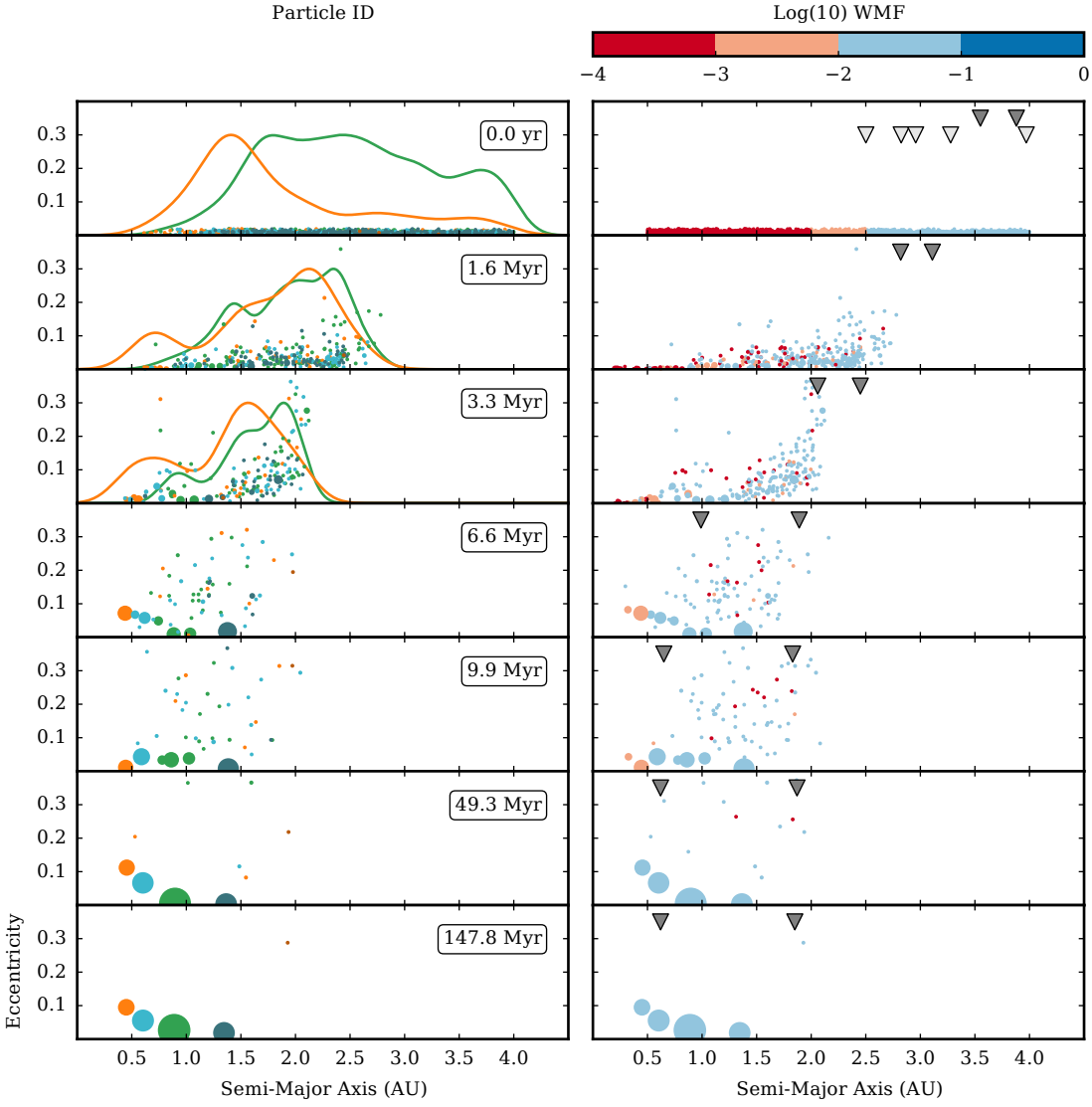

Figure 3.4. Time slices for a representative planet formation simulation. We plot semi-major axis vs. eccentricity. The mass is proportional to the size of the circles. Initially, we distribute 2000 equal mass planetesimals (with a total mass of 5 $M_\oplus$), which we then evolve under their mutual gravitational influence, the influence of Jupiter and Saturn on eccentric orbits (not shown in the figure), and a dissipating gas disk that interacts with the planetesimals and planets via hydrodynamic drag and type I migration. *Left:* In the bottom panel, we colour-code the final five planets. In the panels above, the same colours indicate the corresponding planetesimals that will eventually collide to make a given final planet. On the top three panels, we also indicate the corresponding distribution (as a kernel density estimate) of source planetesimals for two of the planets. *Right:* Same as left, except that the colour now indicates the water mass fraction (WMF). On top, we show the fiducial WMF that is initially imprinted. In each collision, the WMF of the resulting body is calculated. We also indicate the location of the 3:1, 5:2, 7:3, 2:1, and 3:2 mean motion resonances with Jupiter (light triangles) as well as the ν_5 and ν_6 secular resonances with the Jupiter-Saturn system (dark triangles). They sweep inwards as the gas dissipates.

fraction. Triangles indicate mean motion (with Jupiter) and secular resonances (with the Jupiter-Saturn system) and the top panel corresponds to the initial condition.

A typical simulation evolves as follows. In the inner system (at semi-major axis $a \lesssim 1$ AU), collision timescales of planetesimals are short and planetary embryos form rapidly. As they grow in mass, they begin to interact gravitationally with the gas disk, leading to inward type I migration. Consequentially, most of them now fall into the star. At intermediate distances ($1 \lesssim a \lesssim 2$ AU), collision timescales are somewhat longer and planets grow slower. By the time they become massive enough to interact gravitationally with the gas, the disk has dissipated sufficiently for radial migration to merely drive them to smaller a, but not onto the star. These embryos end up on short period orbits at $a \sim 0.5$ AU. In the outer regions ($a \gtrsim 2$ AU), the planetesimals evolution is different because they interact with mean motion and secular resonances with Jupiter and Saturn. Planetesimals in resonances are dynamically excited (their orbital eccentricity increases), although hydrodynamic drag from the gas dampens them. As the gas dissipates, damping becomes less effective and planetesimals can remain on sufficiently eccentric orbits to collide with objects closer to the star. At the same time, the change in gravitational potential from the dissipating gas moves the locations of the secular resonances with the Jupiter-Saturn system inwards (the dark triangle in Figure 3.4 move left), which causes some planetesimals to be swept inwards ahead of these resonances. As they are swept inwards, planetesimals tend to move on similar orbits, leading to more frequent collisions which build up embryos and planets. After ~ 10 Myr, most of the gas has dissipated, and the locations of the secular resonances become fixed, the outer one of which effectively demarcates terrestrial planet region.

We have dealt with three types of planets at this point. The planets that formed from material at the inner edge of the disk fell into the star, planets formed from planetesimals at intermediate distances are now close to the star ($a \lesssim 0.8$ AU), and embryos from material further out are located between at $0.8 \lesssim a \lesssim 1.5$ AU. For all planets, over 70 per cent of their source mass originates from semi-major axis larger than their final location. This is illustrated in Figure 3.4 by comparing the colours of the final planets on the bottom left with the two exemplary distributions shown on the top left.

After 10 Myr, the evolution of the planetary systems becomes decidedly less exciting. The system now consists of a few oligarchs that have cleared out the immediate neighbourhood as well as about two dozen dynamically excited planetesimals. Over the next ~ 40 Myr, the oligarchs accrete the remaining planetesimals (by now, these are moon-sized objects) in potentially disruptive collisions before resigning themselves to orbiting their host star on well-separated and uneventful journeys until the simulation terminates. However, not all planetary systems evolve in such an uneventful fashion. Depending on the details of the architecture formed by the 10 Myr mark, close encounters may occur between planets which can result in catastrophic collisions or ejections from the system.

At any point in time, we know the full accretion history of all planetesimals and planets. Using this, we can imprint initial distributions of chemical or physical quantities we may want to investigate onto the initial planetesimals. For example, we may want to ascribe an initial water mass fraction in an attempt to quantify the

expected amount of water in the final terrestrial planets (O'Brien et al., 2006; Raymond et al., 2004) or track isotope ratios that may be indicative of core-formation and impact events (Nimmo & Agnor, 2006; Nimmo et al., 2010). We illustrate the former in the right column of Figure 3.4. Initially, we ascribe each planetesimal a water mass fraction (WMF) of some fiducial form. In each collision, we update the WMF of the resulting particle. Over time, we then obtain the final water content of the formed planets, which we may compare to measurements. By considering the final water content and the feeding zones of the planets side-by-side, we can gain an appreciation for how the dynamics of different models shape water delivery. For example, we may investigate what effect omission of the giant planets or a longer decay timescale of the gas disk would have.

There are two important differences between our simulations and more classical approaches that are initialised by embedding embryos in a disk of planetesimals (O'Brien et al., 2006; Raymond et al., 2009, 2004, 2006). First, we find planetesimal growth to be an inside-out process in the sense that the most massive embryos first appear close to the star. This contrast the classical initial conditions that distributed embryos of increasing mass further from the star. Secondly, we show that the final planets tend to have material that samples wide regions of the initial disk. If simulations are initialised with seeded embryos, then, by definition, most of the mass is local, which is a questionable assumption given our results. Thirdly, simulations do not include the gravitational and hydrodynamic influence of the gas disk lack the mechanism of sweeping secular resonances to concentrate material into the inner disk. They instead rely on whatever planetesimals are seeded in the fixed locations of the secular resonances to reach the inner disk. We address all these issues – to varying levels of detail – in the papers that constitute Chapters 5 and 6.

Finally, the simulation we have presented here is just a single realisation of a terrestrial planet formation simulation. As it turns out, if we initialise the same simulation (with *identical* initial conditions) again, a new run with Genga will generate an entirely different system of planets. Deferring details to our paper on *Chaos in Terrestrial Planet Formation* in Chapter 5, it appears that numerical round-off errors that arise from run-time rearrangement in the order of certain compute operations cause planetesimals orbits to diverge on timescales of 400 years. Once diverged, the entire collisional history of a given planetesimal is altered across the two simulation runs, which gives rise to the assembly of a very different final system.[12]

3.6. Tweaking Models

The simulations we have just outlined are unable to capture the dynamics of the entire Solar Systems and therefore cannot hope to match all of the chronological, compositional, and dynamical constraints – only some of which we have described – of the Solar System. We now briefly address a few more constraints and outline the myriad of models that have been formulated around them. In none of the cases, the

[12]Physically, this is a manifestation of the chaotic behaviour readily observed in non-linear systems, where initial displacements grow exponentially fast. In the context of our simulations, the initial displacements are induced by numerical round-off errors that differ across simulations runs.

last words have yet been spoken, and we should take all these model for what they are: possible steps in the right direction, but unlikely to be the ultimate truth.

Giant Planet Architecture, Lunar Cataclysm To probe the evolution of the outer planets in the early Solar System, Masset & Snellgrove (2001) performed numerical simulations of pairs of Jupiter- and Saturn sized protoplanets. They found that two planets tend to get locked into a $2:3$ mean motion resonance, independent of whether the outer planet catches up during their inward migration or is formed in-situ. In such a configuration, the gaps opened by both planets overlap, which appears to prevent them from migrating further inwards (Morbidelli & Crida, 2007). By dropping in further giant planets with masses comparable to the ice giants Uranus and Neptune, Morbidelli et al. (2007) and Batygin & Brown (2010) demonstrated that migration and gravitational interactions can drive a sequence of four large planets into a stable multiresonant compact configuration.

Such a configuration is very different from the present orbital architecture of the gas and ice giants, which are neither in resonance nor spaced in a particularly compact fashion. As it turns out, gravitational interactions of the giant planets with a massive, exterior distribution of planetesimals (the remnants of which corresponding to the present-day Kuiper belt) can sap energy from the giant planets through secular interactions and mean motion resonances (Levison et al., 2011). As a consequence, the gas giants migrate inwards – Saturn faster than Jupiter – while the outer ice giant is slowly pulled outward. At some point, the gas giants cross their $5:3$ and $2:1$ mean motion resonances, at which point the system rapidly destabilises. Beyond rearranging the giant planets into their present-day configurations, this instability would also have scattered a significant amounts of planetesimals from the outer disk towards the inner system to act as source of the (still disputed) Lunar Cataclysm (Gomes et al., 2005) and claims to explain the capture of the Trojan asteroid groups by Jupiter (Morbidelli et al., 2005).

In its original incarnation (Tsiganis et al., 2005), this 'Nice model' (named after the city on the French Riviera) of early Solar System evolution has received two major points of criticism. Firstly, the initial conditions for the orbits of the giant planets were somewhat arbitrary, but this gave way to more a natural configuration rooted in migration simulations detailed above. Secondly, the timing of the instability required significant fine-tuning of the extent and mass of the exterior planetesimals disk.[13] More recent criticism is levelled towards the inherently stochastic nature of the simulations. For example, out of ~ 300 simulations, Kaib & Chambers (2016) report that only one per cent result in configurations of giant and terrestrial that mimic the present-day.

[13]This argument can of course be reversed. If the Lunar Cataclysm interpretation of the Moon's impact breccia (timed at ~ 600 Myr after CAIs) and the initial configuration of giant planets in the Nice model are indeed correct, then we are simply answering the question of what the exterior planetesimal disk must have looked like to reproduce such dynamics.

Truncated Disk While the Nice model somewhat successfully reconstructs the orbital architecture of the outer Solar System and accounts for a possible Lunar Cataclysm, the inner orbital architecture and distribution of terrestrial planets as well as the apparent depletion and dynamic excitement of the asteroid belt remain unaddressed.

As demonstrated, classical simulations of terrestrial planet formation reliably form a few terrestrial planets of roughly equal mass in the inner regions. This is in stark contrast to reality, where we find the massive terrestrial planets Earth and Venus flanked by two much less massive ones – Mercury and Mars. This has come to be described as the *small Mars problem*. Given the constraints on the formation timescales of Mars from Hf-W dating (0 to 20 Myr) and the fact that its mass (~ 0.1 $M_\oplus$) is on the order of the isolation mass, it appears that Mars may be little more than an embryo that failed to acquire more mass in the late-accretion stage. This requires the orbital feeding zone of Mars to be severely depleted which is compatible with a model of terrestrial planet formation where the planet forming planetesimals disk would be constrained to a much tighter region of space ('truncated') instead of being spread out over the entire inner system (Hansen, 2009; Morishima et al., 2008). This truncation could be provided by a trapping mechanism such as a smeared out vortex (Surville et al., 2016). Other models propose a mechanism where the planetesimals disk was initially spread out, but was truncated dynamically by a temporary inward migration of Jupiter and Saturn followed by a rapid reversal back outwards – a 'Grand Tack', as it were (Walsh et al., 2011). In principle, sweeping secular resonances can also provide a pathway to truncate the disk, although they do not appear to produce small enough masses for Mars analogues, cf. Chapter 5.

Asteroid Belt If we subscribe to the notion that the asteroids in the belt are remains of the original planetesimal population, we may expect the total belt mass to be on the order of one Earth mass with a dynamically unexcited population (Weidenschilling, 1977). At present, however, the total mass of the asteroid belt is estimated at $\sim 4.5 \times 10^{-4}$ $M_\oplus$ with median eccentricities (inclinations) of 0.145 and 11 degrees with substantial dispersions (Petit et al., 2002), so neither of the expectations are met. Taken together, both observations warrant a scenario where some dynamical event significantly stirred up the asteroid belt in the past. This is further supported by partial mixing of taxonomic types with semi-major axis (Morbidelli et al., 2015) as well as estimates of a steady collision rates that would put the asteroid belt age beyond ~ 8 Gyr (Bottke et al., 2005).

There are three basic mechanisms that can potentially account for the mixing, increased collision rates, mass depletion and dynamical excitation of the asteroid belt: (i) sweeping of secular resonances due to changing gravitational potential of the depleting planetesimal disk (Heppenheimer, 1980; Lecar & Franklin, 1997; Ward, 1981), (ii) dynamical interactions with a population of embryos (Chambers & Wetherill, 2001; Wetherill, 1992), and (iii) a sweeping of giant planets through the belt region (Walsh et al., 2011).

In the first model, the location of secular resonances in the eigenfrequencies of the dynamical system consisting of Jupiter, Saturn, and the protoplanetary disk moves inwards as the gas disk dissipates (Nagasawa et al., 2000). As we reviewed in Section 2.1.4, this means that the location of the resonances moves inward as the gas dissipates, thereby exciting as well as sweeping planetesimals in front of them. In principle, this model can account for the constraints on the asteroid belt as well as the truncation of the planetesimal disk. However, it appears that in order to sufficiently excite planetesimals in a scenario that is compatible with the Nice model, gas disk lifetimes on the order of ~ 20 Myr would be required, which is significantly longer than expected (Podosek & Cassen, 1994; Russell et al., 2006). On the other hand, if we do not subscribe to the Nice model to explain the orbital architecture of the outer planets (and the hypothetical Lunar Cataclysm), inward sweeping resonance appear to be compatible with some the constraints.[14] To some degree, we address this in our paper on *Chaos in Terrestrial Planet Formation* in Chapter 5.

In the second model, the disk region hosting the present-day asteroid belt was cleared by perturbation from Jupiter and the mutual interactions between planetary embryos. This model is also compatible with asteroid belt constraints, but cannot account for the required truncation of the planetesimal disk to solve the problem of a small Mars.

The 'Grand Tack' scenario which we have outlined above can remedy this issue by postulating that Jupiter and Saturn first migrate inwards up to a heliocentric distance of ~ 1.5 AU, where they 'tack' to reverse their migration and move outwards. Like the Nice model, this idea is rooted in the result of hydrodynamic simulations. During their inward migration, planetesimals from the asteroid belt are dynamically excited; some of them enough to be scattered to orbits exterior of Jupiter and Saturn. Once migration reverses, a smaller fraction of originally scattered planetesimals is thrown back in close to their original location, which addresses all of the constraints (belt mass depletion, radial mixing, dynamical excitation, truncation of the planetesimal disk) we observe (Walsh et al., 2012).

[14] The apparent mixing of taxonomic types remains a serious problem in the model of sweeping resonances.

4

Exoplanets: Observations & Models

"*[...] – Oh my God! – It's full of stars!*"

– Arthur C. Clarke, *2001: A Space Odyssey (1968)*

The first fortuitous exoplanet detection (Wolszczan & Frail, 1992) sparked a deluge of observing programmes and even dedicated space-based facilities to detect and characterise planets orbiting distant stars. Propelled by the relentless march of progress in instrument design and signal processing, we have to date (30 January 2016) detected 2056 planets in 1304 extrasolar systems, most of which have little in common with the architecture of our Solar System. In this Chapter, we review current exoplanet detection methods (Section 4.1), the dynamical and physical properties of exoplanets (Section 4.2), as well as recent developments in formation models as applicable to the architecture of extrasolar system (Section 4.3).

4.1. Observational Techniques

4.1.1. Radial Velocity

Motions in planetary systems are never entirely heliocentric. Instead, both the planets and host star orbit around their common barycentre (which can be inside the host star). The radial velocity (RV) technique is based on measuring the (line of sight, i.e. radial) component $v_{\mathrm{R}}(t)$ of the orbital motion of the host star over time t, from which some of the planetary orbital parameters can be reconstructed (Perryman, 2011, Chapter 2).

Technique	Surveys	Orbital Parameters	Physical Parameters
Radial Velocity	HARPS	a, e, ω, ν	$M_{\rm P} \sin i$
Astrometry	Hipparcos, HST, Gaia	$a, e, i, \Omega, \omega, \nu$	$M_{\rm P}$
Transit	WASP, Kepler, CoRoT TESS, CHEOPS	a, e, i, ω	$R_{\rm P}$

Table 4.1. Summary of observational techniques with some sample survey and the orbital as well as physical parameters that can be recovered for the planets. As usual, a, e, i, Ω, ω, ν are the semi-major axis, eccentricity, inclination, nodal line, argument of perigee, and true anomaly. In addition, $M_{\rm P}$ is the planetary mass and $R_{\rm P}$ the radius. In all cases, the stellar parameters must be known from prior classification (usually from spectra or luminosity). Note that, for a given technique, derived orbital and physical parameters may be degenerate. Observations with different techniques can usually break these.

A single planet orbiting a host star will induce a radial velocity

$$v_{\rm R}(t) = K \left[\cos(\omega + \nu(t)) + e\cos(\omega)\right], \tag{4.1}$$

where e is the eccentricity, ω the argument of perigee, $\nu(t)$ the true anomaly, and

$$K = \frac{2\pi}{P} \frac{a_\star \sin i}{\sqrt{1-e^2}} \tag{4.2}$$

the *radial velocity semi-amplitude* with P being orbital period, $a_\star$ the semi-major axis of the star (orbiting its barycentre), i the inclination, and e the eccentricity as above. For a given orbit, $v_{\rm R}$ oscillates between $K(e\cos\omega + 1)$ and $K(e\cos\omega - 1)$ as the planet moves around the star with the shape of the measurement depending on the orbital parameters and viewing inclination of the system.

We now note three features of the RV method. First, if we observe the system face-on ($i = 90°$), $K = 0$ and we recover no signal. Second, we can only recover the product of $a_\star \sin i$, but neither individually. Third, when writing the Kepler's third law around the barycentre,[1] we find

$$K^2 = \frac{G}{(1-e^2)} \frac{1}{a_\star \sin i} \underbrace{\left(\frac{M_{\rm P}^3 \sin^3 i}{(M_\star + M_{\rm P}^2)}\right)}_{\mathcal{M}}, \tag{4.3}$$

with $M_{\rm P}$ being the planetary mass and G the gravitational constants. Noting that $M_\star \gg M_{\rm P}$, the last term becomes

$$\mathcal{M} \simeq \frac{M_{\rm P}^3 \sin^3 i}{M_\star^2}, \tag{4.4}$$

which suggests that even if we determine $M_\star$ (from spectral type or luminosity class), the mass of the planet can only be determined up to a factor $\sin i$.

[1] In barycentric coordinates, we have $a_\star^3/P^2 = GM'/(4\pi^2)$ where $M' = M_{\rm P}^3/(M_\star + M_{\rm P})^2$.

The radial velocity itself is determined from Doppler shifted stellar emission lines with signals being on the order of 0.1 to 10 m/s. For example, observing our Solar System, a lonely astronomer on Alpha Centauri would need to measure $v_{\mathrm{R}} \sim 12.5$ m/s or $v_{\mathrm{R}} \sim 0.09$ m/s to detect Jupiter or Earth, respectively. One of the most advanced instruments available today (HARPS) can measure at an accuracy of ~ 1 m/s (Mayor et al., 2003), so our friend (assuming he is at the same technological level) would find Jupiter, but not Earth.

For single planet systems, fitting the orbital parameters that reconstruct K and v_{R} is a fairly straightforward fitting problem and a number of efficient algorithms exist. For multiple planet systems, the parameter space can quickly become overwhelming large, however. Here, use of N-Body simulations to reject dynamically unstable solutions has recently gained significant traction.

4.1.2. Astrometry

Astrometric observations are complimentary to RV techniques in the sense that they measure the transverse (instead of radial) motion of stars on the sky to detect remnant 'wobbles' due to the presence of orbiting planets. This excess motion (once corrected for observer motion as well as the proper motion of the star) describes the orbit of the star about the barycentre of a system consistent of the star and the planets it may be hosting. Provided that the mass of the star can be estimated by spectroscopic or luminosity classification, the geometry and amplitude of the motion about the barycentre can be used to constrain the planets orbits and masses. In the case of a single planet, the reconstruction is easily conceptualised by Kepler's third law written in the barycentric frame, viz.

$$\frac{a_\star^3}{P^2} = \frac{GM'}{4\pi^2}, \qquad M' = \frac{M_{\mathrm{P}}^3}{(M_\star + M_{\mathrm{P}})^2}. \tag{4.5}$$

If we measure the semi-major axis $a_\star$ and period P of the stellar orbit about the barycentre, and know the stellar mass $M_\star$, the planetary mass M_{P} can be unambiguously reconstructed. Orbital reconstruction is somewhat more involved as it involves rewriting the orbital elements in terms of an astrometric signal Λ (Fischer et al., 2014, Eqn. 7) which is then fitted. Doing so allows unambiguous reconstruction of the ascending node Ω and orbital inclination i, both of which are unavailable from RV measurements. As for RV signals, fitting of single planet signals is relatively straightforward, but multi-planet fits are computationally demanding.

The largest drawback of astrometric techniques is the required precision. For a given geometry, the induced angular displacement is

$$\alpha = \frac{M_{\mathrm{P}}}{M_\star + M_{\mathrm{P}}}\, a_\star\, d^{-1}, \tag{4.6}$$

where d is the distance to the star. In other words, the technique is particularly sensitive to massive planets on wide orbits around that are not 'too far away'. For example, observing a Jupiter mass planet at $d = 10$ pc orbiting a star at $a = 5$ AU gives $\alpha = 0.5$ mas (milli-arcseconds). Observing an Earth mass planet at the same distances requires $\alpha = 0.0003$ mas (Perryman, 2011, Table 3.1). Worse, to

reconstruct the complete astrometric signal, reliable observations covering the entire duration of the planetary orbit are required.

Using the ground-based interferometric and adaptive optics systems, current angular resolutions are pushed to the 0.01 mas limit which would be sufficient to detect Jupiter in a long survey. Last generation spaced-based systems such as Hipparcos[2] or the HST[3] have no such capabilities, but can still be used to better constrain RV measurements (Fischer et al., 2014, Section 8.3). Current-generation systems such as Gaia,[4] on the other hand, can reach 0.02 to 0.05 mas precision and are expected to return large numbers of astrometric detections once their observing period is complete.

4.1.3. Transits

If a planet passes between its host star and an observer, the observed flux from the star dims in proportionality to the planetary radius and orbital period. Provided sufficiently sensitive instruments are available, this transit signal (called a *light curve*) can be observed and used to reconstruct dynamical and physical quantities of the system. At the most rudimentary level, there are three basic observables – the transit depth (flux decrease) ΔF, total transit duration t_{T}, and the duration of the fully occulted part of the transit t_{F}. Using some geometry, Seager & Mallén-Ornelas (2003) find

$$\Delta F \sim \left(\frac{R_{\mathrm{P}}}{R_\star}\right)^2, \tag{4.7}$$

$$\sin\left(\frac{t_{\mathrm{T}}\pi}{P}\right) = \frac{R_\star}{a}\sqrt{\frac{\left[1+(R_{\mathrm{R}}/R_\star)\right]^2 - \left[(a/R_\star)\cos i\right]^2}{1-\cos^2 i}}, \tag{4.8}$$

and

$$\frac{\sin\left(t_{\mathrm{F}}\pi/P\right)}{\sin\left(t_{\mathrm{T}}\pi/P\right)} = \frac{\sqrt{\left[1-(R_{\mathrm{P}}/R_\star)^2\right] - \left[(a/R_\star)\cos i\right]^2}}{\sqrt{\left[1+(R_{\mathrm{P}}/R_\star)^2\right] - \left[(a/R_\star)\cos i\right]^2}}, \tag{4.9}$$

where P is the orbital period, a the semi-major axis, i the orbital inclination, and R_{P} and $R_\star$ the radii of the planet and star. Provided that $R_\star$ is estimated from spectral or luminosity classification, the remaining parameters can be solved for. Beyond exploiting the equations above to derive basic properties, more recent advances also exploit secondary eclipses (the planet reflects light towards the observer just before and after it passes behind the star) and wavelength dependent transit depth to estimate atmospheric extent and composition. Asymmetries in the light curves can also be used to estimate orbital parameters beyond the semi-major axis and inclination. Final determination of orbital parameters then proceeds through fitting schemes similar to those used in RV and astrometric observations.

[2] http://sci.esa.int/hipparcos/
[3] http://hubblesite.org/
[4] http://sci.esa.int/gaia/

Transit analysis is of particular interest because it allows us to determine the planetary radius, which – combined with mass estimates from other measurements – give access to densities and thus a first glance at the bulk composition of the planet. Unfortunately, it is also exceedingly difficult and requires special geometries. For example, observing a Jupiter size planet around a Sun-like star has a transit depth of $\Delta F \approx 10^{-2}$. For Earth or Mars sized planets, this drops to $\Delta F \approx 10^{-5}$. However, transit depths $\gtrsim 0.05$ may occur for planets around M-dwarfs and white dwarfs due to their low intrinsic luminosity (Drake et al., 2010; Faedi et al., 2011; Haghighipour et al., 2010).

The probability of observing a transit is given by $p \sim R_\star/a$ (Borucki & Summers, 1984). Hot Jupiters on short period orbits (~ 3 days) have $p \sim 10$ per cent, super-Earth to sub-Neptune type planets $p \sim 2.5$ per cent, and Earth type planets $p \sim 0.5$ per cent. For the same population, the transit duration is on the order of three, six, and fifteen hours, respectively (Fischer et al., 2014, Section 5.2).

Although ground-based observations at the required photometric accuracy are difficult due to atmospheric extinction and scintillation, advances in instrumentation and data processing over the past decade have led to large numbers of transit detections by surveys such as HAT or WASP. More recently, however, CoRoT and Kepler have taken the step to space which has significantly boosted detection rates and the next generation of satellites (TESS and CHEOPS, for example) is already moving beyond the drawing board.

4.1.4. Transit Timing, Microlensing, Direct Imaging

Beyond the veritable avalanche of data from radial velocity and transit surveys and the promise inherent in astrometric observations, there are three other observing techniques that rely on special physical configurations to be feasible: timing variations, microlensing, and direct imaging.

Radial velocity and astrometric techniques measure induced variations in the orbits of the gravitational primary of the system. If the primary emits a periodic signal, the gravity of the planet induces a travel time variation τ of the signal from which the orbital parameters of the orbiting planet can be reconstructed, viz.

$$\tau = \frac{a \sin i}{c} \frac{M_\mathrm{P}}{M_\star} \tag{4.10}$$

For example, a typical pulsar has $M_\star = 1.35\ \mathrm{M}_\odot$, leading to timing variations on the order of milliseconds (Wolszczan, 1997). This is perfectly well within the accuracy of available clocks. Beyond pulsars, other sources of periodic signals include intrinsically pulsating stars or eclipsing binaries (Perryman, 2011, Chapter 4).

In cosmology, gravitational lensing is used constrain the distribution of matter on scales of galaxy clusters. In essence, the foreground gravity of massive cluster distorts ('lenses') the light of a background sources. Given suitable modelling and knowledge of the background source, the foreground mass distribution of the lens can be recovered (Bartelmann, 2010). In microlensing, the same idea is applied to stellar scale objects. If a background star passes behind some foreground star, the

image of the background star is distorted.[5] If the foreground star hosts a planet, there will be perturbations (called caustics) on the expected lensing curve. Since microlensing does not require detection of light from the star, it is uniquely suited to detect free-floating planets. Interestingly enough, Sumi et al. (2011) suggest that there exist two free-floating Jupiter-mass planet for each star in the Milky Way.

Ultimately, all techniques discussed so far give only indirect detections of exoplanets and direct imaging is required to conclusively confirm their existence as well as pave the way towards spectroscopic analysis. As yet, there remain two key challenges (Perryman, 2011, Chapter 7). First, the small ratio between the stellar and planetary fluxes. For Jupiter-size planets orbiting a Sun-like star at a distance of 10 pc away, the ratio is on the order of 10^{-9} and decreases further to 10^{-10} for an Earth-like planet. For interesting exoplanet candidates, flux ratios are expected to range from 10^{-5} at infrared wavelengths to 10^{-10} in the optical. Second, stars and planets tend to have very small angular separations on the order of 0.1 to 0.5 mas. At these separations, the stellar light tends to completely dominate the total flux. Mitigating these issues remains the premier technical challenge to date, but adaptive optics, coronagraphical masks, and polarimetric systems have begun to deliver first detections at wide separations.

4.2. Properties of Exoplanetary Systems

At the time of writing (11 January 2016), there are 2043 exoplanets recorded in the *Extrasolar Planets Encyclopaedia*[6] (Schneider et al., 2011). These exoplanets cover a huge dynamic range in terms of their orbital and physical parameters. Observed semi-major axes and masses range from 0.004 to 6650 AU and 0.067 Earth masses to 63.3 Jupiter masses. Lower mass objects exists, but these are isolated and somewhat special detections. For example, Konacki & Wolszczan (2003) detected a 1.8 Moon mass object around the pulsar PSR 1257 12, the same object about which one of the first exoplanets was detected (Wolszczan & Frail, 1992). Even an (apparently disintegrating) planetesimal sized object designated WD 1145+017 b orbiting a white dwarf at a mass corresponding to five per cent of our Moon was recently discovered (Vanderburg et al., 2015). The smallest 'main-line' planet is Kepler-138 b, which is a Mars analogue at 0.067 $M_\oplus$ orbiting 0.07 AU from its host star (Jontof-Hutter et al., 2015).

While no doubt fascinating, focussing on individual planets and systems blinds us to the impressive picture the entirety of these detections paint, which we have attempted to summarise in Figure 4.1 by showing the distribution of planetary mass with semi-major axis (left) as well as the mass-radius relationship (right) enabled by transit surveys such as Kepler. There appear to be four distinct populations of

[5] The typical angular scale of a lens (the foreground) is on the order of 0.3 mas (Fischer et al., 2014, Eqn. 4), which we cannot hope to resolve as an image. Therefore, microlensing observations are purely light curve observations.

[6] http://www.exoplanet.eu

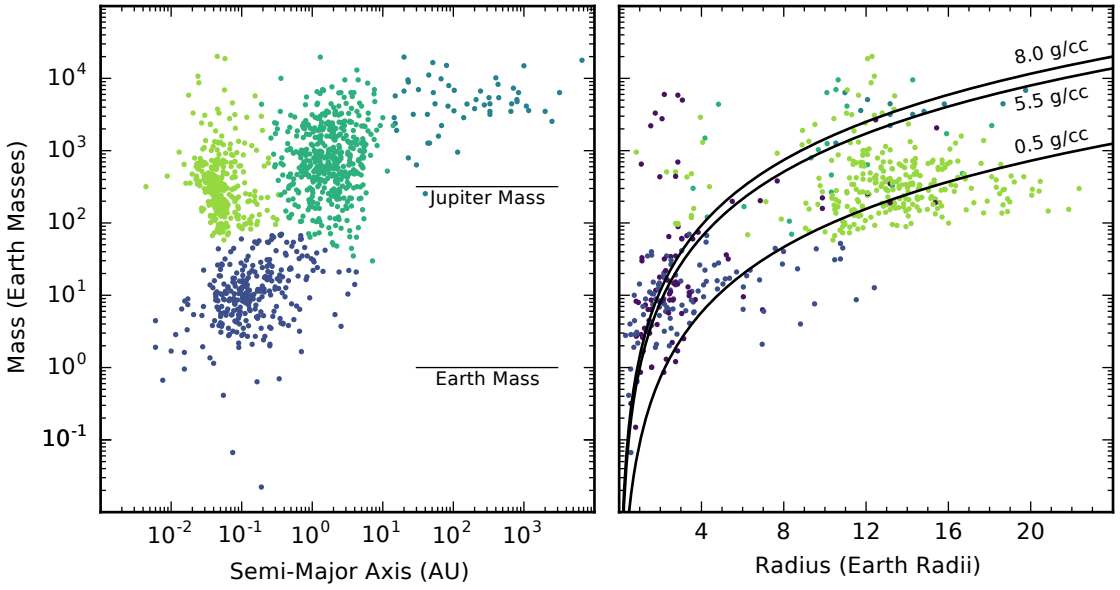

Figure 4.1. Mass vs semi-major axis (left), and mass-radius relationship (right) for subsets of exoplanets with available data. There are four clusters in the space of semi-major axis and mass, which we have coloured. Colours carry over to the mass-radius relation. We also indicate three mass-radius isodensity lines for orientation (see annotation). Note that not all observations from the left plot are available on the right.

Cluster	Median Semi-Major Axis	Median Mass
Hot Jupiters	0.05 AU	0.92 M_{Jupiter}
Giants	1.71 AU	2.29 M_{Jupiter}
Wide Giants	103.00 AU	14.00 M_{Jupiter}
Super-Earths, Sub-Neptunes	0.12 AU	10.59 M_{Earth}

Table 4.2. Median semi-major axis and mass for exoplanet cluster in Figure 4.1. Clusters are identified by a k-means algorithm on the subset of planets that have valid observations for mass and semi-major axis. Note the different mass units.

exoplanets which we have highlighted.[7] Planets with masses comparable to Jupiter at small semi-major axes are referred to as *Hot Jupiters*, while successively more massive objects at increasing semi-major axes are labelled *Giants* and *Wide Giants*. All remaining planets at lower mass are lumped into the *Super-Earth and Sub-Neptune* category, although isolated detections at sub-Earth masses exist (as illustrated above).

To some degree, the populations mirror observational biases inherent to different observing techniques. For example, massive objects at large semi-major axes tend to be directly imaged, while the closer objects tend to be detected by radial velocity measurements and transits, with radial velocity detections biased towards more massive planets. Microlensing and timing detections are rare, but can in principle access any part of the parameter space. In practice, they result in detections of fairly massive exoplanets.

With the advent of transit surveys such as CoRoT and Kepler (see above), data on exoplanet sizes became available. Combining these with RV detections (which constrain the mass up to the orbital inclination), bulk densities of exoplanets and therewith first hints of their interior structure became available. Where available, we show mass and radius measurements in the right panel of Figure 4.1 with overplotted isodensity contours for $\rho = 0.5$, 5.5, and 8.0 g/cm^3. For comparison, Jupiter and Saturn have $\rho \simeq 1.3$ and $\simeq 0.7$ g/cm^3, the Earth has $\simeq 5.5$ g/cm^3, and iron comes in at $\simeq 7.8$ g/cm^3 at room temperature. At a superficial level, this suggests a large population of Jupiter-like and Saturn-like objects with low bulk densities (the bright green population in Figure 4.1) as well as population with bulk densities comparable to Earth and masses on the order of a few Earth masses (the dark blue markers). In both cases, these similarities gave rise to the description of *Hot Jupiters* and *Super-Earths/Sub-Neptunes*. However, we must note that the spread about the isodensity contours is significant. This is particularly interesting for planets in the *Super-Earth* category, where low bulk densities suggest they may have formed beyond the snow line (Marcy et al., 2014). At this point, further progress in characterising exoplanet composition requires construction of more elaborate multi-layer composition models describing differentiated interiors or cores with thick gaseous envelopes (Thiabaud et al., 2014). In the Solar System, in-situ observations are typically available, such that compositional models are more sophisticated (although they tend to be degenerate – cf. Helled et al. (2014)). Modelling of exoplanets is more difficult and models are typically simpler, although they can field multi layer structures (Seager et al., 2007) and be informed by the proximity to the star and possible evidence for atmospheres (Kitzmann et al., 2010).

Out of 2043 exoplanet detections in 1291 star systems, we detect only a single planet in 788 systems (61 per cent). It remains unclear whether this is due to observational biases or representative of the true population of exoplanets. Given that formation models routinely generate groups of planets as well as first hand evidence from the Solar System, we would expect single planet systems to be the exception rather than the norm. The bulk of the remaining systems hosts either two (338 sys-

[7] The populations are clearly visible to the naked eye in a scatter plot, but for purposes of visualisation and statistical description we have used k-means clustering algorithm (Lloyd, 1982) to automate detection.

tems, 26 per cent) or three planets (110 systems, 8.5 per cent). Systems with up to seven detected planets exist, but are rare at this point.

To develop an appreciation for the orbital architectures of multi-planet systems, we now consider the semi-major axis distribution of planets in a subset of data taken from the *Extrasolar Planets Encyclopaedia*. Rejecting all single planet systems (788) as well as systems in which any of the detections has missing data in either the mass or semi-major axis,[8] we are left with 156 star systems of interest, which we have arranged in Figure 4.2. From a purely qualitative inspection, we can make two obvious observations. Firstly, within a single system, semi-major axes tend to span one or two order of magnitude. Secondly, although there are some systems with architectures reminiscent of the Solar System (giants on semi-major axis above 5 to 10 AU, smaller planets closer to the star at a few AU), most systems have their planets significantly closer to the host star than in our Solar System. In particular, the 10, 50, and 90 percentile semi-major axis over all planets in the set of 156 systems are 0.06, 0.31, and 3.6 AU. Even if we weight the statistics by the planetary mass (making the 10, 50, and 90 percentiles 0.2, 1.9, and 17.8 AU), systems are consistently more compact.

Comparing the multiplanet extrasolar systems to our own challenges our notion that the Solar System should not be a special place. Oddly enough, the architecture of our system does differ significantly from that of many extrasolar systems. This is most obvious in the planetary masses and compactness, although we cannot exclude observational biases at work – indeed, there may be a hidden population of systems very similar to our own still waiting to be detected.

4.3. Formation Models

Universally valid planetary formation models need to account for both our Solar System as well as the architectures of extrasolar systems, preferably in a unified framework. In extrasolar systems, the most obvious feature is the presence of massive planets close to the star, either as gas giants or Super-Earths.

There are two (not mutually exclusive) scenarios of how these may have ended up in their present locations: in-situ formation and orbital migration from their original formation site. In-situ formation requires huge local densities[9] (Chiang & Laughlin, 2013) which could have resulted from prior migration of planetesimals (Hansen & Murray, 2012, 2013) and/or the activity of pile-up mechanisms (Boley & Ford, 2013; Chatterjee & Tan, 2014; Hansen, 2014). Criticism against in-situ

[8] Missing values in the catalogues are a problem and it is not always clear (without referencing the detection paper) what their origin is. For example, for some planets, only the mass or the semi-major axis is given. Simply removing this 'unclean' data is an appealing way to trim down the set of planets to something we can grasp at glance.

[9] On the order of 50 to 100 $M_\oplus$ within an AU, cf. Hansen & Murray (2012). Typical initial conditions for terrestrial planet formation type simulations based on the Minimum Mass Solar Nebula (Hayashi, 1981; Weidenschilling, 1977)) distribute on the order of 5 to 10 $M_\oplus$ in the inner system.

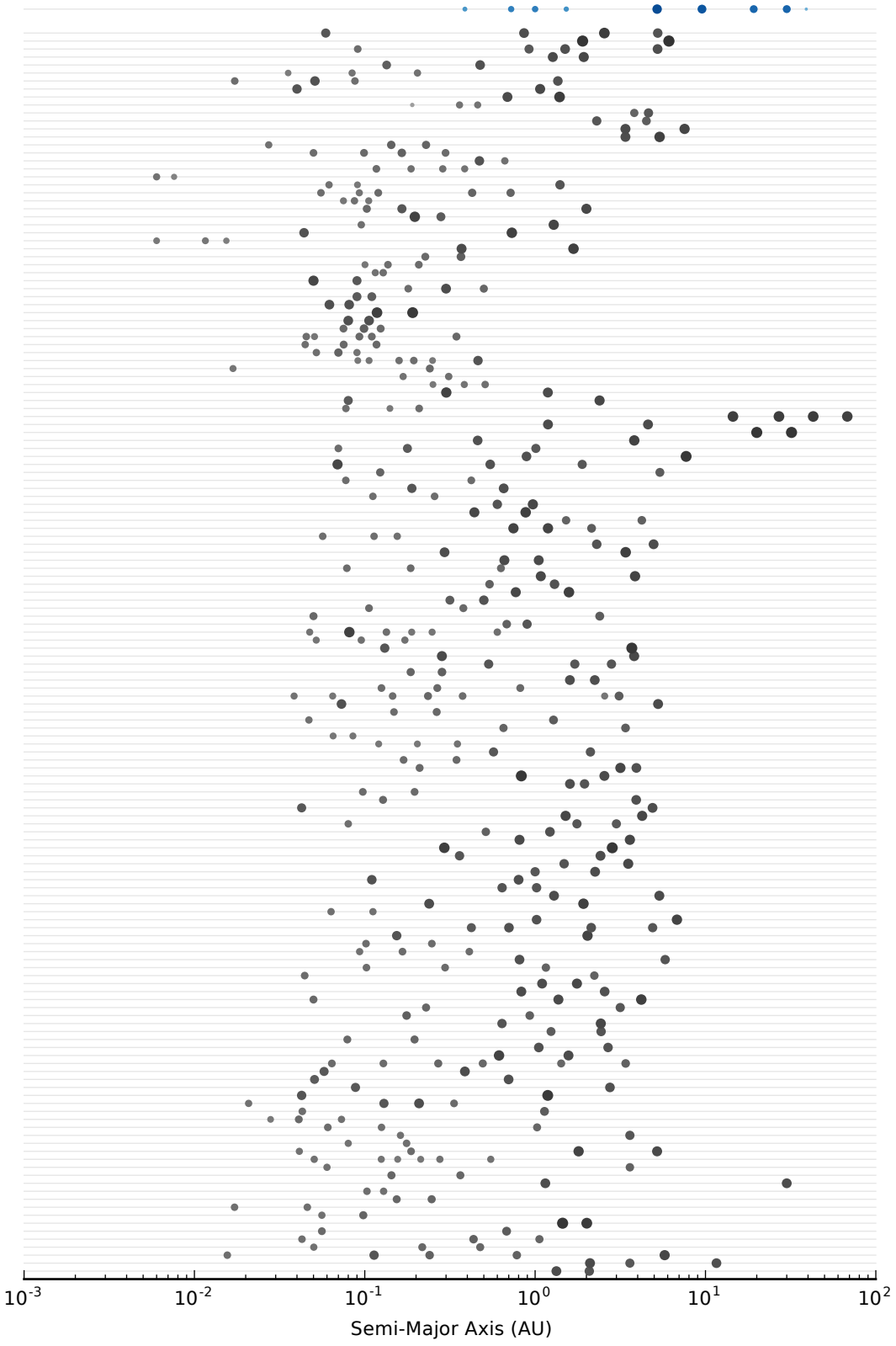

Figure 4.2. Orbital architecture of 156 star systems with at least two planets and no gaps in the data for any of them. Shade and size of the markers correlate with the (base-10) logarithm of mass. On top, we show the Solar System for reference.

formation is usually levelled by inescapability of orbital migration[10] for massive enough planets and disk (Papaloizou et al., 2007; Papaloizou & Terquem, 2006) and the difficulty of constructing surface density profiles consistent with in-situ formation (Raymond & Cossou, 2014). Additionally, a significant fraction of Super-Earth type planets appear to have low bulk densities which is indicative of core formation beyond the snow line (Helled et al., 2014). On the other hand, migration models predict that systems of multiple Super-Earths should be locked in mutual mean motions resonances (Ogihara & Kobayashi, 2013; Rein et al., 2012), but this is seldomly observed. In some cases, models invoking additional stochastic torques to mimic the turbulent nature of disks are able to better match the observed constraints (Rein, 2012).

In the context of the Solar System, the particular mass and period ratios of Jupiter and Saturn could have prevented both from migrating closer to the Sun. In a massive gas disk, both Jupiter and Saturn open a gap, but Saturn would migrate inwards faster than Jupiter. Once Saturn catches up and crosses into a low order mean motion resonance, both could have been pulled outward,[11] establishing a dynamical barrier preventing inward migration of Uranus and Neptune (Izidoro et al., 2015), and remain sufficiently far away from the inner system for late-stage accretion of terrestrial planets to proceed undisturbed. However, even in systems where giant planets do migrate through the inner regions where terrestrial planets assemble, these may yet survive if their migration timescales are sufficiently short (Izidoro et al., 2014).

[10] At small radii, planetary accretion timescales are short enough for the planets to fully form before the dissipation of the gas disk, whereafter they should migrate into the star. One may argue that the only way for planets to survive their migration is to form at sufficiently large distances.

[11] This is the essence of the 'Grand Tack' model, cf. Section 3.6.

5

Chaos in Terrestrial Planet Formation

In this paper, we discuss the effects of divergence of initially identical planetesimal orbits. Across two simulation runs, their orbits diverge as perturbations seeded by round-off errors are amplified. Within a few hundred years, identical initial conditions lead to dynamically very different systems. We characterise these outcomes for a variety of initial conditions, each of which we evolve multiple times to account for the divergence of orbits. We find that the interaction with giant planets with the gaseous disk strongly shapes the dynamical evolution of planetesimals and their growth of into embryos and terrestrial planets.

The paper has been submitted to *Monthly Notices of the Royal Astronomical Society*. At this stage, we are preparing submission of the revised edition in which we have significantly expanded the systems we have evolved. The version presented here is a draft of the revised version.

MNRAS **000**, 1–21 (2015) Preprint 25 July 2016 Compiled using MNRAS LATEX style file v3.0

Chaos in Terrestrial Planet Formation

Volker Hoffmann,[1]⋆ Simon L. Grimm,[1,2] Ben Moore[1] and Joachim Stadel[1]

[1]*Institute for Computational Science, University of Zürich, CH-8057 Zürich, Switzerland*
[2]*Center for Space and Habitability, University of Bern, CH-3012 Bern, Switzerland*

Accepted ..... Received .....; in original form .....

ABSTRACT

Terrestrial planets are thought to be the result of a vast number of gravitational interactions and collisions between smaller bodies. We use numerical simulations to show that practically identical initial conditions result in a wide array of final planetary configurations. This highly chaotic behaviour questions the predictability of different scenarios for the formation and evolution of our solar system and planetary systems in general. However, multiple realisations of the same initial conditions can be used to predict certain global statistics. We present two sets of numerical experiments that quantify this behaviour. Firstly, we demonstrate that simulations with slightly displaced particles are completely divergent after ~ 500 years, irrespective of initial displacement, particle number, and code accuracy. If a single planetesimal is moved by less than one millimetre, then a different set of planets results – this timescale for chaotic divergence decreases with increasing particle number. Secondly, we show final planetary configurations of initially similar simulations with and without giant planets after evolving them for ~ 148 Myr. We find that the same simulations including giant planets tend to generate higher mass planets at lower semi-major axes than simulations without gas giants. This prediction can be tested with forthcoming observational programs. By extracting outliers in the observations, we cautiously predict that Kepler-10, Kepler-9, 61 Vir, HD 134060, and HD 51608 may host as yet undetected giant planets.

Key words: planets and satellites: formation – planets and satellites: terrestrial planets – planets and satellites: dynamical evolution and stability – chaos – methods: numerical – celestial mechanics.

1 INTRODUCTION

Numerical simulations suggest that our solar system is inherently chaotic and any small changes to the planets' initial positions diverge exponentially in time with e-folding times on the order of 5 to 20 Myr (Sussman & Wisdom 1988; Laskar 1989; Quinn et al. 1991; Sussman & Wisdom 1992; Laskar 1994). Although the outer solar system planets appear to be remarkably stable against developing crossing orbits on Gyr timescales (Ito & Tanikawa 2002), this may not be the case for the inner solar system planets (Laskar 2008; Laskar & Gastineau 2009).

On such timescales, chaos is mediated by overlapping resonances (Nesvorný & Morbidelli 1998; Murray & Holman 1997; Moons & Morbidelli 1995; Morbidelli & Moons 1993; Laskar et al. 1992; Laskar 1990; Franklin et al. 1984; Wisdom 1980; Chirikov 1979) to which minor bodies are particularly sensitive. Analytical and numerical work suggests that overlapping resonances account for the observed distribution of bodies in the asteroid belts (Moons et al. 1998; Gladman et al. 1997; Wisdom 1985, 1983, 1982), in the inner (Evans & Tabachnik 1999; Mikkola & Innanen 1995) and outer solar system (Morbidelli et al. 2005; Grazier et al. 1999a,b; Holman & Wisdom 1993; Holman 1995; Duncan & Quinn 1993; Gladman & Duncan 1990; Franklin et al. 1989; Everhart 1973; Lecar & Franklin 1973), as well as within the Kuiper belt (Duncan & Levison 1997; Levison & Duncan 1997; Holman & Wisdom 1993; Levison & Duncan 1993; Torbett & Smoluchowski 1990; Torbett 1989).[1]

During the epoch of terrestrial planet formation, the solar system environment was rather different than today. Set against a backdrop of migrating giant planets (Walsh et al. 2011; Levison et al. 2011; Morbidelli & Crida 2007; Morbidelli et al. 2007; Tsiganis et al. 2005), and embedded in a gas disk (Pfalzner et al. 2014; Mamajek 2009; Haisch et al. 2001), planetesimals are thought to grow collisionally and hierarchically into terrestrial planets (Kokubo & Ida 2000, 1998; Weidenschilling et al. 1997; Kokubo & Ida 1996; Ida & Makino 1992b,a; Greenzweig & Lissauer 1992, 1990; Wetherill & Stewart 1989; Greenberg et al. 1978; Safronov & Zvjagina 1969). Planetesimals undergo perturbational encounters with each other (to within a few Hill radii) about once per orbit, whereas

⋆ E-mail: volker@physik.uzh.ch

[1] The literature on resonances is large and an extensive overview is given in Lecar et al. (2001).

perturbations from resonant configurations with giant planets require hundreds of orbital periods to cause noticeable effects. Planetesimal disk dynamics resemble those of stellar systems, in which small orbital perturbations grow exponentially fast (Hut & Heggie 2002; Valluri & Merritt 2000; Goodman et al. 1993; Kandrup & Smith 1991; Miller 1964). This is the essence of chaos in planetesimal disks.

Numerical simulations probe this regime by tracking the collisional evolution of planetesimals. Such simulations can address the formation and composition of the terrestrial planets (Chambers & Wetherill 1998; Chambers 2001; Raymond et al. 2004, 2005b; Kokubo et al. 2006; O'Brien et al. 2006; Raymond et al. 2006a, 2009; Morishima et al. 2010) and the extrasolar systems (Ogihara et al. 2014; Izidoro et al. 2014a; Raymond et al. 2006b, 2005a).[2]

The initial conditions of such simulations are generated by drawing realisations from some underlying solid mass distribution, possibly subject to stability constraints if planetary embryos are implanted directly (Chambers et al. 1996). As the system is inherently chaotic, we expect that different initial conditions drawn from the same underlying distribution will lead to different final systems (as is the case in simulations of stellar dynamics (Parker & Goodwin 2012; Allison et al. 2010)). To date, few contributors have evolved multiple realisations of the same distribution as limited computational resources are typically focussed on parameter studies.[3] Those that did report distinctly different outcomes for different realisations of the same underlying distribution (Izidoro et al. 2014b; Walsh et al. 2011; Kokubo et al. 2006; Raymond et al. 2009). Therefore, just how reliable are simulations of the collisional growth of terrestrial planets – do they have predictive power?

This question is at the heart of our paper and we tackle it in a threefold manner. First, we evolve identical realisations of a planetesimal disk multiple times. Due to differences in round-off errors, simulations will terminate with different planetary configurations. We assess the statistical spread of several diagnostics. Second, we evolve the planetesimal disk in the absence and presence of Jupiter and Saturn (in two configurations). We compare diagnostics across them, and check whether trends in the diagnostics are visible or buried in the statistical spread. Third, we empirically determine the rate at which planetesimal orbits of initially identical disks diverge.

The paper is organised as follows: In Section 2, we outline numerical methods, initial conditions and the analytic gas model used. In Section 3, we address the collisional evolution and statistical spread of diagnostics for different planetesimal disks. In Section 4, we apply some results from Section 3 to observations and suggest follow-up observations. In Section 5, we discuss the mechanism and timescales of orbital divergence in planetesimal disks. We conclude the paper in Section 6. Supplementary work on orbital divergence and numerical accuracy is contained in Appendices A and B.

2 N-BODY METHODS, INITIAL CONDITIONS

In this work, we use the GPU code GENGA (Sections 3 and 5) and a patched version of PKDGRAV (Section 5) to follow the collisional evolution of planetesimal disks. Although GENGA is both more accurate and faster, PKDGRAV allows us to experiment with particles numbers $N_p > 2048$. We now describe these two codes, the issue of program execution order, the initial conditions of the planetesimal disk, and the gas disk model.

2.1 GENGA

GENGA (Grimm & Stadel 2014) is a hybrid symplectic integrator similar to MERCURY (Chambers 1999), but running in parallel on Graphics Processing Units (GPUs). The integration scheme treats gravitational interactions between bodies as perturbations of their Keplerian orbits. GENGA uses democratic coordinates (heliocentric positions, barycentric velocities) (Duncan et al. 1998). This allows the code to separate close encounter pairs from the rest of the system, and integrate them separately with a direct N-Body integrator up to machine precision. Outside of close encounters, the bodies are integrated with a symplectic integrator. The hybrid symplectic integrator has excellent energy conservation over a large number of orbits. Accelerations between bodies are computed directly. This requires $\mathcal{O}(N^2)$ operations, which is more efficiently calculated on a GPU and is more accurate than a tree-based method. GENGA supports the same analytical gas disk as PKDGRAV. The code is available online.[4]

2.2 PKDGRAV

PKDGRAV (Stadel 2001) is a parallel N-Body code originally developed for cosmological dark matter simulations. The tree structure requires $\mathcal{O}(N \log N)$ force evaluates, which enables (collisionless) billion particles simulations. Morishima et al. (2010) extensively modified the code with a mixed variable symplectic integrator similar to the SyMBA method (Duncan et al. 1998). This integrations scheme splits the Hamiltonian into a Keplerian and an interaction part. While the Keplerian part can be computed analytically, interactions between bodies act as perturbations. The code supports an analytical gas disk model interacting with the particles. The implementation is described in Morishima et al. (2010).

2.3 Forcing the Order of Program Execution

To exactly reproduce numerical results, the order of execution of steps within the program must be fixed.[5] While this is easily controlled in single threaded applications, multi-threaded programs require additional logic. To ensure reproducibility of the experiments in this paper, we have implemented such logic in GENGA, and used PKDGRAV in single-thread mode only.

The most likely source of variations in the order of operations is the parallel sum operation. In GENGA, this is implemented as a parallel reduction formula within one thread block and always operates in the same order. As such, all summation operations are excluded as the source of round-off error variations. The only remaining possible source is in the creation of the close encounter list. If a close encounter pair is found, a counting variable is increased through an `_atomicAdd()` operation. The order of this operation is not well defined across threads. A different order of the close encounter pair list leads to a different order of bodies in the direct N-Body integrator. For multiple close encounter groups, this can lead to a different result. We prevent this behaviour through

[2] The literature on terrestrial planet formation can be overwhelming. Excellent reviews include Raymond et al. (2013) and Morbidelli et al. (2012).
[3] Instead of parameters sweeps, Richardson et al. (2000) tackled numerical issues and pushed the number of massive particles to 10^6.
[4] https://bitbucket.org/sigrimm/genga
[5] In computer arithmetic, $a+b+c \neq a+c+b$ because storage space for each number is finite, such that round-off errors will differ.

an additional sorting step, which reorders the close encounter list, but induces a performance penalty. The behaviour is controlled at compilation through the `SERIAL_GROUPING` flag.

All GENGA simulations in Section 5 run with this flag enabled. Simulations in Section 3 run with this flag disabled because we rely on variations in round-off errors to induce orbital divergence. Tests show that individual runs of Section 3 can be reproduced exactly if we enable `SERIAL_GROUPING`.

2.4 Initial Conditions, Gas Disk

Initial conditions (ICs) are generated the same way as in Morishima et al. (2010), where a number of samples (planetsimals of equal mass) are drawn from an underlying distribution of Keplerian elements. This generates a realisation with a particular surface density profile and total mass. We generate realisations by drawing 2000 samples such that the radial surface density profile is

$$\Sigma_{\rm Disk}(r) = \begin{cases} \Sigma_{\rm Disk,0} \left(\frac{r}{1\,\rm AU}\right)^{-p} & 0.5\ \rm AU < r < 4\ \rm AU, \\ 0 & \text{otherwise}, \end{cases} \quad (1)$$

for total disk mass of

$$M_{\rm Disk} = 2\pi \int_{0.5}^{4} \Sigma(r)\, r\, {\rm d}r. \quad (2)$$

In this paper, we adopt $p = 1$ and 1.5 as well as $M_{\rm Disk} = 5\,M_{\rm Earth}$ and $10\,M_{\rm Earth}$ (see Section 3.1 and Table 1). All planetesimals have mass $M \sim 0.04\,M_{\rm Lunar}$ ($\sim 0.08\,M_{\rm Lunar}$ for $10\,M_{\rm Earth}$ disks) and are on nearly circular ($e < 0.02$), low inclination ($i < 0.75^\circ$) orbits. The planetesimals are embedded in a gas disk described by an analytical model. The gas surface density follows a power law and decays exponentially in time, i.e.

$$\Sigma_{\rm Gas}(r,t) = \Sigma_{\rm Gas,0} \left(\frac{r}{1\,\rm AU}\right)^{-1} \exp\left(-\frac{t}{\tau}\right), \quad (3)$$

where τ is the decay time of the gas disk. For all simulations, $\tau = 1$ Myr, $\Sigma_{\rm Gas,0} = 2000\ {\rm g/cm^2}$. After ~ 4.6 Myr, only 1% of the gas remains.

Particles exchange angular momentum with the gas disk in three ways: (i) hydrodynamic drag due to differences in velocity, (ii) torques arising from spiral density waves launched by massive particles, and (iii) gravitational interactions between particles and the massive disk. Note that we artificially enhance hydrodynamic drag for particles with masses $< 0.01\,M_\oplus$ to correct for the large initial planetesimal mass. For more details, see Morishima et al. (2010). We stress that these interactions are modelled analytically. Our simulations would benefit from a full hydrodynamic model,[6] which may affect some of the results in this work.

3 COLLISIONAL EVOLUTION

We now discuss the collisional evolution and statistical variations of different simulation sets. After describing the simulations, we address differences in the disk mass evolution, the mass distribution, mass functions, orbital parameters and diagnostics used in Solar System formation.

3.1 Simulation Setup, Post-Processing

We generate planetesimal disks by drawing a single realisation for three different distributions: (i) a reference disk, (ii) a disk with a steeper surface density profile, and (iii) a more massive disk. For each realisation, we generate two sets of simulations with giant planets – one with Jupiter and Saturn on circular orbits (CJS) and one with Jupiter and Saturn on eccentric orbits (EJS). The EJS set corresponds to the present-day Solar System and the CJS set to the initial conditions of the original Nice model (Tsiganis et al. 2005). The Jovian planets are inserted at the start of the simulations. We also generate a set based on the reference disk without giant planets (NJS). Table 1 summarises our initial conditions.

Each set is evolved 12 times for a total of 84 runs covering 9 billion steps ($t \sim 147.84$ Myr, $\Delta t = 6$ days). Computing time per run is about a month on a NVIDIA GeForce GTX 590. We treat particle collisions as inelastic mergers. Particles are removed from the simulations if their heliocentric distance falls below 0.2 AU or exceeds 20 AU. The relative energy error remains $\Delta E/E_0 < 4.3 \times 10^{-4}$ at all times. All the outputs are available online.[7]

In post-processing, we load the outputs from all twelve runs per set, calculate various diagnostics for each run, and plot/tabulate their median, as well as 10/90 and 25/75 percentile spreads across the twelve runs. In the text, we quote only median values and 10/90 percentile ranges.

For simulations with giant planets we compute the location of the ν_5, ν_6, ν_{15}, and ν_{16} secular resonances to overlay during the analysis. The calculation is implemented as in the appendix of Nagasawa et al. (2000) with the following caveats: (i) the locations are exact only for massless test particles with on low eccentricity/inclination orbits, (ii) they are computed to first order and therefore only depend on the semi-major axis a (as well as the masses and semi-major axes of the giants), (iii) the gas disk is modelled as in Eqn. (3), ignoring modifications of the potential by spiral density waves (whose effect is modelled analytically). We thus expect the location of the resonances in the simulation to slightly differ from the values derived in post-processing. Also note that the ν_{15} resonance does not appear in the region of interest, and that – as the gas dissipates – the ν_{16} resonance appears in two locations. See also Figure 4 in Nagasawa et al. (2000).

3.2 Disk Evolution

Figure 1 shows a time sequence of the semi-major axis and eccentricity for two of the twelve simulations launched without Jupiter and Saturn. By 14.98 Myr, the simulations have clearly evolved different groups of planetary embryos as well as populations of remaining planetesimals. After 147.84 Myr, the simulations terminate with distinctly different terrestrial planets.

We now explore how the collisional evolution for a given set of simulations differs. Figure 2 shows the total mass bound in (i) the disk, (ii) planetary embryos and (iii) surviving planetesimals as well as the amount of mass removed from the system by colliding with the host star or by ejection. As in Morishima et al. (2010), a planetary embryo is an object with mass $M > M_{\rm Cut} = 3.3 \times 10^{26}$ g,

[6] In particular, spiral density waves launched from multiple massive bodies will locally modify the hydrodynamic drag, mutually interact, and affect the gravitational potential of the disk. Neither of these effects are captured in an analytic model.

[7] https://cheleb.net/astro/chaos15

Table 1. Orbital elements of Jupiter and Saturn as well as initial planetesimal disk conditions for our simulation sets. For the giant planets, the three angular arguments are initialised to zero. The CJS set corresponds to the initial conditions of the Nice model (Tsiganis et al. 2005). The EJS set corresponds to the present-day Solar System. In all cases, we start with 2000 planetesimals.

Set	a_J (AU) [a]	e_J [b]	i_J (Deg) [c]	a_S (AU) [a]	e_S [b]	i_S (Deg) [c]	Σ_{Disk} [d]	$\Sigma_{Disk,0}$ (g/cm^2) [e]	M_{Disk} (M_{Earth}) [f]	N_{Runs} [g]
NJS	–	–	–	–	–	–	$\propto r^{-1}$	6.1	5	12
EJS	5.2	0.048	1.30	9.55	0.056	2.49				
CJS	5.45	0.0	0.0	8.18	0.0	0.5				
EJS/Steep	5.2	0.048	1.30	9.55	0.056	2.49	$\propto r^{-1.5}$	8.2	5	
EJS/Heavy							$\propto r^{-1}$	12.4	10	
CJS/Steep	5.45	0.0	0.0	8.18	0.0	0.5	$\propto r^{-1.5}$	8.2	5	
CJS/Heavy							$\propto r^{-1}$	12.4	10	

[a] Semi-Major Axis. [b] Eccentricity. [c] Inclination. [d] Surface Density Profile. [e] Surface Density at 1AU. [f] Disk Mass. [g] Number of Independent Runs.

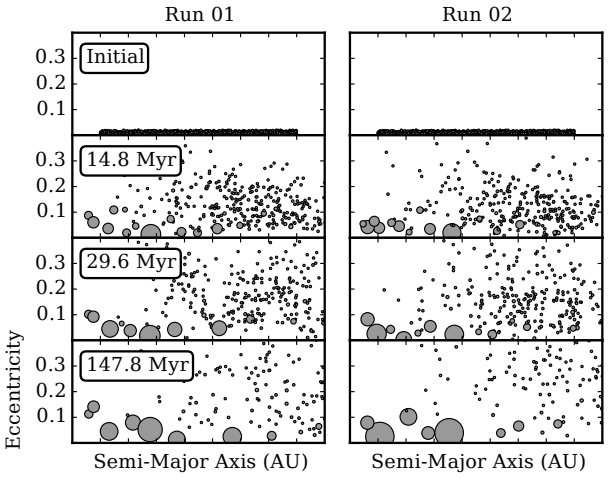

Figure 1. Semi-major axis and eccentricity for two identical initial conditions (columns) at four time slices (rows). Each marker represents a single body. Larger markers indicate more massive bodies.

which is about the mass of Mercury. Although embryos grow into planets, we do not label them separately. Objects with $M < M_{Cut}$ are classified as planetesimals. Tables 2 and 3 tabulate the ranges indicated in Figure 2.

3.2.1 *Reference Disk*

Initially, all simulation sets evolve identically. After 10^5 years, the first planetary embryos become visible. It takes about four equal mass collisions to reach the cutoff mass, so the observed early-time collision rate of ≈ 0.03 collisions per year per 2000 particles agrees with this build-up. After 1 Myr, all simulations have assembled between 1.5 and 2.0 $M_\oplus$ into embryos. By this time all disks lose 0.56 to 0.93 $M_\oplus$ between the 1 and 3 Myr. The mass-loss is driven by hydrodynamic drag and type I migration, which by now have delivered particles to the inner edge of the disk, where we remove them from the simulation. In fact, the first particles already fall in around 2×10^5 years, but they do not carry significant mass. After 3 Myr, the gas disk is depleted by a factor of 20 and becomes dynamically irrelevant. At this stage, all simulations host between 5 and 18 oligarchic embryos at semi-major axes $a \lesssim 2$ AU.

Table 2. Total disk mass and total mass locked up in embryos. We show median mass, offsets from median to 25/75 percentile, and offsets from 25/75 to 10/90 percentile as sub-/superscripts.

Set	Time	M_{Disk} [a,c]	$M_{Embryos}$ [b,c]
NJS	1 Myr	$4.87^{+0.04(+0.04)}_{-0.05(-0.09)}$	$1.73^{+0.07(+0.04)}_{-0.09(-0.15)}$
	End	$4.22^{+0.09(+0.04)}_{-0.15(-0.16)}$	$3.30^{+0.08(+0.05)}_{-0.13(-0.14)}$
EJS	1 Myr	$4.91^{+0.07(+0.01)}_{-0.12(-0.05)}$	$1.95^{+0.06(+0.03)}_{-0.12(-0.09)}$
	End	$3.38^{+0.15(+0.06)}_{-0.27(-0.04)}$	$3.38^{+0.13(+0.07)}_{-0.27(-0.04)}$
CJS	1 Myr	$4.92^{+0.06(+0.01)}_{-0.06(-0.02)}$	$1.83^{+0.05(+0.08)}_{-0.07(-0.04)}$
	End	$3.09^{+0.06(+0.26)}_{-0.15(-0.26)}$	$2.99^{+0.08(+0.24)}_{-0.10(-0.28)}$
EJS/Steep	1 Myr	$4.26^{+0.08(+0.04)}_{-0.09(-0.04)}$	$1.84^{+0.09(+0.07)}_{-0.08(-0.04)}$
	End	$3.12^{+0.12(+0.10)}_{-0.21(-0.05)}$	$3.11^{+0.12(+0.10)}_{-0.20(-0.05)}$
EJS/Heavy	1 Myr	$8.51^{+0.18(+0.18)}_{-0.19(-0.03)}$	$3.24^{+0.26(+0.14)}_{-0.07(-0.30)}$
	End	$4.15^{+0.35(+0.14)}_{-0.27(-0.33)}$	$4.15^{+0.34(+0.15)}_{-0.28(-0.34)}$
CJS/Steep	1 Myr	$4.28^{+0.10(+0.06)}_{-0.09(-0.07)}$	$1.70^{+0.13(+0.09)}_{-0.04(-0.07)}$
	End	$2.83^{+0.13(+0.10)}_{-0.08(-0.11)}$	$2.78^{+0.11(+0.11)}_{-0.14(-0.09)}$
CJS/Heavy	1 Myr	$8.95^{+0.09(+0.04)}_{-0.15(-0.07)}$	$2.34^{+0.23(+0.16)}_{-0.09(-0.02)}$
	End	$4.57^{+0.15(+0.23)}_{-0.24(-0.35)}$	$4.54^{+0.16(+0.20)}_{-0.26(-0.38)}$

[a] Total mass in disk. [b] Total mass in embryos. [c] In Earth Masses.

During the first 3 Myr, the differences between sets are small, largely because gas drag acts as an equaliser that dampens eccentricity excitements from resonant interaction between planetesimals and Jupiter. At later times, we observe three marked differences. First, simulations with giant planets are much more efficient at assembling embryos. At ~ 50 Myr, EJS simulations have converted all low-mass particles. CJS simulations are slower, and retain $\sim 0.08\ M_\oplus$ in the low-mass regime when the simulations terminate. The process is slower in simulations without giant planets, which retain $\sim 1\ M_\oplus$ in low-mass objects at termination. Second, simulations with giant planets continue to lose mass after 3 Myr, eventually bringing the remaining disk mass down to $\sim 3.38\ M_\oplus$ (EJS) and $\sim 3.09\ M_\oplus$ (CJS). Third, there is a significant difference in how EJS and CJS simulations lose disk mass. For EJS, all lost mass is lost onto the host star, while CJS simulations eject about

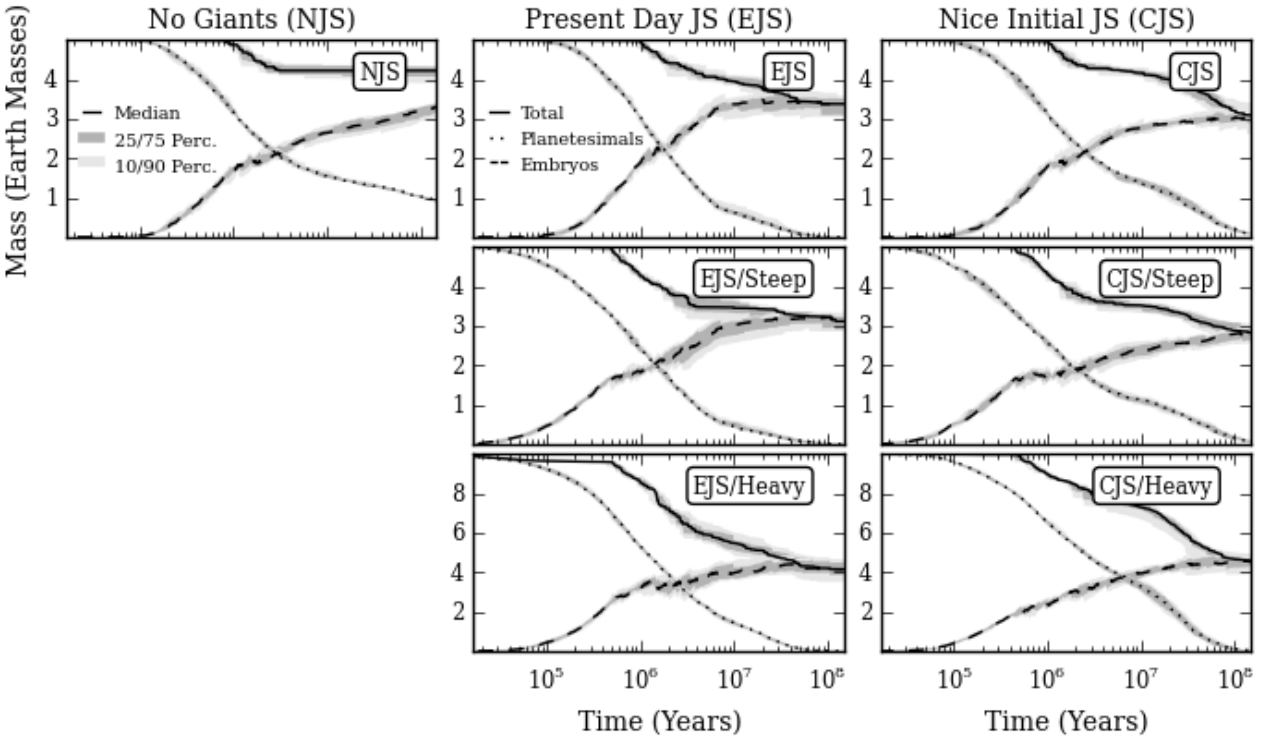

Figure 2. Remaining solid mass as a function of time for twelve initially identical simulation runs. Dotted and dashed lines indicate the aggregate mass (per run) in planetesimals and planetary embryos. The solid lines indicate the total remaining particle mass. Lines, light, and dark grey shading indicate median, 25/75, and 10/90 percentiles across runs. *Columns (Left to Right)*: Runs without Jupiter and Saturn, Jupiter and Saturn on their present-day eccentric orbits, Jupiter and Saturn on circular orbits. *Rows (Top to Bottom)*: Reference initial planetesimal disk, steep disk, more massive initial disk.

half the lost mass from the system. However, these processes are limited to late times.

The spread of tracked mass ranges is never uncomfortably large, such that the 10 and 90 percentiles are never more than 15 per cent off the median. The exception to this is the total planetesimal mass, which suffers from small number statistics as planetesimals deplete at times $\gtrsim 100$ Myr. Overall, the tight spread suggests that the range of evolutionary paths available to individual runs in a set is limited. However, we do observe three key trends in statistical spread with simulation sets. First, the spread is consistently smallest in masses below the cutoff mass. Second, the spread across runs in total disk mass is larger in simulations that include giant planets. Third, the probability of larger excursions is higher in the EJS and CJS simulations. For EJS sets, the $10/90$ percentiles tend to be a factor 2 further off the median than the $25/75$ percentiles. In CJS sets, the difference grows and exceeds factors of 3 for the 90 percentile in mass above the cutoff.

3.2.2 *Steep and Heavy Disks*

At small semi-major axis, relative velocities between planetesimals are higher, leading to shorter timescales of collision and thus growth. Runs with steeper initial surface density profiles therefore start assembling embryos already after $\sim 2 \times 10^4$ years. As a consequence, more embryos are driven close to the star by type I migration, where they are removed from the simulation. This effectively stalls the conversion of planetesimals into embryos between 5×10^5 and 10^6 years. Although the conversion process picks up again, initially steep disks still tend to host ~ 8 per cent less total mass in terrestrial planets than the reference disks. Apart from the short stall, the fraction of mass in embryos grows continuously until ~ 10 Myr, whereafter it slows down significantly. This is irrespective of the orbit of the giant planets, although conversion of mass into embryos proceeds slightly faster if giant planets are on eccentric orbits.

In massive disks, conversion of planetesimals into embryos begins earlier than in the reference run (but later than in runs with steep initial surface density profiles). This is likely a numerical artefact related to the doubling of the initial planetesimal mass.[8] More robustly, we find that the fraction of mass in embryos either (i) stops increasing significantly after ~ 1 Myr (eccentric giant planets) or (ii) proceeds slower overall (circular giant planets) for initially massive disks. However, in absolute terms, it does settle at a higher level ($6\,M_{\rm Earth}$ vs $\sim 3\,M_{\rm Earth}$ for less massive disks).

Despite the slower rate of embryo assembly and smaller total mass fraction of embryos, both steep and massive disks loose total mass earlier and more efficiently than the reference profiles. For the reference disks, mass loss only sets in after ~ 1 Myr; almost 0.5 Myr later than when steep and massive disks begin loosing material. Most extremely, systems hosting massive disks with eccentric giant planets begin loosing mass almost immediately at the 2×10^4 yr mark. These systems must be dynamically more ac-

[8] In massive disks, only three instead of four equal mass collisions are required to reach the cutoff mass for classification as embryo. To avoid such numerical effects, future simulations that vary the total disk mass should keep a constant mass resolution.

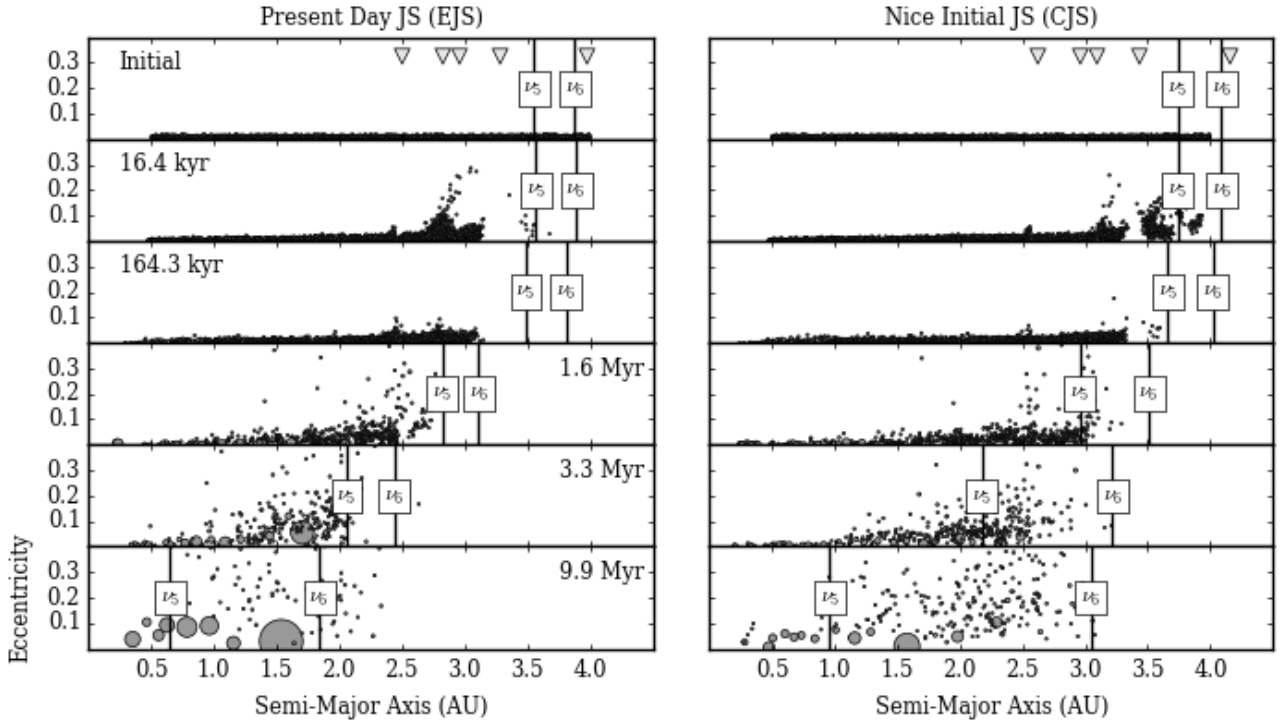

Figure 3. Semi-major axis and eccentricity for a single run with EJS (left) and CJS (right) conditions at six time slices (rows). Markers represent single bodies with size is proportional to the mass. Triangles indicate the location of (from left to right) 3:1, 5:2, 7:3, 2:1, and 3:2 mean motion resonances with Jupiter. Vertical bars indicate the location of the secular resonances ν_5 and ν_6, which sweep inwards as the gas disk dissipates. We do not show the ν_{16} resonance which settles ~ 0.1 AU beyond the ν_6 resonance at ~ 9.9 Myr. Animations are available at https://cheleb.net/astro/chaos15/media/.

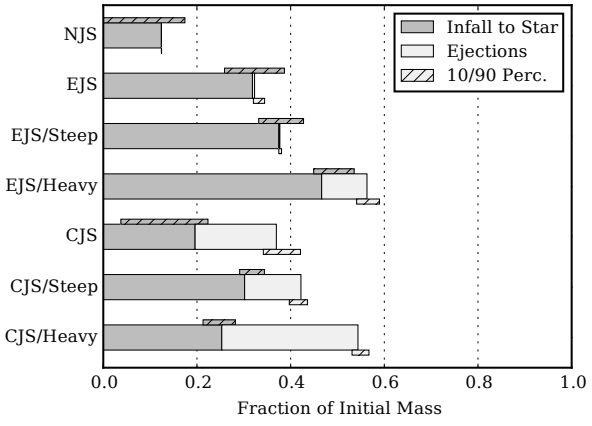

Figure 4. Fraction of initial solid disk mass that falls onto the star (heliocentric distance $r < 0.2$ AU or is ejected from the system ($r > 20.0$ AU). We show the median over twelve runs for each set of simulations as the main bars. The small bars below and above indicate the 10/90 percentile spread of ejected and mass deposited onto the star, respectively.

tive than the reference profiles, such that more orbits can deliver mass onto the star, out of the system, or onto the giants.

In fact, no single planetesimal or embryo collides with Saturn, and we record only three to four planetesimals (corresponding to 0.01 to 0.05 $M_{\rm Earth}$) impacting on Jupiter per run, but only in runs with massive planetesimal disks. There are occasional collisions with Jupiter in other runs, but these are isolated events and do not occur in all runs of a given configuration. Most of the mass loss is thus onto the star or through ejection from the system and the mechanics vary depending on the configuration, see Figure 4. In systems without giant planets and with giant planets on eccentric orbits, almost all mass is lost onto the star, although massive disks in EJS configurations eject ~ 10 per cent of the lost mass. For configurations of giants on circular orbits, between 20 and 50 per cent of the lost solid mass is ejected. For both giant planet configurations, initially massive disks appear to eject the largest fraction of their initial mass.

As for the reference runs, the spread of the masses remains well-bound. Except for outliers from small number statistics in the planetesimal mass at late times, the 10 and 90 percentiles of the masses remain within 15 per cent off the median. For eccentric giant planets, steep initial disks have a smaller and massive initial disks a larger spread than the reference case. For giants on circular orbits, steep profiles have comparable spreads to the initial profile. Massive planetesimals disks in CJS configurations show no definite trends either. For example, the 90 percentile mass in embryos in massive disks has a smaller offset from the median than the reference profile (7.2 vs. 9.2 per cent) while the 75 percent has a larger offset (5.17 vs. 2.70 per cent).

3.2.3 *Sweeping Secular Resonances, Mean Motion Resonances, and Dynamical Friction as Disk Sculptors*

The defining difference between simulations is the presence and orbital configuration of giant planets. Through mean motion and secular resonances, they can transfer significant angular momentum onto the planetesimals efficiently. This exchange also proceeds without resonances, but is less effective. Unless dampened, thusly

Table 3. Percentile offsets from median: (i) total mass, (ii) total mass in embryos and (iii) total mass in planetesimals. The offsets are averaged (50 percentile) in time.

Set	Percentile	$M_{\rm Disk}$ [a,d]	$M_{\rm Embryos}$ [b,d]	$M_{\rm Planetesimals}$ [c,d,e]
NJS	90	+0.13	+0.12	+0.08
	75	+0.10	+0.10	+0.03
	25	−0.15	−0.15	−0.04
	10	−0.31	−0.27	−0.06
EJS	90	+0.27	+0.24	+0.18
	75	+0.15	+0.13	+0.06
	25	−0.12	−0.22	−0.05
	10	−0.32	−0.32	−0.08
CJS	90	+0.22	+0.27	+0.15
	75	+0.10	+0.08	+0.11
	25	−0.13	−0.08	−0.07
	10	−0.27	−0.22	−0.15
EJS/Steep	90	+0.12	+0.13	+0.13
	75	+0.09	+0.09	+0.07
	25	−0.19	−0.19	−0.03
	10	−0.30	−0.32	−0.04
EJS/Heavy	90	+0.51	+0.50	+0.11
	75	+0.35	+0.34	+0.05
	25	−0.26	−0.26	−0.07
	10	−0.60	−0.63	−0.14
CJS/Steep	90	+0.20	+0.16	+0.10
	75	+0.14	+0.08	+0.04
	25	−0.10	−0.15	−0.06
	10	−0.20	−0.24	−0.12
CJS/Heavy	90	+0.34	+0.33	+0.37
	75	+0.13	+0.23	+0.23
	25	−0.27	−0.25	−0.23
	10	−0.61	−0.53	−0.35

[a] Total mass in disk. [b] Total mass in embryos. [c] Total mass in planetesimals. [d] In Earth Masses. [b] Only considers times < 32.9 Myr.

excited planetesimals can either be launched into the inner solar system or ejected from the system. They can also be trapped in or repelled by resonances. Locking planetesimals in resonances perpetually excites their eccentricities unless dampened. Those repelled by resonances are effectively blocked off from accessing regions of phase space.

Due to their mutual gravitational interaction, the Jupiter-Saturn systems has four eigenfrequencies labelled f_1, f_2, g_1, and g_2. Linear combinations of these drive secular variations in eccentricity and inclination (Murray & Dermott 1999). They depend on the planetary masses, orbital configuration, and gravitational potential of the gas disk in which they are embedded (Brouwer & Clemence 1961; Heppenheimer 1980; Ward 1981; Nagasawa et al. 2000). Given interactions with Jupiter and Saturn as well as the gravitational potential of the gas disk, planetesimals are subjected to perturbations with frequencies f and g. At particular locations in the disk, these frequencies match, driving resonances labelled ν_5 ($g = g_1$), ν_6 ($g = g_2$), ν_{15} ($f = f_1$), and ν_{16} ($f = f_2$). They pump eccentricities (ν_5, ν_6) or inclinations (ν_{15}, ν_{16}).

Figure 3 shows the location of the secular resonances at different timeslices. As time moves on, the gas dissipates and the secular resonances sweep inwards, pushing planetesimals in front of them. For the EJS configuration, ν_5 and ν_6 remain closer together for longer than for the CJS case. In the EJS case, ν_5 also settles at smaller semi-major axes a once the gas disappears. The net effect is that more material is delivered to smaller a (where growth timescale are faster) in EJS configurations. This leads to faster assembly and growth of planetary embryos.

Mean motion resonances occur at semi-major axes where the orbital phases of planetesimals and Jupiter line up periodically. We indicate five of the lowest order mean motion resonances by triangles in Figure 3. As the simulations evolve, their location remains approximately fixed. At early times, they are efficient at exciting planetesimals, although eccentricities are rapidly dampened by hydrodynamic drag. As time evolves, planetesimals are cleared from their sphere of influence. Since there appears to be no difference in the early-time collision rate across simulations, we conclude that mean motion resonances do not drive the dynamics of collisional growth. They do, however, help to drive ejection of material on timescales of 10 to 100 Myr. In CJS configurations, planetesimals still populate the regions covered by the 3 : 1, 5 : 2, and 7 : 3 mean motion resonances ($2.5 \lesssim a \lesssim 3.2$ AU). Over time, angular momentum exchange with Jupiter excites surviving planetesimals in this region onto hyperbolic orbits. This ejects them from the system.

Irrespective of the orbits of the giant planets, the dynamical evolution of planetesimals in initially massive disks is more complicated. Although the initial excitement from resonances is similar to configurations with the reference and steep profiles, dampening by hydrodynamic drag is much less effective due to the larger planetesimal mass; see Figure 1 in Morishima et al. (2010). This has three consequences. Firstly, sweeping secular resonances move fewer planetesimals inward. Secondly, the richly excited planetesimals actually remove angular momentum from Jupiter through dynamical friction (e.g., Kokubo & Ida (2012)), although this also happens to a lesser degree for disks following the reference and steep profiles. For example, the mean eccentricity of Jupiter during the first 312 kyr is $e_{\rm J,Ref} = 0.0678$ and $e_{\rm J,Heavy} = 0.0738$ for RUN01 in the EJS and EJS/HEAVY sets. After 10 Myr, the 312 kyr averaged eccentries are $e_{\rm J,Ref} = 0.0474$ and $e_{\rm J,Heavy} = 0.0385$, corresponding to a decrease of 43 and 91 per cent, respectively. Thirdly, a small population of planetesimals actually manages to move outwards past the orbits of Jupiter and Saturn. Although most are promptly ejected (on timescales of $\sim 10^5$ years), a single planetesimal (across twelve runs) is caught by Jupiter as a moon![9]

The dynamical outcome of a planetesimal passing through a resonance depends sensitively on the initial orbit. For two initially almost identical orbits, the more resonances the particles pass through, the farther their orbits can diverge. Therefore, simulations where particles are exposed to a larger number of resonances have more evolutionary pathways available. The wider spread of of EJS/CJS runs with respect to NJS is then hardly surprising. By the same argument, we naively expect EJS runs to have a larger spread than CJS runs because more particles cross the sweeping ν_6 resonance. While this holds at the 25/75 percentile level, it does not always hold at the 10/90 percentile level. Closer inspection of Figure 3 reveals that in CJS runs, the 3:1 and 5:2 mean motion resonances with Jupiter remains within the planetesimal disk, and the final location of the ν_6 and ν_{16} (not shown) resonances are within 0.07 AU of the 7:3 resonance. Over Myr timescales, such close stacking provides pathways for particle orbits to diverge and promotes ejection of bodies from the disk. As the effects of secular resonances and mean motion resonance cannot be readily distinguished, we cau-

[9] For videos and time-sliced figures of the planetesimals dynamics of all simulations, we refer the reader to the supplementary website.

tion from attributing to them any differences across CJS and EJS runs.

3.3 Disk Mass Distribution, Mass Functions

In terms of aggregate mass bound up in planetesimals, embryos, and the solid disk as a whole, runs within sets of initially identical conditions have variance below the 15 per cent level. But what about the mass distributions and functions at the end of the simulations? Do the systems look architecturally similar? Is the mass distributed similarly? What drives any trends we might find?

Figure 5 illustrates the diverse architectures of systems we have generated after 147.84 Myr. Considering the twelve runs within sets, find we the arrangement of final planets to vary substantially. Nevertheless, the impact of adding or adjusting the configuration of the giant planets has an even stronger impact that can easily be discerned visually over the different architectures generated by the same configuration. On the other hand, runs with different initial surface density profiles appear difficult to visually discern from the stochastic variations in architecture. For massive disks, this is easier because they tend to host massive terrestrial planets.

To be more quantitative, we analyse the mass distributions (mass per semi-major axis) and functions (particle counts per mass bin) for various giant planets configurations and initial planetesimal distributions. In both cases, we use non-parametric kernel density estimates (KDE) to derive the distribution functions for all runs in a set. We then combine these statistically; see Figures 6 and 7.

3.3.1 *Reference Disk*

Simulations without giant planets distribute mass most evenly with semi-major axis, while CJS and EJS simulations concentrate progressively more mass at smaller semi-major axes. The EJS systems tend to be truncated around 2 AU. In CJS systems, terrestrial planets populate a region out to 3.5 AU, but most mass is concentrated within 2.2 AU. In simulations with giant planets, there appear to be regions that are preferably populated by terrestrial planets. Most notably, these are at 0.8, 1.2 (EJS) as well as at 0.9, 1.5, and 2.2AU (CJS), although the last peak is arguably weak. However, we observe significant variations in the distribution of mass and planets with semi-major axis within sets. These are smallest in systems without giant planets and largest in systems with giants on circular orbits. For example, the 90 percentile masses are (by median) 25, 50, and 69 per cent off the median mass (in order, NJS, EJS, CJS).

The lack of giant planets severely stunts growth of terrestrial planets, and these systems retain larger numbers of planetesimals at their origin mass. In contrast, EJS configurations are the most efficient at assembling terrestrial planets with masses on the order of an Earth mass, while CJS runs populate a middle ground. Irrespective of presence and configuration of giant planets, there is significant variance in the mass function. For NJS runs, the scatter is most significant at intermediate mass ranges 0.03 to 0.3 $M_{\rm Earth}$, with the 25/75 percentiles off by a factor of about two from the median. The same holds for CJS configurations. For EJS configurations, the mass functions are more difficult to interpret because almost no planetesimals remain. Focussing on planetary masses (0.5 to 1.5 AU), we find a larger spread across EJS runs than for CJS runs (10 to 20 per cent vs. factors of two).

3.3.2 *Steep and Heavy Disks*

Initialising the planetesimals to follow a steeper surface density profile has a surprisingly small effect. For the CJS case, we find no obvious discernible trends, although we do note two changes for EJS configurations. Firstly, more mass is concentrated at smaller semi-major axis, which is a consequence of more mass being initially distributed here. This is only significant in EJS configurations because the semi-major axis range populated by terrestrial planets is tighter here. Secondly, the mass range covered by planets widens a bit and we find that more EJS runs retain some planetesimals in initially steep disks. This still holds for less than half of the runs, which is still more than in the reference profile.

Increasing the initial disk mass has a more drastic effect on the distributions. Across the entire semi-major axis range populated by the terrestrial planets, both CJS and EJS configurations record a higher median mass as well as a larger scatter. Massive initial disks also generate a wider range of planet masses (both at the lower and upper mass end), which essentially flattens out the mass functions, although the dip around 0.1 $M_{\rm Earth}$ in CJS configurations remains and exhibits a large scatter. For EJS runs, we find more (but still not all) simulations to retain planetesimals, which puts power into the lower end of the mass function. Nevertheless, large spreads remain here as the number of surviving planetesimals per run is still in the single digits.

3.3.3 *Shaping System Architectures with Sweeping Resonances*

Our most obvious observation thus far is that configurations with giant planets produce more compact systems of terrestrial planets and most of the mass delivered to $a < 2$ (EJS) and $a < 3$ AU (CJS). As outlined in Section 3.2.3, this is the result of secular resonances sweeping material inwards as the gas dissipates. In systems without giant planets, no secular resonances exist, and planetesimal material remains constrained to the region they are initially placed in. Once the gas dissipates (~ 10 Myr), the location of the secular resonances becomes fixed. At this point, the inner (ν_5) secular resonance has swept large amounts of material to ~ 0.9 AU, significantly enhancing the local density of material available for embryos to accrete from. This biases formation and growth of terrestrial planets to its vicinity.

During dissipation of the gas, planetesimals that have avoided being swept up by the ν_5 resonance soon face the ν_6 resonance on its inward sweep. Most of the remaining planetesimals are now also forced inwards, although a few manage to avoid this fate. Although it does not drag planetesimals along, the ν_{15} resonance also sweeps outward and settles near ν_6. Once the gas is gone, their location demarcates the outer boundary of the region populated by terrestrial planets. Those trapped in their vicinity find themselves excited onto eccentric orbits that either deliver them to the inner system to collide with embryos, fall onto the star, or be ejected from the system. After 148.47 Myr, most of the planetesimals beyond the ν_6 and ν_{15} resonances have been removed, although stragglers remain. By being separated from the inner regions, they have avoided being accreted onto larger embryos, thus covering a wide range of masses.

The net effect of inward sweeping ν_5 and ν_6 resonances is to deliver planetesimals from the disk and trap them in the orbital region between. The region between these resonances is wider in EJS configurations that in CJS ones. Naturally, this leads to a higher mass concentration in EJS runs as well as a more complete conversion of planetesimals into planets, i.e. only a very weak bimodal

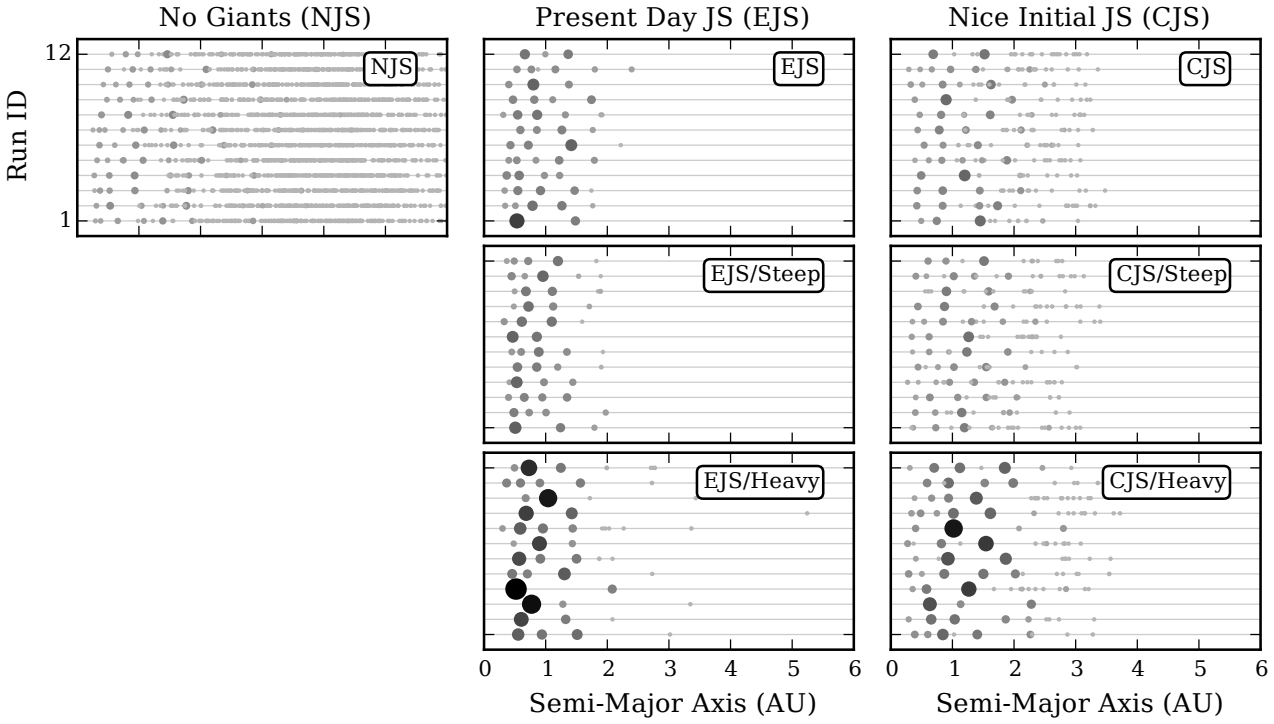

Figure 5. Distribution of planets/planetesimals with semi-major axis for all 7×12 initially identical runs after 147.84 Myr. Each line indicates a separate run. Darker colours and bigger circles indicte more massive particles. *Columns (Left to Right)*: Runs without Jupiter and Saturn, Jupiter and Saturn on their present-day eccentric orbits, Jupiter and Saturn on circular orbits. *Rows (Top to Bottom)*: Reference initial planetesimal disk, steep disk, more massive initial disk.

signature in the mass function. Configurations with giant planets on circular orbits trap less mass per AU in the inner regions, which retards conversion of planetesimals into planets. As such, they retain a bimodal mass function even after 147.84 Myr. Statistically, we may also expect runs with EJS configurations to produce more massive planets at smaller semi-major axes than runs with CJS configurations. We demonstrate this in Section 3.4.

In disks with initially steep density profiles, sweeping resonance are even more efficient in shepherding material inwards because they start out with fewer planetesimals at larger semi-major axis. Their final mass distributions and system architectures appear almost indistinguishable from the reference disks. For massive initial disks, we might expect the situation to be different. As discussed, planetesimals excited by sweeping resonances have both longer damping timescales (gas drag affects them less) and experience stronger dynamical friction with Jupiter. Although fewer planetesimals are shepherded to the inner regions than for other disk profiles, this is compensated by the larger initial mass of planetesimals. After 147.84 Myr, the architecture, mass distributions, and mass functions are therefore similar to other configurations. The only striking remaining difference is that a larger amount of mass remains simply by virtue of starting out with more mass.

On timescales of a few 100 Myr, stability for two orbiting planets against close encounters requires their orbital separation Δa to exceed $\Delta a > 10\,R_{\rm H}$, where $R_{\rm H} = ((m_1+m_2)/M_\odot)^{1/3}\,(a_1+a_2)/2$ is the mutual Hill radius of two neighbouring planets (Gladman 1993; Chambers et al. 1996). For more planets, the threshold increases to $\Delta a \gtrsim 20$ for systems with 10 to 20 planets. By this criterion, we find over 90 per cent of all planets to be on stable orbits. The remaining ten percent (corresponding to about one planet per run) have separations as small as two $R_{\rm H}$, and we expect these to meet a violent fate not far in the future. In runs without giant planets, 35 per cent of planets are spaced $< 20\,R_{\rm H}$ and 10 per cent $< 10\,R_{\rm H}$. In these system, we expect further dynamical evolution.

Finally, it remains to characterise what sets the spacing of terrestrial planets. In particular, the double peaked structures of the mass distribution for some of our simulations (EJS, CJS, and EJS/Steep) suggests preferred orbital spacings, which may be indicative of chains of mean motion resonances. However, out of a total of 35′554 planet pairs, we find that only 13 (0.036 per cent) are no further than 0.001 AU away from a the semi-major axis ratio required for any of the mean motion resonances considered (3:1, 5:2, 7:3, 2:1, and 3:2). Even if we are willing to relax the distance to the resonance to 0.01 AU, only 117 (0.33 per cent) of planet pairs are in resonance. We conclude that resonances between the formed terrestrial planet are rare and do not drive the double peaked mass distribution seen in some configurations.

3.3.4 *Comment on Small Number Statistics*

In closing, we wish to comment on the robustness of using kernel density estimates (KDEs) to characterise the mass distributions and mass functions.

Fitting a KDE amounts to attempting to estimate the underlying distribution of planetesimals that is sampled by the simulation particles. For each sample (particle), the algorithm drops a Gaussian kernel of a width depending on the spacing of samples. The KDE is then sum of kernels. For NJS runs, this works well because the distribution per run is fit to between 150 and 200 samples. For CJS and EJS configurations, the number of available samples drops

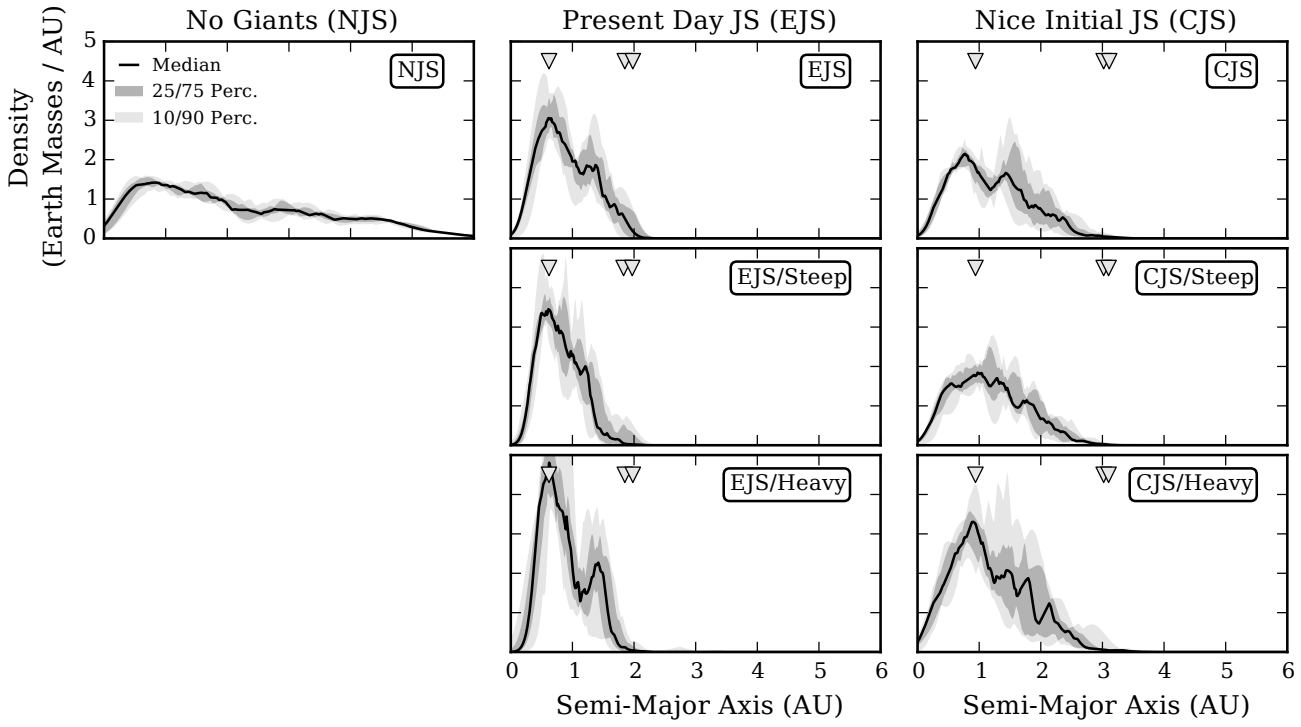

Figure 6. Median and statistical spreads of the mass-distribution each set of 7×12 runs shown in Figure 5. Mass distributions are kernel density estimates of the mass-weighted particle distribution $\mathrm{d}M/\mathrm{d}a$ along the semi-major axis a. Black lines indicate the median. The shadings indicate 25/75 and 10/90 percentile ranges. Tiangles indicate (from left to right) the locations of the ν_5, ν_6, and ν_{16} secular resonances for runs with giant planets. *Columns (Left to Right)*: Runs without Jupiter and Saturn, Jupiter and Saturn on their present-day eccentric orbits, Jupiter and Saturn on circular orbits. *Rows (Top to Bottom)*: Reference initial planetesimal disk, steep disk, massive initial disk.

Table 4. Median terrestrial planet mass M, semi-major axis a, eccentricity e, inclination i across all 12 simulations of a set. N is the median number of planets per simulation in a set. Sub-/superscripts are 10/90 percentiles.

Set	M ($M_\oplus$)	a (AU)	e	i (Degree)	N
NJS	$0.28\,^{0.61}_{0.04}$	$2.40\,^{4.55}_{0.49}$	$0.06\,^{0.16}_{0.02}$	$2.89\,^{6.92}_{1.01}$	$12\,^{12}_{10}$
EJS	$0.78\,^{1.27}_{0.40}$	$0.86\,^{1.77}_{0.40}$	$0.08\,^{0.24}_{0.03}$	$5.18\,^{13.93}_{2.42}$	$4\,^{5}_{3}$
EJS/Steep	$0.80\,^{1.33}_{0.32}$	$0.79\,^{1.66}_{0.45}$	$0.06\,^{0.14}_{0.03}$	$3.31\,^{9.00}_{1.74}$	$4\,^{4}_{3}$
EJS/Heavy	$1.14\,^{2.45}_{0.08}$	$0.93\,^{2.02}_{0.49}$	$0.08\,^{0.20}_{0.04}$	$4.06\,^{16.48}_{1.68}$	$3\,^{5}_{2}$
CJS	$0.52\,^{1.02}_{0.12}$	$1.20\,^{2.29}_{0.44}$	$0.08\,^{0.24}_{0.03}$	$4.23\,^{11.03}_{1.76}$	$5\,^{6}_{4}$
CJS/Steep	$0.49\,^{1.01}_{0.10}$	$1.17\,^{2.33}_{0.41}$	$0.08\,^{0.20}_{0.03}$	$3.14\,^{9.37}_{1.48}$	$5\,^{6}_{4}$
CJS/Heavy	$0.75\,^{1.74}_{0.20}$	$1.03\,^{2.48}_{0.38}$	$0.05\,^{0.15}_{0.01}$	$2.84\,^{9.51}_{0.95}$	$5\,^{6}_{3}$
SS	$0.46\,^{0.94}_{0.07}$	$0.86\,^{1.37}_{0.49}$	$0.06\,^{0.17}_{0.01}$	$1.93\,^{5.10}_{1.61}$	$4\,^{4}_{4}$

to between 10 and 20 (CJS), respectively 5 to 10 (EJS). The algorithm compensates by dropping much wider Gaussian kernels. Stacking runs and computing percentiles over these kernels leads to wide regions with jagged edges that are especially apparent in the mass functions of EJS and EJS/Steep runs. We thus caution from attributing too much meaning to these regions because they are very sparsely sampled.

3.4 Orbital Parameters, Total Solution Space

Numerically speaking, all particle distributions that are evolved from the same initial conditions are equally valid configurations (solutions) of the planetary system. We may thus argue that (at present) we have no means of determining the *actual* solution of the system. This leaves us with two choices of analysis. We could (i) try to determine the most likely actual solution, or (ii) explore the range of permitted solutions to characterise the solution space. If we do the former, we may be tempted to declare the median of all solutions as the true solution. This is by no means well-justified, and would require a large number of simulation runs to escape the confines of small number statistics. Given this complication, we instead settle for an exploration of the solution space.

We construct the total solution space by stacking data from all runs in a given simulation set. We restrict our analysis to particles $M > M_{\mathrm{Cut}}$, but make no distinction between planets or planetary embryos. Figure 8 shows the raw data as well as median and 10/90 percentile ranges of the semi-major axis a, mass M, orbital eccentricity e, and orbital inclination i. Results are also tabulated in Table 4 where we list the number of planets per system.

3.4.1 *Reference Disk*

We find that the presence and configuration of giant planets has the largest effect on the final configuration of terrestrial planets. In the absence of giant planets, we find 10 to 12 terrestrial planets per system. Of these, 90 per cent have mass $M < 0.6\,M_\oplus$, and half have $M < 0.3\,M_\oplus$. By number, they are spread evenly across a

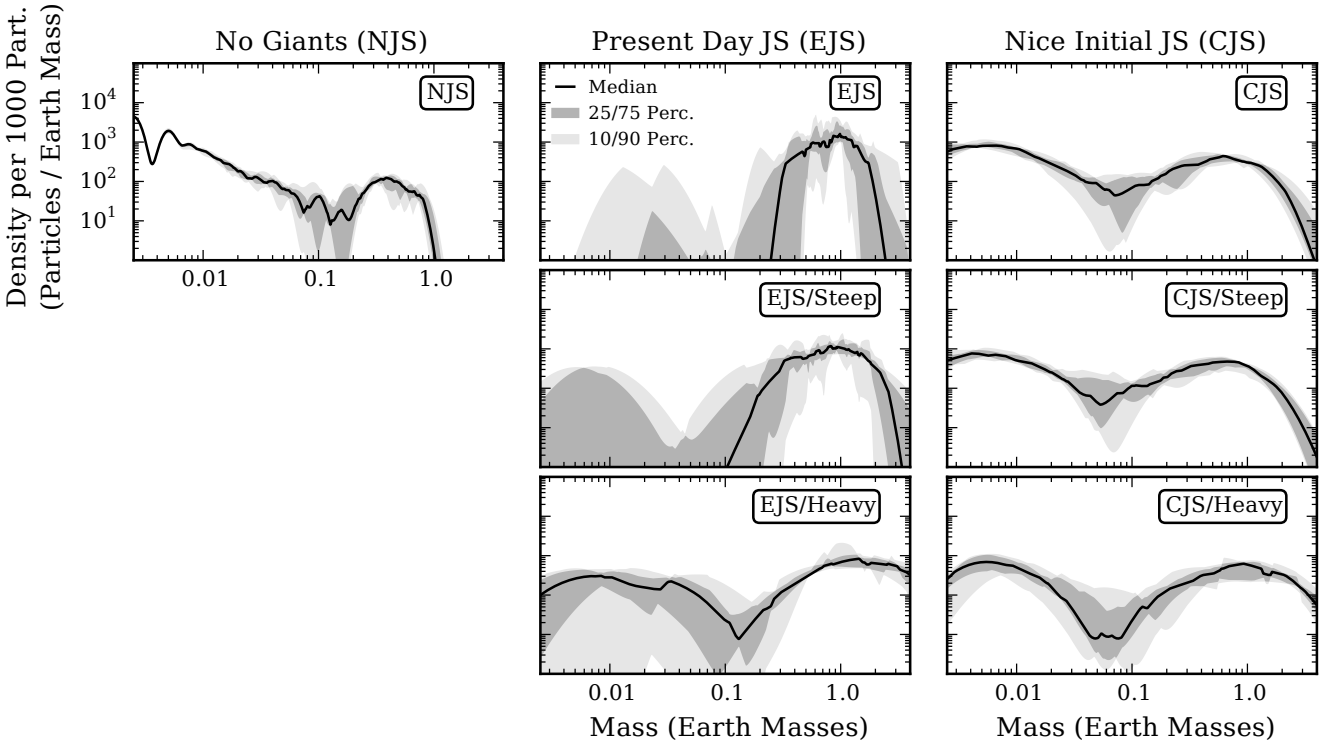

Figure 7. Median (black lines) and statistical spreads (grey shading) of the differential mass function (i.e., the number of particles per mass bin – dN/dM) for our simulation sets. Mass functions are computed as kernel density estimates. *Columns (Left to Right)*: Runs without Jupiter and Saturn, Jupiter and Saturn on their present-day eccentric orbits, Jupiter and Saturn on circular orbits. *Rows (Top to Bottom)*: Reference initial planetesimal disk, steep disk, more massive initial disk.

wide range of semi-major axes with more massive planets closer to the host star. If giant planets are present, the number of terrestrial planets per systems drops to 4 or 5. They are more massive with 50 per cent having $M > 0.5$ to 0.8 $M_\oplus$, depending on the giant planet configuration. Most (90 per cent) are below 1.2 $M_\oplus$, but we find isolated 1.6 $M_\oplus$ planets. They also cover a much narrower range of semi-major axes and are closer to the host star.

Systems with Jupiter and Saturn on eccentric orbits (EJS) tend to have (by median) 50 per cent more massive planets than systems with Jupiter and Saturn on circular orbits (CJS). They place terrestrial planets at smaller semi-maxis axis. Note that these are broad trends. Both configurations can produce terrestrial planets $M > 1\,M_\oplus$, although EJS simulations are more likely to do so. Simulations with eccentric giants planets also tend to have one or two fewer planets per system. Except for a few outliers, all planets are in orbits with low inclination and eccentricity. Overall, 50 per cent of all planets are at inclinations $i < 5^\circ$ and eccentricities $e < 0.1$. More inclined and eccentric orbits are restricted to simulations with giant planets, where 10 per cent of planets can reach $i > 15^\circ$ or $e > 0.25$.

These observations are consistent with those of Levison & Agnor (2003), who report systems hosting embryos on more eccentric orbits to result in fewer, more massive, and closer-in terrestrial planets. Excitation of planetesimal (and ultimately terrestrial planet) eccentricity increases in the presence of giant planets, especially when those are on eccentric orbits. Raymond et al. (2004) find similar correlations. Furthermore, they find the total mass of terrestrial planets to be slightly lower in systems with more eccentric Jupiters. We observe the opposite (cf. Figure 2), but point out their use of a different inital surface density profile.

3.4.2 *Steep and Heavy Disks*

For a given giant planet configuration, changing the slope of the initial the planetesimal mass distribution has a much smaller effect than adjusting the mass of planetesimal disk. Changes to the median mass and semi-major axis of the formed terrestrial planets remain below 10 percent for both EJS and CJS runs. In both cases, the width of the range populated by 80 per cent of all planets also remains similar. Irrespective of giant planet orbits, terrestrial planet inclinations decrease by 26 (CJS) to 36 per cent. Eccentricities are only visibly stunted for EJS runs where their median decreases by 25 per cent.

Predictably, heavier planetesimal disks produce more massive terrestrial planets. The most massive planets are 3.71 $M_{\rm Earth}$ (EJS) and 3.05 $M_{\rm Earth}$ (CJS). At the 90 per cent level, terrestrial planets in initially massive disks exceed those in the reference by 93 (70) per cent in EJS (CJS) configurations. The situation is less clean-cut in in semi-major axis, eccentricity, and inclination. For systems with eccentric giant planets, there is weak trend for terrestrial planets to end up at larger semi-major axis, although though median only differs by 8 per cent. For systems with giants on circular orbits, the trend is reversed such that the terrestrial planets tend to form 15 per cent closer to the stars. Dynamically, planets tend to be less excited in initially massive disks. This holds especially in CJS configurations where eccentricities and inclinations decrease by 35 per

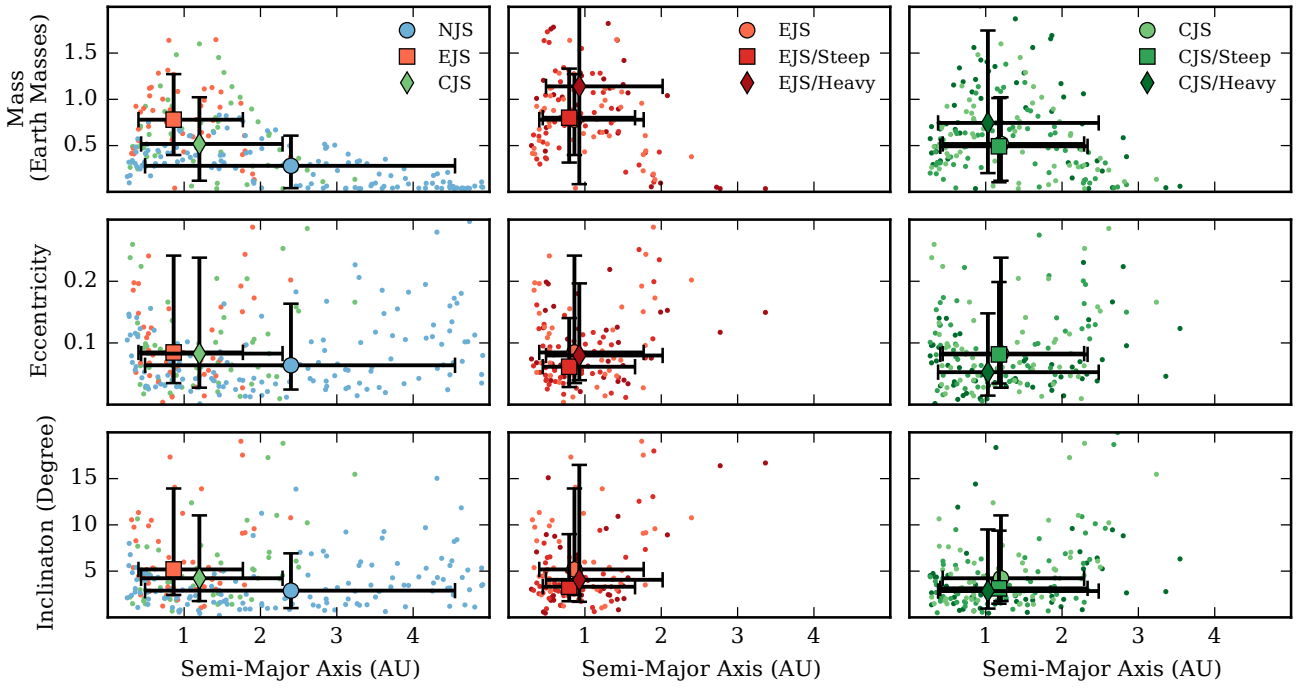

Figure 8. Final distribution of (rows, from top to bottom rows) mass, eccentricity, and inclination with semi-major axis of all terrestrial planets in the simulations. Small markers indicate the formed terrestrial planets (we exclude remaining planetesimals). The large overlaid markers indicate the median and 10/90 percentile range. Note that there exist points outside the view of the Figure, although their fraction of the total is at or below the 10 percent level. We chose a zoomed view to focus on the differences in median and percentile spreads. *Columns (Left to Right)*: Reference initial planetesimal disk with different giant planet configurations, Jupiter and Saturn on present-day eccentric orbits for different planetesimal disks, Jupiter and Saturn on circular orbits for different planetesimal disks.

cent. In EJS runs, the effect is weaker. Here, eccentricities are approximately the same. Although inclinations are reduced by 20 per cent for most planets, they in fact increase for at least a tenth of all planets.

3.4.3 *Sweeping Resonances: Take Three*

At this point, it may be superfluous to again point out that sweeping secular resonances drive the final orbital distribution of terrestrial planets. Without giant planets, much less material is delivered to the inner regions and embryos tend to grow locally. Given a smaller collision rate, dynamical friction from a substantial population of planetesimals keeps embryos and terrestrial planets dynamically cool over the entire course of the simulation. Adding giant planets on eccentric orbits confronts planetesimals with two closely spaced sweeping resonances (ν_5 and ν_6) that significantly excite and constrain large amounts of material $a \lesssim 2$ AU. For CJS configurations, the larger spacing between the ν_5 and ν_6 excites planetesimals less, and distributes material over a wider range ($a \lesssim 3$ AU).

By biasing the planetesimal distribution towards smaller semi-major axes, fewer planetesimals are swept up and excited by the sweeping resonances, resulting in dynamically colder terrestrial planets in configuration with steep initial disks. For initially more massive disks, the dynamical effects are more opaque. On the one hand, more massive planetesimals are more difficult to excite. On the other hand, excited planetesimals are more difficult to dampen from hydrodynamic drag due to their size. Taking these together, it appears that the more excited planetesimals are ejected from the system (or fall into the star) while the less excited ones are swept along into the inner system to build up terrestrial planets.

3.5 Solar System

So far, we deliberately omitted reference to the solar system. Although our initial conditions are based on simulations for exploring the formation of the solar system, our goal was not to assess their viability for this. They are in fact not well suited. For explorations of more suitable initial conditions and simulation parameters, see for example Izidoro et al. (2014b), Izidoro et al. (2014a), Walsh et al. (2011), Morishima et al. (2010), Raymond et al. (2009), Kokubo et al. (2006), and Chambers (2001).

Solar system formation simulations invoke diagnostics such as the Angular Moment Deficit (AMD) and the Radial Mass Concentration (RMC) to compare how close they resemble the solar system. Due to their stochastic nature, we expect initially identical simulations to produce different values for AMD and RMC. A large spread might overlap with values derived from other simulations and cast doubt on their diagnostic power. The AMD and RMC are

$$\mathrm{AMD} = \max\left(\frac{\sum_j m_j}{\sum_j m_j \left[\log_{10}\left(a/a_j\right)\right]^2}\right), \tag{4}$$

where the sum is over the mass m_j and semi-major axis a_j of the terrestrial planets, and we search for the maximum in a semi-

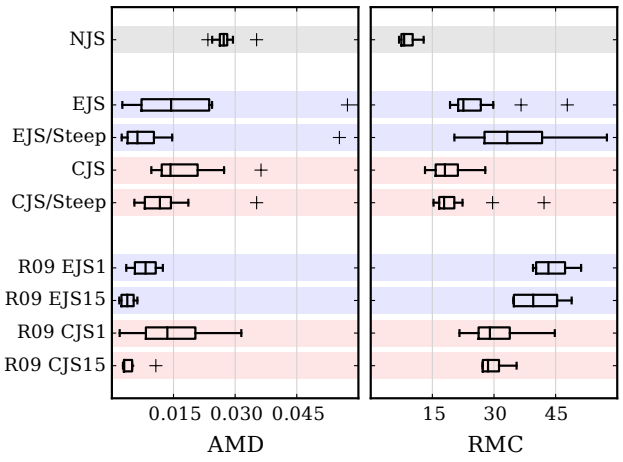

Figure 9. Box plots of the Angular Momentum Deficit (AMD) and Radial Mass Concentration (RMC) obtained from (i) seven (out of nine) of our sets (NJS, EJS, EJS/Steep, CJS, CJS/Steep) and (ii) corresponding simulations from Raymond et al. (2009) (R09 EJS1, R09 EJS15, R09 CJS1, R09 CJS15). For visual aid, we indicate similar giant planet configurations through the background colour. Boxes indicate the 25/75 range with the median marked in the box. Whiskers extend to 1.5 times the inter-quartile range and crosses indicate outliers.

major axis range covering all terrestrial planets (Laskar 1997). The RMC is

$$\mathrm{RMC} = \frac{\sum_j m_j \sqrt{a_j} \left(1 - \cos(i_j) \sqrt{1-e_j^2}\right)}{\sum_j m_j \sqrt{a_j}}, \quad (5)$$

where m_j, a_j, e_j, and i_j are the mass, semi-major axis, eccentricity, and inclinations of the terrestrial planets (Chambers 2001).

A number of authors report AMD and RMC for their solar system formation simulations, but have only run a single instance for each set of simulation parameters (Chambers 2001; Morishima et al. 2010). To our knowledge, only Kokubo et al. (2006), Raymond et al. (2009), as well as Izidoro et al. (2014b) account for stochastic variations across runs by running similar initial conditions multiple times.[10,11] Of these, Raymond et al. (2009) (hereafter R09) consider and present simulations most similar to our own, and we include some of their results here for comparison.

Figure 9 shows the AMD and RMC from seven of our nine simulation sets as well as corresponding simulations from R09 (i.e., identical initial solid surface density profiles and giant planets orbits). Box plots are generated from (i) twelve runs per set (our runs), or (ii) four runs per set (R09).

We find that our simulations without giant planets have small spreads in the AMD and RMC values. Simulations including giant planets have larger spreads, especially in the AMD. Values derived from EJS and CJS sets also overlap, and only the overall statistics reveal a trend towards smaller RMC values in CJS runs. Spreads in runs with a steeper planetesimal distribution tend to be smaller except for RMC in EJS/Steep runs.

Although the ranges in AMD and RMC populated by our runs and those of R09 tend to be misaligned, they generally show overlap. More importantly, at least some trends resulting from changing the orbits of the giant planets and initial planetesimal mass distribution appear to robust. For example, in CJS runs, moving to steeper initial planetesimal distribution decreases the AMD while the RMC remain approximately the same. For EJS runs, steeper initial profiles also decrease the AMD in both cases, although the RMC responds differently in the runs of R09 vis-à-vis our runs. Changing the orbits of the giant planets is much more robust and exhibits the same trends in both sets (when judging by the median).

Overall, it appears that runs in R09 follow clear trends and are not as burdened by overly wide spreads and outliers as ours. Unfortunately, this clarity appears to be a consequences of simplifications made to conform to the computational resources available at the time. In particular, recall that depending on the giant planet configuration and initial planetesimal distribution, inward sweeping secular resonances generate a particular distribution of embryos after the gas disk has dissipated. It is only at this point that R09 initialise their simulations, by necessity with a more generic embryo distribution. This distribution lacks the imprint of the important dynamics that took place as the gas dissipated. As much of the shaping of the final system has already happened at this point, it should not be surprising that their runs produce smaller spreads in diagnostics.[12]

Finally, let us drive home two points. Firstly, modelling of the initial phase of planetesimals embedded in a dissipating gas disk is essential. Omitting this stage neglects much of the dynamics that shape the final architecture of the system, and restricts us to a smaller subset of the solution space. Secondly, the significant spread in all diagnostics emphasises the need for a statistical approach. Running only one simulation per set, pathological cases with reversed trends could arise, leading us to draw potentially wrongful conclusions.

4 COMPARISON WITH OBSERVATIONS

Sub-Neptune exoplanets are more massive and located at smaller semi-major axes than the terrestrial planets in our simulations (Mayor et al. 2011; Borucki et al. 2011; Howard et al. 2010). The validity of a comparison between observational trends and simulations then rests on the question of whether they form in-situ (Chiang & Laughlin 2013) or migrate inwards from their formation site (Kennedy & Kenyon 2008). Some models invoking migration introduce forming giant planets as barriers that divide systems into sub-Neptune populations located inward and outward of the giants (Izidoro et al. 2014a). Also see Haghighipour (2013), Raymond et al. (2013), and Morbidelli et al. (2012) for reviews.

Our simulations only support scenarios where sub-Neptunes form inwards of giants. It is unlikely that all observed exoplanet systems have formed this way, but discrimination of the evolutionary pathway of a given system is difficult. We therefore make the assumption that all system considered hereafter have evolved similar to our simulations. Under this assumption, the driving forces

[10] In contrast to our simulations, Kokubo et al. (2006) and Raymond et al. (2009) do not evolve identical initial conditions, but rather redraw different initial conditions from the same underlying distribution. We are uncertain what is done in Izidoro et al. (2014b).

[11] Levison & Agnor (2003) and Raymond et al. (2004) also report stochastic variations across simulations, but do not report the RMC or AMD due to their focus on different aspect.

[12] Of course, we have been wholly ignorant about the fact that giant planets may not yet be present (or massive enough) on their orbits as we start our runs. Future work will likely improve upon this and cheerfully point out this shortcoming.

Table 5. Median and 10/90 percentiles of mass M, semi-major axis a, and number of planets N_P for the sub-Neptune ($M < M_\oplus$) population of two sets of exoplanet systems. The number of system fulfilling the filtering criteria is N_S, and f_S the corresponding fraction out of 1228 total systems.

Set	M ($M_\oplus$)	a (AU)	N_P	N_S	f_S (Per cent)
No Giants	$6.61^{+6.27}_{-3.84}$	$0.12^{+0.23}_{-0.07}$	2^{+1}_{-1}	43	3.5
Giants	$8.58^{+4.52}_{-5.68}$	$0.09^{+0.16}_{-0.05}$	1^{+2}_{-0}	19	1.5

that set the architecture of the inner planets are inward sweeping secular resonances with the giant planets. Peaks and truncations in the distribution of sub-Neptunes with semi-major axis are then associated with the final location of the resonances. There is no reason to assume for extrasolar systems to have mass-peaks at the same location as we find in our simulations. These are set by the masses and orbital motions of giant planets, which are markedly different than in our runs.[13] Nevertheless, the underlying mechanism is the same, such that we are confident the analysis is applicable.

As all simulations generate systems with $\geqslant 1$ terrestrial planet, we focus on multi-planet extrasolar systems. We import raw data from the *Extrasolar Planet Encyclopedia*[14] database (Schneider et al. 2011), using the snapshot from 02 August 2015. The entire set contains 1228 planetary systems. We apply two filtering operations. First, we reject all single-planet systems. Second, we reject all systems where at least one planet lacks mass or semi-major axis data. The latter criterion may seem overly constraining, but selectively removing only a subset of planets from a given system would skew the statistics. The dataset is now reduced to 62 systems. Finally, we split the data into two subsets, depending on whether they host giant planets ($M > 50\,M_\oplus$) or not.

Figure 10 is a visual representation of the architecture of the retained planetary systems. Figure 11 shows all sub-Neptune planets ($M \leqslant 17.14\,M_\oplus$) as well as median and 10/90 percentiles in the two sets. The statistics are tabulated in Table 5.[15] We emphasize that we report on the statistical properties of the sub-Neptune population only. Planets with masses $M > M_{\rm Neptune} = 17.14\,M_\oplus$ are not included. We find that the observations follow the same trends as the simulations, i.e. that systems hosting giant planets tend to have fewer, and more massive sub-Neptune planets at smaller semi-major axes. The statistics are robust with respect to varying the cut-off mass for giant planet classification in our reduction steps. Compared to $M_{\rm Giant} \geqslant 50\,M_\oplus$, changing cut-offs to $M_{\rm Giant} \geqslant 30\,M_\oplus$ and $M_{\rm Giant} \geqslant M_{\rm Neptune} = 17.14\,M_\oplus$ conserves all trends. The median and 10/90 percentiles change by < 10 and < 15 per cent, respectively.

Consider now the outliers, i.e. sub-Neptunes in systems with no detected giant planets meeting the following criteria: (i) mass larger than the 90 percentile mass of sub-Neptunes in systems with giant planets ($13.10\,M_\oplus$), (ii) semi-major axis smaller than the 10 percentile semi-major axis of sub-Neptunes in systems with giant planets (0.04 AU) and (iii) number of planets at most equal to the 10 percentile number of sub-Neptunes in systems with giant planets (one). Systems with planets meeting these criteria would be a better fit to the statistics of systems that do host giant planets. We thus propose that systems with planets meeting at least two of the criteria host undetected giant planets. The criteria are matched by three systems: Kepler-10, Kepler-9, and HD 51608. If we relax the mass and semi-major axis limits to the 75 and 25 percentiles ($11.44\,M_\oplus$, 0.05 AU) and allow up to two sub-Neptunes per system, we match an additional six systems: 61 Vir, CoRoT-7, HD 134060, HD 20003, HD 51608, and Kepler-18.

What now is the influence of the intermediate mass planets ($17.14\,M_\oplus < M < 50.0\,M_\oplus$) we have ignored thus far? Inspection of Figure 10 suggests that most of them are located outwards of the sub-Neptunes. This suggests they are small gas giants with correspondingly short formation timescales. As such, they would be present early enough to dynamically contribute to the configuration of secular resonances sweeping up planetesimals. We can therefore justify lowering the thresholds to $M_{\rm Giant} > 30\,M_\oplus$ or even $M_{\rm Giant} > M_{\rm Neptune} = 17.14\,M_\oplus$, and repeating the outlier detection with a larger set of giant planets. Doing so predicably decreases the number of candidate systems because we classify more of the would-be-predicted giants as actual giants. For a giant planet threshold of $30\,M_\oplus$, we retain six candidate systems: 61 Vir, CoRoT-7, HD 20003, HD 20781, HD 51608, Kepler-10, and Kepler-18. Further decreasing the threshold to $M_{\rm Neptune}$ retains only three candidates: CoRoT-7, HD 20003, and HD 20781.

These candidates match our most stringent constraints. They are indicated by a red background in Figure 10, and visual inspection indeed suggests the architecture to be more in line with systems that do host giant planets. There are also number of systems where a planet that we initially classified to be in the intermediate mass range appears in systems that would have been predicted to host giant planets with a larger mass cutoff.

Finally, although present-day observational techniques lack sensitivity to detect systems with comparable architecture to our simulation results, future (and longer) surveys could lift these constraints. For such surveys, we predict that terrestrial planets in systems hosting giant planets are fewer, more massive, and closer-in than those in systems without giant planets.

5 ORBITAL DIVERGENCE, CAUSE & TIMESCALES

Numerically evaluated trajectories of the N-Body problem for $1/r$ potentials diverge exponentially fast as perturbations seeded by round-off errors are amplified in close encounters. This is a classical result from stellar (Miller 1964) (Broekholt/Zwart, ...) and molecular dynamics (YYY), where individual simulations loose predictive power on the dynamical timescale (Goodman et al. 1993). In planetary systems without close encounters, trajectories also diverge exponentially, but on timescales of millions of dynamical times (Laskar, etc). Here, divergence is driven by the integral effect of periodic gravitational perturbations (AAA).

As planetesimals undergo frequent close encounters with each other, we may reason that their trajectories diverge in the same fashion as stellar systems. Thus far, little work has attempted to characterise this regime – a gap we now fill. In order, we now reiterate the mechanism for seeding and growth of position errors in the context of planetesimal disks, empirically determine rates of divergence, and compare to dynamically similar systems.

[13] There is an additional caveat. In our runs, we remove particles at heliocentric distances < 0.2 AU for computatioanl reasons. In the first few Myr, gas drag might remove planetesimals that would otherwise grow into embryos and planets here.

[14] http://www.exoplanet.eu

[15] Owing to observational uncertainties, we characterise planets by their mass and orbital semi-major axis only. More sophisticated techniques may allow consideraion of eccentricites in similar analyses (Van Eylen & Albrecht 2015).

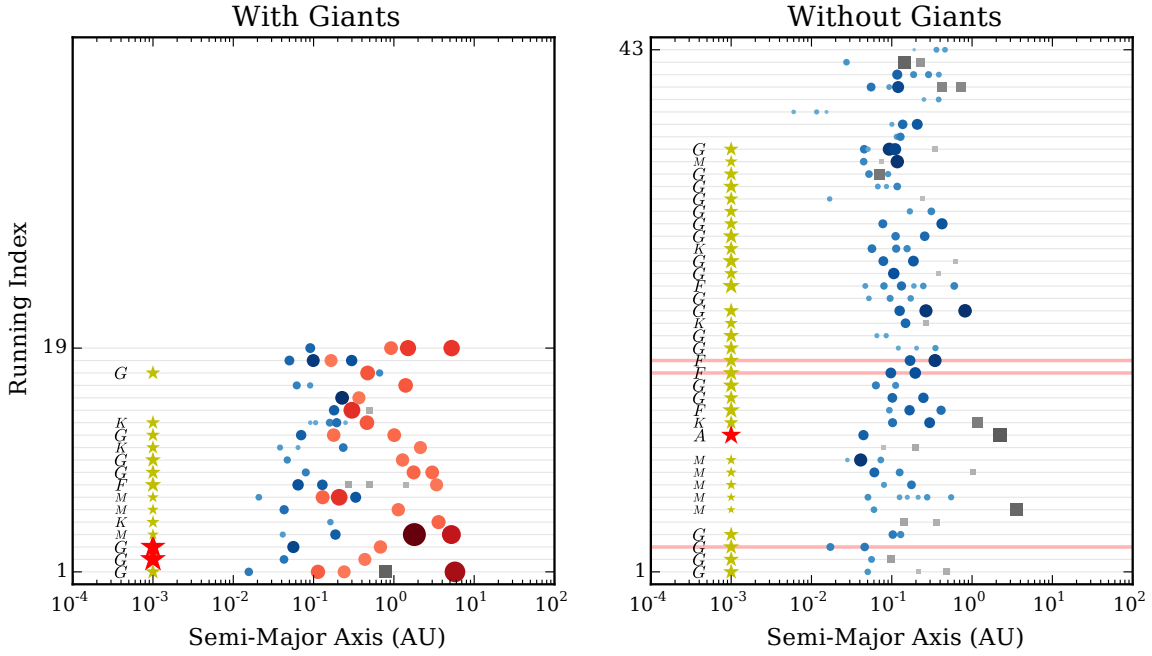

Figure 10. Architectures for the filtered (see text) set of exoplant systems. Blue and red circles indicate sub-Neptune ($M < 17.14\,M_\oplus$) and giant ($M \geqslant 50 M_\oplus$) planets. Planets with intermediate masses are indicated as grey squares. Marker size and shading scales linearly with planet mass, but the scale is not continuous between the three sets. Red highlights behind the planets indicate suspected, but undetected, giant planets present in the system. Where available, letters and size of the star symbol indicate the spectral class and mass $M_\star$ of the host star. Red star symbols indicate $M_\star > 1.5\,M_\odot$. *Left:* Systems with detected giant planets. *Right:* Systems without detected giant planets.

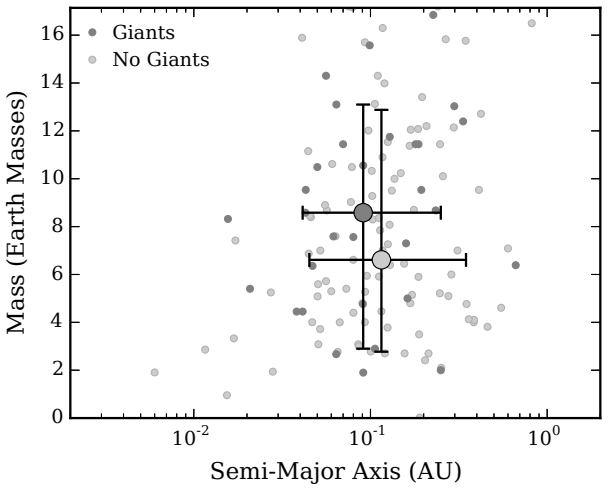

Figure 11. Mass and semi-major axis for all sub-Neptunes ($M < 17.14\,M_\oplus$) in the reduced (see text) sample of observed exoplanets. Small points are observational data. Light and dark grey points are planets in systems with and without detected giant ($M \geqslant 50\,M_\oplus$) planets in the same system. Large circles and lines indicate the median as well as 10/90 percentiles for the two sets.

[Footnote: Different names in literature, but the exponential divergence is caused by the same underlying reasoning: the phase-space trajectories are chaotic, i.e. exponetial growth]

5.1 Mechanism of Orbital Divergence

5.1.1 *Seeding Position Errors*

Modern planetary formation codes are based on a symplectic mapping to evolve particles (Wisdom & Holman 1991; Duncan et al. 1998; Murray & Dermott 1999; Chambers 1999; Grimm & Stadel 2014). A suitable Hamiltonian for a planetary system around a massive central object is

$$H = H_{\rm Kep} + H_{\rm Interact}, \tag{6}$$

where $H_{\rm Kep}$ is the Keplerian trajectory of the particles about the central mass and $H_{\rm Interact}$ the mutual gravitational interaction between particles. Being inherently discrete, numerical schemes evolve only an approximate Hamiltonian

$$\widetilde{H} = H + H_{\rm Trunc} + H_{\rm Round-Off}, \tag{7}$$

where $H_{\rm Trunc} \sim \mathcal{O}(\Delta t^n)$ is the truncation error set by the order of the integrator n for a given step size Δt, and $H_{\rm Round-Off}$ the numerical round-off error. While the former lends itself to formal analysis (Saha & Tremaine 1992), the round-off error depends on the numerical implementation and underlying hardware.

Two identical initial conditions ($H_1 = H_2$) evolved with the same order of integrator and timestepping ($H_{\rm Trunc,1} = H_{\rm Trunc,2}$) will diverge if their round-off errors differ. In parallel computing, the behaviour of certain intrinsic functions may be ill-defined. If such intrinsics are used to constructs lists of operations, the order of operations may not be the same across runs, thus driving different round-off errors and simulation divergence. See also Section 2.3.

Round-off errors act at the level of floating point precision ($\sim 10^{-15}$ for numbers of order unity using double precision), so

they accumulate slowly. However, they modify the geometry of the simulation ever so slightly. Such perturbations cause orbits in simulations to diverge exponentially, as we now show.

5.1.2 Amplifying Position Errors

In their introduction, Goodman et al. (1993) describe a simple model for the divergence of nearby orbits. Although limited in scope, we adapt this intuitive model to give context to the empirical results below.

Consider a single planetesimal. As it goes about its way, the orbit is governed by the central object as well as the interactions with all other planetesimals. Now consider its identical twin that has been displaced by a round-off error $\delta s(0)$. Their respective interaction geometries with other disk particles are subtly altered. In the impulse approximation, the position error δs after X encounters grows to

$$\delta s^{(X)} \sim \prod_{i}^{X} \left(1 + \frac{Gm\tau_i}{b_i^2 v_i}\right) \delta s^{(0)}, \tag{8}$$

where m is the particle mass, b the impact parameter, τ the time between interactions, i the running index over encounters, v the relative velocity of interacting particles, and

$$\tau \sim \frac{1}{nb^2 v} \tag{9}$$

the time between encounters for a planetesimal number density n in the disk. Deferring details to Appendix X, we note:

(i) The form of Eqn. (8) suggests that the position error grows exponentially fast. As demonstrated in Appendix X, we expect e-folding times on the order of a few years.

(ii) There are more encounters at large impact parameters, but they result in small displacements. Conversely, encounters at small impact parameters are rare, but induce a larger displacement. There exists some range in b that drives divergence. This turns out to be on the order of a few Hill radii. See Appendix X.

(iii) At smaller semi-major axes, Keplerian shear (and thus the relative velocity between particles) is larger. Here, we expect δs to grow fastest.

(iv) Increasing the mass resolution increases the number density n and decreases the mass m. This decreases the time between encounters, but also diminishes their strength. In the context of the simple model, we expect no resolution dependence.

The model has the key assumptions that our twin planetesimals interact with the same set of disk planetesimals, in the same order, and at comparable geometries. With e-folding times of a few years, these assumptions break down quickly. At this point, we are relegated to numerical experiments.

5.2 Resolution Dependence & Timescales

As capabilities to handle larger numbers of simulation particles improve, we are forced to consider how long a given numerical solution can be considered accurate, and beyond which point it holds only in a statistical sense. Although the simple analytical description above suggests resolution independence, numerical investigations in stellar and molecular dynamics indicate resolution dependence (XXX, YYY, ZZZ). To settle this discrepancy, we empirically determine the divergence of nearby orbits as a function of the number of simulation particles.

Table 6. Overview of simulations. Perturbations are applied at the level of double precision floating point accuracy. Three dots indicate a range of simulations with N_p increasing in powers of 2. Comparisons of PKDGRAV and GENGA are shown in Appendix B.

N_p [a]	N_r [b]	Δt [c]	Code
$8, 16, \ldots, 256, 512$	128	6 Days	PKDGRAV
1024	32	6 Days	PKDGRAV
2048	64	6 Days	PKDGRAV
$4096, \ldots, 32768$	8	6 Days	PKDGRAV
2048	64	6 Days	PKDGRAV
	64	6 Days	GENGA
2048	64	0.6 Days	PKDGRAV
	64	0.6 Days	GENGA

[a] Number of particles. [b] Number of realisations. [c] Time step.

5.2.1 Measuring Orbital Separation

Measuring phase-space distances in velocity or position space is unsuitable for Keplerian disks because shear naturally drifts particles apart. A more suitable metric would be based on integrals of motion. For orbits in a $1/r$ potential, the specific angular momentum vector $h = \vec{r} \times \vec{v}$ and the Laplace-Runge-Lenz vector $\vec{e} = (\vec{v}_i \times \vec{h})/\mu - \vec{r}/r$ are such integrals. Here, $\mu = G(M+m)$ is the standard gravitational parameter for a mass m orbiting a host mass M, $\vec{r}$ the position vector, and $\vec{v}$ the velocity vector. In the absence of external perturbations, $\vec{h}$ and $\vec{e}$ retain their magnitude and direction at any point along the orbit. The numerical eccentricity of the orbit is $e = |\vec{e}|$. Based on $\vec{h}$ and $\vec{e}$, Kholshevnikov (2008) constructed a metric where the distance between two orbits is

$$\delta\ell = \sqrt{\frac{1}{L\mu}\left(\vec{h}_1 - \vec{h}_2\right)^2 + (\vec{e}_1 - \vec{e}_2)^2}, \tag{10}$$

where L is a scaling parameter (which we conveniently set to 1 AU). We note that (10) is valid for curvilinear orbits ($e < 1$), but refer to Kholshevnikov (2008) for an extension to rectilinear orbits.

5.2.2 Simulations, Post-Processing

We explore the growth of perturbations by considering pairs of simulations. First, we draw a realisation of the initial conditions from Section 2.4 with N_p particles. This is the reference run. We copy the disk and randomly change the (x,y,z) coordinates of all particles by $\pm 10^{-15}$ to emulate round-off errors. Code units are AU, so the shift is ~ 0.15 mm. This generates the perturbed run.[16] We evolve both runs for ~ 2000 years (single core, no gas disk, no giant planets, 6 days timestep, collisions as inelastic mergers) and keep track of initially identical particle pairs. We repeat this for a range of N_p. For $N_p \leqslant 2048$, we use both PKDGRAV and GENGA, and for $N_p > 2048$ only PKDGRAV. Results reported here are from PKDGRAV runs, but Appendix B contains a comparison. Table 6 contains a summary of the simulations run.

In post-processing, we track the orbital separation $\delta\ell$ of all

[16] Shifting just a single particle is a functionally equivalent procedure. In this case, orbital divergence of other particles is delayed until they become "infected" by the initial shift. This also introduces sensitivity to the location of the initially perturbed particle. By perturbing all particles at once, we avoid this complication.

initial particle pairs. For each particle, $\delta\ell$ changes randomly and in discrete steps, cf. Appendix A. We therefore compute the geometric mean normalised to the initial separation over all N_p particle pairs to characterise the entire disk, viz.

$$\langle\Delta\ell\rangle = \left(\prod_j^{N_p}\Delta\ell_j\right)^{1/N_p} = \left(\prod_j^{N_p}\frac{\delta\ell_j(t)}{\delta\ell_j(t=0)}\right)^{1/N_p}, \quad (11)$$

where j is the running index of the particle pairs and we omit the explicit time dependence $\langle\Delta\ell(t)\rangle$ for brevity of notation. For most experiments, we have evolved N_r realisations so that we compute the geometric mean over all $N_p \times N_r$ particles instead.

5.2.3 *Results*

Figure 12 shows the growth of $\langle\Delta\ell\rangle$ as a function of time, number of particles, and semi-major axis. For all depicted cases, $\langle\Delta\ell\rangle$ evolves in three distinct stages. Initially fast exponential growth first transitions into a slower exponential, and then settles into a slow power law. For $N_p < 512$, growth slows with as N_p decreases and distinction between the exponentials disppears for $N_p < 64$.[17] As we reach $N_p = 8$, we approach the regime of a tightly packed planetary systems whose stability is investigated in Chambers et al. (1996). At this point, increasing the planetary spacing leads into the regime of chaos in the solar system with Myr timescales.

As we focus on orbits in planetesimal disks (rather than tightly packed systems of planets or planetary embryos), we only consider systems where $N_p \geqslant 64$. To quantify the growth of $\langle\Delta\ell\rangle$, we (i) fit exponential functions through the two exponential growth phases to determine the e-folding times t_{e1} and t_{e2}, (ii) fit power-laws through the post-exponential phase, and (iii) record the time required for $\langle\Delta\ell\rangle \geqslant 10^{11}$. This is the time to divergence $t_{\rm div}$. All are shown in Figure 13, along with their dependence on the number of particles N_p (and semi-major axis a), to which we fit power-laws. We make five principal observations:

(i) E-folding times are shorter for simulations with more particles. The dependence on particle number is matched by power laws $t_{e1} \sim N_p^{-0.33}$ and $t_{e1} \sim N_p^{-0.30}$.
(ii) In simulations with more particles, orbits diverge faster. The time to divergence behaves as $t_{\rm div} \sim N_p^{-0.22}$.
(iii) Orbits with smaller semi-major axes diverge faster. The trend is linear, i.e. $t_{\rm div} \sim a$.
(iv) As N_p increases, exponential growth transitions into power-law growth earlier and at smaller values of $\langle\Delta\ell\rangle$.
(v) The late time power-law becomes shallower as we increase the number of particles. It is well-fitted by $t_{\rm pow} \sim N^{-0.1}$.

The first three are rooted in the rate and strength of gravitational interactions in the planetesimal disk. As suggested in Section **??**, interactions with impact parameters b of a few times the Hill radius $R_{\rm Hill}$ drive orbital divergence. Assuming a particle in a box model, the mean free path between such encounters is $\lambda = 1/(n\Lambda)$, where $\Lambda \sim b^2 \sim R_{\rm Hill}^2$ is the interaction cross-section and $n \sim N_p$ the particle number density. With a particle mass of $m \sim 1/N_p$, we find $R_{\rm Hill} \sim N_p^{-2/3}$, such that $\lambda \sim N_p^{-1/3}$. The more particles in the disk, the shorter the mean free path between encounters on the order $R_{\rm Hill}$ and the faster orbital differences grow. On the other hand, for a surface density profile $\Sigma \sim 1/r$, the volume density is $n \sim 1/r^2$, and $\Lambda \sim R_{\rm Hill} \sim r^2$, such that λ is constant with heliocentric distance r. Here, the relative Keplerian velocity between neighbouring orbits decreases as $r^{-3/2}$. This increases the mean time between encounters, leading to fewer encounters, and slower orbital divergence.[18]

5.3 Comparison to Stellar Dynamics & Timescales

Kandrup & Smith (1991), Goodman et al. (1993), and Hemsendorf & Merritt (2002) explore the short-time (a few crossing times) growth of perturbations in N-Body realisations of uniform density and Plummer potentials. They find exponential growth and report e-folding times on the order, but independent of, the crossing time. With crossing times of order unity (a year at 1 AU), we see similar behaviour. These authors also report dependence on the number of particles. Kandrup & Smith (1991) finds $t_e \sim 1/N_p$, while the latter two suggest $t_e \sim 1/\ln(N_p)$ or $t_e \sim 1/\ln(\ln(N_p))$, which are difficult to discriminate, yet markedly different from our $\sim N_p^{-0.3}$ scaling. There is also a dependence on the gravitational softening (Kandrup et al. 1992), which sets a minimum impact parameter. This is absent in our simulations. Valluri & Merritt (2000) demonstrate saturation of exponential growth depending on N_p, which corresponds to our fourth principal observation. Starting from separations comparable to those where growth saturated in Valluri & Merritt (2000) and experimenting with a range of softening parameters, Kandrup & Sideris (2001) and Sideris & Kandrup (2002) find further linear growth on timescales $t_{\rm grow} \sim \sqrt{N_p}$ instead of saturation,[19] which they attribute to their use of gravitational softening. This is the late-time regime, where we find power-law growth with scaling as $t_{\rm pow} \sim N_p^{-0.1}$ instead. We attribute this difference to the influence of a massive object which accelerates divergence (El-Zant & Gurzadyan 1998).[20]

Hut & Heggie (2002) suggest that in the long term, orbits diverge on timescales comparable to the relaxation time. In planetesimals disks, two-body relaxation converts Keplerian shear into random motions. Absent damping, the velocity dispersion evolves as $\sigma \propto t^{1/4}$ (Ida & Makino 1992a; Kokubo & Ida 1992), which is slightly slower than the behaviour of our late-time divergence. The caveat here is that we have stopped integrations after 2000 years, which may well be too short to probe this regime properly.

6 SUMMARY & CONCLUSIONS

In this work, we have addressed the chaotic nature of terrestrial planet formation. Orbits which are initially identical up to one part

[17] We do not show $\langle\Delta\ell\rangle$ for $N_p < 512$ to avoid visual clutter. The aforementioned trends should become apparent through mental extrapolation.

[18] Once relative orbital velocities drop below the disk velocity dispersion, the encounter rate is driven by the velocity dispersion instead. We have omitted this complication in the main text to avoid confusion and focus on a simple explanation.

[19] Kandrup & Sideris (2001) and Sideris & Kandrup (2002) also report short-time averaged Lyapunov exponents independent of N_p. These are different indicators than our e-folding times. Since they are derived using renormalization techniques, they probe only the smallest perturbations, i.e. that corresponding to bottom left corner in our Fig. 12. There, $\langle\Delta\ell\rangle$ is indeed independent of N_p.

[20] As we increase N_p, the mass ratio between the central object and the particles increases, which accelerates divergence. Lacking a central object, this effect is absent in Plummer and uniform-density potentials.

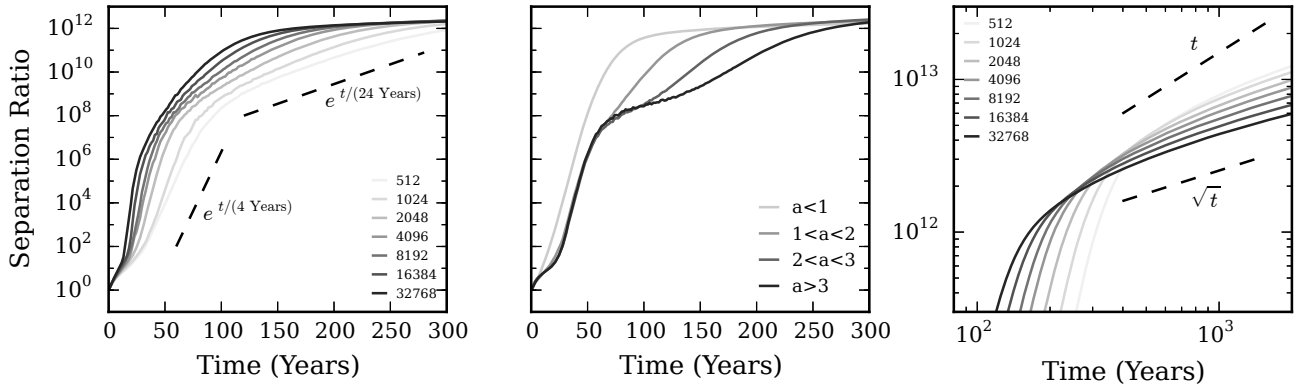

Figure 12. Geometric mean separation ratio $\langle\Delta\ell\rangle$ versus time as a function of particle number N_p and semi-major axis a. The left and middle panels are $\log_{10}$-linear such that exponentials are straight lines. The rightmost panel is $\log_{10}$-$\log_{10}$ such that power-laws are straight lines. Unless otherwise noted, geometric means are computed over all $N_r \times N_p$ particles, cf. Eqn. (11). *Left:* Separations for runs with 512 to 32768 particles. We indicate slopes corresponding to two different e-folding times. *Middle:* Separations for runs with 2048 particles, grouped by semi-major axis. The mean is taken over all particles across runs in identical semi-major axes ranges. *Right:* Like the leftmost panel, but zoomed on the transition region between exponential and power law growth. We indicate two power-law slopes, which bound the observed slopes.

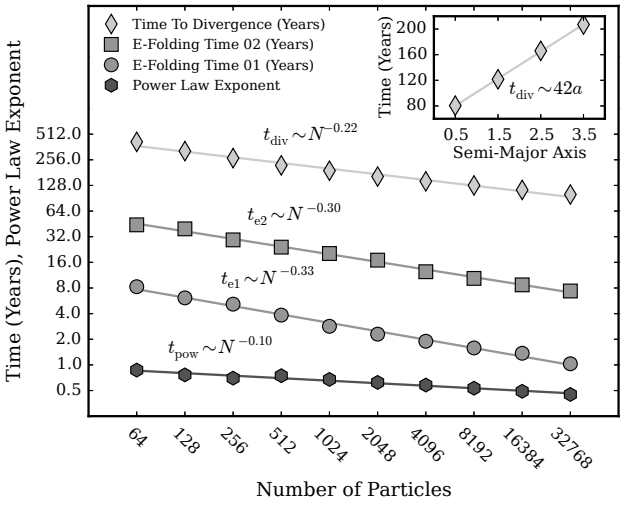

Figure 13. E-Folding times t_e, power-law slopes t_{pow}, and time to divergence t_{div} (time until $\langle\Delta\ell\rangle \geqslant 10^{11}$) as functions of the number of simulation particles N, cf. legend. We also show the time to divergence as a function of semi-major axis a (inset). Markers least-squares fits to $\langle\Delta\ell\rangle$ in the corresponding range (e-folding times, power-law exponents), or automated detection (time to divergence). Lines are least-squares power-law fits to the markers. Axes are $\log_2$-$\log_2$ such that straight lines are power-laws.

in 10^{15} ($\sim$ double precision floating point accuracy) diverge exponentially until their separation becomes limited by the accessible phase-space. The divergence is driven by differences in the geometry of successive close encounters with other particles. We find that the rate of divergence increases with the number of simulation particles. At larger semi-major axes, orbits diverge more slowly. After ~ 500 years, orbits have diverged far enough for the collisional history of two simulations with initially nearby orbits to differ. They are now fully diverged, and produce distinctly different planetary systems within our simulation times of ~ 147.84 Myr.

If the position of a single planetesimal in our simulation is changed by less than one millimeter, the positions, orbits and masses of the resulting planets are all different. We find that the e-folding timescale to orbital divergence decreases as the number of particles increases. There is no reason to expect that this behaviour does not continue to much smaller scales. Perhaps if our early solar system had contained one extra molecule, the Earth would not have formed at all.

Even if simulations are initialised with identical initial conditions, variations in round-off errors quickly seed differences in the planetesimal orbits, which are amplified by sequences of close encounters. The variations are caused by the ill-defined behaviour of certain intrinsic functions available in parallel programming. They cause loss of control over the order of operations in the code. Although this can be mitigated, the extreme sensitivity on the order of operations implies the existence of multiple, numerically equally valid, solutions for any given initial condition. Individual simulations therefore lack predictive power, and we are relegated to characterising the global solution space by stacking multiple simulations. Unfortunately at present, it remains unclear how many runs are required to adequately sample the underlying solution space. We advocate at least 8 runs per initial condition. This would generate two samples per quartile given an underlying uniform distribution.

Analysing our simulations, we find that varying the configuration of giant planets in systems has statistically robust results in line with previous work. Systems with giant planets tend to form fewer, more massive, and more eccentric terrestrial planets at smaller semi-major axes than those without. Although we probe different mass and orbital regimes, observations of sub-Neptune mass planets appear to support these trends. By extracting outliers in the observations, our analysis also suggests that Kepler-10, Kepler-9, 61 Vir, HD 134060, and HD 51608 may host as yet undetected giant planets.

ACKNOWLEDGMENTS

We are grateful to Ryuji Morishima for help with PKDGRAV, Rok Roškar, Thomas Peters, George Lake, and Michael Rieder for useful discussions, as well as Doug Potter for computational support. Simulations were run on the Tasna GPU cluster and the zBox4

CPU cluster at the Institute for Computational Science, University of Zürich. We also acknowledge use of Numpy, Scipy, IPython, Matplotlib, and Colorbrewer2 for post-processing.

REFERENCES

Allison R. J., Goodwin S. P., Parker R. J., Portegies Zwart S. F., de Grijs R., 2010, MNRAS, 407, 1098
Borucki W. J., et al., 2011, ApJ, 736, 19
Brouwer D., Clemence G. M., 1961, Methods of celestial mechanics
Chambers J. E., 1999, MNRAS, 304, 793
Chambers J. E., 2001, Icarus, 152, 205
Chambers J. E., Wetherill G. W., 1998, Icarus, 136, 304
Chambers J. E., Wetherill G. W., Boss A. P., 1996, Icarus, 119, 261
Chiang E., Laughlin G., 2013, MNRAS, 431, 3444
Chirikov B. V., 1979, Phys. Rep., 52, 263
Duncan M. J., Levison H. F., 1997, Science, 276, 1670
Duncan M. J., Quinn T., 1993, ARA&A, 31, 265
Duncan M. J., Levison H. F., Lee M. H., 1998, AJ, 116, 2067
El-Zant A. A., Gurzadyan V. G., 1998, Physica D Nonlinear Phenomena, 122, 241
Evans N. W., Tabachnik S., 1999, Nature, 399, 41
Everhart E., 1973, AJ, 78, 329
Franklin F., Lecar M., Wiesel W., 1984, in Greenberg R., Brahic A., eds, IAU Colloq. 75: Planetary Rings. pp 562–588
Franklin F., Lecar M., Soper P., 1989, Icarus, 79, 223
Gladman B., 1993, Icarus, 106, 247
Gladman B., Duncan M., 1990, AJ, 100, 1680
Gladman B. J., et al., 1997, Science, 277, 197
Goodman J., Heggie D. C., Hut P., 1993, ApJ, 415, 715
Grazier K. R., Newman W. I., Kaula W. M., Hyman J. M., 1999a, Icarus, 140, 341
Grazier K. R., Newman W. I., Varadi F., Kaula W. M., Hyman J. M., 1999b, Icarus, 140, 353
Greenberg R., Hartmann W. K., Chapman C. R., Wacker J. F., 1978, Icarus, 35, 1
Greenzweig Y., Lissauer J. J., 1990, Icarus, 87, 40
Greenzweig Y., Lissauer J. J., 1992, Icarus, 100, 440
Grimm S. L., Stadel J. G., 2014, ApJ, 796, 23
Haghighipour N., 2013, Annual Review of Earth and Planetary Sciences, 41, 469
Haisch Jr. K. E., Lada E. A., Lada C. J., 2001, ApJ, 553, L153
Hemsendorf M., Merritt D., 2002, ApJ, 580, 606
Heppenheimer T. A., 1980, Icarus, 41, 76
Holman M. J., 1995, in Kinoshita H., Nakai H., eds, 27th Symposium on Celestial Mechanics,. p. 116
Holman M. J., Wisdom J., 1993, AJ, 105, 1987
Howard A. W., et al., 2010, Science, 330, 653
Hut P., Heggie D. C., 2002, Journal of Statistical Physics, 109, 1017
Ida S., Makino J., 1992a, Icarus, 96, 107
Ida S., Makino J., 1992b, Icarus, 98, 28
Ito T., Tanikawa K., 2002, MNRAS, 336, 483
Izidoro A., Morbidelli A., Raymond S. N., 2014a, preprint, (arXiv:1408.1215)
Izidoro A., Haghighipour N., Winter O. C., Tsuchida M., 2014b, ApJ, 782, 31
Kandrup H. E., Sideris I. V., 2001, Phys. Rev. E, 64, 056209
Kandrup H. E., Smith Jr. H., 1991, ApJ, 374, 255
Kandrup H. E., Smith Jr. H., Willmes D. E., 1992, ApJ, 399, 627
Kennedy G. M., Kenyon S. J., 2008, ApJ, 682, 1264
Kholshevnikov K. V., 2008, Celestial Mechanics and Dynamical Astronomy, 100, 169
Kokubo E., Ida S., 1992, PASJ, 44, 601
Kokubo E., Ida S., 1996, Icarus, 123, 180
Kokubo E., Ida S., 1998, Icarus, 131, 171
Kokubo E., Ida S., 2000, Icarus, 143, 15
Kokubo E., Ida S., 2012, Progress of Theoretical and Experimental Physics, 2012, 010000
Kokubo E., Kominami J., Ida S., 2006, ApJ, 642, 1131
Laskar J., 1989, Nature, 338, 237
Laskar J., 1990, Icarus, 88, 266
Laskar J., 1994, A&A, 287, L9
Laskar J., 1997, A&A, 317, L75
Laskar J., 2008, Icarus, 196, 1
Laskar J., Gastineau M., 2009, Nature, 459, 817
Laskar J., Quinn T., Tremaine S., 1992, Icarus, 95, 148
Lecar M., Franklin F. A., 1973, Icarus, 20, 422
Lecar M., Franklin F. A., Holman M. J., Murray N. J., 2001, ARA&A, 39, 581
Levison H. F., Agnor C., 2003, AJ, 125, 2692
Levison H. F., Duncan M. J., 1993, ApJ, 406, L35
Levison H. F., Duncan M. J., 1997, Icarus, 127, 13
Levison H. F., Morbidelli A., Tsiganis K., Nesvorný D., Gomes R., 2011, AJ, 142, 152
Mamajek E. E., 2009, in Usuda T., Tamura M., Ishii M., eds, American Institute of Physics Conference Series Vol. 1158, American Institute of Physics Conference Series. pp 3–10 (arXiv:0906.5011), doi:10.1063/1.3215910
Mayor M., et al., 2011, preprint, (arXiv:1109.2497)
Mikkola S., Innanen K., 1995, MNRAS, 277, 497
Miller R. H., 1964, ApJ, 140, 250
Moons M., Morbidelli A., 1995, Icarus, 114, 33
Moons M., Morbidelli A., Migliorini F., 1998, Icarus, 135, 458
Morbidelli A., Crida A., 2007, Icarus, 191, 158
Morbidelli A., Moons M., 1993, Icarus, 102, 316
Morbidelli A., Levison H. F., Tsiganis K., Gomes R., 2005, Nature, 435, 462
Morbidelli A., Tsiganis K., Crida A., Levison H. F., Gomes R., 2007, AJ, 134, 1790
Morbidelli A., Lunine J. I., O'Brien D. P., Raymond S. N., Walsh K. J., 2012, Annual Review of Earth and Planetary Sciences, 40, 251
Morishima R., Stadel J., Moore B., 2010, Icarus, 207, 517
Murray C. D., Dermott S. F., 1999, Solar system dynamics
Murray N., Holman M., 1997, AJ, 114, 1246
Nagasawa M., Tanaka H., Ida S., 2000, AJ, 119, 1480
Nesvorný D., Morbidelli A., 1998, AJ, 116, 3029
O'Brien D. P., Morbidelli A., Levison H. F., 2006, Icarus, 184, 39
Ogihara M., Kobayashi H., Inutsuka S.-i., 2014, ApJ, 787, 172
Parker R. J., Goodwin S. P., 2012, MNRAS, 424, 272
Pfalzner S., Steinhausen M., Menten K., 2014, ApJ, 793, L34
Quinn T. R., Tremaine S., Duncan M., 1991, AJ, 101, 2287
Raymond S. N., Quinn T., Lunine J. I., 2004, Icarus, 168, 1
Raymond S. N., Quinn T., Lunine J. I., 2005a, Icarus, 177, 256
Raymond S. N., Quinn T., Lunine J. I., 2005b, ApJ, 632, 670
Raymond S. N., Quinn T., Lunine J. I., 2006a, Icarus, 183, 265
Raymond S. N., Barnes R., Kaib N. A., 2006b, ApJ, 644, 1223
Raymond S. N., O'Brien D. P., Morbidelli A., Kaib N. A., 2009, Icarus, 203, 644
Raymond S. N., Kokubo E., Morbidelli A., Morishima R., Walsh K. J., 2013, preprint, (arXiv:1312.1689)
Richardson D. C., Quinn T., Stadel J., Lake G., 2000, Icarus, 143, 45
Safronov V. S., Zvjagina E. V., 1969, Icarus, 10, 109
Saha P., Tremaine S., 1992, AJ, 104, 1633
Schneider J., Dedieu C., Le Sidaner P., Savalle R., Zolotukhin I., 2011, A&A, 532, A79
Sideris I. V., Kandrup H. E., 2002, Phys. Rev. E, 65, 066203
Stadel J. G., 2001, PhD thesis, UNIVERSITY OF WASHINGTON
Sussman G. J., Wisdom J., 1988, Science, 241, 433
Sussman G. J., Wisdom J., 1992, Science, 257, 56
Torbett M. V., 1989, AJ, 98, 1477
Torbett M. V., Smoluchowski R., 1990, Nature, 345, 49
Tsiganis K., Gomes R., Morbidelli A., Levison H. F., 2005, Nature, 435, 459

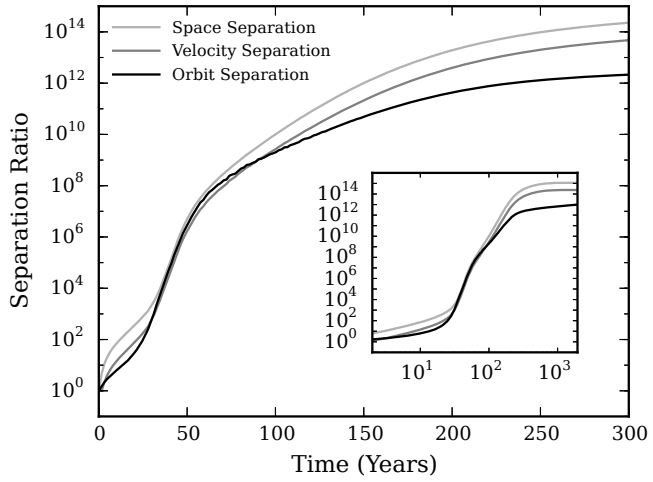

Figure A1. Geometric mean separation ratios for three different distance measures (see legend). The configuration- and velocity-space separations track particles and the orbital separation is measured by Eqn. (10). The inset covers a wider range in time. Each line is the geometric mean over 64 simulation pairs with 2048 particles each.

Valluri M., Merritt D., 2000, in Gurzadyan V. G., Ruffini R., eds, The Chaotic Universe. p. 229
Van Eylen V., Albrecht S., 2015, ApJ, 808, 126
Walsh K. J., Morbidelli A., Raymond S. N., O'Brien D. P., Mandell A. M., 2011, Nature, 475, 206
Ward W. R., 1981, Icarus, 47, 234
Weidenschilling S. J., Spaute D., Davis D. R., Marzari F., Ohtsuki K., 1997, Icarus, 128, 429
Wetherill G. W., Stewart G. R., 1989, Icarus, 77, 330
Wisdom J., 1980, AJ, 85, 1122
Wisdom J., 1982, AJ, 87, 577
Wisdom J., 1983, Icarus, 56, 51
Wisdom J., 1985, Icarus, 63, 272
Wisdom J., Holman M., 1991, AJ, 102, 1528

APPENDIX A: DISTANCES & MEANS

Neither the most appropriate distance metric nor choice of mean are immediately obvious a priori, and we have investigated a range of choices. Here, we recall (i) the behaviour of two other distance metrics, (ii) the distributions of particle separations and (iii) different means computed from this distribution.

A1 Distance Measures

In addition to the orbital distance $\langle\Delta\ell\rangle$ described in Eqn. (10) and used throughout the paper, more intuitive choices include configuration and velocity-space distances δs and δv. For each particle, these are

$$\delta s = \sqrt{(x_1-x_2)^2+(y_1-y_2)^2+(z_1-z_2)^2}, \quad \text{(A1)}$$

$$\delta v = \sqrt{(v_{x1}-v_{x2})^2+(v_{y1}-v_{y2})^2+(v_{z1}-v_{z2})^2}, \quad \text{(A2)}$$

along with the geometric means of their normalised versions

$$\langle\Delta s(t)\rangle = \left(\prod_j^{N_p}\frac{\delta s_j(t)}{\delta s_j(t=0)}\right)^{1/N_p}, \quad \text{(A3)}$$

$$\langle\Delta v(t)\rangle = \left(\prod_j^{N_p}\frac{\delta v_j(t)}{\delta v_j(t=0)}\right)^{1/N_p}, \quad \text{(A4)}$$

Fig. A1 shows our three distance measures. We clearly see initial transients in $\langle\Delta x\rangle$ and $\langle\Delta v\rangle$ which are absent in $\langle\Delta\ell\rangle$. These arise from the differential rotation. After ~ 20 years, all separation measures evolve similarly and we find initial exponential growth until $\{\langle\Delta\ell\rangle,\langle\Delta x\rangle,\langle\Delta v\rangle\}\approx 10^7$, followed by a transition to a shallower exponential. The second exponential flattens out $\{\langle\Delta\ell\rangle,\langle\Delta x\rangle,\langle\Delta v\rangle\}\approx 10^{12}$. Here, $\langle\Delta x\rangle$ and $\langle\Delta v\rangle$ transition to a linear regime, before saturating at $\langle\Delta x\rangle\approx 10^{15}$ and $\langle\Delta v\rangle\approx 10^{14}$. The geometric mean particle separation is now ~ 2.0 AU, comparable to the mean semi-major axis, and oscillates strongly on the level of individual particles. These suggest that $\langle\Delta s\rangle$ is dominated by shifts in the orbital phase. The mean velocity separation (~ 0.12 km/s) is on the order of the velocity dispersion ($\sigma\sim 0.18$ km/s) of the disk, suggesting we are seeing the disk velocity distribution instead of diverging orbits.

A2 Distance Distribution, Different Means

Figure A2 shows kernel density estimates[21] of the orbital separation $\Delta\ell$, different global measures of the distribution, as well as the evolution of $\Delta\ell$ for three representative orbits.

The separation of individual orbits changes in discrete steps, the largest corresponding to few strong interactions at small impact parameters. At each step, $\Delta\ell$ can increase or decrease, but the the net trend is always towards growing separations. Around $\Delta\ell\sim 10^8$, the growth slows down and is dominated by fewer, yet larger, jumps. The distribution of separations over all particles evolves rapidly and is consistent with an exponentially fast increase. By construction, all orbits have initial separation $\Delta\ell(t=0)=1$. They evolve towards $\Delta\ell\approx 10^{15}$ within ~ 1000 years and there is a range of ~ 4 orders of magnitude at any given time in between. The distribution appears uni-, bi-, or trimodal at different times and can change significantly on timescales as short as ~ 2 years. Evidently, we are dealing with a distribution that is difficult to characterise by a single measure, so we should compare different measures and test whether they are consistent. For comparison, we plot the evolution of (i) the geometric mean via Eqn. (11), (ii) the algebraic mean $(1/N_p)\sum_j^{N_p}\Delta\ell_j$, and (iii) the root mean squared $[(1/N_p)\sum_j^{N_p}\Delta\ell_j^2]^{1/2}$, where j is the running index over all N_p particles. In practice, we sum (multiply) over $N_p\times N_r$ obtained from N_r runs instead.

All three measures suggest initial exponential evolution followed by a transition into a power law. Only the geometric mean produces a smooth evolution and suggests the presence of two distinct exponentials. As pointed out in the main text, we caution that the second exponential is the result of averaging over a large number of particles that have few discrete, but large, jumps.

The algebraic mean and root mean square increase much

[21] Kernel density estimates are histograms with a twist. Instead of placing datapoints in discrete bins, each point is fitted by a Gaussian of width depending on the neighbouring points. The final plot is a properly normalised sum of such Gausssian.

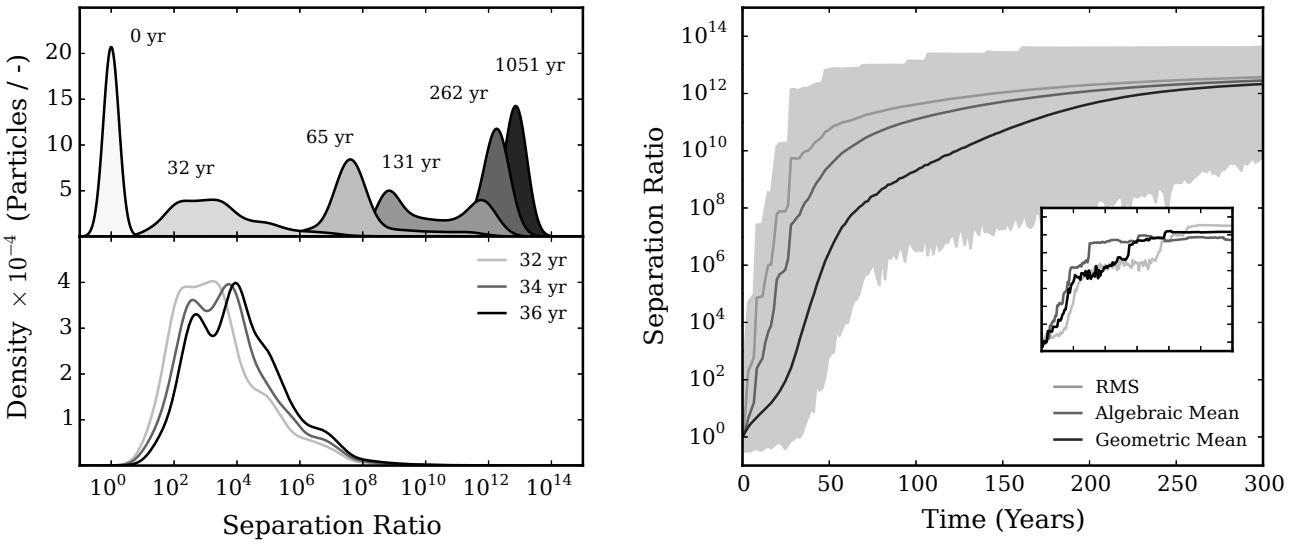

Figure A2. Distributions and means of the separation ratio $\Delta\ell$. These are computed from 64 runs with 2048 particles each. *Left:* Kernel density estimate $\mathrm{d}N/\mathrm{d}\log_{10}(\Delta\ell)$ of the orbital separation distribution over $N = 64 \times 2048$ particles at different times. Initially, all particles are at $\Delta\ell = 1$, but the kernel density estimate spreads the delta-function into a Gaussian. *Right:* Evolution of three mean measures (see legend) taken over the distribution. Grey shading indicates the full (minimum to maximum) range of $\Delta\ell$. *Right Inset:* Evolution of $\Delta\ell$ for three representative particle orbits at initial semi-major axes $a = \{0.95, 1.40, 1.96\}$ AU. Both axes are identical to the main plot.

faster than the geometric mean. Both are biased towards largest separations in the distribution (consider, e.g., $(10^2 + 10^8)/2 \approx 10^8$), which neglects the state of most orbits. The geometric mean – the algebraic mean in logarithmic space – captures the distribution much better (consider, e.g. $(10^2 \times 10^6)^{1/2} = 10^4$), and is the most appropriate choice.

APPENDIX B: GENGA VS. PKDGRAV

In Section 5 we have used PKDGRAV (Morishima et al. 2010; Stadel 2001) instead of GENGA (Grimm & Stadel 2014) despite the latter being superior in terms of accuracy, speed, and scaling. Principally, this was done to probe $N_p > 2048$ particles, which presently is a limitation in GENGA. Here, we compare the two codes in the ranges of N_p they both cover.

Figure B1 shows the separation $\langle\Delta\ell\rangle$ for sets of simulations evolved with both codes for (i) different numbers of particles, and (ii) different step sizes. For $N_p = 128$, both codes agree well, but for $N_p = 2048$, there are some differences. Most strikingly, the second exponential at $\langle\Delta\ell\rangle \geqslant 10^8$ is steeper in PKDGRAV, irrespective of the step size. Conversely, at small separations, PKDGRAV delays the growth of separations by a few years. With a smaller step size, GENGA also delays growth of the separation, so it is unclear which solution is to be trusted and considered the reference here. Increasing N_p, we expect the solutions given by the two codes decouple further. Unable to (for now) run large N_p simulations with GENGA, we must accept this limitation, but keep in mind that we (i) overestimate the steepness of the second exponential, and (ii) overestimate the time to divergence. In both cases, the difference is on the order of a few years.

Figure B2 shows the averaged energy conservation during the last 100 simulations steps for both codes and a range of step sizes and particle numbers. We find that (i) GENGA consistently conserves energy better, (ii) shorter step sizes improve energy conservation, and (iii) simulations with more particles conserve energy

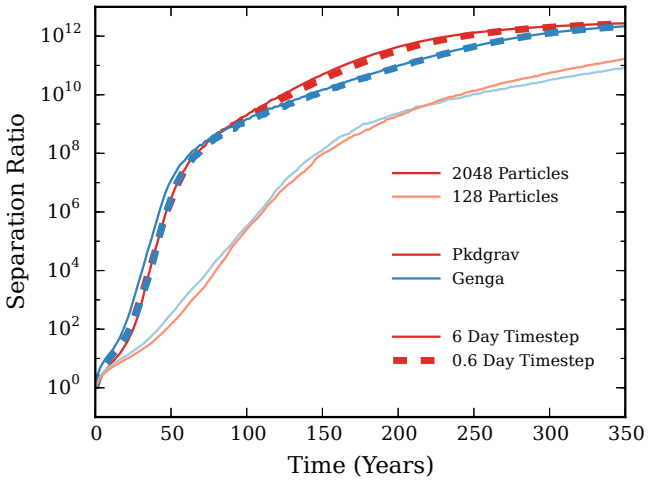

Figure B1. Geometric mean separation ratio for two different numbers of simulation particles (2048 and 128), two different timesteps (6 days, 0.6 days), and two codes (GENGA, PKDGRAV).

better. We ascribe the latter to the smoother mass distribution at larger N_p which softens the contribution of host star to the overall Hamiltonian, cf. Eqn. (3) in Grimm & Stadel (2014).

This paper has been typeset from a TEX/LATEX file prepared by the author.

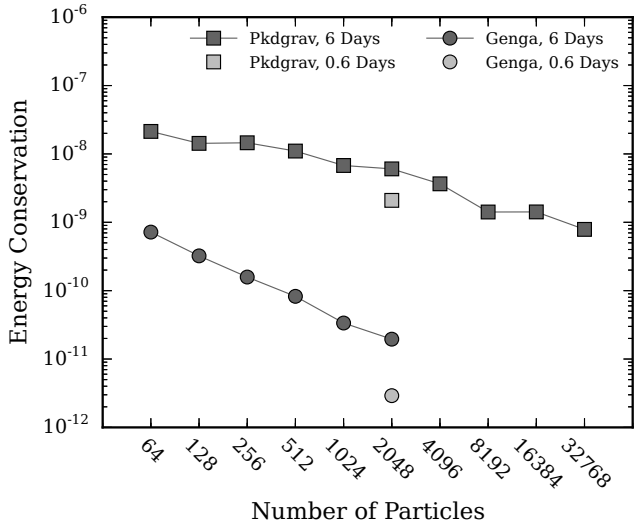

Figure B2. Conservation of total energy $\Delta E = [E(t) - E(0)]/E(0)$ for simulations with different numbers of particles, codes, and timesteps. We show the geometric of ΔE taken over the final 100 simulation steps of all N_r runs per set (number of particles).

6

Wet Terrestrial Planets: Fact or Artifact?

In this paper, we address the expected water contents of terrestrial planets that form in hypothetical extrasolar systems that do not host giant planets such as Jupiter or Saturn. We find that modelling of planetesimal growth in the presence of a gas disk (as opposed to dropping in a seeded distribution of embryos) is essential when trying to reconstruct their feeding zones, which are needed to derive their water content from an initial water distribution. Without exception, the terrestrial planets we generate host at least dozens, usually hundreds of Earth oceans, clearly not in line with systems in our Solar System. To account for this unexpected result, we attempt to quantify sources of water loss as well as the quality of our initial water distribution.

The paper is currently being prepared for submission to *Monthly Notices of the Royal Astronomical Society*. The version presented here is the most up to date draft.

MNRAS **000**, 1–19 (2015) Preprint 1 February 2016 Compiled using MNRAS LATEX style file v3.0

Wet Terrestrial Planets: Fact or Artifact?

Volker Hoffmann,[1]⋆ Joanna Drążkowska,[1] and Ben Moore[1]

[1]*Institute for Computational Science, University of Zürich, CH-8057 Zürich, Switzerland*

Accepted ..... Received .....; in original form .....

ABSTRACT

To determine the water contents around hypothetical extrasolar systems consisting of only terrestrial planets, we imprint an initial water distribution onto a disk of $N = 2000$ planetesimals and evolve a suite of simulations growing these into embryos and planets in the presence of the gas disk. We vary the lifetime of the gaseous disk and adjust the surface density profile (baseline $\Sigma \propto r^{-1}$) and mass (baseline 5 $M_\oplus$) of the initial planetesimal disk. Most formed planets are at semi-major axis $0.2 \lesssim a \lesssim 3.0$ AU, have masses $0.1 \lesssim M \lesssim 1.3$ $M_\oplus$, and host several hundreds of Terrestrial Oceans (TOs) of water. For longer gas disk lifetimes (95 per cent dispersal in 3, 5, and 15 Myr), the final terrestrial planets are less massive, closer to the host star, and host successively more water by mass. In absolute terms, they host (by median) 173, 221, and 166 TOs. Given some fixed gas disk lifetime, planetesimal disks with steeper initial surface density profiles $\Sigma \propto r^{-1.5}$ generate planets that are less massive and drier by mass (hosting, by median, 105 TOs). Massive disks (10 $M_\oplus$) build the most massive planets with the largest water fractions, corresponding to 211 TOs (by median). High-resolution ($N = 8192$) runs of the reference profile ($\Sigma \propto r^{-1}$, 5 $M_\oplus$) generate lower mass planets at depressed water mass fractions, suggesting lack of numerical convergence. However, other indicators (such as the distribution of feeding zones) do appear to be converged. Derived water contents are upper limits and collision geometries suggest that significant melt in giant impacts can remove ~ 40 per cent of the water (dozens of TOs), whereas surface water and atmospheric stripping from impacts or stellar winds only removes a few TOs.

We also quantify the impact of modelling differences with respect to simulations initialised with a number of embryos embedded in a planetesimal disk after gas dispersal. Our comparison indicates that starting simulations from seeded embryos biases their feeding zones to their neighbourhood, whereas growing planetesimals in gas disk shows the final planets to derive their composition from material originating over wide range of semi-major axes. For any initial water distribution, this has consequences for the final water contents.

Given the uncertainties in initial water distribution, N-Body modelling, avenues for water loss, and differences to observations (Venus, Earth, Mars), it remains unclear whether the large observed water fractions are indicative of reality or merely represent a modelling artifact. We therefore caution against proclaiming an expectation of a large number of 'water-worlds'.

Key words: planets and satellites: formation – planets and satellites: terrestrial planets – planets and satellites: oceans planets and satellites: dynamical evolution and stability – methods: numerical – celestial mechanics.

1 INTRODUCTION

The rocky terrestrial planets form by accretion of smaller bodies called planetesimals. Planetsimals are believed to form quickly (Johansen et al. 2007) and thus should be composed of the material present at a corresponding location in the protoplanetary disk. This means that planetesimals in the inner regions of the disk are dry, because water is not available in the solid state closer than a few AU to the central star (Trigo-Rodríguez & Martín-Torres 2013). However, the water mass fraction of the Earth is of the order of 10^{-3}, higher than predicted by protoplanetary disk models and higher than other bodies further away from the Sun, such as the E-type asteroids at 1.8 AU which water mass fraction is of the order of 10^{-4} (Marty 2012; Morbidelli et al. 2012). Water had to be delivered to the Earth from the outer part of the disk during the final accretion of our planet. Indeed, studies of the isotopic composition reveal that the water on Earth comes mostly from the water-rich asteroids that were located in the outer ateroid belt and only a small part of the Earth's water comes from comets (Morbidelli et al. 2000; Cleeves et al. 2014).

⋆ E-mail: volker@physik.uzh.ch

The water delivery to the Earth is connected to the influence of the giant planets in the state-of-the-art models (Raymond et al. 2009; O'Brien et al. 2014). The most notable influence of giant planets is the excitation of planetary embryos that leads to higher impact velocities and speeds up the accretion. At the same time, the giant planet in the vicinity of the ice line scatters the water-rich bodies close to it and previous simulations found that a large fraction of these bodies is scattered outwards and removed from the Solar System (Raymond et al. 2006). Thus, giant planets restrict the water delivery to the inner planets, preventing them from becoming water world. This may seem to be bad for life, but it would not help either if the Earth had too much water (Kitzmann et al. 2015).

It is believed that the presence of Jupiter and Saturn prevented accretion of another terrestrial planet in the asteroid belt region as it had been dynamically excited. On the other hand, gravitational perturbations of Jupiter caused ejection of majority of the asteroids, while sending some of them towards the Earth and enabling water delivery. Martin & Livio (2013) suggest that this setup of strongly depleted asteroid belt and Jupiter might have been necessary for emergence of life on Earth.

It is known that a typical extrasolar planetary system does not look like the Solar System (Fang & Margot 2012). Not every planetary system has to form giant planets. Can Earth-type planets with relatively high water content still exist in the habitable zone of the systems that had not formed giant planets? Is water delivery still possible in such systems and is the water content right on the Earth analogs? What are the dominant factors that regulate delivery of material from the outer to the inner part of protoplanetary disk? We attepmt to answer these question with a suite of N-body simulations of terrestrial planet accretion that do and do not include giant planets.

.....

In attempts to reproduce the architectural and chemical constraints of our Solar System, classical simulations of terrestrial planet formation (Chambers & Wetherill 1998; Chambers 2001; Raymond et al. 2004) are initialised with a population of embryos and planetesimals with masses and surface density profiles scaled to the Minimum Mass Solar Nebula (Hayashi 1981; Weidenschilling 1977) in the inner region. This is very similar to the intial conditions we used in this paper, except that we generate a population of planetesimals embedded in a gas disk instead of considering the embryos already grown and the gas dissipated. By imprinting an initial water mass fraction (WMF) and tracking collisions, the final state of such runs can then be used to determine whether the water distribution among the terrestrial planets matches observational constraints. Although such classical models of planetesimal disk evolving in the presence of static giant planets have largely been superceded by truncated disks (Morishima et al. 2008; Hansen 2009) and migrating giant planets (Walsh et al. 2011; O'Brien et al. 2014) in the context of Solar System formation,[1] we can still use them as a baseline comparison to illustrate the importance of self-consistent growth of planetesimals to embryos.

This paper is organized as follows. In Section 2, we describe our numerical methods, initial conditions, simulation runs, and post-processing methods. In Section 3, we illustrate the differences that arise in the source regions and final water contents of the terrestrial planets depending on whether we grow embryos from planetesimals embedded in gas disk or start from a seed population of embryos and planetesimals in the absence of gas. We show difference for a Solar System type configuration with giant planets before moving on to systems without giant planets. In Section 4, we present results from our ensemble of simulations runs for different gas disk lifetimes, planetesimal disk masses, density profiles, and mass resolutions. In Section 5, we discuss disk dynamics, source regions, final water mass fractions, and attempt to put bounds on the amount of water that can be lost from planets over the course of the simulation.

[1] More recently, Surville et al. (2016) showed that sheared out vortices can generate rings of dust. If this dust can grow into planetesimals, this may be another avenue of generating an initially annular planetesimal distribution.

2 METHODS, INITIAL CONDITIONS, SIMULATIONS

2.1 GENGA

To follow the orbital and collisional evolution of planetesimal, embryos, and planets, we use the hybrid symplectic integrator GENGA (Grimm & Stadel 2014). The code is similar to MERCURY (Chambers 1999), but runs exclusively on NVIDIA Graphics Processing Units (GPUs). The scheme evolves particles along their Keplerian orbits and treats the gravitational interactions from other particles as perturbations. By using democratic coordinates (heliocentric positions, barycentric velocities) (Duncan et al. 1998), the code can separate out close encounters and integrate them with a direct integrator up to machine precision. Outside of close encounters, GENGA uses a symplectic integrator. Forces between particles are computed directly. Although this scales as $\mathcal{O}(N^2)$ for N particles, the calculation can be done efficently on GPUs. By avoiding tree-based methods, this hybrid symplectic scheme has excellent energy conservation over large numbers of orbits. Finally, GENGA incorporates the same analytical gas disk model as the patched version of PKDGRAV used in Morishima et al. (2010), and is available online.[2]

2.2 Initial Conditions, Gas Disk

We generate initial conditions (ICs) by drawing a number of samples (planetesimals of equal mass) from an underlying distribution of orbital elements. This generates a realisation of a planetesimal swarm following some prescribed surface density profile $M_{\rm Disk}(r)$ and total mass $M_{\rm Disk}$. In particular, we draw samples such that surface density at heliocentric distance r is

$$\Sigma_{\rm Disk}(r) = \begin{cases} \Sigma_{\rm Disk,0} \left(\frac{r}{1\,\mathrm{AU}}\right)^{-p} & 0.5\ \mathrm{AU} \leqslant r \leqslant 4\ \mathrm{AU}, \\ 0 & \text{otherwise.} \end{cases} \quad (1)$$

Drawing $N_{\rm P}$ samples (planetesimals) of mass $m_{\rm P}$ each, this integrates to total disk mass of

$$M_{\rm Disk} = 2\pi \int_{0.5}^{4} \Sigma(r)\, r\, \mathrm{d}r = m_{\rm P} N_{\rm P} \quad (2)$$

In this paper, we generate of initial conditions various combinations drawn from the sets $p = \{1, 1.5\}$, $M_{\rm Disk} = \{5 M_{\rm Earth}, 10 M_{\rm Earth}\}$ and $N_{\rm P} = \{2000, 4000, 8192\}$. For more details, see Section 2.3. All planetesimals we initialise are on nearly circular ($e < 0.02$), low-inclination ($i < 0.75^\circ$) orbits.

We embed planetesimals in gas disk described by an anlytical

[2] https://bitbucket.org/sigrimm/genga

Table 1. Initial conditions for our simulations. Empty cells take the value of the row above. The EJS runs contain Jupiter and Saturn on eccentric orbits, viz. (a_J, e_J, i_J) = (5.2 AU, 0.048, 1.30 Degree) and (a_S, e_S, i_S) = (9.55 AU, 0.056, 2.49 Degree) with their angular arguments initialised to zero.

Set	Giants [a]	τ_{Gas} (Myr) [b]	Σ_{Disk} [c]	$\Sigma_{Disk,0}$ (g/cm^2) [d]	M_{Disk} (M_{Earth}) [e]	N_P [f]	M_{Disk}/N_P (M_{Moon}) [g]	N_{Runs} [h]
NJS/Gas00	(No Giants)	(No Gas)	$\propto r^{-1}$	6.1	5	2000	0.2	12
NJS/Gas01		1						
NJS/Gas03		3						
NJS/Gas05		5						
NJS/Steep		1	$\propto r^{-1.5}$	8.2				
NJS/Heavy			$\propto r^{-1}$	12.4	10	4000	0.2	
NJS/HiRes				6.1	5	8192	0.05	
EJS/Steep/Gas00	EJS	(No Gas)	$\propto r^{-1.5}$	8.2	5	2000	0.2	
EJS/Steep/Gas01		1						

[a] Giant Planet Configuration. [b] Gas Disk E-Folding Time. [c] Surface Density Profile. [d] Surface Density at 1 AU. [e] Total Solid Disk Mass. [f] Number of Particles. [g] Mass Resolution. [h] Number of Independent Runs.

model. The gas surface density follows a power-law and decays exponentially in time, i.e.

$$\Sigma_{Gas}(r,t) = \Sigma_{Gas,0}\left(\frac{r}{1\,\mathrm{AU}}\right)^{-1}\exp\left(-\frac{t}{\tau}\right), \quad (3)$$

where τ_G is a decay timescale of the gas disk, r the heliocentric distance, t the simulation time, and $\Sigma_{Gas,0} = 2000$ g/cm^2. We only consider gas in the range $0.1 < r < 36.0$ AU. In this work, we draw the gas disk e-folding time from the set $\tau_G = \{1, 3, 5\}$ Myr$\}$. Some simulations host no gas. For example, using $\tau_{Gas} = 1$ Myr, 99 per cent of the gas has dissipated by ~ 4.6 Myr.

Particles exchange angular momentum with the gas through (i) hydrodynamic drag due to differences in velocity, (ii) torques arising from spiral density waves launched by massive particles, and (iii) gravitational interactions between particles and the massive disk. We also artificially enhance hydrodynamic drag for particles with masses $< 0.01\ M_\oplus$ to correct for the large initial planetesimal mass. For more details, see Morishima et al. (2010).

2.3 Simulations

To determine the potential architecture of (as well as water content and feeding zones of terrestrial planets in) extrasolar systems that do not host giant planets, we perform a non-exhaustive[3] sweep of the parameter space spanned by the slope of the planetesimal disk surface density p, the total disk mass M_{Disk}, and the gas disk e-folding time τ_{Gas}. To serve as reference, we draw an ensemble of $N_P = 2000$ planetesimals following $\Sigma(r) \propto r^{-1}$ with total mass $M_{Disk} = 5\ M_{Earth}$, and evolve the resulting planetesimal disk in gas disk with $\tau_G = 1$ Myr. This run is labelled NJS/GAS01, although we also refer to it as "1 Myr Disk" or simply "Reference Run" in the text. We then evolve the same planetesimal distribution, but vary the lifetime of the gas disk (GAS03, GAS05). For one set, we omit the gas and evolve the planetesimals in isolation (GAS00). To test the effects of the initial planetesimal surface density distribution and total mass, we generate initial conditions where $\Sigma(r) \propto r^{-1.5}$ (NJS/STEEP) and $M_{Disk} = 10\ M_{Earth}$ (NJS/HEAVY), both evolved in gas disk with $\tau_G = 1$ Myr e-folding time. Note that we hold the massive disk at constant mass resolution, i.e. they run at double the number of simulation particles. We also re-generate and re-run the reference planetesimal disk with 8192 particles (the limit in GENGA) to check for numerical convergence. Finally, to facility comparisons with the literature, we also evolve our NJS/STEEP planetesimal disks in the presence of Jupiter and Saturn on their present-day eccentric orbits; without and with gas (EJS/GAS00, EJS/GAS00). All simulations are summarised in Table 1.

To account for the stochastic nature of the terrestrial planet formation process (Hoffmann et al. 2015), we evolve each initial conditions twelve times, making for a total of 108 runs. Computing time can vary substantially, depending on how fast the number of simulation particles decreases. Most runs require on the order of four to five weeks on NVIDIA Tesla K80 cards. The high resolution runs require eight to nine weeks on the same hardware. We evolve all runs for ~ 147.84 Myr (9×10^9 steps, $\Delta t = 6$ days) and treat all collisions as inelastic mergers. Particles are removed from the simulation if their heliocentric distance falls below 0.2 AU or exceeds 20 AU. The relative energy error remains $\Delta E/E_0 \leqslant XXX$ at all times. All outputs, initial conditions, and parameter files are available online.[4]

2.4 Post-Processing

2.4.1 *Water Mass Fraction*

The simplest way to assign an initial water mass fraction (WMF) to a given planetesimal population is to impose their present-day values. Based on WMF measurements of carbonaceous, ordinary, and enstatite chondrites summarised in Abe et al. (2000), Raymond et al. (2004) constructed an initial WMF distribution increasing with semi-major axis a in a stepwise fashion, viz.

$$\mathrm{WMF}_{01}(a) = \begin{cases} 10^{-5} & a < 2\ \mathrm{AU}, \\ 10^{-3} & 2\ \mathrm{AU} < a < 2.5\ \mathrm{AU}, \\ 0.05 & a > 2.5\ \mathrm{AU}. \end{cases} \quad (4)$$

This formulation has since been used to adress various aspects

[3] In other words, we do not check all possible combinations of parameters.

[4] https://cheleb.net/astro/water15.

of water delivery into the inner Solar System (Raymond et al. 2006, 2007, 2009), which we will use as a baseline in Section 3.1.

To assign initial water mass fractions to cometary material, Mandell et al. (2007) extended this stepwise description to include a WMF of 50 per cent at $a > 5$ AU. Noting that a deficit of short lived radioisotopes (SLRs, for example ^{26}Al) in extrasolar systems can lead to planetesimals retaining larger amounts of water, Ciesla et al. (2015) modified this description to include a reservoir of wet planetesimals beyond 2.7 AU. The corresponding initial distribution then becomes

$$\mathrm{WMF}_{02}(a) = \begin{cases} 10^{-5} & r < 2 \text{ AU}, \\ 10^{-3} & 2 \text{ AU} < r < 2.5 \text{ AU}, \\ 0.05 & 2.5 \text{ AU} < r < 2.7 \text{ AU}, \\ 0.5 & r > 2.7 \text{ AU}. \end{cases} \tag{5}$$

This distribution is also adopted in Ronco & de Elía (2014), which we use as a comparison baseline in Section 3.2.

In this work, we primarily use Equation (5) to set the initial water mass fraction of planetesimals. As would any other, this choice of initial distribution depends on a particular set of assumptions regarding the chemical state of the disk during planetesimal formation, the timescale of planetesimal formation, as well as the chemical evolution of the planetesimals with regards to how well they retain water. We adress these in the latter part of Section 5.2.

2.4.2 Giant Impacts: Impact Energy & Melt Fraction

In Section 5, we attempt to put bounds on the amount of water lost during giant impacts. In such events, water can be removed if the impact energy is large enough to gravitationally unbind atmosheric water. Further losses occur if energies are large enough to evaporate surface water as well as melt a significant fraction of hydrated rocky material. Quantifying the water loss then amounts to computing the specific impact energy as well as the melt fraction during a collision, which we do as follows.

Specific Impact Energy – Without applying any corrections, the specific impact energy Q for an impactor of mass m_{Impactor} hitting a target of mass m_{Target} with a velocity of v_{Impact} is

$$Q = \frac{\mu v_{\mathrm{Impact}}^2}{2(m_{\mathrm{Impactor}} + m_{\mathrm{Target}})}, \tag{6}$$

where $\mu = \left(m_{\mathrm{Impactor}} m_{\mathrm{Target}}\right) / \left(m_{\mathrm{Impactor}} + m_{\mathrm{Target}}\right)$ is the reduced mass of the system. Applying the geometric corrections outlined in Leinhardt & Stewart (2012), we obtain

$$Q' = \frac{\mu_\alpha}{\mu} Q, \tag{7}$$

where Q is as above and μ_α is the reduced mass corrected to consider the area of overlap between target and impactor during the collision. Using hydrodynamic corrections from (Lock+ 2015), we obtain the form of the specific impact energy we use, viz.

$$Q_{\mathrm{S}} = Q' \left(1 + \frac{m_{\mathrm{Impactor}}}{m_{\mathrm{Target}}}\right) (1 - b), \tag{8}$$

where b is the impact parameter. For an illustrated description of the corrections, we refer to Quintana et al. (2015).

Melt Fraction – Assuming perfect sticking, the volume fraction of the post-collision body that has undergone melting is simply the ratio of the melt volume to the total volume of the two bodies, i.e.

$$f_{\mathrm{Melt}} = \frac{V_{\mathrm{Melt}}}{V_{\mathrm{Total}}} = \frac{V_{\mathrm{Melt}}}{m_{\mathrm{Impactor}}/\rho_{\mathrm{Impactor}} + m_{\mathrm{Target}}/\rho_{\mathrm{Target}}}, \tag{9}$$

where m and ρ are the masses and mass densities of impactor and targets. We obtain the melt volume from Abramov et al. (2012) who have synthesized SPH collision simulations and previous work on scaling laws to yield an updated scaling for the melt volume, viz.

$$V_{\mathrm{Melt}} = 0.22\, E_{\mathrm{M}}^{-0.85} \frac{\rho_{\mathrm{Impactor}}}{\rho_{\mathrm{Target}}} D_{\mathrm{Target}}^3 v_{\mathrm{Impact}}^{1.7} \sin^{1.3}\theta, \tag{10}$$

where E_{M} is the specific internal energy of melting, D_{Impactor} the impactor diameter, v_{Impact} the impact velocity, and θ the impact angle (related to the impact parameter as $b = \sin\theta$). For all bodies, we assume $\rho = 2.0$ g/cm^3 and $E_{\mathrm{M}} = 7 \times 10^6$ J/kg (halfway between values for Granite and Basalt, cf. Table 1 in Abramov et al. (2012)).

3 IMPORTANCE OF GAS, FULLY INTERACTING PLANETESIMALS, AND GROWING EMBRYOS

To expedite time to solution, terrestrial planet formation simulations frequently embed planetary embryos in a field of planetesimals instead of growing them self-consistently. This initial growth phase also corresponds to the phase during which the interactions of planetesimals with gas are most relevant. As such, the modelling of the gas disk is usually bypassed as well. To further speed up the computation, gravitational interactions between planetesimals are also frequently ignored and only their aggregate effect on the embryos (and vice versa) is computed.

While system architectures resulting from such simplified simulations tend to be consistent with more complete simulations, their inferred planetary compositions are mismatched due to a lack of radial planetesimal mixing prior to assembly of the first embryos.

In this section, we take an illustrative approach to demonstrate to importance of self-consistent growth of embryos from planetesimals embedded in a gas disk. We place emphasis on the inferred water mass fraction (WMF) derived by tracking the collisional history. We consider cases for planetesimal disks in the presence and absence of giant planets, mimicking previous work: (i) Raymond et al. (2009) for runs including Jupiter and Saturn, and (ii) Ronco & de Elía (2014) for isolated disks.

3.1 Giants

Before moving on to hypothetical extrasolar systems, let us first illustrate the differences between modelling planetesimal growth in a gas disk and injecting embryos and planetesimals after gas dissipation for a Solar System like configuration. We proceed in two steps. First, we evolve two runs. In the first run, planetesimals are initially embedded in gas disk and grow from there. In the second run, we use the same initial planetesimal distribution, but do not include gas. This means that they grow into embryos locally, thereby mimicking more traditional simulations. In both cases, we imprint the initial WMF from Eqn. (4) and track collisions to derive the final water mass fraction of the terrestrial planets. Second, we compare our runs to four runs of a simulation previously published in Raymond et al. (2009), which has an experimental setup similar to

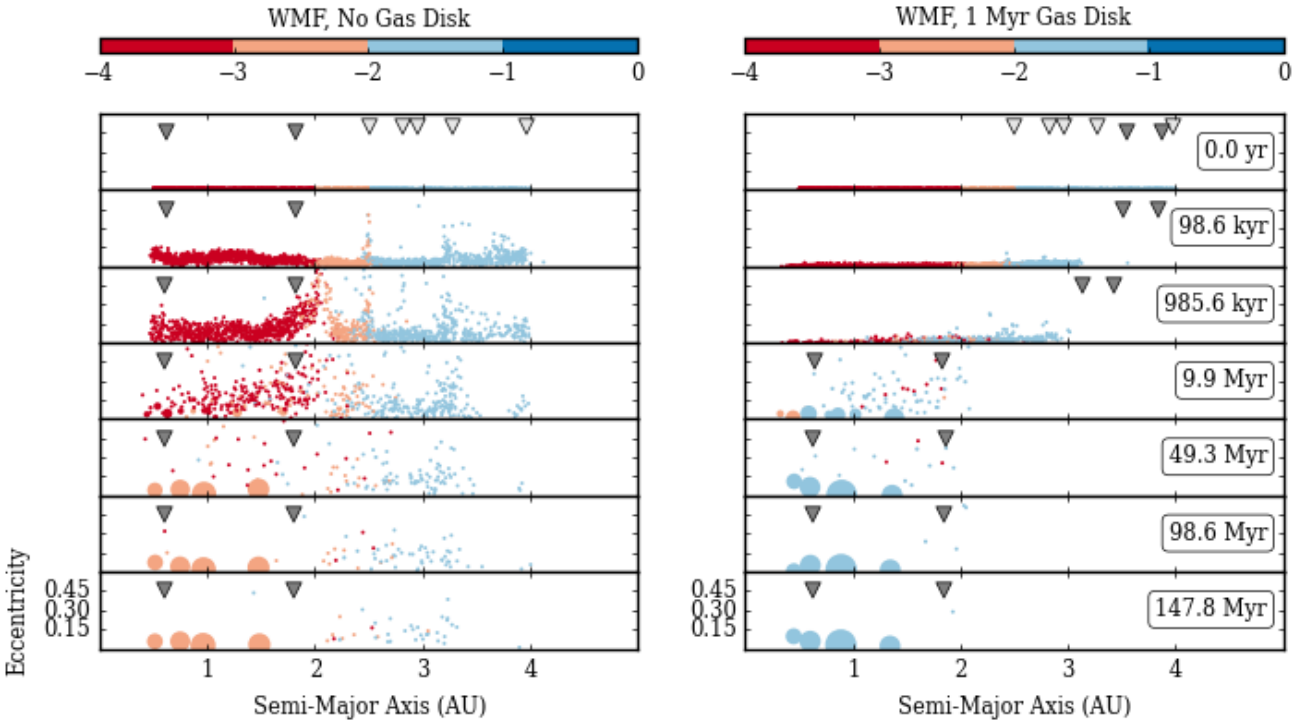

Figure 1. Time slices (from top to bottom, see annotations) of semi-major axis vs eccentricity of planetesimals (circles) for two different simulation runs of an planetesimal disk. Gas giants are included. Larger circles indicate more massive objects. The shading indicates the water mass fraction (WMF) of the object at a given time, computed via Eqn. (4). Light grey triangles indicate the location of (from left to right) 3:1, 5:2, 7:3, 2:1, and 3:2 mean motion resonances with Jupiter. These remain (almost) stationary across panels, so we only show them once. Dark grey triangles indicate the location of the ν_5 (left) and ν_6 (right) secular resonances with the Jupiter-Saturn system. These sweep inwards as the gas dissipates, so we indicate their location in every panel. *Left*: The planetesimals disk evolves in complete isolation. The location of all resonances is fixed. *Right*: The planetesmals are embedded in a gas disk. The location of the secular resonances sweeps inwards as the gas dissipates.

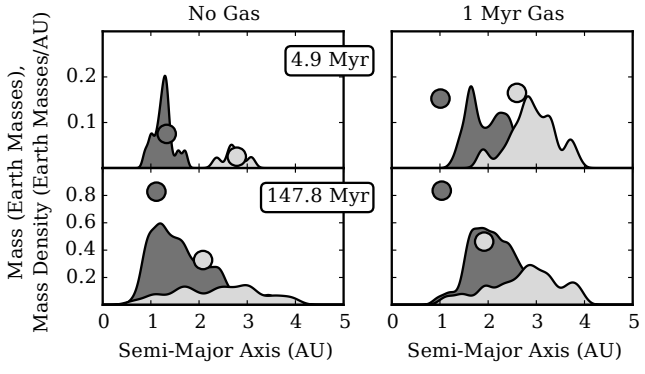

Figure 2. Distribution of source material for two planets at two time slices (rows). We show semi-major axis and mass of the planets. For the sources, we show the distribution of mass with semi-major axis $\mathrm{d}M/\mathrm{d}a$. Details are tabulated in Table 2. *Left:* Planets formed from a planetesimal disk in the presence of gas giants. *Right:* Planets formed from planetesimals embedded in a gas disk, and in the presence of gas giants.

ours. We also link to more recent simulations that more explicitly include feeding zones.

Table 2. Semi-major axis, mass, water mass fraction, and source distribution for four planets. Two evolved in the presence of a gas disk, two evolved from an isolated planetesimal disk. Gas giants were included in the simulations. For a visual representation, see Figure 2.

Run	a_{Planet} [a,e]	M_{Planet} [b,f]	$\mathrm{WMF}_{\mathrm{Planet}}$ [c]	$a_{\mathrm{Src,10/50/90}}$ [d,e]
NoGas	0.96	0.92	1.31×10^{-3}	0.76/1.20/2.03
Gas	0.89	1.19	2.46×10^{-2}	1.58/2.47/3.67
NoGas	1.49	0.80	3.26×10^{-3}	1.06/1.56/2.27
Gas	1.34	0.75	2.56×10^{-2}	1.69/2.57/3.70

[a] Planet Semi-Major Axis. [b] Planet Mass. [c] Planet Water Mass Fraction.
[d] Source Semi-Major Axes – 10/50/90 Percentiles.
[e] In AU. [f] In Earth Masses.

3.1.1 *Growth from Planetesimals: Gas Disk vs. No Gas Disk*

Figure 1 shows the water mass fraction for two runs chosen from the sets EJS/STEEP/GAS00 (no gas disk) and EJS/STEEP/GAS01 (gas disk with $\tau_{\mathrm{G}} = 1$ Myr) in Table 1. We also select two representative particles at the final snapshot, tabulate their properties in Table 2 and show their source mass distribution in Figure 2. Comparing the runs and particles, we find the following.

(i) Planets grown in a gas disk are substantially wetter than planets grown in isolated disks. At $a < 1.5$, the median WMF is 1.94×10^{-3}, increasing to 2.21×10^{-2} for disks with gas – more than an order of magnitude increase. Beyond $a > 1.5$, the me-

dian WMF also increases by as much from 1.8×10^{-3} (no gas) to 2.78×10^{-2} (gas).

(ii) The two representative particles follow the same trend. At both $a \sim 1$ AU and $a \sim 1.5$ AU, the WMFs for runs with gas are more than an order of magnitude larger than for runs without gas.

(iii) The width of the source regions are significantly wider for runs including gas. At $a \sim 1$ AU, 80 per cent of the mass is delivered from an annulus 1.27 AU (2.09 AU) wide for runs without (with) gas. At $a \sim 1.5$ AU, mass is sourced from 1.21 AU (2.01 AU) annuli for disks without (with) gas.

(iv) The shapes of the source mass distribution also differ significantly, especially at early times. In disks without gas, initial growth is heavily localised. In disks with gas, substantial amounts of material have already been delivered from the outer disk at ~ 5 Myr. At the end of the simulations, runs without gas have also experienced mixing, but are still biased to their initial location. The source mass distribution in runs without gas does not change significantly after the first few Myr.

(v) In either case, we retain between 3 and 4 terrestrial planets. In runs without gas, we also find 34 surviving planetesimals, whereas no planetesimals remain at the end of the run that includes a gas disk. planetesimals in gas runs.

There are four dynamical effects that drive the radial migration and therefore the mixing of material from different semi-major axis: (i) hydrodynamic drag, (ii) secular resonances with the Jupiter-Saturn system, (iii) mean motion resonances with Jupiter, and (iv) gravitational interaction with the gravitational potential of the gas (Type I migration). Migration of planetesimal sized bodies is mostly driven by hydrodynamic drag whereas embryo and planet sized bodies are driven by their Type I migration. Secular and mean motion resonances can affect bodies of any size, but are more effective in influencing planetesimals than embryos.

In simulations without gas disks, neither hydrodynamic drag nor Type I migration can contribute to the radial mixing of material, and the position of secular resonances is fixed in space. We find the disk segmented into an inner and outer part, with the effective (although not impermeable) boundary demarcated by the ν_5 resonance at 1.85 AU. Planetesimals grow into embryos on either side of the boundary (inheriting the local water mass fraction) with the occasional delivery of material from the outer to the inner regions by planetesimals that find themselves sufficientlty excited at either of the resonances. Within the first 4.9 Myr, almost no material is delivered onto the embryos from further out, but over the course of 147.8 AU, there appear to be enough such stochastic deliveries to account for at least ~ 50 per cent of the final mass budget of the planet. This type of evolution matches the picture of stochastic delivery of water championed in Morbidelli et al. (2000)

Once we include interactions with a gaseous disk, a much wider range of dynamics opens up. Beyond hydrodynamic drag for small planetesimals and Type I migration for embryos, secular resonances sweep through the disk (Nagasawa et al. 2000), which drives substantial amounts of material inwards (Morishima et al. 2010; Hoffmann et al. 2015). Even after the first 4.9 Myr, over 90 per cent of the material making up the embryos originates from beyond their present semi-major axis. Clearly, modelling gas dynamics during the growth phase of planetesimals is extremely important to correctly reconstruct source regions.

3.1.2 *Implanted Embryos: No Gas Disk*

We now perform a cursory comparison with previous simulations that employed similar initial conditions. In particular, we compare to the runs marked EJS15 in Raymond et al. (2009), but note that these (i) neglect gas, (ii) implant embryos directly, and (iii) do not compute gravitational interactions between planetesimals. To be consistent, we have adopted their initial WMF above.

(i) Within the region $0.75 < a < 1.25$ AU, Raymond et al. (2009) report a mean[5] WMF of 2.38×10^{-4}. For disks without (with) gas, we find median WMFs of 2.0×10^{-3} (2.5×10^{-2}) in our runs – one (two) orders of magnitude larger.

(ii) The final number of planets we obtained in runs with and without gas disks is comparable to those found in Raymond et al. (2009). For planetesimals, no data is available.

The mismatch in water mass fraction between our runs without gas and the EJS15 runs in Raymond et al. (2009) is somewhat puzzling. After initial growth of embryos in our runs, both sets should behave identically, yet we consistently obtain WMFs an order of magnitude larger. Without access to the dynamical and collisional history of their runs, we can only venture two speculative guesses as to the origins of this difference: (i) through biasing the source regions by distributing the initial embryos in a fashion inconsistent with collisional growth from planetesimals, and/or (ii) depressing the eccentricity of the planetesimals swarm by not resolving their mutual gravitational interactions. Let us explain.

First, comparing Figure 2 in Raymond et al. (2009) to our Figure A1 in Appendix A, it appears that the natural growth (faster growth in the inner disk) of embryos is at odds with their assumed initial distribution (which puts more massive embryos in the outer disk). In effect, this traps (by local accretion) wet material in the outer disk and relies on stochastic giant impacts to deliver water to the inner disk. Unfortunately, launching outer-disk projectiles onto crossing orbits (by transfer of angular momentum from the giant planets at resonances) can also launch them onto orbits that remove them from the simulation (either by accretion onto the star, collision with a giant, or launch onto hyperbolic trajectory). Therefore, implanting (unrealistically) massive embryos in the outer disk artifically reduces the efficiency of delivery to the inner system.

Secondly, repeated two-body encounters between pairs of planetesimals raises the mean orbital eccentricity of the entir epopulation (viscous stirring), which potentially delivers more planetesimals onto orbits crossing into the inner system. By omitting the calculations of their mutual gravitational interaction, fewer planetesimals can deliver water rich material from the outer system inwards, thereby depressing the final WMF.[6]

Given all of the above, it should be clear that self-consistent growth of planets through collisions of fully-interacting planetesimals in the presence of a gaseous disk is essential to reconstruct the source regions for terrestrial planets.

[5] See the entries for the EJS15-$\{1 \ldots 4\}$ runs in their Table 2. We use the mean instead of the median because only 4 samples are reported.

[6] An additional, secondary, effect of omitting the interactions between planetesimals is a change in how excitement by dynamical friction propagates through the disk. Normally, a massive planet would excite planetesimals, which would excite other planetesimals through two-body encounters. Lacking planetesimal-planetesimal interaction, the efficiency of how dynamical friction excites the planetesimal disk is limited to only the direct interaction with the massive embryos.

Table 3. Semi-major axis, mass, water mass fraction, and source distribution for four planets. Two evolved in the presence of a gas disk, two evolved from an isolated planetesimal disk. No gas giants were included. For a visual representation, see Figure 4.

Run	$a_{\rm Planet}$ [a,e]	$M_{\rm Planet}$ [b,f]	$\rm WMF_{Planet}$ [c]	$a_{\rm Src,10/50/90}$ [d,e]
NoGas	1.12	0.83	0.042	0.92/1.55/2.54
Gas	1.04	0.84	0.116	1.57/2.16/3.21
NoGas	2.08	0.33	0.195	1.11/2.41/3.59
Gas	1.92	0.46	0.299	1.62/2.82/3.71

[a] Planet Semi-Major Axis. [b] Planet Mass. [c] Planet Water Mass Fraction.
[d] Source Semi-Major Axes – 10/50/90 Percentiles.
[e] In AU. [f] In Earth Masses.

3.2 No Gas Giants

We now make the jump to hypothetical extrasolar systems by considering the growth of embryos from planetesimals in the absence of giant planets. We proceed as before by evolving an identical initial distribution of planetesimals in the presence and absence of a gaseous disk. Again, we follow this up by comparing to similar work done in the literature (Ronco & de Elía 2014) to argue for the importance of growing embryos instead of seeding them. To make a consistent comparison, we imprint an initial water mass fraction identical to theirs, i.e. we use Eqn. (5) instead of Eqn. (4).

3.2.1 Growth from Planetesimals: Gas Disk vs. No Gas Disk

Figure 3 shows the water mass fraction for two runs chosen from the sets NJS/GAS00(no gas disk) and NJS/GAS01 (gas disk, $\tau_{\rm G} = 1$ Myr) in Table 1. As before, we select two representative particles from each run. We tabulate their properties in Table 3 and show their source mass distribution in Figure 4. Based on these, we find the following trends.

(i) Runs with a gas disk produce wetter planets than runs without a gas disk. For $a < 1.5$, the median WMF for planets[7] is 0.044 (no gas) and 0.069 (gas); an 56 per cent increase. For $1.5 < a < 2.5$, the median WMF increases by 86 per cent from 0.121 (no gas) to 0.225 (gas). For $a > 2.5$, the increase is 24 per cent; from 0.278 (no gas) to 0.344.

(ii) The two representative particles follow the same trends (planets grown in a gas disk are wetter). At $a \sim 1$ AU, their WMFs differ by 176 per cent. At $a \sim 2$ AU, their WMFs still differ, but only at the 56 per cent level.

(iii) The width of the source regions exhibits inconclusive trends. For planets at $a \sim 1$ AU, 80 per cent of the mass comes from an annulus 1.62 AU wide in runs without gas. It is only marginally wider (1.64 AU) if gas is considered. At $a \sim 2$ AU, the trend reverses. Here, the feeding zones are 2.47 AU (no gas) and 2.09 AU (gas) wide.

(iv) More important are the shapes of the source distributions and how they evolve in time. After 5 Myr (when embryos have assembled and gas – if present – dissipated), the distributions are heavily localized in runs without gas, but already draw in significant amounts of material from the outer disk in runs with gas. At the end of the simulations (147.8 Myr), this is washed out (by late impacts from plantesimal originating in the outer disk) for both planets, yet remains particulary strongly imprinted in the distribution for planets at $a \sim 1$ AU.

(v) Simulations without gas retain almost twice as many primordial planetesimals, but host comparable numbers of planets. On average, we find only 176 remaining planetesimals in runs with gas, but 337 in runs without gas. Both host, on average, about 11 planets, although runs with gas host significanly (72 per cent) more massive planets (median masses are 0.18 vs. 0.32 $M_{\rm Earth}$).

Lacking giant planets, the dynamical evolution of planetesimals in simulations with a gas disk is driven only by hydrodynamic drag (for planetesimals), Type I migration (for embryos), and mutual gravitational interactions. Absent a gaseous disk, only gravitational interactions remain. In this sense, the driving dynamics are much easier to discern than in the case where mean motion and sweeping secular resonances affect the system.

For planetesimal-sized objects, hydrodynamic drag drives loss of orbital angular momentum. This causes the planetesimal orbits to decay, delivering them to the inner regions of the disk, where collisional growth proceeds rapidly. The same process also delivers unlucky planetesimals onto the star. Loosing planetesimals to the star and growing them into more massive planets faster thus depletes their population more effectively in the case with gas. Planetesimal disks without gas have no mechanism (beyond excitation from viscous stirring and – once embryos have grown – dynamical friction) to efficiently deliver planetesimals to the inner regions. This significantly extends growth timescales.

3.2.2 Implanted Embryos: No Gas Disk

Recently, Ronco & de Elía (2014) also characterised water delivery in extrasolar systems of terrestrial planets that do not host giant planets. They evolved isolated planetesimal disks with surface density profiles similar to ours, but (i) implant embryos directly, (ii) neglect gas, (iii) ignore gravitational interactions between planetesimals, and (iv) extends their initial disk to 5 AU. Comparing their runs to ours, we note the following.

(i) Within their habitable zone[8] ($q > 0.8$, $Q < 1.5$ AU), Ronco & de Elía (2014) report (for their $\gamma = 1$ simulations, see their Table 2) mean[9] WMFs of 0.047. Our runs without gas have a comparable median value (0.052), whereas runs with gas have a median about twice that (0.117). Note that they also report one planet at significantly higher water mass fraction (0.09), but the timing of the last giant impact suggests a single stochastic event has delivered most of the water.

(ii) Within the region $q > 0.8$ and $Q < 1.5$ AU, our runs with and without gas have almost identical median planetary masses (0.65 vs 0.58 $M_{\rm Earth}$). This is almost twice the mean mass (0.36 $M_{\rm Earth}$) found by Ronco & de Elía (2014), despite their 56 per cent more massive initial disk (7.92 $M_{\rm Earth}$).

It appears as though simulations that implant embryos, neglect the gas disk, and omit gravitational interactions between planetesimals, have severely stunted radial transport of mass. The absence of hydrodynamic drag and the gravitational potential of the gas precludes planetesimals and embryos from migrating, whereas the lack

[7] We discard planetesimals below the cutoff mass in the analysis.

[8] We do not adopt a habitable zone in this paper. The concept adds too much dependence on the mass and age of the star as well as the mass and atmosphere of the formed planets, which detracts from our key points.
[9] We compute the mean as their distribution of three planets is ill-described by the median.

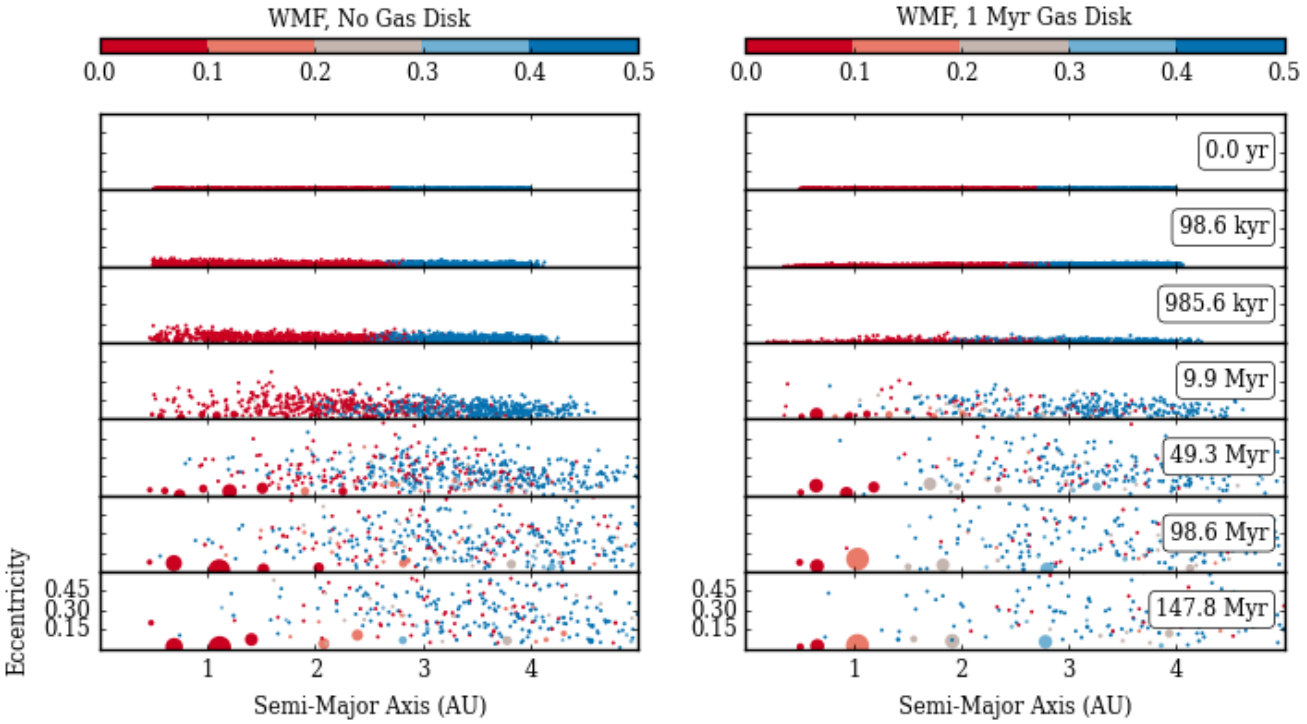

Figure 3. Time slices (from top to bottom, see annotations) of semi-major axis vs eccentricity of planetesimals for two different simulation runs of an planetesimal disk. No giant planets are included. Larger markers indicate more massive objects. The shading indicates the water mass fraction (WMF) of the object at a given time, computed via Eqn. (5). *Left*: The planetesimals disk evolves in complete isolation. *Right*: The planetesmals are embedded in a gas disk.

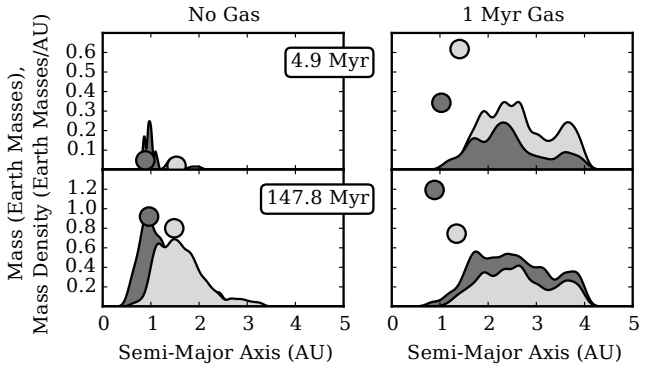

Figure 4. Distribution of source material for two planets at two time slices (rows). We show semi-major axis and mass of the planets. For the sources, we show the distribution of mass with semi-major axis $\mathrm{d}M/\mathrm{d}a$. Details are tabulated in Table 3. *Left:* Planets formed from a isolated planetesimal disk. *Right:* Planets formed from planetesimals embedded in a gas disk.

of gravitational interactions between planetesimals dampens their ability to reach crossing orbits in the same manner as described in Section 3.1.2. As such, the final terrestrial planets end up less massive and their source regions biased to the seed location of the embryos they are grown from.

The strongest effect of the inward drift is the delivery of material even before embryos form. Once they do, they already contain material from the outer regions of the disk. Therefore, the common practice of manually implaning embryos in a field of planetesimals requires reconsideration of what their initial source mass distribution (and, as a consequence, their initial WMF) should be. As a quick fix, we propose adopting initial WMFs for embryos implanted at $a < 2.5$ AU that are a factor of two larger than the field planetesimals at the same location.

A more elaborate fix derives the initial distribution and WMF of embryos and planetesimals from semi-analytic models (Brunini & Benvenuto 2008; Guilera et al. 2010; de Elía et al. 2013). Recently, Ronco et al. (2015) compared simulations of initial conditions generated from such models to traditional approaches. They conclude that the system architectures are weakly only affected, but that the compositional differences are significant. However, mean final planetary masses differ by 7 per cent only. This reinforces the notion that neglecting viscous stirring leads us to underestimate the final masses.

4 RESULTS: GAS DISKS & INITIAL PROFILES

We now describe the result of our sets of simulations. In the first part, we focus on the case where we varied (or removed entirely) the decay timescale of the gas disk. In the second part, we focus on runs where we varied the initial profile, total mass, and mass resolution of the planetesimal distribution.

4.1 Gas Disk Lifetimes

In turn, we adress the final dynamical state of the generated systems, the origin of the material making up the final planets, and – as an illustrative application to this – the water mass fraction of the final planets. We restrict our analysis to the time at which the sim-

ulations terminate (147.84 Myr). For each τ_G (as well as the case without gas), we evolved twelve runs.

4.1.1 *System Architecture & Dynamical State*

Figure 5 and Table 4 summarise the final architectures and dynamical properties of our simulations. Additionally, Figure 6 shows (top panel), the mass-distribution with semi-major axis. Focussing on the masses, number, and level of dynamical excitement (eccentricity and inclination) of both planets and planetesimals, we observe the following.

(i) Runs without gas assemble the most massive planets. The most massive planets is 1.04 $M_{\rm Earth}$, although 90 per cent of planets have masses below 0.72 $M_{\rm Earth}$. Adding a gas disk with increasing longer lifetime systematically decreases the most massive planet that assembled in the simulations. In particular, for $\tau_G = 1$, 3, and 5 Myr, the most massive planets is 0.84, 0.44, and 0.24 $M_{\rm Earth}$.

(ii) For runs without gas and runs with short ($\tau_G = 1$ Myr) gas decay times, the most massive planets are constrained in the region $a < 3$ AU (with the largest fraction at $a < 2$ AU), but there is a tail of small planets out to 6 AU. For longer gas-disk lifetimes, this tail moves inwards and the mass-distribution flattens outs because the surviving planets in the inner regions are less massive.

(iii) Despite the strong influence on the mass of the final planets, the presence and lifetime of the gas disk affects the number of planets weakly. For all disks, the inner regions $a < 2$ AU host four to six planets. In the outermost regions $a \geqslant 4$ AU, the differences are larger, with 6 planets in simulations without gas, and successively fewer planets as the gas disk lives longer.

(iv) Considering gas and successively increasing its lifetime decreases the total mass remaining in both planets and planetesimals. Without gas, the mean total mass in planets is 3.39 $M_{\rm Earth}$. This drops to (by) 3.29 (5 per cent), 1.5 (55 per cent), and 0.83 $M_{\rm Earth}$ (76 per cent) for $\tau_G = 1$, 3, and 5 Myr. In the same vein, the mass locked up in the remaining planetesimals decreases from 1.60 to (by) 0.91 (43 per cent), 0.4 (75 per cent), and 0.31 $M_{\rm Earth}$ (81 per cent), respectively. In all runs, most planetesimals ($\gtrsim 70$ per cent) end up at semi-major axis $a > 3$ AU.

(v) Across the board, planetesimals are dynamically hotter than planets with both eccentricities and inclinations higher by factors of about four. For planets, the presence and successively longer lifetimes of the gas disk dampens eccentricities by about 20 per cent each time (NoGas $\rightarrow \tau_G = 1$, $\tau_G = 1 \rightarrow \tau_G = 3$ Myr, ...). For planetesimals, introducing a gas disk affects median eccentricities only at the per cent level, but increasing τ_G successively decreases the median eccentricity by 30 per cent. The same holds for the inclinations.

4.1.2 *Feeding Zones*

We now consider the feeding zones[10] of the planets as well as the final location of the surviving planetesimals. Figure 7 shows the initial distribution for the material making up planets in a given

[10] Usually, *feeding zone* refers to the initial spatial distribution of material making up a given planet. We generalise this concept by considering the initial distribution of material making up all planets in a particular semi-major axis range. We determine the zones by following the merger tree of planets back in time to the initial conditions.

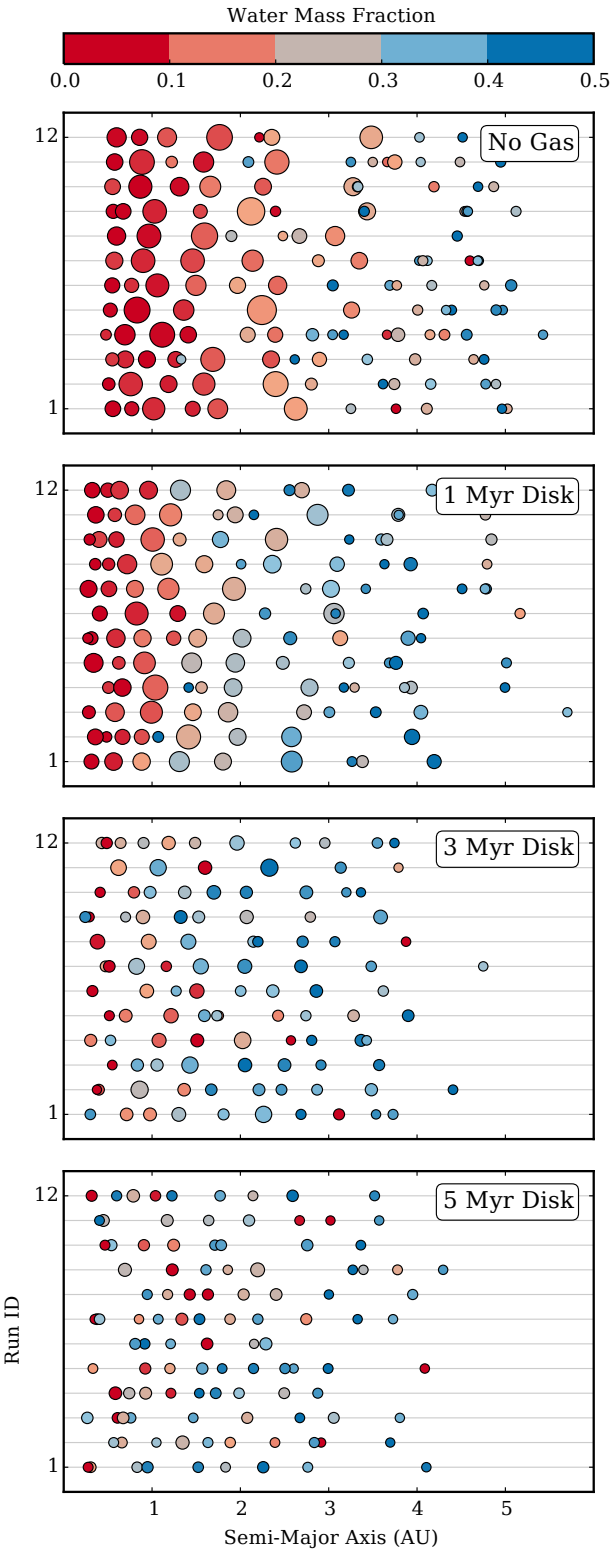

Figure 5. System architectures for runs performed with varying gas disk decay timescale after after 147.84 MYr. From top to bottom, no gas disk present, $\tau_G = 1$ Myr, $\tau_G = 3$ Myr, and $\tau_G = 5$ Myr. We show only planets (i.e., not the surviving planetesimals). The colouring indicates the water mass fraction of the objects.

Table 4. Summary of relevant statistics for four simulations after 147.84 Myr: (i) runs containing no gas, and (ii-iv) runs with gas disk e-folding times of 1, 3, and 5 Myr. For water mass fraction and source material statistics, we only consider the final planets (remaining planetesimals are ignored).

Range	Run	$M_{P,50}$ [a]	$M_{P,90}$ [a]	WMF_{50} [b]	WMF_{90} [b]	$a_{Src,10}$ [c]	$a_{Src,50}$ [c]	$a_{Src,90}$ [c]	N_P/N_R [d]	N_{Ps}/N_R [e]
(All)	No Gas	0.20	0.76	0.166	0.398	0.76	1.79	3.25	11	323
	1 Myr Disk	0.29	0.63	0.228	0.439	1.26	2.31	3.52	11	166
	3 Myr Disk	0.14	0.31	0.384	0.440	2.21	3.15	3.84	9	58
	5 Myr Disk	0.09	0.17	0.416	0.470	2.38	3.31	3.88	9	36
$a < 1$	No Gas	0.40	0.77	0.041	0.075	0.56	0.99	2.59	2	2
	1 Myr Disk	0.37	0.55	0.036	0.104	1.07	1.61	2.74	3	1
	3 Myr Disk	0.14	0.32	0.335	0.386	2.02	3.00	3.76	3	0
	5 Myr Disk	0.11	0.17	0.401	0.452	2.27	3.23	3.87	3	1
$1 \leqslant a < 2$	No Gas	0.59	0.81	0.081	0.142	0.95	1.70	3.03	2	16
	1 Myr Disk	0.47	0.74	0.208	0.312	1.66	2.42	3.50	2	11
	3 Myr Disk	0.22	0.33	0.365	0.423	2.21	3.11	3.83	2	4
	5 Myr Disk	0.10	0.17	0.415	0.459	2.37	3.30	3.87	3	2
$2 \leqslant a < 3$	No Gas	0.33	0.83	0.170	0.323	1.26	2.21	3.42	2	50
	1 Myr Disk	0.33	0.63	0.299	0.420	1.91	2.82	3.69	1	29
	3 Myr Disk	0.13	0.31	0.409	0.446	2.37	3.27	3.87	2	10
	5 Myr Disk	0.09	0.15	0.428	0.473	2.46	3.39	3.90	2	7
$a \geqslant 3$	No Gas	0.06	0.28	0.278	0.454	1.49	2.62	3.65	5	255
	1 Myr Disk	0.10	0.29	0.367	0.468	2.12	3.01	3.77	4	126
	3 Myr Disk	0.09	0.17	0.404	0.475	2.40	3.33	3.90	2	44
	5 Myr Disk	0.04	0.07	0.467	0.488	2.63	3.41	3.89	1	26

[a] Mass of Final Planets (Earth Masses) – 50/90 Percentiles.
[b] Water Mass Fraction of Final Planets – 50/90 Percentiles.
[c] Source Mass Origin (Semi-Major Axes, AU) – 10/50/90 Percentiles.
[d] Average Number of Planets (Total Planets / Number of Runs).
[e] Average Number of Remaining Planetesimals (Total Planetesimals / Number of Runs).

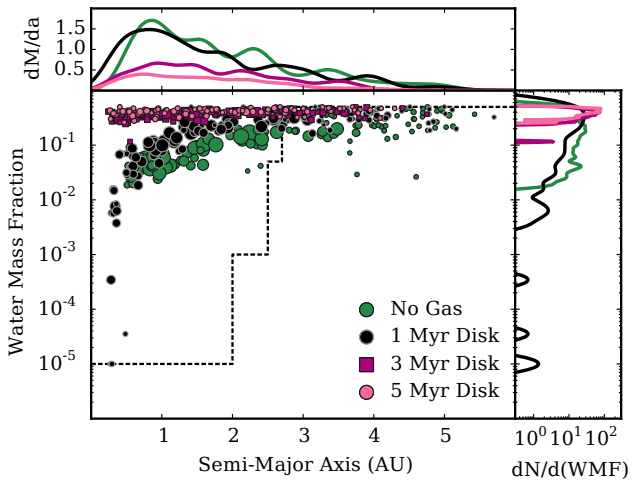

Figure 6. Distribution of water mass fraction (WMF) with semi-major axis for (i) runs without gas, (ii) and three runs with successively longer gas disk lifetimes (see legend). We stack all six runs per set and show the state at the end of the simulations (147.84 Myr). The main panel shows a scatterplot and the side/top panels the marginal distributions. The dashed line indicates the initial WMF, cf. Eqn. (5). *Top:* Marginal distribution dM/da of mass with semi-major axis in units of Earth Masses/AU. *Right:* Marginal distribution of the number of particles per WMF, $dN/d(WMF)$. Note that the marginal distributions integrate to the average mass (number of particles) over all twelve runs.

semi-major axis range. Figure 8 shows the initial and final semi-major axis of surviving planetesimals as well as the mass-weighted distribution at the end of the simulations. We find the following.

(i) In runs without gas, the feeding zones are largely local. In the inner regions, 55 ($a < 1$ AU) and 51 per cent ($1 \leqslant a < 2$ AU) originate in the same range of semi-major axes. For the outer regions, most material actually originates interior to the final semi-major axis bin. For example, in the $2 \leqslant a < 3$ AU bin, 37 per cent of the material is local, 40 per cent comes from $a \leqslant 2$ AU, and only 22 per cent from $a > 3$ AU. At $a > 3$ AU, 61 per cent of material comes from the interior $a \leqslant 3$ AU.

(ii) The presence and longevity of a gas disk pushes the feeding zones outwards. For example, in runs where $\tau_G = 1$ Myr, only 5 (25) per cent of material making up planets in the $a < 1$ AU ($1 \leqslant a < 2$ AU) bin is local, but 69 (48) per cent comes from the next larger semi-major axis bin ($1 \leqslant a < 2$ AU, $2 \leqslant a < 3$ AU, respectively). Increasing τ_G pushes the feeding zone further outwards. For $\tau_G = 3$ Myr, 51 per cent of planetary material at $a < 1$ AU originates at $a > 3$ AU. For $\tau_G = 5$ Myr, the fraction increases to 62 per cent.

(iii) Irrespective of presence and dissipation time of the gas, the majority of surviving planetesimals ends up at larger semi-major axes than where they started. For runs without gas, this holds for 75 per cent of planetesimals. In simulations with gas, this fraction decreases as the gas disk dissipates slower. For $\tau_G = 1$, 3, and 5 AU, 69, 64, and 55 per cent of planetesimals end up outward of their initial location. The final distribution of planetesimals is reminiscient (especiall for $\tau_G = 1$ Myw and runs with gas) of a Gaussian centered at $a \sim 4$ AU. This suggests a diffusion process.

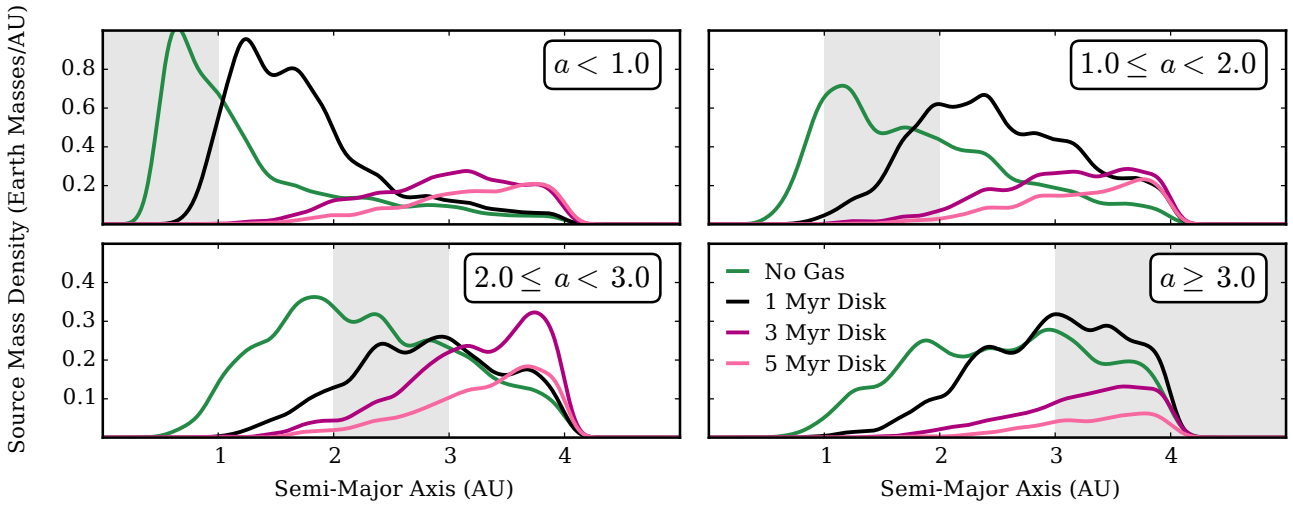

Figure 7. Distributions of source material (dM/da) for four simulations (no gas, and $\tau_G = 1$, 3, and 5 Myr gas disks; see legend) and four target regions (panels, indcated by the shaded area). For example, the top left panel shows the initial distribution of origin material for planets with semi-major axis $a < 1$ AU, the top right the source distributions for all planets at $1 \leqslant a < 2$ AU, and so on. Each distribution integrates to the average number of initial particles per run.

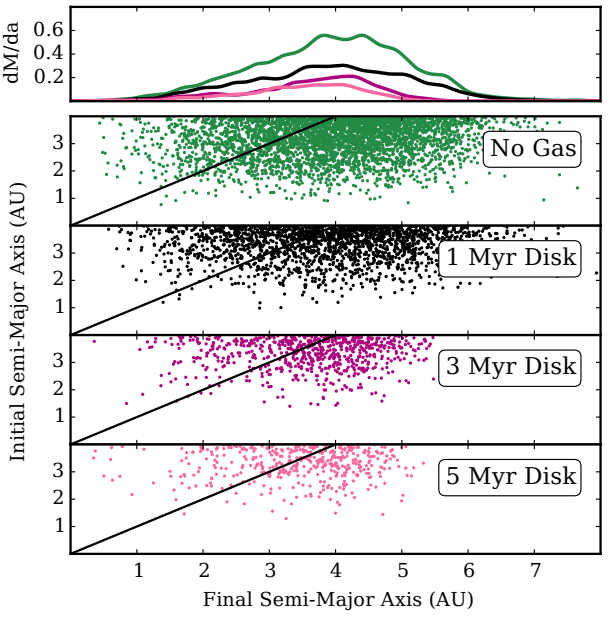

Figure 8. *Bottom Four*: Initial and final semi-major axis for all surviving planetesimals in (from second top to bottom, see labels) simulations (i) without gas, and (ii)-(iv) four different gas disk lifetimes. Data taken at the end of simulations; 147.84 Myr. Planetesimals to the right (left) of the diagonal black lines end up at larger (smaller) semi-major axes than they start out. *Top*: Mass distributions with semi-major axis (dM/da; units of Earth Masses per AU) of surviving planetesimals, integrating to the (average) total mass remaining in planetesimals per run.

4.1.3 Water Mass Fraction

We use the source distribution described above to determine the water mass fraction (WMF) of the final planets, but caution that these results have a number of important biases. These are addressed in Section 5. Figure 6 shows a scatterplot of WMF with semi-major axis as well as marginal distribution of the number of particles at a given WMF. Our observations are as follows.

(i) Except for two outliers, the smallest observed WMF is $> 5 \times 10^{-3}$, irrespective of semi-major axis of the object and lifetime of the gas disk.

(ii) In order, simulations without gas, and simulations with increasing longer gas disk lifetimes produce, by median, planets with larger WMF. Similarly, planets at larger semi-major axis tend to be wetter than planets in the inner regions. The trends are most pronounced in simulations without gas and short-lived gas disks. For $\tau_G = 3$ and $\tau_G = 5$ Myr runs, there is – on average across runs – little variation in the WMF throughout the disk. However, if we compare individual runs within one set, there can be substantial variations in the WMF. For example, while Run 03 in the $\tau_G = 3$ Myr cases produces almost uniformly wet ($WMF \sim 0.3$ to 0.5) planets, Run 06 in the same set intersperses wet and dryer planets.

(iii) Especially for the inner regions ($a < 2.7$ AU), the initial signature (dashed line in Figure 6) of the WMF is rapidly lost as planets build up. In simulations without gas and with short-lived ($\tau_G = 1$ Myr) gas disks, planets > 2.7 AU are 30 to 40 per cent dryer than the planetesimals initially placed at this location. For $\tau_G = 3$ and 5 Myr, planets is this region are also dryer, but only at the 10 to 15 per cent level. In these cases, the trend towards a uniform WMF throughout the disk is the most remarkable feature.

(iv) For all simulations including gas ($\tau_G = 1, 3, 5$ Myr), 90 per cent of the surviving planetesimals have WMF > 0.1. This is irrespective of their final location. For $a < 2.7$ AU, their WMF is also consistently in excess of the initial WMF at this location. For runs without gas and $a > 2.0$ AU, we record water mass fractions below the corresponding initial value at their location for ~ 20 per cent of planetesimals.

4.2 Initial Profiles

4.2.1 System Architecture & Dynamical State

(i) Unsurprisingly, simulations with more massive disks also generate the most massive final planets. In these runs, the most massive planet is 1.34 $M_{\rm Earth}$. Here, 90 per cent of planets are less massive than 0.89 $M_{\rm Earth}$, which is 41 per cent above the 90 percentile mass of the reference disk. Simulations with steep profiles generate the least massive planets. Here, the most massive planet is 0.66 $M_{\rm Earth}$ with only 10 per cent of planets more massive than 0.53; 16 per cent percent below the 90 percentile mass of the reference run.

(ii) Again, the most massive planets are constrained to the inner regions $a < 3$ AU with peak masses at $2 \leqslant a < 3$ AU. Across simulations, the mass distributions appear similar. There is no flattening as in the case of simulations with longer gas disk lifetimes. (Compared to the reference, steep initial profiles do not appear to deliver more massive planets to the inner $a < 1$AU regions (as we may reference like we might naively expect).

(iii) However, steeper initial profiles do tend to deliver more planets to the inner region, driving up the total mass in the region when compared to the reference. Considering the entire disk, steep profiles and the reference profile from comparable number of planets. Initially more massive disks form more planets, especially at large semi-major axis $a > 3$ AU. There is considerable spread across individual runs though. For example, compare RUN02 and RUN05 in the NJS/HEAVY set.

(iv) Mirroring the trend of planetary masses, disks with steeper profiles and more initial mass retain less, respectively more total mass in planets (2.79 $M_{\rm Earth}$, 4.93 $M_{\rm Earth}$, i.e. -15 per cent, $+51$ per cent) and planetesimals (0.69 $M_{\rm Earth}$, 1.41 $M_{\rm Earth}$, i.e. -24 per cent, $+55$ per cent) than the reference runs (3.27 $M_{\rm Earth}$ in planets, 0.91 $M_{\rm Earth}$ in planetesimals). Over 75 per cent of planetesimals are located at $a > 3$ AU when the simulations terminate, irrespective of initial conditions.

(v) In all simulations, planetesimals are dynamically more excited than planets. For both planets and planetesimals, steeper profiles marginally lower median eccentricites (11 and 8 per cent, respectively), while more massive initial disks boost median eccentricities significantly (58 and 23 per cent). Inclinations follow the same trends.

(vi) (...HiRes...)

4.2.2 Feeding Zones

(i) The feeding zones of planets generated from steep profiles are similar to those in the reference simulations. This holds especially for $a < 1$ AU, where the majority (75 and 69 per cent, for NJS/STEEP and NJS/GAS01, respectively) of the material originates at $1 \leqslant a < 2$ AU. There is a weak overall trend for source material to originate closer to the final location in simulations with steep initial profiles. For example, planets at $1 \leqslant a < 2$ AU are sourced to 73 per cent from material between 1 and 3 AU in reference runs. This increases to 85 per cent in for steep profiles.

(ii) Initially massive disks tend to source more mass in the outer regions than the steep or reference disks. For instance, only 35 per cent of the material for planets at $a < 1$ AU originates between 1 and 2 AU (down from 69 per cent in the reference runs), while 64 per cent originate $a > 2$ AU. The trend continues for planets found beyond $a > 2$ AU.

(iii) As before, more than 60 per cent of surviving planetesimals end up exterior to their initial location. For steep initial profiles,

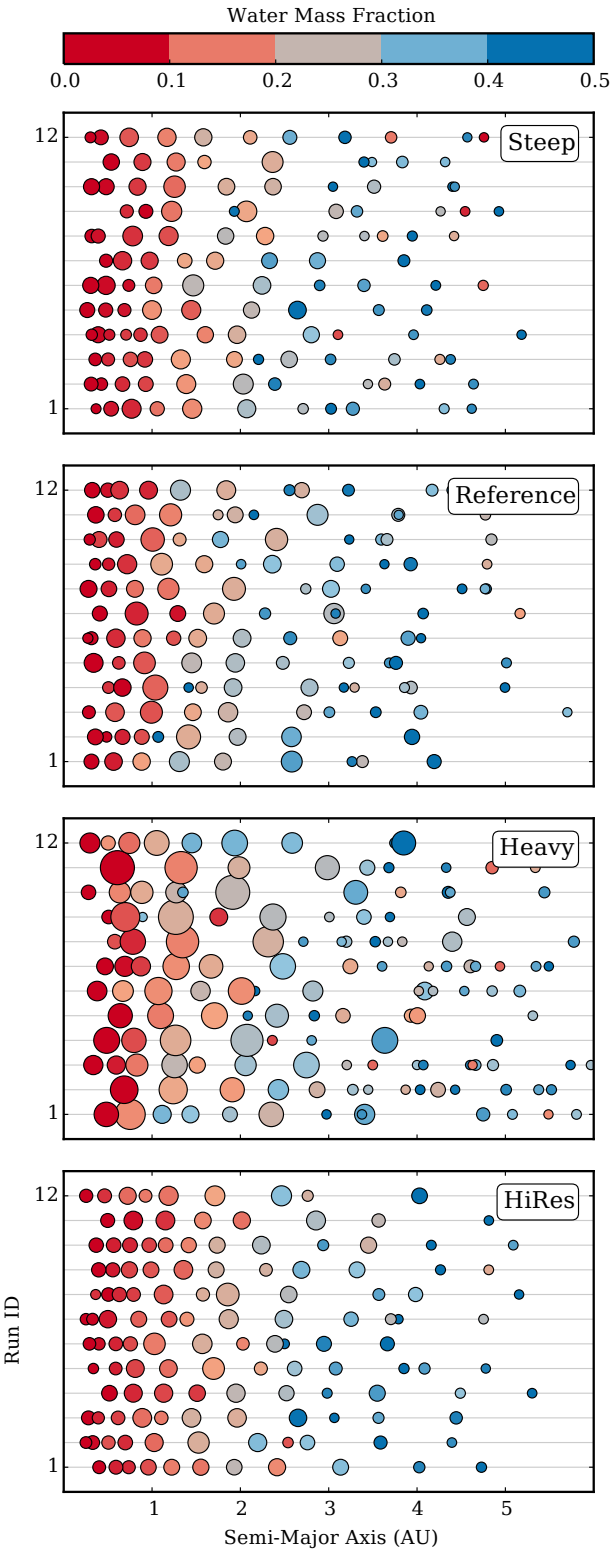

Figure 9. System architecture for simulations performed with varying initial planetesimal disk profile shown at 147.84 MYr. From top to bottom, the reference disk with surface density $\Sigma \propto r^{-1}$, a steep initial profile with surface density $\Sigma \propto r^{-1.5}$, and a disk twice as massive (10 $M_{\rm Earth}$). We show all planets, but none of the surviving planetesimals. The size and colour of the circles correspond to mass and water mass fraction.

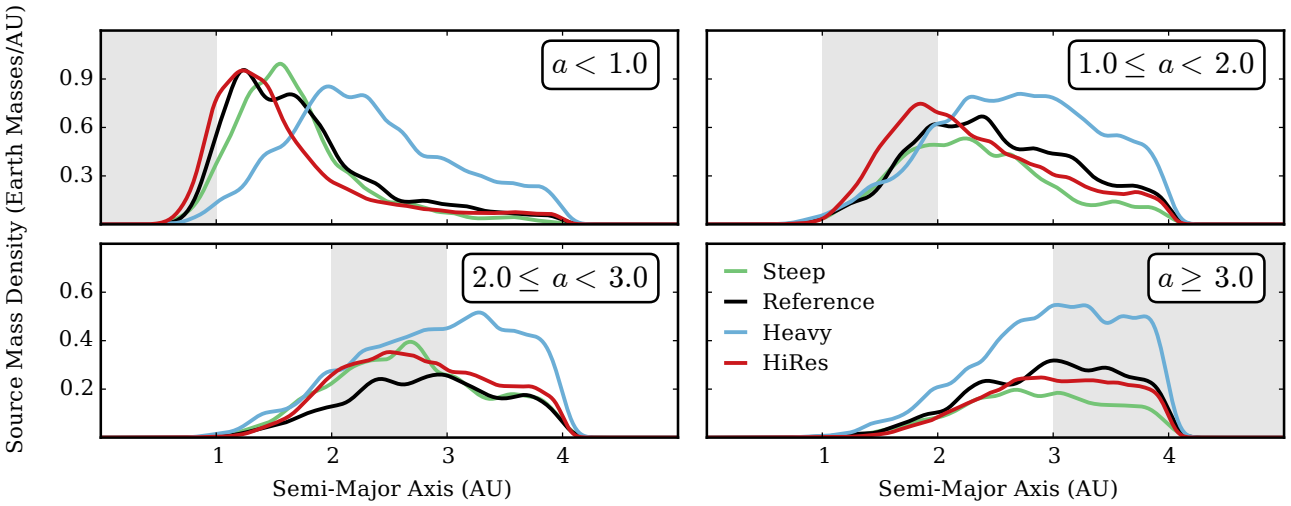

Figure 10. Distribution of source material for three simulations (reference, steep, and heavy disk; see legend) and four target regions (panels, shaded). For example, the top left panel shows the initial distribution of origin material for planets with semi-major axis $a < 1$ AU, the top right the source distributions for all planets at $1 \leqslant a < 2$ AU, and so on.

Table 5. Summary of key statistics for three simulations after 147.84 Myr for the reference, steep, and heavy disks. For water mass fraction and source material, we compute statistics over embryos and planets only.

Range	Run	$M_{P,50}$ [a]	$M_{P,90}$ [a]	WMF_{50} [b]	WMF_{90} [b]	$a_{Src,10}$ [c]	$a_{Src,50}$ [c]	$a_{Src,90}$ [c]	N_P/N_R [d]	N_{Ps}/N_R [e]
(All)	Steep	0.25	0.53	0.161	0.394	1.30	2.15	3.36	10	136
	Reference	0.29	0.63	0.228	0.439	1.26	2.31	3.52	11	166
	Heavy	0.24	0.89	0.317	0.435	1.71	2.70	3.69	13	238
	HiRes	0.29	0.51	0.151	0.390	1.20	2.19	3.51	11	612
$a < 1$	Steep	0.31	0.50	0.017	0.066	1.11	1.59	2.44	3	1
	Reference	0.37	0.55	0.036	0.104	1.07	1.61	2.74	3	1
	Heavy	0.63	1.00	0.156	0.209	1.45	2.26	3.40	2	1
	HiRes	0.27	0.45	0.045	0.087	0.97	1.42	2.66	4	4
$1 \leqslant a < 2$	Steep	0.44	0.58	0.127	0.210	1.54	2.27	3.29	2	8
	Reference	0.47	0.74	0.208	0.312	1.66	2.42	3.50	2	11
	Heavy	0.83	1.21	0.265	0.314	1.76	2.70	3.65	2	10
	HiRes	0.49	0.65	0.139	0.210	1.50	2.20	3.38	3	35
$2 \leqslant a < 3$	Steep	0.39	0.58	0.235	0.365	1.81	2.65	3.61	2	24
	Reference	0.33	0.63	0.299	0.420	1.91	2.82	3.69	1	29
	Heavy	0.61	0.92	0.336	0.473	1.92	2.93	3.76	2	25
	HiRes	0.34	0.48	0.267	0.380	1.92	2.71	3.67	2	100
$a \geqslant 3$	Steep	0.07	0.19	0.331	0.465	1.99	2.83	3.72	4	104
	Reference	0.10	0.29	0.367	0.468	2.12	3.01	3.77	4	126
	Heavy	0.06	0.34	0.358	0.450	2.09	3.05	3.80	7	202
	HiRes	0.12	0.37	0.370	0.465	2.18	3.02	3.77	3	473

[a] Mass of Final Planets (Earth Masses) – 50/90 Percentiles.
[b] Water Mass Fraction of Final Planets – 50/90 Percentiles.
[c] Source Mass Origin (Semi-Major Axes, AU) – 10/50/90 Percentiles.
[d] Average Number of Planets (Total Planets / Number of Runs).
[e] Average Number of Remaining Planetesimals (Total Planetesimals / Number of Runs).

the figure is 65 per cent – slightly below the 69 per cent in the reference simulations. For massive disks, this figure is increases to 79 per cent. We also note that half the planetesimals are scattered to semi-major axes $a > 4.63$ AU in massive disks (up from 3.96 AU and 3.74 AU for the reference and steep profiles) with the furthest one out at 10.60 AU.

(iv) (...HiRes...)

4.2.3 *Water Mass Fraction*

(i) Except for three very dry planets close to the star in both steep and reference simulations, all planets have water mass fractions exceeding 2×10^{-3}.

(ii) Overall, simulations with steep initial profiles, the reference profile, and massive disks produce planets with successively larger median water mass fractions. Planets further out tend to be wetter

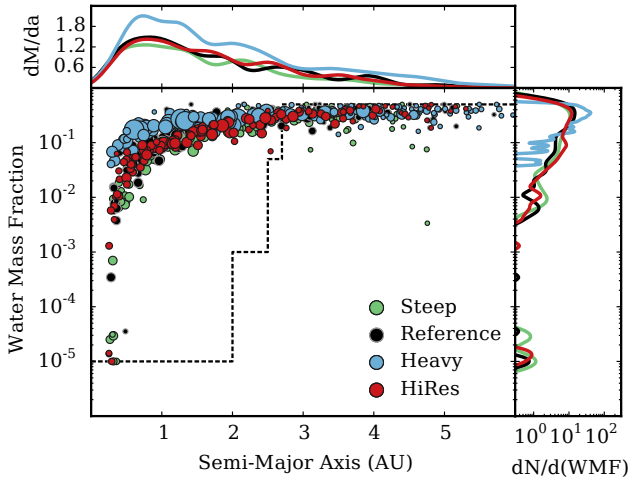

Figure 11. Distribution of water mass fraction (WMF) with semi-major axis for simulations with the (i) reference disk, (ii) steep intial disk, and (iii) heavy initial disk. See the legend. We stack all six runs per set and show the state at the end of the simulation (147.84 Myr). The main panel shows the scatterplot in the (a, WMF) plane and the side/top panels shows the corresponding marginal distribution. In the scatterplot, the dashed line indicates the initial WMF; cf. Eqn (5). *Top:* Marginal distribution of the mass with semi-major axis; $\mathrm{d}M/\mathrm{a}$ in units of Earth Mass per AU. *Right*: Marginal distribution over the number of planets N per WMF bin; $\mathrm{d}N/\mathrm{d}(\mathrm{WMF})$.

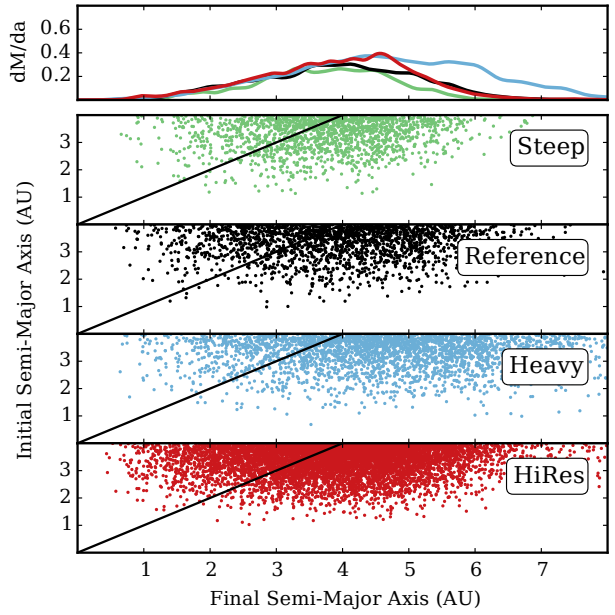

Figure 12.

than planets at small semi-major axis, although there is significant spread especially for steep initial profiles at $a > 3$ AU. In all simulations, there can be significant variations across runs of set. For example, RUN02 of the NJS/HEAVY set produces a neat gradient of increasing WMF with semi-major axis, whereas RUN01 of the same set intersperses wet with dry planets in the region $a < 3$ AU.

(iii) Except for a few outleir, the initially imprinted WMF is lost as the simulation terminates. Interior to 2.5 AU, planets are substantially wetter than the initial WMF at this location. In the outer regions $a > 2.7$ AU, planets are (by median) 30 to 35 per cent dryer than the planetesimals initially found in this region.

(iv) Irrespective of the initial planetesimals distribution, about 80 per cent of all surviving planetesimals have WMF > 0.1. The dryest planetesimals are found in simulations of massive disks, which pushes the fraction down from 90 per cent when compared to simulations that varied the gas disk. Interior to $a < 2.7$ AU, all planetesimals have WMFs in excess of inital values at their corresponding location. Beyond $a > 2.7$ AU, about 20 per cent of planetesimals are dryer than the intial WMF in this range.

(v) (...HiRes...)

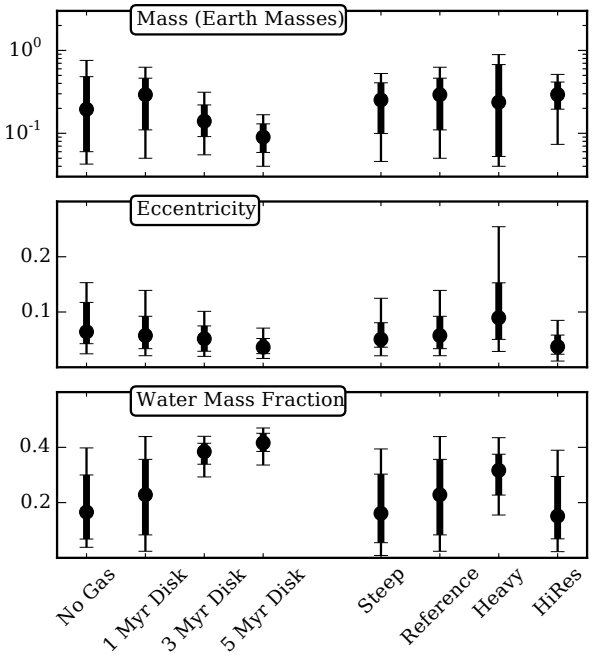

Figure 13. Summary of key diagnostics (see inset titles) for our simulations. We show diagnostics for planets (stacked over all individual runs) remaining at the end of the simulation (147.84 Myr). Indicated are the median (circle), 25/75 percentile range (thick line), and 10/90 percentile range (thin lines). Note that 1 Myr Disk refers to the same simulations as Reference Disk, but has been repeated for visual convenience.

5 DISCUSSION: GAS DISKS & INITIAL PROFILES

We now summarise and discuss the dynamical state, mass distribution, feeding zones, and final water mass fractions across all simulations and address the physical mechanisms behind the differences.

5.1 Mass, Dynamics, Mixing

Planetesimal dynamics are driven by a number of processes. First, viscous stirring increases the velocity dispersion of planetesimals through mutual gravitational interactions. Ordered motion (Keplerian shear) is converted into ranodm motions, i.e. more eccentric and inclined orbits. Second, dynamical friction decreases the velocity dispersion of larger bodies and increases those of the planetesimals. Here, angular momentum is tansferred from larger bodies (embryos and planets) to smaller ones. Third, hydrodynamic drag from the gas dampens random motions of planetesimals. As

the gas rotates at sub-Keplerian velocities, planetesimals also feel a headwind which removes angular momentum and causes an inward drift. Finally, for larger bodies, gravitational interactions trigger spiral waves in the gas which transfer angular momentum from planets to the gas, causing them to drift inwards.

The presence of a gas disk is a double-edged sword. On the one hand, it promotes collisional growth by drifting planetesimals to the inner disk (where growth timescales are short; Appendix A) and damping inclined orbits (which have lower collision probability). On the other hand, it delivers planetesimals (hydrodynamic drag) and embryos (type I migration) to the inner edge of the simulation domain where they fall onto the star. The net effect on our simulations is threefold. First, simulations with longer gas disk lifetimes host successivly less massive planets. Although the planets tend to assemble faster, fewer embryos and planets survive at the inner edge of the disk after they are assembled. In like fashion, fewer planetesimals survive as the disk gas propels them onto the host star over longer timescales. Second, as hydrodynamic drag dampens excursions from Keplerian orbits, the final eccentricities and inclinations of planets are lower in disks with longer gas-disk lifetimes. Thirdly, in simulations with longer gas disk lifetimes, the final water mass fraction tends to be larger as more material is delivered (through hydrodynamic drag) from the outer regions of the disk and initially dry material at small semi-major axis tends to be removed from the simulation onto the star.

Simulations without gas evolve markedly slower. Compared to those with gas, they host more planets, retain more planetesimals, and host planets covering a wide range of masses. Without gas, there is little inward inward migration of material such that embryos accrete mostly local material. Once formed, they tend to remain in the part of the disk they form at. This prevents them from falling into the star, growing further once local material is depleted, and colliding with embryos in other regions of the disk. Of course, this does not preclude them from accreting planetesimals from other disk entirely. Without hydrodynamic drag, planetesimal excited onto eccentric orbits are not damped, thereby potentially delivering material to the entire disk, although more inclined orbits tend to lower collision probabilities. However, the process is more stochastic than in simuations with gas that reliably feed embryos growing in the inner disk regions. This leads to large dispersions in mass and WMF for scenarios without gas.

Disks with steeper surface density profiles bias mass towards the inner regions. With short collision timescales, embryos and planets assemble quickly, but also tend to drift to the inner edge of the simulation domain where they fall onto the star. The total disk mass and the amount of surviving planetesimals is therefore lower than in the references runs, leading to lower median planet masses. Planets are also dynamically colder due to the decreased rate and strength of gravitational interacts. However, their WMF ... (which means they still sample wide regions of the disks....) For heavy disks, ...

Heavy/Steep

Dispersion in planetesimals locations...

OVerall, wet.... (Especially gas.... all material from outer regions [infall, etc])/ Adress below.

- mixing: in all cases, substantial migration of planetesimals occurs both in and outward. inwards, planetesimals are driven by (i) gas drag, (ii) type i migration (the heavier ones), and (iii) gravitational scattering. outward movement only happens by gravitational scattering. once the gas is gone, only grav. scattering drives migration; angular momentum conservation spreads the distribution out (every body that goes inward, another body must go outward) ==¿ gaussian distribution (Fig. X) is characteristic of a diffusion process
- (This suggests that majority of terrestrial planets forming in planets without giant are very wet!)
- (Again underscores the need for statistical approaches. The individual systems can be VERY different! As such, we expect real planets to also have a significant spread in their WMF)
- Comparison of dynamical state to CJS/EJS runs? Presumably much less excited b/c we do not have sweeping/mean motion resonances. Also compare dynamics to Kokubo & Ida papers (whom did not have gas!)

5.2 Water Mass Fraction

At present, Venus, Earth, and Mars hold approximately 4.3×10^{-6} (Donahue & Hodges 1992; Donahue et al. 1997; Taylor et al. 1997), 1.0, and 3.0×10^{-3} (Smith et al. 1999) Terrestrial Oceans (TO, $\sim 1.39 \times 10^{21}$ kg) of water on their surfaces. More is likely locked up in subsurface reservoirs, but these are subject to significant uncertainties (Lécuyer et al. 1998; Abe et al. 2000; Chassefière et al. 2012; Krasnopolsky 2000; Donahue 2001). Over the past 4.5 Gyr, Venus and Mars lost (or subducted) substantial amounts of water. For Venus, estimates of (total) initial water content range from 0.3×10^{-3} (Donahue 1999; Kulikov et al. 2006) through 0.8 (Lécuyer et al. 2000) and up to ~ 5 TOs (Gillmann et al. 2009; Chassefière et al. 2012). For Mars, they range from 0.02 (Krasnopolsky 2000) through 0.05 (Carr 1996; Baker 2001) to 0.2 (Donahue 2001; Villanueva et al. 2015) TOs. This pegs the expected[11] initial water mass fractions at 3.0×10^{-5} (Venus), 5.0×10^{-4} (Earth), and 1.3×10^{-4} (Mars).

By these measures, all but a few of the planets generated in our simulations are extremely wet. Even in the dryest of runs, 90 per cent of planets host more than 10 TOs, and the wettest planets can exceed 1000 TOs. To order of magnitude, these results are in line with similar works by Ronco & de Elía (2014) and Ciesla et al. (2015), although we consistently exceed their WMF by factors of a few. This is expected due to our modelling of the early stages of planetesimal growth, cf. Section 3. Nevertheless, how can we produce terrestrial planets that host so much more water than their Solar System cousins?

Beyond the possibility of severely underestimating the water contents of the terrestrial planets,[12] there are a number of systematics we do not model: (i) outgassing of atmospheric and surface water, (ii) loss of volatiles during planetesimal-planetesimal collisions as well as giant impacts, and (iii) the admittedly somewhat ad-hoc initial WMF distribution. We now attempt to quantify these.

Close to the star ($a \lesssim 1$ AU), atmospheric water can be driven off by solar wind and XUV photons. Calculations for the early Venus ($a \sim 0.8$ AU) suggest losses of a 0.1 to a few TOs on ~ 100 Myr timescales (Donahue 1999; Kulikov et al. 2006; Gillmann et al. 2009). Similar calculations for hypothetical Earth-mass

[11] For Venus and Mars, we compute the geometric mean over the various estimates given in the literature. For Earth, we also account for an additional ocean's worth of subsufrace water; cf. Lécuyer et al. (1998).

[12] For example, Ceres is estimated to hold up to 30 per cent of water by mass (Küppers et al. 2014). Moreover, Chassefière et al. (2012) argues for initial water reservoirs of ~ 10 TO on Venus, Earth, and Mars. Past N-Body runs also deposit between 10 and 160 TOs on these planets (Raymond et al. 2006; O'Brien et al. 2006). The mantle water content of the Earth is also constrained only to factors of two within a dozen TOs (Hauri et al. 2006; Inoue et al. 2010; Cowan & Abbot 2014).

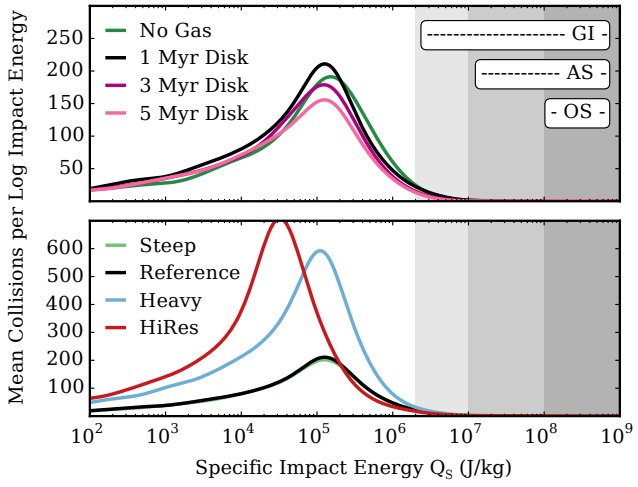

Figure 14. Distribution of collisions at a given specific impact energy for all simulations. More specifically, we show the logarithmic collisions density function, $dN_{\rm Coll}/d\log(Q_S)$ normalized (i.e., integrating) to 4000 collisions. There is a long tail $< 10^2$ populated by ~ 10 per cent of collisions. The 1 Myr Disk in the top panel is the same as what is labelled Reference Disk in the lower panel. Shaded regions correspond to the regions of Q_S above which giant impacts and partial atmospheric stripping (GI), full atmospheric stripping (AS), and oceanic stripping (OS) occur.

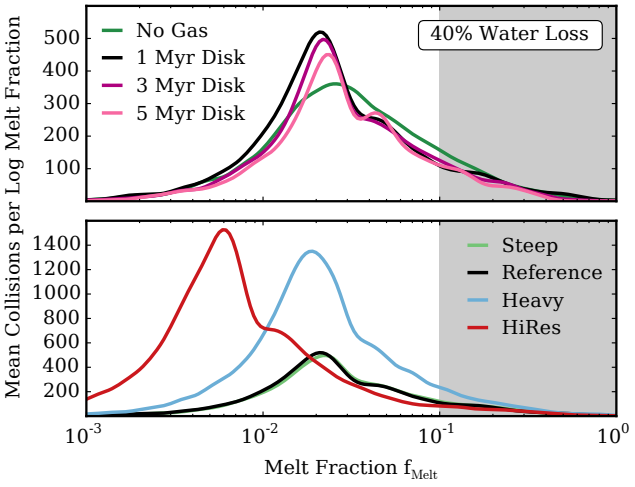

Figure 15. Distribution of collisions resulting in a particular melt fraction for all simulations, see legend. We show the logarithmic collision density function $dN_{\rm Coll}/d\log(f_{\rm Melt})$ normalized (i.e., integrating) to 4000 collisions. Note that the 1 Myr Disk refers to the same simulation as the Reference Disk. Melt fractions > 0.1 (shaded grey) occur, on average, five times for each planet and can deplete up to ~ 40 per cent of water.

planets around extrasolar G stars loose ~ 0.1 TOs over the same timescales (Erkaev et al. 2013). Much higher loss rates are possible, but constrained to distances $a \lesssim 0.1$ AU (Kurosaki et al. 2014) which we do not model due to computational constraints. At distances $a > 1.0$ AU, loss rates drop significantly, such that Mars type planets require Gyr timescales to outgas even 0.1 TOs. Over ~ 100 Myr timescale, we therefore do not expected atmospheric water loss > 1 TO for the planets generated in our models. This is also supported by population synthesis models accounting for XUV fluxes. For example, Tian & Ida (2015) retain partial or complete ocean cover (WMF $\sim 10^{-4}$, $> 10^{-3}$) in 67, respectively 22, per cent of planets in their habitable zones.

Giant impacts can potentially strip volatiles from both impactor and targets. Using SPH simulations, Canup & Pierazzo (2006) found significant (> 50 per cent) water being stripped from completely icy impactors (targets were rocky) for impact parameters $b \geqslant 0.7$. For partially (10 per cent) icy impactors, water loss fractions started at 30 per cent, but also increased with impact velocity. In our simulations, ~ 50 per cent of collisions[13] occur at $b \geqslant 0.7$. Although it appears that water stripping from impactors is feasible pathway to lowering the WMF of the final planets, the discussion in Section 3 concludes that embryos are already born wet (i.e., the material for the first few collisions assembling the embryo partially originates in initially wet regions). Thus, while we definetly overestimate delivery of water from wet impactors, they represent only a small contribution to the total water budgets.

Assuming a terrestrial planet hosting the equivalent of one Terrestrial Ocean, Genda & Abe (2005) find that successive giant impacts can severely (90 to 99 per cent) deplete the atmosphere, and thereby remove water. Extensions by Stewart et al. (2014) suggest that impacts with specific impact energies $Q_S > 10^7$ J/kg ($> 10^8$ J/kg) are capable of stripping the entire atmosphere (ocean) from planets, although consistent partial stripping exceeding 20 per cent of an atmopshere begins at $\sim 2 \times 10^6$ J/kg.[14] In our simulations, only small fractions out of all collisions exceed specific impact energies required for atmospheric or ocean stripping, cf. Figure 14. For example, across six runs of the NJS/GAS01 case ($\tau_G = 1$ Myr) record a total of 2408 collisions with targets being at least embryos. Out of those, only 36, 6, and 4 exceed the $Q_S = 2.0 \times 10^6$, 10^7, and 10^8 J/kg thresholds, corresponding to 1.25, 0.25, and 0.17 per cent. For an average of 10 planets per system, this means that roughly one in every two planets experienced an impact energetic enough to strip an astmosphere and a single ocean worth of water. For other simulations, numbers are similar.

Finally, energetic collisions can melt substantial fractions of the targets and impactor (Tonks & Melosh 1993). This facilitates evaporation and subsequent escape of volatiles from the host. Although the fraction of evaporated material that actually escapes massive bodies is impossible to determine without dedicated simulations, we can set an upper bound by considering to amount of melt generated per impact. Figure 15 shows the distribution of the melt fraction $f_{\rm Melt}$ for our simulations. Across all runs, 90 per cent of collision lead to melt fractions $\lesssim 0.1$, and half of all collisions generate fractions below 0.02. Across all runs, we record 1765 collisions with $f_{\rm Melt} > 0.1$. With, on average, 10 planets per system and six runs per set, this means that each planet undergoes an average of five collisions of melt fractions above 10 per cent. For a representative $M \sim M_{\rm Earth}$ planet hosting 175 TOs (WMF ~ 0.04) of hydrated silicates, this means a potential water loss of 67 TOs (38 per cent), dropping the WMF to 0.02.[15] If only a fraction of the evaporated water is stripped from planet, the water loss decreases

[13] Here, we only consider collisions where at least one body is classified as planet or embryo, i.e. exceeds the threshold mass $M = 3.3 \times 10^{26}$ g.

[14] Note that the ocean and atmospheric masses are scaled the to the target mass, such that a less massive planet hosts a correspondingly smaller ocean.

[15] Here, we assume that 92 per cent of the water locked up in the melt

correspondingly and should thus be considered an upper bound. On the other hand, collisions generating larger melt fraction increase the amount of dissipated water.

For lower mass impactors, Schlichting et al. (2015) suggest that successive collisions with impactors with radii $\lesssim 12$ km can substantially erode planetary atmospheres. Given a power law mass function of planetesimals, such impacts may have been numerous enough to dissipate water bearing atmospheres. They may therefore provide an efficient way to strip volatiles previously evaporated from melt from the atmosphere. Unfortunately, modelling such objects currently remains beyond the resolution limit of our simulations and we are therefore unable to properly quantify their collision rates.

Substantial uncertainties are associated with the initial water mass fraction imprinted on the planetesimals. The initial WMF depends on the evolution of the snow line location, the formation timescales of planetesimals, and the subsequent chemical evolution of planetesimals. The location of the snow line depends on the temperature structure of the gaseous disk, which in turn depends on the stellar output as and density structrue of the disk (Armitage 2011). During the first Myr, these all evolve so that the snow line moves about (Siess et al. 2000; Ciesla et al. 2015). It remains unclear at which point the compositional gradient of the disk is imprinted onto the forming planetesimals.

Once formed, planetesimals of a given composition are chemically active. If they incorporate substantial amounts of SLRs, radiogentic heating can melt water, which can either be locked up in hydrated minerals, dissipate into space, or form frozen surfaces than can be eroded by impacts. For varying SLR abundances, we may therefore expect significant variance across different planetary systems. In fact, the ^{26}Al abundance in molecular clouds appears to increase over time (Vasileiadis et al. 2013), although it remains driven by stochastic processes (Adams et al. 2014). As such that, we may expect systems that host populations of comet-like material instead of hydrated minerals even in inner disk regions (Ciesla et al. 2015).

All in all, there are significant uncertainties involved in determining the initial chemical composition of planetesimals in our simulations. Short of consistent end-to-end modelling of chemically active planetesimals forming in thermally evolving hydrodynamic disk, they remain very difficult to constrain at present.

- With this in mind, are our initial WMF estimates actually useless? We may be imprinting them too early. At this stage, the snow line was probably somewhere else (further away)? Then again, if we look at Fig1 in Ciesla 2015, a ice line at 2.7 AU corresponds to a time of 3×10^5 years, so that's not so bad. Nevertheless, we may overestimate the amount of water just by virtue of our ice line location.
- Maybe we can generate more suitable initial conditions by asking where we would have to put some initial planetesimals so that their WMF matches those in Eqn. (4) and (5) *once the gas has dissipated*?

5.3 Numerical Convergence

(High-Res Converged? Include in results section. We find (i) mre low velocity collisions, (ii) slightly different feeding zones, (iii) slightly different final orbital parameters and masses. So, how bad is this? Or no problem? Also discuss the important catch in the drag formulation.)

dissipates, cf. Table 5 in Bond et al. (2010) as well as Davis (2006) and Lodders (2003).

6 CONCLUSIONS

In this paper, we have addressed the formation of terrestrial planets in the absence of giant planets by means of N-Body simulations of collisional growth of planetesimals. Lacking the required observational fidelity, such an architecture is currently hypothetical, but not implausible given the existence of our own Solar System. We have paid particular attention to the amount of water hosted by these hypothetical planets.

Dynamically, planetesimals growing in gaseous disks with successively longer lifetimes tend to build systems with less massive terrestrial planets on tighter orbits around their host star. For a given gas disk lifetime, disks with steeper surface density profiles lead to marginally more massive terrestrial planets on marginally wider orbits, whereas more massive initial disks end up with significantly more massive planets on even wider orbits. (HiRes?)

An important result from dynamical models covering the formation and early orbital evolution of terrestrial planets is a description of their feeding zones, i.e. the initial orbital distribution of the planetesimals which collided to build a given planet. Given the feeding zones and some initial distribution of water, we can reconstruct an upper limit to the expected distribution of water of the formed terrestrial planets.

For all configurations, we generate exceedingly wet planets, 90 per cent of which host water equivalent to anywhere between 10 and 1000 Terrestrial Oceans (TOs). The driest planets assemble in scenarios with steep surface density profiles and short gas disk lifetimes, but even these are orders of magnitude above even the wettest estimates for the initial water contents of the Venus, Earth, and Mars. To obtain more realistic estimates, we have attempted to quantify sources of water loss which include (i) outgassing from melt generated in giant impacts, (ii) stripping and of atmospheric and ocean water during impacts, (iii) incomplete transfer of water from impactors to targets, and (iv) atmospheric stripping due to strong stellar fluxes.

In order, multiple energetic impacts that melt a substantial fraction of the target appear to outgas up to 67 TOs from a planet hosting a total of 175 TOs, corresponding to a 40 per cent drop. Atmospheric and ocean stripping by less energetic giant impacts removes at most a few TOs, and is therefore much less effective. For oblique impacts, water delivery efficiency appears to be capped at around 70 per cent. Atmospheric stripping due to stellar fluxes is much less effective. Even for Venus type orbits, the stellar flux induces to water loss of at most a few TOs.

There are also significant uncertainties involved in our initial distribution of water (or any other compound one may wish to track) and it is not at all clear whether it is indeed representative of the initial state of the planetesimals. Given this, we have lent particular focus to the dynamics which determine the feeding zones of the final planets and how common modelling short-cuts in affect them. Due to computational constraints, such short-cuts include (i) not evolving this gaseous disk and its interaction with planetesimals and embryos, (ii) seeding an initial embryo distribution instead of growing them from planetesimals, and (iii) neglecting the gravitational interactions between planetesimals. Through more accurate modelling, we find that these common short-cuts induce two important inaccuracies. First, implanting embryos directly strongly biases their feeding zones to their immediate neighbourhood. In-

stead, we find that embryos grown from planetesimals in a gas disk sample material from a wide range of the disk. Secondly, embryos grow inside out, i.e. the first massive embryos appear close to the star, which is orthogonal to initial distributions frequently imposed in the the literature.

Therefore, we strongly argue that if accurate representations of the feeding zones are required, suitable modelling of the hydrodynamic and gravitational effects of the gas disk as well as the full set of mutual gravitational interactions between all planetesimals is essential. If such modelling is computationally infeasible, researcher should at the very least correct the initial distribution of the tracked compounds for the bias induced by seeding embryos instead of growing them.

ACKNOWLEDGMENTS

We are grateful to XXX, as well as Doug Potter for computational support. Simulations were run on the Tasna and Vesta GPU clusters at the Institute for Computational Science, University of Zürich. We also acknowledge use of Numpy, Scipy, IPython, Matplotlib, and Colorbrewer2 for post-processing.

REFERENCES

Abe Y., Ohtani E., Okuchi T., Righter K., Drake M., 2000, Water in the Early Earth. pp 413–433
Abramov O., Wong S. M., Kring D. A., 2012, Icarus, 218, 906
Adams F. C., Fatuzzo M., Holden L., 2014, ApJ, 789, 86
Armitage P. J., 2011, ARA&A, 49, 195
Baker V. R., 2001, Nature, 412, 228
Bond J. C., Lauretta D. S., O'Brien D. P., 2010, Icarus, 205, 321
Brunini A., Benvenuto O. G., 2008, Icarus, 194, 800
Canup R. M., Pierazzo E., 2006, in Mackwell S., Stansbery E., eds, Lunar and Planetary Science Conference Vol. 37, 37th Annual Lunar and Planetary Science Conference. p. 2146
Carr M. H., 1996, Planet. Space Sci., 44, 1411
Chambers J. E., 1999, MNRAS, 304, 793
Chambers J. E., 2001, Icarus, 152, 205
Chambers J. E., Wetherill G. W., 1998, Icarus, 136, 304
Chassefière E., Wieler R., Marty B., Leblanc F., 2012, Planet. Space Sci., 63, 15
Ciesla F. J., Mulders G. D., Pascucci I., Apai D., 2015, ApJ, 804, 9
Cleeves L. I., Bergin E. A., Alexander C. M. O. ., Du F., Graninger D., Öberg K. I., Harries T. J., 2014, Science, 345, 1590
Cowan N. B., Abbot D. S., 2014, ApJ, 781, 27
Davis A. M., 2006, Volatile Evolution and Loss. pp 295–307
Donahue T. M., 1999, Icarus, 141, 226
Donahue T. M., 2001, Proceedings of the National Academy of Science, 98, 827
Donahue T. M., Hodges Jr. R. R., 1992, J. Geophys. Res., 97, 6083
Donahue T. M., Grinspoon D. H., Hartle R. E., Hodges Jr. R. R., 1997, in Bougher S. W., Hunten D. M., Phillips R. J., eds, Venus II: Geology, Geophysics, Atmosphere, and Solar Wind Environment. p. 385
Duncan M. J., Levison H. F., Lee M. H., 1998, AJ, 116, 2067
Erkaev N. V., et al., 2013, Astrobiology, 13, 1011
Fang J., Margot J.-L., 2012, ApJ, 761, 92
Genda H., Abe Y., 2005, Nature, 433, 842
Gillmann C., Chassefière E., Lognonné P., 2009, Earth and Planetary Science Letters, 286, 503
Grimm S. L., Stadel J. G., 2014, ApJ, 796, 23
Guilera O. M., Brunini A., Benvenuto O. G., 2010, A&A, 521, A50
Hansen B. M. S., 2009, ApJ, 703, 1131
Hauri E. H., Gaetani G. A., Green T. H., 2006, Earth and Planetary Science Letters, 248, 715
Hayashi C., 1981, Progress of Theoretical Physics Supplement, 70, 35
Hoffmann V., Grimm S. L., Moore B., Stadel J., 2015, preprint, (arXiv:1508.00917)
Inoue T., Wada T., Sasaki R., Yurimoto H., 2010, Physics of the Earth and Planetary Interiors, 183, 245
Johansen A., Oishi J. S., Mac Low M.-M., Klahr H., Henning T., Youdin A., 2007, Nature, 448, 1022
Kitzmann D., et al., 2015, MNRAS, 452, 3752
Krasnopolsky V., 2000, Icarus, 148, 597
Kulikov Y. N., et al., 2006, Planet. Space Sci., 54, 1425
Küppers M., et al., 2014, Nature, 505, 525
Kurosaki K., Ikoma M., Hori Y., 2014, A&A, 562, A80
Lécuyer C., Gillet P., Robert F., 1998, Chemical Geology, 145, 249
Lécuyer C., Simon L., Guyot F., 2000, Earth and Planetary Science Letters, 181, 33
Leinhardt Z. M., Stewart S. T., 2012, ApJ, 745, 79
Lodders K., 2003, ApJ, 591, 1220
Mandell A. M., Raymond S. N., Sigurdsson S., 2007, ApJ, 660, 823
Martin R. G., Livio M., 2013, MNRAS, 428, L11
Marty B., 2012, Earth and Planetary Science Letters, 313, 56
Morbidelli A., Chambers J., Lunine J. I., Petit J. M., Robert F., Valsecchi G. B., Cyr K. E., 2000, Meteoritics and Planetary Science, 35, 1309
Morbidelli A., Lunine J. I., O'Brien D. P., Raymond S. N., Walsh K. J., 2012, Annual Review of Earth and Planetary Sciences, 40, 251
Morishima R., Schmidt M. W., Stadel J., Moore B., 2008, ApJ, 685, 1247
Morishima R., Stadel J., Moore B., 2010, Icarus, 207, 517
Nagasawa M., Tanaka H., Ida S., 2000, AJ, 119, 1480
O'Brien D. P., Morbidelli A., Levison H. F., 2006, Icarus, 184, 39
O'Brien D. P., Walsh K. J., Morbidelli A., Raymond S. N., Mandell A. M., 2014, Icarus, 239, 74
Quintana E. V., Barclay T., Borucki W., Rowe J. F., Chambers J. E., 2015, preprint, (arXiv:1511.03663)
Raymond S. N., Quinn T., Lunine J. I., 2004, Icarus, 168, 1
Raymond S. N., Quinn T., Lunine J. I., 2006, Icarus, 183, 265
Raymond S. N., Quinn T., Lunine J. I., 2007, Astrobiology, 7, 66
Raymond S. N., O'Brien D. P., Morbidelli A., Kaib N. A., 2009, Icarus, 203, 644
Ronco M. P., de Elía G. C., 2014, A&A, 567, A54
Ronco M. P., de Elía G. C., Guilera O. M., 2015, preprint, (arXiv:1509.07217)
Schlichting H. E., Sari R., Yalinewich A., 2015, Icarus, 247, 81
Siess L., Dufour E., Forestini M., 2000, A&A, 358, 593
Smith D. E., et al., 1999, Science, 284, 1495
Stewart S. T., Lock S. J., Mukhopadhyay S., 2014, in Lunar and Planetary Science Conference. p. 2869
Surville C., Mayer L., Lin D. N. C., 2016, preprint, (arXiv:1601.05945)
Taylor F. W., Crisp D., Bézard B., 1997, in Bougher S. W., Hunten D. M., Phillips R. J., eds, Venus II: Geology, Geophysics, Atmosphere, and Solar Wind Environment. p. 325
Tian F., Ida S., 2015, Nature Geoscience, 8, 177
Tonks W. B., Melosh H. J., 1993, J. Geophys. Res., 98, 5319
Trigo-Rodríguez J. M., Martín-Torres F. J., 2013, in Trigo-Rodriguez J. M., Raulin F., Muller C., Nixon C., eds, Astrophysics and Space Science Proceedings Vol. 35, The Early Evolution of the Atmospheres of Terrestrial Planets. p. 85, doi:10.1007/978-1-4614-5191-4˙7
Vasileiadis A., Nordlund Å., Bizzarro M., 2013, ApJ, 769, L8
Villanueva G. L., et al., 2015, Science, 348, 218
Walsh K. J., Morbidelli A., Raymond S. N., O'Brien D. P., Mandell A. M., 2011, Nature, 475, 206
Weidenschilling S. J., 1977, Ap&SS, 51, 153
de Elía G. C., Guilera O. M., Brunini A., 2013, A&A, 557, A42

APPENDIX A: PLANETESIMALS GROW INSIDE-OUT

Find some papers that support this inside-out growth.

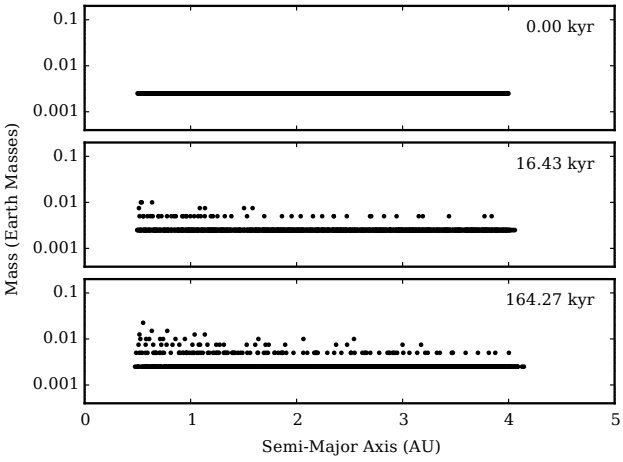

Figure A1. Snapshots of planetesimal semi-major and mass at three different times for a representative run taken from the NJS/NoGas set. From top to botton: initial conditions, the first output, tenth output. It is evident that collisional growth proceeds inside out.

This paper has been typeset from a TEX/LATEX file prepared by the author.

7

Conclusions & Outlook

"*But al shal passe; and thus take I my leve.*"

– Geoffrey Chaucer, *Troilus and Criseyde (1380s)*

7.1. Conclusions

In this work, we have set out to better characterise the (i) influence of giant planets and gaseous protoplanetary disk on the formation of embryos and planets from planetesimals as well as (ii) the expected water contents of hypothetical terrestrial planets in the systems that do not host giant planets. While doing so, we have paid special attention to the consequences of common model simplification as well as chaotic nature of the gravitational dynamics problem. We have come to four major conclusions, the latter two of which we consider as important lessons in the setup of numerical experiments by the conscientious modeller. They are as follows:

Dynamic Drivers – The primary means by which giant planets interact with planetesimals is by secular resonances that sweep inwards as the gas dissipates. Depending on the orbital configuration and masses of the giant planets, they end up truncating the planetesimals disk at different heliocentric distances, below which they concentrate planetesimals.

System Architecture – Planetesimals that evolve against a backdrop of Jupiter and Saturn on their present eccentric orbits form comparatively tight systems with the most massive terrestrial planets. For systems with Jupiter and Saturn on circular orbits (as suggested by the Nice model), the resulting terrestrial planets are on wider orbits and tend to be less massive. Finally, in systems

without giant planets, terrestrial planets are the least massive and occupy almost the entire orbital region in which planetesimals were seeded.

Water Content – Terrestrial planets forming in the absence of giant planets appear to host hundreds of oceans worth of water. In our simulations, we find their water content to be substantially larger than in previous work because our feeding zones are much wider. This is a consequence of growing embryos from planetesimals embedded in a gas disk. We find hydrodynamic drag to be responsible for delivering a substantial amount of planetesimals from the outer disk regions. Previous simulations did not grow embryos, but seeded them in their initial conditions, which biases the feeding zones of planets. Even in experiments where insufficient computing resources are available, we propose that this bias can be at least be offset by choosing a more suitable initial embryo distribution and correcting any initially imprinted distribution (of water, volatiles, or isotopic tracers) by considering the source regions from which a given embryo should have formed.

Orbital Divergence – Displacing a single planetesimal by a less than a millimetre has a knock-on effect and causes the orbits of all planetesimals to diverge exponentially fast on timescales of a few to a few dozens of years. The sobering extrapolation of this is that if the Solar System has looked just slightly different, there would unlikely be an Earth for humans to populate. Fortunately, the statistical properties over a number of simulations runs with minimal initial differences remain consistent. The above extrapolation thus becomes somewhat less threatening in the sense that, even if our Earth would not exist, there would likely be a very similar planet, but maybe it would orbit a bit further out, be a bit less massive, and its inhabitants be a bit greener. To account for this spread, any model will have to be evolved multiple times and the results analysed statistically.

7.2. Prospects

Of course, the above findings and lessons learned represent mere baby-steps in the grand scheme of planet formation models. Our simulations remain addled with layers upon layers of assumptions, poorly constrained 'sub-grid' physics, and numerical short-cuts. We now address the four worst offenders and consider prospects for their resolution.

Water Loss, Initial Distribution – The terrestrial planets we form in hypothetical extrasolar systems without giant planets host hundreds of oceans of water. Finding such ubiquity difficult to reconcile with our evidence from the Solar System, we attempted to quantify possible sources of water loss from impacts and began to reconsider the initial conditions used to imprint an initial water distribution on the initial planetesimals. Unfortunately, both issues remain poorly constrained at present. For atmospheric stripping, current simulations of giant impacts lack prescriptions to actually model atmospheres. At best, models consider the delivered impact energy and estimate the fraction energy

that can be used to gravitationally unbind some fraction of the atmosphere (Schlichting et al., 2015). While deriving the melt fraction generated in large impacts is comparatively accessible with scaling laws derived from elaborate shock-physics (Abramov et al., 2012; Tonks & Melosh, 1993), the amount of volatiles that can be outgassed in such events is more difficult to pin down without elaborate laboratory experiments (Bond et al., 2010; Davis, 2006; Lodders, 2003). The final, and possibly most vexing, uncertainty relates to the imprint of an initial water distribution onto our planetesimals. Improvement to this ad-hoc choice (which is entirely based on Solar System evidence) requires improved understanding of the evolution of temperature structure of protoplanetary disks as well as the formation timescale and mechanism of planetesimals.

Numerical Resolution – Most of our simulations are initialised with $N = 2000$ planetesimals summing up to a total mass of five Earth masses. If we spread this mass out evenly across planetesimals, each planetesimal has a mass of about 1/5-th of the Moon with a radius of about 1200 km (assuming a volume mass density of 2 g/cm^3). This is much larger than the size planetesimals are thought to form at, although estimates cover wide range from km sizes to a few hundred km (Chambers, 2010; Cuzzi et al., 2008; Johansen et al., 2015; Morbidelli et al., 2009). As such we are left to evolve only the top end of the planetesimals mass distribution, leaving us exposed to omission of relevant small scale dynamics.

We have also performed a suite of control runs with 8192 planetesimals, which corresponds to planetesimal masses of about 1/20-th of the moon mass and radii of roughly 750 km. Although differences are far from drastic, planetary properties such as the masses, semi-major axes, and shape of the feeding zones differ from similar runs initialised with 2000 planetesimals. This suggests that the simulations have not yet converged in a numerical sense. Future work will have to investigate to what degree we will have to keep pushing the number of planetesimals until the difference in simulation results becomes statistically insignificant. Unfortunately, this is a difficult problem because energy conservation requirements for accurately evolving tens of millions of orbits dictate direct force integration, which scales as $\mathcal{O}(N^2)$. For example, while evolving a 2000 particle disk requires about a month of Nvidia Tesla K80 graphics card, evolving 8192 particles requires three months. Without further algorithmic optimizations, successive increases of the number planetesimals may bump compute times for single runs into the order of years.

Worse yet, increasing the number of particles appears to accelerate divergence of nearby orbits, so that we may need to evolve even more individual runs to properly sample the solution space.

Collision Model – One of the strongest limitations affecting our simulations is the assumption of perfect sticking of colliding particles. Depending on the specific energy and geometry of the collision, the impactor could shatter the target, be fully absorbed, or be only partially accreted. In particular, identification of

the last scenario is of interest because such a hit and run scenario could have have formed the Moon (Reufer et al., 2012). Although recent developments suggest that a more accurate treatment of collisions appears to have only minor effects on the dynamical properties of the final systems, we expect the final composition of the planets to be altered significantly (Carter et al., 2015).

Implementing a more sophisticated collision model in a given N-Body code could proceed in two steps. In the first step, an analytic prescription for the outcome depending on the collision geometry (which is available on-the-fly) would be implemented (Genda et al., 2012; Leinhardt & Stewart, 2012; Stewart & Leinhardt, 2012). In the second step, recorded collisions geometries of suites of simulations can be evolved with a dedicated SPH code, thereby generating a library of collision geometries and outcomes. These can, in turn, be connected back into the orbital dynamics code by way of a lookup table. Either way, shattering collisions could generate large numbers of additional particles that must be integrated. To prevent the number of simulation particles to grow without bound, we must ignore particles below some mass threshold – a procedure that may bring along its own issues. Some simulations codes can somewhat alleviate this issue by considering each simulation particle to represent a large number of smaller particles that obey a mass function that can evolve during collisions (Levison et al., 2012; Morishima, 2015).

Gas Disk Model – We devoted much of this work to stressing the importance of the interaction between the gaseous disk, the giant planets, and the planetesimals during their collisional growth into embryos and planets. However, the gas model currently implemented in GENGA is a very basic implementation. In essence, the gas is modelled as a perfectly laminar, (azimuthally and vertically) symmetric flow that steadily dissipates only in the sense that an exponential decay function is applied. Based on gas distribution, hydrodynamic drag is applied based on the local density and rotation speed, the global nebular force is a precomputed integral over the mass, and Type I migration and damping due planet-disk interactions is implemented analytically (Morishima et al., 2010).

It is clear that a realistic protoplanetary disk is far from a static laminar state with a well-defined power-law in surface density and temperature. Additionally, more detailed investigations of planet-disk interactions reveal a complicated dependence of radial migration and damping on the temperature structure of the disk, so our simple migration and dampening descriptions are quite possibly erroneous (Armitage & Rice, 2005). Although a fully self-consistent self-gravitating model of an accretion disk is (at present) out of the question, successive improvements could see the switch to an actively accreting disk (inducing a radial component to the velocity field), an implementation of hydrodynamic evolution in the disk plane plane, gravitational feedback of the planets and planetesimals onto the disk itself, and possibly a more realistic dissipation mechanism.

Bibliography

Abramov, O., Wong, S. M., & Kring, D. A. 2012, Icarus, 218, 906

Alexander, R., Pascucci, I., Andrews, S., Armitage, P., & Cieza, L. 2014, Protostars and Planets VI, 475

Alexander, R. D., Clarke, C. J., & Pringle, J. E. 2006, MNRAS, 369, 229

Altwegg, K., Balsiger, H., Bar-Nun, A., et al. 2015, Science, 347, 1261952

Amelin, Y., Krot, A. N., Hutcheon, I. D., & Ulyanov, A. A. 2002, Science, 297, 1678

Andrews, S. M., & Williams, J. P. 2007, ApJ, 659, 705

Andrews, S. M., Wilner, D. J., Hughes, A. M., Qi, C., & Dullemond, C. P. 2009, ApJ, 700, 1502

—. 2010, ApJ, 723, 1241

Armitage, P. J. 2007, ArXiv Astrophysics e-prints, astro-ph/0701485

—. 2011, ARA&A, 49, 195

Armitage, P. J., & Rice, W. K. M. 2005, ArXiv Astrophysics e-prints, astro-ph/0507492

Asphaug, E. 2014, Annual Review of Earth and Planetary Sciences, 42, 551

Balbus, S. A., & Hawley, J. F. 1998, Reviews of Modern Physics, 70, 1

Bally, J., & Scoville, N. Z. 1982, ApJ, 255, 497

Barge, P., & Sommeria, J. 1995, A&A, 295, L1

Barnes, J., & Hut, P. 1986, Nature, 324, 446

Bartelmann, M. 2010, Classical and Quantum Gravity, 27, 233001

Batygin, K., & Brown, M. E. 2010, ApJ, 716, 1323

Benz, W., Slattery, W. L., & Cameron, A. G. W. 1988, Icarus, 74, 516

Bergin, E. A., & Tafalla, M. 2007, ARA&A, 45, 339

Binney, J., & Tremaine, S. 2008, Galactic Dynamics: Second Edition (Princeton University Press)

Boley, A. C., & Ford, E. B. 2013, ArXiv e-prints, arXiv:1306.0566

Bond, J. C., Lauretta, D. S., & O'Brien, D. P. 2010, Icarus, 205, 321

Borucki, W. J., & Summers, A. L. 1984, Icarus, 58, 121

Bottke, W. F., Durda, D. D., Nesvorný, D., et al. 2005, Icarus, 175, 111

Bottke, W. F., Walker, R. J., Day, J. M. D., Nesvorny, D., & Elkins-Tanton, L. 2010, Science, 330, 1527

Bouvier, J., Alencar, S. H. P., Harries, T. J., Johns-Krull, C. M., & Romanova, M. M. 2007, Protostars and Planets V, 479

Brahe, T. 1610, Astronomiae instauratae progymnasmata, doi:10.3931/e-rara-315

Brett, R. 1984, Geochim. Cosmochim. Acta, 48, 1183

Brouwer, D., & Clemence, G. M. 1961, Methods of celestial mechanics

Bruno, A. D. 1994, The restricted 3-body problem: plane periodic orbits, Vol. 17 (Walter de Gruyter)

Canup, R. M. 2004, ARA&A, 42, 441

Carter, P. J., Leinhardt, Z. M., Elliott, T., Walter, M. J., & Stewart, S. T. 2015, ApJ, 813, 72

Casoli, J., & Masset, F. S. 2009, ApJ, 703, 845

Chaisson, E., & McMillan, S. 2005, Astronomy Today, Volume 1: The Solar System

Chambers, J. E. 1999, MNRAS, 304, 793

—. 2001, Icarus, 152, 205

—. 2010, Icarus, 208, 505

Chambers, J. E., & Wetherill, G. W. 1998, Icarus, 136, 304

—. 2001, Meteoritics and Planetary Science, 36, 381

Chapman, C. R., Cohen, B. A., & Grinspoon, D. H. 2007, Icarus, 189, 233

Chatterjee, S., & Tan, J. C. 2014, ApJ, 780, 53

Chiang, E., & Laughlin, G. 2013, MNRAS, 431, 3444

Chiang, E. I., & Goldreich, P. 1997, ApJ, 490, 368

Citron, R. I., Genda, H., & Ida, S. 2015, Icarus, 252, 334

Cleeves, L. I., Bergin, E. A., Alexander, C. M. O. ., et al. 2014, Science, 345, 1590

Connelly, J. N., Bizzarro, M., Krot, A. N., et al. 2012, Science, 338, 651

Copernicus, N. 1543, D revolutionibus orbium coelestium

Cuzzi, J. N., Dobrovolskis, A. R., & Champney, J. M. 1993, Icarus, 106, 102

Cuzzi, J. N., Hogan, R. C., & Shariff, K. 2008, ApJ, 687, 1432

D'Alessio, P., Cantö, J., Calvet, N., & Lizano, S. 1998, ApJ, 500, 411

Davies, M. B., Adams, F. C., Armitage, P., et al. 2014, Protostars and Planets VI, 787

Davis, A. M. 2006, Volatile Evolution and Loss, ed. D. S. Lauretta & H. Y. McSween, 295–307

Donahue, T. M. 1999, Icarus, 141, 226

Donahue, T. M., & Hodges, Jr., R. R. 1992, J. Geophys. Res., 97, 6083

Drake, A. J., Beshore, E., Catelan, M., et al. 2010, ArXiv e-prints, arXiv:1009.3048

Drake, M. J., & Righter, K. 2002, Nature, 416, 39

Dullemond, C. P., & Dominik, C. 2005, A&A, 434, 971

Dullemond, C. P., van Zadelhoff, G. J., & Natta, A. 2002, A&A, 389, 464

Dunham, M. M., Stutz, A. M., Allen, L. E., et al. 2014, Protostars and Planets VI, 195

Durisen, R. H., Cai, K., Mejía, A. C., & Pickett, M. K. 2005, Icarus, 173, 417

Eberhardt, P., Reber, M., Krankowsky, D., & Hodges, R. R. 1995, A&A, 302, 301

Faedi, F., West, R. G., Burleigh, M. R., Goad, M. R., & Hebb, L. 2011, MNRAS, 410, 899

Federrath, C., Roman-Duval, J., Klessen, R. S., Schmidt, W., & Mac Low, M.-M. 2010, A&A, 512, A81

Fischer, D. A., Howard, A. W., Laughlin, G. P., et al. 2014, Protostars and Planets VI, 715

Fraknoi, A., Morrison, D., & Wolff, S. 2000, Voyages Through the Universe (Harcourt College Publishers)

Frank, J., King, A., & Raine, D. J. 2002, Accretion Power in Astrophysics: Third Edition, 398

Frisch, U. 1996, Turbulence, 310

Gaffney, V., Fitch, S., Ramsey, E., et al. 2013, Internet Archaeology, 34, doi:10.11141/ia.34.1

Galilei, G. 1610, Sidereus nuncius magna, longeque admirabilia spectacula pandens lunae facie, fixis innumeris, lacteo circulo, stellis nebulosis, ... Galileo Galileo : nuper a se reperti beneficio sunt observata in apprime vero in quatuor planetis circa Iovis stellam disparibus intervallis, atque periodis, celeritate mirabili circumvolutis ... atque Medicea sidera nuncupandos decrevit, doi:10.3931/e-rara-695

Gammie, C. F. 1996, ApJ, 457, 355

—. 2001, ApJ, 553, 174

Genda, H., Kokubo, E., & Ida, S. 2012, ApJ, 744, 137

Goldreich, P., & Tremaine, S. 1979, ApJ, 233, 857

—. 1980, ApJ, 241, 425

Goldreich, P., & Ward, W. R. 1973, ApJ, 183, 1051

Gomes, R., Levison, H. F., Tsiganis, K., & Morbidelli, A. 2005, Nature, 435, 466

Grimm, S. L. 2015, PhD thesis, University of Zurich

Grimm, S. L., & Stadel, J. G. 2014, ApJ, 796, 23

Gullbring, E., Hartmann, L., Briceño, C., & Calvet, N. 1998, ApJ, 492, 323

Haghighipour, N., Vogt, S. S., Butler, R. P., et al. 2010, ApJ, 715, 271

Halliday, A. N. 2000, Earth and Planetary Science Letters, 176, 17

—. 2003, Treatise on Geochemistry, 1, 711

Hallis, L. J., Huss, G. R., Nagashima, K., et al. 2015, Science, 350, 795

Hansen, B. M. S. 2009, ApJ, 703, 1131

—. 2014, MNRAS, 440, 3545

Hansen, B. M. S., & Murray, N. 2012, ApJ, 751, 158

—. 2013, ApJ, 775, 53

Harrison, T. M. 2009, Annual Review of Earth and Planetary Sciences, 37, 479

Hart, P. J. 1969, Washington DC American Geophysical Union Geophysical Monograph Series, 13, doi:10.1029/GM013

Hartmann, L., Calvet, N., Gullbring, E., & D'Alessio, P. 1998, ApJ, 495, 385

Hartmann, L., & Kenyon, S. J. 1996, ARA&A, 34, 207

Hartmann, W. K. 1975, Icarus, 24, 181

Hartmann, W. K., Quantin, C., & Mangold, N. 2007, Icarus, 186, 11

Hartogh, P., Lis, D. C., Bockelée-Morvan, D., et al. 2011, Nature, 478, 218

Hayashi, C. 1981, Progress of Theoretical Physics Supplement, 70, 35

Helled, R., Bodenheimer, P., Podolak, M., et al. 2014, Protostars and Planets VI, 643

Henon, M. 1997, Generating Families in the Restricted Three-Body Problem

Heppenheimer, T. A. 1980, Icarus, 41, 76

Hernández, J., Hartmann, L., Calvet, N., et al. 2008, ApJ, 686, 1195

Hughes, A. M., Wilner, D. J., Qi, C., & Hogerheijde, M. R. 2008, ApJ, 678, 1119

Ida, S. 1990, Icarus, 88, 129

Ida, S., & Makino, J. 1992a, Icarus, 96, 107

—. 1992b, Icarus, 98, 28

—. 1993, Icarus, 106, 210

Isella, A., Carpenter, J. M., & Sargent, A. I. 2009, ApJ, 701, 260

Izidoro, A., Morbidelli, A., & Raymond, S. N. 2014, ApJ, 794, 11

Izidoro, A., Morbidelli, A., Raymond, S. N., Hersant, F., & Pierens, A. 2015, A&A, 582, A99

Johansen, A., Mac Low, M.-M., Lacerda, P., & Bizzarro, M. 2015, Science Advances, 1, 1500109

Johansen, A., Youdin, A., & Klahr, H. 2009, ApJ, 697, 1269

Johnson, B. M., & Gammie, C. F. 2003, ApJ, 597, 131

Jones, J. H., & Drake, M. J. 1983, Geochim. Cosmochim. Acta, 47, 1199

—. 1986, Nature, 322, 221

Jontof-Hutter, D., Rowe, J. F., Lissauer, J. J., Fabrycky, D. C., & Ford, E. B. 2015, Nature, 522, 321

Kaib, N. A., & Chambers, J. E. 2016, MNRAS, 455, 3561

Kenyon, S. J., & Hartmann, L. 1987, ApJ, 323, 714

Kepler, J. 1609, Astronomia nova.

Kinoshita, H., Yoshida, H., & Nakai, H. 1991, Celestial Mechanics and Dynamical Astronomy, 50, 59

Kitamura, Y., Momose, M., Yokogawa, S., et al. 2002, ApJ, 581, 357

Kitzmann, D., Patzer, A. B. C., von Paris, P., et al. 2010, A&A, 511, A66

Kleine, T., Touboul, M., Bourdon, B., et al. 2009, Geochim. Cosmochim. Acta, 73, 5150

Klessen, R. S. 2011, in EAS Publications Series, Vol. 51, EAS Publications Series, ed. C. Charbonnel & T. Montmerle, 133–167

Kley, W., Bitsch, B., & Klahr, H. 2009, A&A, 506, 971

Kley, W., & Crida, A. 2008, A&A, 487, L9

Kokubo, E., & Ida, S. 1995, Icarus, 114, 247

—. 2012, Progress of Theoretical and Experimental Physics, 2012, 01A308

Konacki, M., & Wolszczan, A. 2003, ApJ, 591, L147

Lambrechts, M., & Johansen, A. 2012, A&A, 544, A32

Laplace, P. S., Bowditch, N., & Bowditch, N. I. 1829, Mécanique céleste

Laskar, J. 1997, A&A, 317, L75

Lecar, M., & Franklin, F. 1997, Icarus, 129, 134

Leinhardt, Z. M., & Stewart, S. T. 2012, ApJ, 745, 79

Levison, H. F., Duncan, M. J., & Thommes, E. 2012, AJ, 144, 119

Levison, H. F., Kretke, K. A., & Duncan, M. J. 2015a, Nature, 524, 322

Levison, H. F., Kretke, K. A., Walsh, K. J., & Bottke, W. F. 2015b, Proceedings of the National Academy of Science, 112, 14180

Levison, H. F., Morbidelli, A., Tsiganis, K., Nesvorný, D., & Gomes, R. 2011, AJ, 142, 152

Lin, D. N. C., & Papaloizou, J. 1980, MNRAS, 191, 37

Lloyd, S. P. 1982, IEEE Transactions on Information Theory, 28, 129

Lodders, K. 2003, ApJ, 591, 1220

Lynden-Bell, D., & Pringle, J. E. 1974, MNRAS, 168, 603

Marchi, S., Bottke, W. F., Elkins-Tanton, L. T., et al. 2014, Nature, 511, 578

Marcy, G. W., Isaacson, H., Howard, A. W., et al. 2014, ApJS, 210, 20

Masset, F., & Snellgrove, M. 2001, MNRAS, 320, L55

Mayor, M., Pepe, F., Queloz, D., et al. 2003, The Messenger, 114, 20

McKee, C. F., & Ostriker, E. C. 2007, ARA&A, 45, 565

McKeegan, K. D., & Davis, A. M. 2003, Treatise on Geochemistry, 1, 711

Miotello, A., Bruderer, S., & van Dishoeck, E. F. 2014, A&A, 572, A96

Mocquet, A., Rosenblatt, P., Dehant, V., & Verhoeven, O. 2011, Planet. Space Sci., 59, 1048

Morbidelli, A., Bottke, W. F., Nesvorný, D., & Levison, H. F. 2009, Icarus, 204, 558

Morbidelli, A., Chambers, J., Lunine, J. I., et al. 2000, Meteoritics and Planetary Science, 35, 1309

Morbidelli, A., & Crida, A. 2007, Icarus, 191, 158

Morbidelli, A., Levison, H. F., Tsiganis, K., & Gomes, R. 2005, Nature, 435, 462

Morbidelli, A., Lunine, J. I., O'Brien, D. P., Raymond, S. N., & Walsh, K. J. 2012, Annual Review of Earth and Planetary Sciences, 40, 251

Morbidelli, A., Tsiganis, K., Crida, A., Levison, H. F., & Gomes, R. 2007, AJ, 134, 1790

Morbidelli, A., Walsh, K. J., O'Brien, D. P., Minton, D. A., & Bottke, W. F. 2015, ArXiv e-prints, arXiv:1501.06204

Morbidelli, A., & Wood, B. J. 2015, Late Accretion and the Late Veneer, ed. J. Badro & M. Walter, 71–82

Morgan, J. W., Wandless, G. A., Petrie, R. K., & Irving, A. J. 1981, Tectonophysics, 75, 47

Morishima, R. 2015, Icarus, 260, 368

Morishima, R., Schmidt, M. W., Stadel, J., & Moore, B. 2008, ApJ, 685, 1247

Morishima, R., Stadel, J., & Moore, B. 2010, Icarus, 207, 517

Mundy, L. G., Looney, L. W., Erickson, W., et al. 1996, ApJ, 464, L169

Murray, C. D., & Dermott, S. F. 1999, Solar system dynamics

Murthy, V. R. 1991, Science, 253, 303

Nagasawa, M., Tanaka, H., & Ida, S. 2000, AJ, 119, 1480

Nelson, R. P., & Papaloizou, J. C. B. 2004, MNRAS, 350, 849

Neukum, G., Ivanov, B. A., & Hartmann, W. K. 2001, Space Sci. Rev., 96, 55

Newton, I. 1687, Philosophiae Naturalis Principia Mathematica. Auctore Js. Newton, doi:10.3931/e-rara-440

Nimmo, F., & Agnor, C. B. 2006, Earth and Planetary Science Letters, 243, 26

Nimmo, F., O'Brien, D. P., & Kleine, T. 2010, Earth and Planetary Science Letters, 292, 363

O'Brien, D. P., Morbidelli, A., & Levison, H. F. 2006, Icarus, 184, 39

Ogihara, M., & Kobayashi, H. 2013, ApJ, 775, 34

Paardekooper, S.-J., Baruteau, C., Crida, A., & Kley, W. 2010, MNRAS, 401, 1950

Paardekooper, S.-J., & Papaloizou, J. C. B. 2009, MNRAS, 394, 2283

Papaloizou, J. C. B., Nelson, R. P., Kley, W., Masset, F. S., & Artymowicz, P. 2007, Protostars and Planets V, 655

Papaloizou, J. C. B., & Terquem, C. 2006, Reports on Progress in Physics, 69, 119

Pascucci, I., Gorti, U., Hollenbach, D., et al. 2006, ApJ, 651, 1177

Perryman, M. 2011, The Exoplanet Handbook

Petit, J.-M., Chambers, J., Franklin, F., & Nagasawa, M. 2002, Asteroids III, 711

Petit, J.-M., Morbidelli, A., & Chambers, J. 2001, Icarus, 153, 338

Podosek, F. A., & Cassen, P. 1994, Meteoritics, 29, 6

Pollack, J. B., Hubickyj, O., Bodenheimer, P., et al. 1996, Icarus, 124, 62

Pringle, J. E. 1981, ARA&A, 19, 137

Raymond, S. N., & Cossou, C. 2014, MNRAS, 440, L11

Raymond, S. N., Kokubo, E., Morbidelli, A., Morishima, R., & Walsh, K. J. 2014, Protostars and Planets VI, 595

Raymond, S. N., O'Brien, D. P., Morbidelli, A., & Kaib, N. A. 2009, Icarus, 203, 644

Raymond, S. N., Quinn, T., & Lunine, J. I. 2004, Icarus, 168, 1

—. 2006, Icarus, 183, 265

Raymond, S. N., Schlichting, H. E., Hersant, F., & Selsis, F. 2013, Icarus, 226, 671

Rein, H. 2012, MNRAS, 427, L21

Rein, H., Payne, M. J., Veras, D., & Ford, E. B. 2012, MNRAS, 426, 187

Reufer, A., Meier, M. M. M., Benz, W., & Wieler, R. 2012, Icarus, 221, 296

Ribas, Á., Merín, B., Bouy, H., & Maud, L. T. 2014, A&A, 561, A54

Rice, W. K. M., Lodato, G., Pringle, J. E., Armitage, P. J., & Bonnell, I. A. 2004, MNRAS, 355, 543

Ringwood, A. E. 1966, Geochim. Cosmochim. Acta, 30, 41

Robert, F. 2001, Science, 293, 1056

Robert, F. 2006, Solar System Deuterium/Hydrogen Ratio, ed. D. S. Lauretta & H. Y. McSween, 341–351

Romeo, A. B. 1992, MNRAS, 256, 307

Russell, S. S., Hartmann, L., Cuzzi, J., et al. 2006, Timescales of the Solar Protoplanetary Disk, ed. D. S. Lauretta & H. Y. McSween, 233–251

Ryder, G. 1990, EOS Transactions, 71, 313

Ryder, G. 2001, in Lunar and Planetary Inst. Technical Report, Vol. 32, Lunar and Planetary Science Conference

Ryder, G., Koeberl, C., & Mojzsis, S. J. 2000, Heavy Bombardment on the Earth at ˜3.85 Ga: The Search for Petrographic and Geochemical Evidence, ed. R. M. Canup, K. Righter, & et al., 475–492

Safronov, V. S. 1960, Annales d'Astrophysique, 23, 979

—. 1964, Problems of Cosmogeny, 6, 71

Schlichting, H. E., Sari, R., & Yalinewich, A. 2015, Icarus, 247, 81

Schmitt, F. G. 2007, Comptes Rendus Mecanique, 335, 617

Schneider, J., Dedieu, C., Le Sidaner, P., Savalle, R., & Zolotukhin, I. 2011, A&A, 532, A79

Schubert, G., Solomatov, V. S., Tackley, P. J., & Turcotte, D. L. 1997, in Venus II: Geology, Geophysics, Atmosphere, and Solar Wind Environment, ed. S. W. Bougher, D. M. Hunten, & R. J. Phillips, 1245

Seager, S., Kuchner, M., Hier-Majumder, C. A., & Militzer, B. 2007, ApJ, 669, 1279

Seager, S., & Mallén-Ornelas, G. 2003, ApJ, 585, 1038

Shakura, N. I., & Sunyaev, R. A. 1973, A&A, 24, 337

Shannon, A., Jackson, A. P., Veras, D., & Wyatt, M. 2015, MNRAS, 446, 2059

Shu, F. H. 1992, The physics of astrophysics. Volume II: Gas dynamics.

Shu, F. H., Johnstone, D., & Hollenbach, D. 1993, Icarus, 106, 92

Springel, V. 2010, ARA&A, 48, 391

Stansberry, J., Grundy, W., Brown, M., et al. 2008, Physical Properties of Kuiper Belt and Centaur Objects: Constraints from the Spitzer Space Telescope, ed. M. A. Barucci, H. Boehnhardt, D. P. Cruikshank, A. Morbidelli, & R. Dotson, 161–179

Stewart, S. T., & Leinhardt, Z. M. 2012, ApJ, 751, 32

Sumi, T., Kamiya, K., Bennett, D. P., et al. 2011, Nature, 473, 349

Surville, C., Mayer, L., & Lin, D. N. C. 2016, ArXiv e-prints, arXiv:1601.05945

Tanaka, H., Takeuchi, T., & Ward, W. R. 2002, ApJ, 565, 1257

Teyssier, R. 2002, A&A, 385, 337

Thiabaud, A., Marboeuf, U., Alibert, Y., et al. 2014, A&A, 562, A27

Tonks, W. B., & Melosh, H. J. 1993, J. Geophys. Res., 98, 5319

Toomre, A. 1964, ApJ, 139, 1217

Toro, E. F. 1997, Riemann solvers and numerical methods for fluid dynamics : a practical introduction (Berlin, New York: Springer)

Tsiganis, K., Gomes, R., Morbidelli, A., & Levison, H. F. 2005, Nature, 435, 459

van Hoolst, T., Sohl, F., Holin, I., et al. 2007, Space Sci. Rev., 132, 203

Vanderburg, A., Johnson, J. A., Rappaport, S., et al. 2015, Nature, 526, 546

Vorobyov, E. I., & Basu, S. 2010, ApJ, 719, 1896

Wadsley, J. W., Stadel, J., & Quinn, T. 2004, New A, 9, 137

Walker, R. J. 2009, Chemie der Erde / Geochemistry, 69, 101

Walsh, K. J., Morbidelli, A., Raymond, S. N., O'Brien, D. P., & Mandell, A. M. 2011, Nature, 475, 206

—. 2012, Meteoritics and Planetary Science, 47, 1941

Ward, W. R. 1981, Icarus, 47, 234

—. 1997, Icarus, 126, 261

Warren, P. H., & Taylor, G. J. 2014, The Moon, ed. A. M. Davis, 213–250

Weidenschilling, S. J. 1977, Ap&SS, 51, 153

Wetherill, G. W. 1992, Icarus, 100, 307

Williams, J. P., & Cieza, L. A. 2011, ARA&A, 49, 67

Wisdom, J., & Holman, M. 1991, AJ, 102, 1528

Wolszczan, A. 1997, in Astronomical Society of the Pacific Conference Series, Vol. 119, Planets Beyond the Solar System and the Next Generation of Space Missions, ed. D. Soderblom, 135

Wolszczan, A., & Frail, D. A. 1992, Nature, 355, 145

Zsom, A., Ormel, C. W., Güttler, C., Blum, J., & Dullemond, C. P. 2010, A&A, 513, A57

Zuber, M. T. 2001, Nature, 412, 220